Spectroscopy and chemical synthesis of interstellar ice analogues

Thesis

Spectroscopy and Chemical Synthesis of Interstellar Ice Analogues

A thesis submitted in partial fulfilment for the degree of Doctor of Philosophy

by

Binukumar G Nair

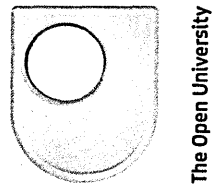

Department of Physical Science

The Open University

September 2014

DATE OF SUBMISSION: 23 SEPT 2014

DATE OF AWARD: 11 DEC 2014

ABSTRACT

Molecular synthesis and chemical evolution in the interstellar medium has been studied under laboratory conditions. The method of preparation and energetic processing of interstellar ice analogues on surfaces, spectroscopic principles for monitoring chemistry and morphology of these ice analogues and analysis methodologies are discussed in detail.

The modification of a portable, ultrahigh vacuum (UHV) system for electron irradiation, vacuum ultraviolet (VUV) spectroscopy and temperature programmed desorption (TPD) of interstellar ice analogues are described in this thesis. Experimental procedures to grow interstellar ice analogues of pure molecules and mixtures are described. The results from the various experiments discussed in this thesis are classified into four main parts: VUV spectroscopy, electron irradiation of interstellar (IS) ice analogues, simultaneous irradiation and generation of IS ice analogues and temperature programmed desorption of interstellar ice analogues.

Temperature dependent vacuum ultraviolet (VUV) photo-absorption spectra of pure molecular ices such as $HCONH_2$, HCOOH, $HCOOCH_3$, CH_2CHCH_2OH CH_3COOCH_3, CH_3CH_2COOH, C_6H_6 and O_3 have been measured on the UV1 beamline of the ASTRID Synchrotron at the University of Aarhus in Denmark and UV A1 beamline at NSRRC, Taiwan. These spectra and photo-absorption cross-sections in the condensed phase are also presented. In particular, temperature dependent VUV photo-absorption characteristics of condensed ice films of O_3 are measured for the first time. Electron induced molecular synthesis in pure organic ice films of $HCONH_2$, $HCOOCH_3$, CH_3COOH, NO and binary ice mixtures of CH_3OH+NO (1:1) are also reported. Newly identified pathways of molecular synthesis are discussed. Molecular synthesis during simultaneous electron irradiation and physisorption of a binary mixture of CH_3OH+NH_3

(1:1) is studied for the first time. Simultaneous irradiation-deposition has shown very interesting behaviour in terms of efficiency of formation of radical species such as OCN^-, NH_4^+ etc and biologically important complex organic species such as $HCONH_2$, $HCOOCH_3$, CH_3COOH, CH_3OCH_3, CH_2CHCHO etc. Simultaneous irradiation-deposition closely simulate the effect of cosmic ray irradiation in a dense molecular cloud and reveal new pathways of formation with higher efficiencies even at lower column densities of reactants. Finally preliminary results of a temperature programmed desorption study of pure NO ice films are also presented along with the future challenges and strategies.

ACKNOWLEDGEMENTS

I would like to extend my gratitude to everyone who generously supported me during the period of my PhD. I express my deepest gratitude to my supervisor, Professor Nigel Mason for the encouragement, excellent guidance, patience and advice provided throughout my PhD. I am extremely grateful to have a supervisor who cared so much about me and my research work. This thesis would not have been possible without the help, support and advice of my second supervisors Professor E. Krishnakumar and Professor Nick Braithwaite, your advice and guidance have been invaluable on both an academic and personal level, for which I am extremely grateful.

I would also like to thank all the members of staff at the Department of Physical Sciences, The Open University, for the fruitful discussion, support and advices. In particular I would like to thank Sandra Mills and Martin Percy who always helped me in the lab. I would like to thank all the members of OU Astrochemistry group, Dr. Helen Fraser, Dr. Anita Dawes, Dr. Jeronimo, Aleksi, Pavel, Natalia, Catherine and Olivier. I would like to thank all my fellow researchers in the department, especially Ewelina, Antony, Ziad, Alexandre and Rob, my research would not have been possible without your help. I am most grateful to Dr. Bhala Sivaraman for the valuable advice, friendship and support throughout my PhD. Special thanks to Dr. Sergio Pilling, and Dr. Antonio Escobar, it was always great to work with you.

Data and experimental results presented here are the outcome of the work performed by collaborating with many external groups. I would like to thank all staff at the ASTRID-UV beamline, especially Dr. Nick Jones, Dr. Soren Hoffmann, and Dr. Smialek Telega who helped me a lot during my experiments. I would like to thank all the staff and students at the NSRRC-VUV beamline, Dr. Cheng, Dr. Lou, Lin, Chou, I am

grateful to all of you. I would like to thank Professor Maria Palumbo, Professor Giovanni and all the staff at INAF, Catania. I am grateful for their support.

It would not have been possible to write this thesis without the help and support of the kind people around me, to only some of whom it is possible to give particular mention here, Ajith, Jino, Valan, Pandi, Siva, Vimal, Anish, Santana, Manimuthu, Deepu and to all my friends, they were always supporting me and encouraging me with their best wishes. I would like to thank all the members of GB group and everyone in JNVV for the motivation and support.

I would like to thank the LASSIE-EU network, for providing funding particularly in the award of an ESR-Studentship that provided the necessary financial support for this research and travel support to attend conferences, workshops and summer schools. Without that, I might not have met so many interesting people; I would like to thank all the members of LASSIE-EU network for their support and help.

Above all, I would like to thank Achan, Amma and Chechi for their unequivocal support throughout my research life, as always, for which my mere expression of thanks likewise can not be sufficient.

CONTENTS

List of Tables

List of Figures

CHAPTER 1

"Twinkle, twinkle, little star
How I wonder what you are."
- Jane Taylor

1.0 Introduction

The physics, chemistry and physio-chemical conditions that support components of intelligent life in our universe are interlinked and one of the crucial, ubiquitous candidates that entwines them are '*stars*'. The evolution of interstellar matter through the life cycle of stars constitutes the chemical complexity of the Universe. The interplay between physics and chemistry in stellar, interstellar, galactic and intergalactic space has a profound interdependence and such interactions, revealed through the interactive behaviour of the microscopic nature of a chemical system, directly influence the macroscopic properties of a system on astronomical scales. Physical phenomena, both on spatial and temporal scales always have a chemical signature and to appreciate the evolution of universe, in terms of matter, radiation and energy exchange; we need a clear picture of both the physical and chemical evolution of the Inter-Stellar Medium (ISM). Therefore investigating the microscopic chemical dynamics of stellar and interstellar systems is vital for determining the wider physical picture and may reveal the route of formation of the extremely complex molecules that are necessary for intelligent life.

Exploring the microscopic chemical behaviour of astronomical systems is extremely challenging because of the enormous spatial and temporal ranges. However, a collective approach through observation, modelling and laboratory based experiments can generate an unambiguous picture of the evolution of matter in

interstellar space and the scale of complexity of chemical, physical and biological (or intelligent life) systems generated through such evolutionary pathways.

1.1 The interstellar Medium (ISM): matter, radiation and evolutionary cycle

The space around and in between the stars and the stellar systems in a galaxy are not empty and this medium is called the 'InterStellar Medium' (ISM). The matter occupying this space is a dynamic component which exchanges matter and energy with other systems in the galaxy and thereby plays a vital role in the evolution, structure and dynamics of a galaxy.

Table 1.1 Physical conditions in various regions of the ISM [Tielens (2006)]

Regions	Number density (cm^{-3})	T (K)	Mass kg	Diameter (m)	Pressure (Atm)
Diffuse clouds (Neutral atomic gas)	50	~80	10^{32}	1×10^{17}	5×10^{-19}
Diffuse clouds (Ionized gas)	100-1000	$100\text{-}10^{5}$	10^{32}	1×10^{17}	1×10^{-19}
Dense molecular clouds	5000	10	10^{34}	2×10^{17}	5×10^{-18}

Observations have revealed that the distribution of interstellar matter doesn't follow a homogeneous and isotropic pattern. Line broadening corresponds to a single transition and Doppler shift broadening can quantify the relative density distribution of matter in the line of sight [Sheldon Green 1981; Tielens 2006]. The distribution of matter in ISM is observed, identified and characterized with respect to gas temperature, density distribution, the availability of energy sources etc. Astrophysical

models confirm these observations and extend this picture to various regions of the ISM [Tielens 2006; Leung 1984].

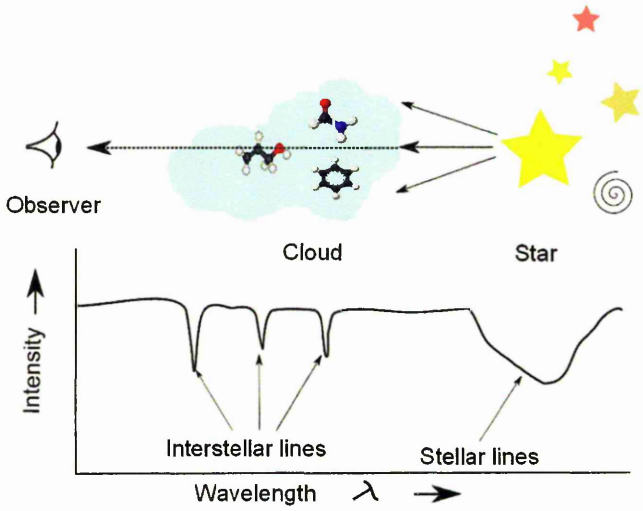

Figure 1.1 Line-of-sight observations of an interstellar cloud, sharp absorption features are the result of molecular or atomic clouds whilst broader absorption features are of stellar origin.

Matter distribution in ISM is structured as diffuse clouds (neutral atomic, ionized or translucent molecular), dense or dark molecular clouds, photodissociation regions (PDRs), supernova remnants (SNR), dark nebulae, reflection nebulae etc [Tielens 2006]. Diffuse clouds have interstellar gas in neutral atomic or ionized phase, a typical number density of the order ~ 10^3 cm^{-3} and temperature in the range of 100-10^6 K, **Table 1.1**(hot inter-cloud and warm ionized medium) [Tielens 2006; Herbst 1995]. The elemental composition of the region strictly follow the cosmic composition, hydrogen and helium constitute 99% of the mass and rest of the gases constitute below 0.1 % of the mass, heavier metal concentrations are below 0.01 % [Herbst 1995; Herbst et al. 2009]. Gas clouds with densities higher than diffuse clouds and lower than molecular clouds are classified as translucent clouds. Diffuse clouds

and translucent clouds are very rich in photo physical-photo chemical processes and exist as ionized gas or neutral gas [Herbst 1995].

Figure1.2 The regions of ISM (a) reflection nebula (b) Dark nebula, Horse head nebula in Orion, (c) Supernova remnant crab nebula, (d) Bernard 68 dark or molecular cloud (Image credit: N.A.Sharp/ NOAO/AURA/NSF)

Dense or dark molecular clouds (**Figure 1.2**) are molecular in nature and have densities in the order of ~ 10^4-10^7 cm^{-3} (**Table 1.1**) with temperatures in the 10-100 K range [Herbst 2005] and as the name depicts the cloud is opaque. In addition to molecules, 10-15% of the mass is composed of dust, made up of silicon or carbon atoms or composite structures [Allamandola 1999]. Molecules and dust co-exist as separate as well as combined entities. The molecular clouds exist as an inhomogeneous entity and there are two different types of dense molecular clouds, those which have a hot molecular core (HMC) with a star or a proto-star in the core and cold molecular core (CMC) without a parent star at core. Hot molecular cores

have temperatures greater than 100 K and size ranging from 0.7 parsec to less than 0.1 parsec in size [Tielens 2006] and support star formation, and function as a 'star nursery' in the interstellar medium [Ehrenfreund 2000]. The Bernard dark cloud (B68), shown in **Figure1.2 (d)** is an example of a star forming region. In-fall and evolution of hot cores results in desorption of the accreted ice mantles whose molecules are released back into the gas phase [Ehrenfreund 2000]. Eventually, during evolution of the star, the surrounding material forms a disc of debris and may leads to formation of planetary bodies around the star. The representative fractional abundances of ions, atoms and molecules in various regions of interstellar medium are shown in **Figure 1.3.**

Photodissociation regions or photo-dominated regions (PDRs) separate the ionized medium from molecular regions of ISM and are primarily neutral atomic or molecular in nature; PDRs emit primarily in the infrared and exist around bright luminous O and B type stars [Hollenbach 1997]. Part of the Orion nebula or NGC 2023 shown in **Figure 1.2 (b)** is an example of a PDR. Far Ultraviolet (FUV) photons with energies range 6-13.6 eV [Hollenbach 1997] interact with atoms and molecules and results in photodissociation and photo-electric heating of gas. In addition, FUV photons cause dust heating, as a result PDRs dominate emission in the observed IR continuum [Tielens 2006].

Dark nebulae are observable only with backlight, in the absence of stars and with a visual extinction coefficient $A_\upsilon > 10$, they are completely dark [Tielens 2006]. However, they can be observed due to the faint reflected light in the optical region or at bright mid-IR and far IR wavelengths. Molecules are also observed in cosmic, intergalactic and circumstellar space.

The physical characteristics of these regions are listed in **Table 1.1**. Gas clouds with densities slightly higher than 10^3 cm^{-3} reflect starlight from B1 type stars

that are recognizable in visible window are classified as reflection nebulae. Even though less luminous, they emit IR from heated dust, **Figure 1.2 (b)** depicts a reflection nebulae. (NGC 2023 in Orion constellation is also an example).

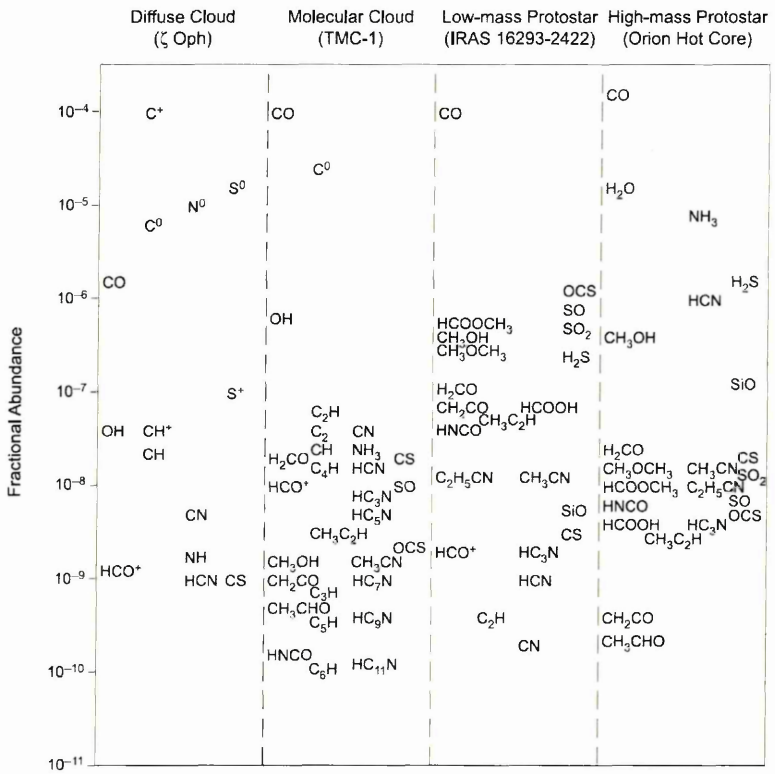

Figure 1.3 The representative fractional abundances of ions, atoms and molecules in various regions of interstellar medium [Sheldon Green 1981; Tielens 2006; and Bottinelli 2004].

Physical and chemical stages of the ISM are regulated by energy sources in the galaxy. Interstellar photon fields, a major factor in processing gas and dust are radiated by early-type stars to late type stars; photons with energy ranges from extreme UV(EUV) to near IR photons infuse the medium and drive the evolution of interstellar matter. Supernova remnants (SNRs) and hot plasma or coronal gas emit high energy photons in the X-ray region, in addition extragalactic sources also contribute photons in this region. EUV photons from stellar sources are almost entirely absorbed by neutral hydrogen up to 13.6 eV [Tielens 2006]. Photo-excited dust grains emit discretely in mid-IR and contribute towards continuum emission in

far-IR and sub-millimetre region [Savage and Mathis 1979]. The millimetre region is dominated by cosmic microwave background radiation. The energy balance in the ISM from various sources is listed in **Table 1.2.**

Table 1.2 Energy sources and energy budget in the ISM (Adapted from Tielens (2006))

Source	Energy density ($eV\ cm^{-3}$)	Heating rate ($erg\ s^{-1}$ H-atom)
Thermal	6.0	-5
UV	0.5	5
Cosmic rays	2.0	3
Turbulence	1.5	1

Cosmic rays consist of relativistic protons with energies ranging from 1-10 GeV, 10% helium atoms, heavier elements and electrons. Cosmic rays (CR) follow galactic magnetic fields and generally are confined to the disk plane. High energy cosmic rays with energy greater than 100 MeV $nucleon^{-1}$ are believed to originate from supernovae; high energy CR protons interact with the interstellar gas and result in gamma ray emission and also result in sputtering of interstellar dust [Black et al. 1987; Salpeter 1977]. Low energy cosmic rays ~ 100 MeV $nucleon^{-1}$ heat and ionize the interstellar gas and result in the formation of radicals and simple molecules such as OH [Snow and McCall 2006]. Sources such as galactic magnetic fields, shocks, out-flow etc also contribute toward the kinetic energy budget of interstellar space. As a result of the interaction with radiation in various physical conditions, interstellar matter undergoes a cycle of evolution. The fusion cycle inside stars contribute much towards the less abundant heavier constituents of ISM. The thermal history of universe and relationship of matter and radiation in early epoch is shown in **Figure 1.4.**

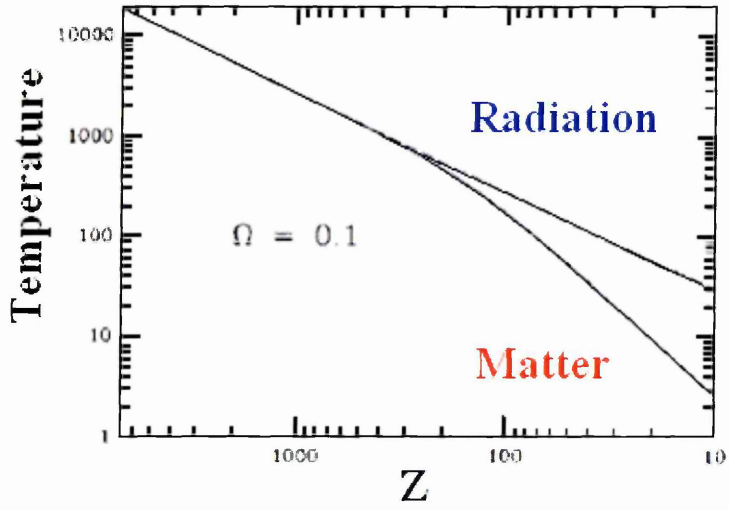

Figure 1.4 The thermal history of universe [Black et al. 1987]

Simple or complex organic and inorganic molecules are processed inside the interstellar clouds or planetary conditions undergoing a cyclic process from solid-to-gas-to solid [Herbst and van Dishoeck 2009]. Appreciating the chemical complexity of the ISM can only be accomplished by investigating the microscopic behaviour of various components of ISM.

1.2 Astrochemistry

The molecular nature of the ISM has been a quest for astronomers since the detection of diatomic CH molecule in the optical emission window in 1941, Turner and Zuckerman 1974 first confirmed the existence of stable molecules and ions in the interstellar environment. Subsequent detection of CH^+ [Jefferts et al. 1970] and CN [Mathis 1990] lead to a wider search for more species and began a quest for finding exotic species in the interstellar environment which eventually led to a new era of molecular astrophysics. However, optical and radio observations were not adequate to detect larger species. The implementation of millimetre wave spectroscopy aided the

detection of polyatomic molecules with high spectral and special resolutions. Then the ultimate question arose, how are these molecules synthesized in the ISM? To appreciate the formation pathway of complex polyatomic molecules we need to quantify the distribution of matter, energy sources and dynamics of such a system in the observed region of interstellar space. Observations alone could not generate a clear picture of such complex systems, therefore employing a combined method of observation, laboratory experiments chemical models could explain the complexities of the system. **Figure 1.5** shows the evolution cycle of matter in the local galactic environment.

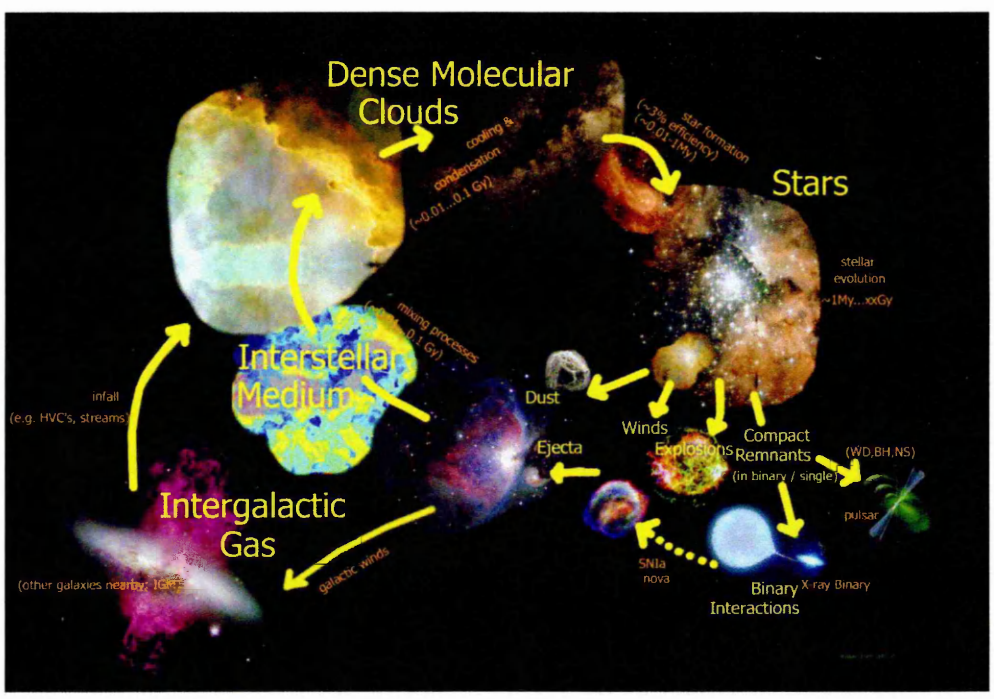

Figure 1.5 Cycle of interstellar matter [Roland Diehl, AWR proceedings 2011]

Astrochemistry or astrophysical chemistry explores the formation, destruction and rearrangement of molecular systems and their influence on the structure, evolution and dynamics of astronomical bodies [Tielens 2006]. To date more than 160

species has been identified in ISM, including planetary bodies, comets and asteroids. A list of the species detected in ISM are given in the **Table 1.3**, the highlighted species are discussed in various studies in this thesis.

1.3 Dust and ice in space

Dust grains accounts for ~10 % of the interstellar mass, they are composed of silicate or carbon atoms and their sizes range from a few atoms to particles of 1 μm in size, shown in Figure 1.6 [Salpeter 1977]. Dying stars are the main source of interstellar dust; cold, dense envelopes of such stars support the nucleation of carbon or heavier atoms (formed through thermonuclear process in the core of stars) to form dust grains, these dust grains are transported out of the stellar envelope by the outflow of the gas-dust mixture generated by the radiation pressure of the parent star, accelerated outflows of a dying star displace the dust into interstellar space and eventually these dust grains permeate the interstellar space along with ambient gas. Novae and supernovae eruptions generate tremendous amounts of dust and gas and also contribute a major portion of heavier elements in the interstellar environment.

Table 1.3 List of interstellar molecules [http://www.astro.uni-koeln.de/cdms/molecules].

2 atoms	3 atoms	4 atoms	5 atoms	6 atoms	7 atoms	8 atoms	9 atoms	10 atoms	11 atoms	12 atoms	>12 atoms
H_2	C_3	c-C_3H	C_5	C_5H	C_6H	CH_3C_3N	CH_3C_4H	CH_3C_5N	HC_9N	c-C_6H_6	$HC_{11}N$
AlF	C_2H	l-C_3H	C_4H	l-H_2C_4	CH_2CHCN	$HC(O)OCH_3$	CH_3CH_2CN	$(CH_3)_2CO$	CH_3C_6H	$C_2H_5OCH_3$	C_{60}
AlCl	C_2O	C_3N	C_4Si	C_2H_4	CH_3C_2H	CH_3COOH	$(CH_3)_2O$	$(CH_2OH)_2$	C_2H_5OCHO	n-C_3H_7CN	C_{70}
C_2	C_2S	C_3O	l-C_3H_2	CH_3CN	HC_5N	C_7H	CH_3CH_2OH	CH_3CH_2CHO	$CH_3OC(O)CH_3$		
CH	CH_2	C_3S	c-C_3H_2	CH_3NC	CH_3CHO	C_6H_2	HC_7N				
CH+	HCN	C_2H_2	H_2CCN	CH_3OH	CH_3NH_2	CH_2OHCHO	C_8H				
CN	HCO	NH_3	CH_4	CH_3SH	c-C_2H_4O	l-HC_6H	$CH_3C(O)NH_2$				
CO	HCO+	HCCN	HC_3N	HC_3NH+	H_2CCHOH	CH_2CHCHO	C_8H–		2 atoms	3 atoms	
CO+	HCS+	HCNH+	HC_2NC	HC_2CHO	C_6H–	CH_2CCHCN	C_3H_6		CF+	AlNC	
CP	HOC+	HNCO	HCOOH	NH_2CHO		H_2NCH_2CN			SiH	SiNC	
SiC	H_2O	HNCS	H_2CNH	C_5N		CH_3CHNH			PO	HCP	
HCl	H_2S	HOCO+	H_2C_2O	l-HC_4H					AlO	CCP	
KCl	HNC	H_2CO	H2NCN	l-HC_4N					OH+	AlOH	
NH	HNO	H_2CN	HNC_3	c-H_2C_3O					CN–	H_2O+	
NO	MgCN	H_2CS	SiH_4	H_2CCNH					SH+	H_2Cl+	
NS	MgNC	H_3O+	H_2COH+	C_5N–					SH	KCN	
NaCl	N_2H+	c-SiC_3	C_4H–	HNCHCN					HCl+	FeCN	
OH	N_2O	CH_3	HC(O)CN						TiO	HO_2	
PN	NaCN	C_3N–	HNCNH						ArH+	TiO_2	
SO	OCS	PH_3	CH_3O						HD		
SO+	SO_2	HCNO	NH_4+						FeO		
SiN	c-SiC_2	HOCN	H_2NCO+						O_2		
SiO	CO_2	HSCN									
SiS	NH_2	H_2O_2									
CS	H_3+	C_3H+									
HF	SiCN	HMgNC									

Dust can easily be detected by its IR emission features, dust absorbs light from a parent star in a cloud or photons from interstellar radiation field and re-radiates in the IR window. The number density of dust in an envelope of a dark cloud is typically ~ 10^{-12} cm^{-3} with respect to the number of hydrogen atoms in the same region [Mathis 1990].

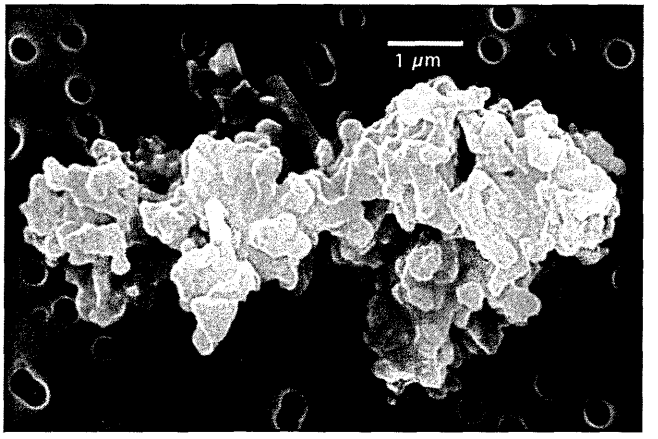

Figure 1.6 Interplanetary dust particle (Image courtesy NASA/JPL/Star dust).

Depending upon the star type and its stage of evolution, the elemental nature of the envelope differs and generally it could be either carbon rich or oxygen rich. In a carbon rich envelope a major fraction of the carbon exists as CO gas or other simple carbon based molecules and the rest of the carbon nucleates and forms carbonaceous dust. Carbonaceous dust has 60 % carbon, 30 % of oxygen and other heavier elements in trace amounts [Van Dishoeck 2004]. In the case of an oxygen rich envelope, excess oxygen supports the formation of heavier oxides and silicates; hence the envelope will be rich in silicate dust grains. Silicate grains incorporate a higher percentage of Mg, Fe etc [Salpeter 1977; Tielens 2006].

Dust is constantly evolving with the dynamical processes in interstellar medium. Shocks generated by supernova can travel into the dense clouds; with magnitudes ranging from 10 to 100 km/s, these shocks can sputter or shatter dust grains and result in a reduction in their size or complete destruction [Salpeter 1977].

Cosmic ray sputtering can change a crystalline silicate to amorphous and also lead to CR induced chemistry which may alter the nature and size of the grain. UV photons also tend to change the chemical nature of the dust, for example, H rich tetrahedral amorphous carbon may be transformed into an H-poor form [Turner and Zuckerman 1974]. Dust coagulation in the vicinity of a low mass stars results in the formation of planetesimals, planets and comets.

In dense molecular clouds, the interstellar gas composition is dominated by simple molecules such as O_2, H_2O, CO, CO_2 etc, these gases condense on to a cold (~ 10 K) dust grain and continuous accumulation of various layers of absorbed (physisorbed) gas generates an icy grain mantle or 'interstellar ice'. Unprocessed interstellar ices in the dense cloud environment have layer sizes ranging from 0.01 μm to 0.5 μm [Ehrenfreund and Charnley 2000; Tielens 2006], but ice in planetary or cometary environment is much thicker and may contain complex organics and simple molecules in much higher quantities. A schematic representation of an interstellar ice mantle is shown in **Figure 1.7**. Gas phase abundances or the composition of the ambient medium have no or little influence on the composition of mantle layers, but chemical reactions between the gas phase species, relative sublimation rates, competition between energetic processing etc influence the composition and generate an ice mantle. However, the H/H_2 ratio influences the molecular composition of the ice mantle, $H/H_2 >> 1$ supports hydrogenation and leads to saturated organic molecules or polar molecules such as H_2O, NH_3, CH_4 etc. Non polar, oxygen or nitrogen rich ices are synthesized in a hydrogen poor environment ($H/H_2 << 1$), molecules such as CO, CO_2, N_2, NO dominate such ices [Grim and Greenberg 1989].

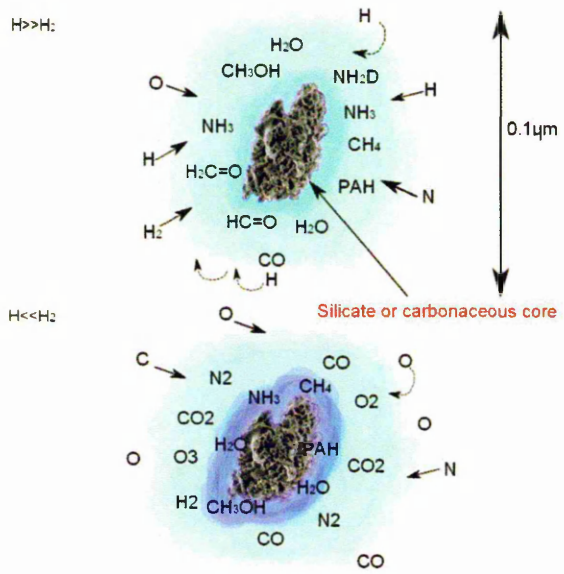

Figure 1.7 The interstellar ices. Without energetic processing the ice mantle is composed of simple molecules. Figure on the top shows an ambient medium where the column density of H>> H_2 and in the case of the bottom figure it is H<<H_2.

The availability of energetic sources leads to the processing of ices and hence synthesizes non-volatile complex organic molecules [Woon 2011; Charnley et al. 1992; Moore et al. 1983] a cartoon of interstellar ice processing is shown in **Figure 1.8**.

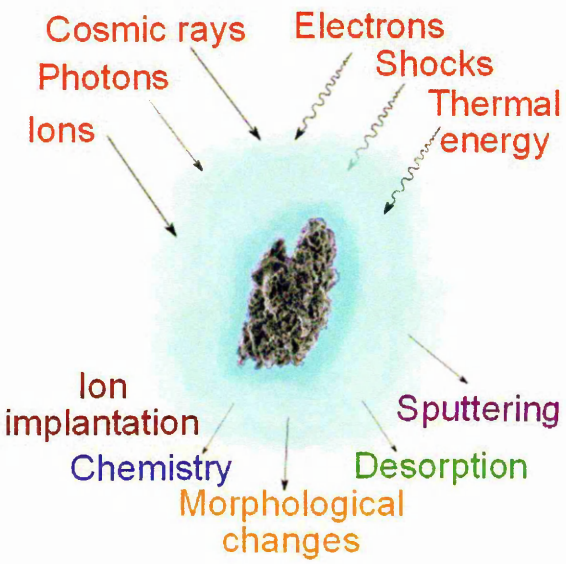

Figure 1.8 Energetic processing and its implications of interstellar ices

1.3.1 Gas phase chemistry

The chemical evolution of the ISM in the gas phase is influenced by the physical conditions of the medium. 70% of interstellar mass is composed of gas (neutral, radicals and ions) [Tielens 2006]. The primary chemistry in ISM is manifested as gas-phase reactions. Since the density of interacting species, radiation field and temperature conditions vary from region to region there are various types of gas phase chemical reactions. Energy sources also play a vital role in the gas phase chemical evolution of ISM. The following are various processes [Tielens 2006] leading to molecular evolution in the galactic and extragalactic space,

Formation of bonds

(a) Radiative association $X + Y \rightarrow XY + h\upsilon$

(b) Associative detachment $X^- + Y \rightarrow XY + e^-$

(c) Grain surface reactions $X + Y{:}g \rightarrow XY + g$

Rearrangement of bonds

(d) Neutral- neutral reactions $X + YZ \rightarrow XY + Z$

(e) Ion-molecule reactions $X^+ + YZ \rightarrow XY^+ + Z$

(f) Charge transfer reaction $X^+ + YZ \rightarrow X + YZ^+$

Destruction of bonds

(g) Dissociative re-combination $XY^+ + e^- \rightarrow X + Y$

(h) Photodissociation $XY + h\upsilon \rightarrow X + Y$

(i) Collisional dissociation $XY + M \rightarrow X + Y + M$

Among the above processes gas phase reactions dominate the list; however, dust-gas interactions and solid-state or surface reactions (c) are also important. The majority of these processes are two-body reactions since the density is of the order of 10^4 - 10^6 cm^{-3}, making the probability of three body interactions low [Leung 1984].

Radiative association is a very slow process and results in bond formation at a rate of $1:10^{10}$, i.e. one bond or a molecule is formed per 10^{10} collisions. However, if we consider electronic excitation and transitions with high barrier, the efficiency of the processes will be considerably enhanced up to $1:10^{5}$ [Tielens 2006]. Radiative association is a very slow and less efficient process, but it is relevant and an inevitable gas phase reaction. Associative detachment and dissociative recombination processes generally occur in ionized regions and conditions similar to early universe. Ion-molecule reactions are rapid even at the low temperature (exothermic reactions) and majority of the reactions (>90%) follow *Langevian* rates but there are exceptions such as $C^+ + OH \rightarrow CO^+ + H$ (ion-polar) which has rate coefficients of the order 10-100 times more than *Langevian* values. Neutral-neutral reactions have to overcome potential barriers in entrance and exit channels, however this type of reactions are fast (higher rate) at low temperatures [Sims 1993]. There are several types of neutral-neutral reactions (i) Molecule-molecule (ii) Radical-saturated molecule (iii) Radical-unsaturated molecule and (iv) Radical - radical reactions [Tielens 2006]. Rate coefficients at various temperatures are computed for the gas phase reactions and incorporated to complex astrochemical models to predict the observed abundance ratios, even though there are large numbers of reaction sets, the model is mainly based on the above basic processes. Astrochemical models also invoke an insight into the potential molecules that can be observed in a known region and also give a design of complexity of the interstellar region of interest.

1.3.2 Surface chemistry in interstellar medium

Gas phase processes occur at extremely slow rates and the products of such reactions existing in gas phase have high probability of destruction, therefore there must be an alternative processes, which is highly efficient, such as a formation pathway via solid-state or surface supported molecular synthesis. Molecular synthesis on an interstellar dust grain mantle surface is well supported by the observational, model and laboratory evidence. Indeed the observed densities of highly abundant molecules such as H_2O, CH_3OH, $HCOOCH_3$ etc and formation of molecular hydrogen (H_2) in ISM can only be explained by surface formation processes. Molecular formation on surfaces may proceed by direct (Langmuir-Hinshelwood) or by diffuse mechanisms (Eley-Rideal).

- Direct mechanism

$$X + Y :g \xrightarrow[\text{Direct reaction}]{} X\text{-}Y:g \longrightarrow XY + g \quad (\text{Desorption})$$

- Diffuse mechanism

$$X+Y:g \longrightarrow X:g:Y \longrightarrow X\text{-}Y:g \longrightarrow XY+ g$$

IR absorption by material in the dense clouds reveals that an ice mantle of several monolayers of H_2O on dust grains exist in the line of sight and in addition, CO and CO_2 constitutes 25% and 22% respectively [Tielens 2006]. In addition to these simple molecules there exists an inventory of complex non-volatile organic species such as PAHs, cyanopolyynes, glycine etc. The survival probability of such species adsorbed on to the dust grain in a dense molecular cloud is high when compared to diffuse or translucent clouds. The prime factor which leads to the detailed

investigation of a surface reaction is to solve the mystery of molecular hydrogen formation (H_2). Gas phase mechanisms can not support the formation of molecular hydrogen formation, and through a detailed systematic modelling and laboratory experiments revealed that efficient mechanism of H_2 formation could be supported by grain surface. When an atom or molecule collides with a dust grain, there will be an exchange of kinetic energy and the dust re-emits in IR and leads to cooling of the local medium. Collisions also transfer excess energy carried by an atom, ion or a radical and stick onto the grain surface with minimum energy. Cold dust grains support adsorption at the highest level, with a sticking coefficient~1. In an ideal situation atoms or ions (except He) adsorbed on the grain surface diffuse or hop (thermal hopping) around the grain surface or tunnel the potential barriers (H, H_2) and congregate together [Tielens 2006]. If the activation barrier is low, it may lead to formation or rearrangement of bonds. Simple molecules are formed and desorbed back into gas phase, the excess energy will be liberated to grain surface.

Thermal, cosmic ray, shock and UV photon processing enhances the chemical synthesis and generates complex molecules, accretion of more and more molecules boosts the reaction rate and develops in the inventory of complex species.

Gas-grain interactions of secondly abundant species such as C, N, O, other atoms, ions and radicals results in the surface accretion of these species. Gas-grain-ice interactions in the vicinity of a molecular cloud core are shown in **Figure 1.9**.

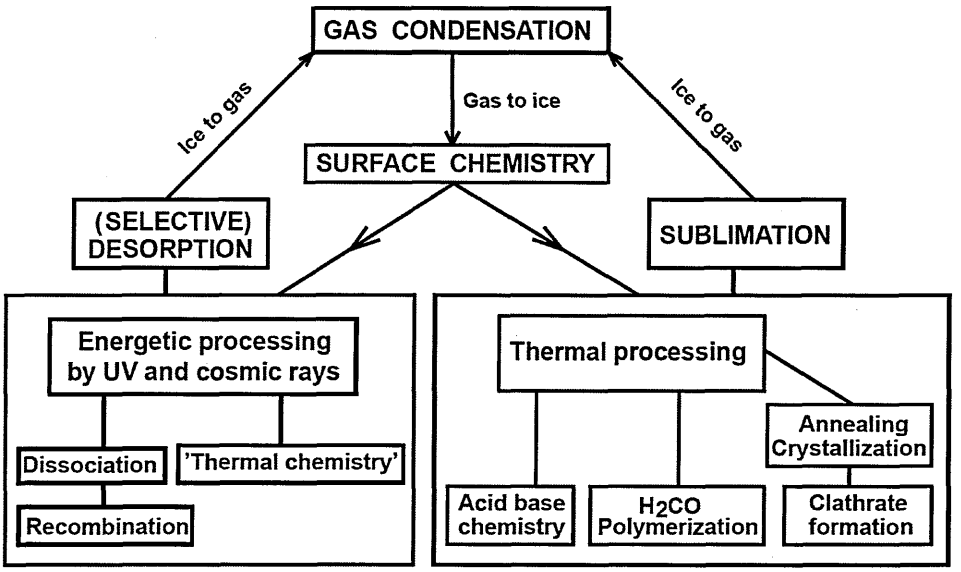

Figure 1.9 Gas-grain-ice interactions in the vicinity of a molecular cloud core [Figure adapted from Ehrenfreund and Charnley 2000]

Mobility and rate of diffusion are different for different species, however, they interact in various ways, and the main types of surface reactions are,

1. Atom-atom reaction $N + O \rightarrow NO$
2. Radical-atom reaction $H + NO \rightarrow HNO$
3. Radical-radical reaction $CH_3 + OH \rightarrow CH_3OH$
4. Radical-H_2 reaction $OH + H_2 \rightarrow H_2O$
5. Molecule-atom reaction $CO + O \rightarrow CO_2$
6. Hydrogen abstraction reaction $H_2CO + H \rightarrow HCO + H_2$

The above reactions perform as well connected surface chemical networks which contribute towards the extremely complex and enormous molecular inventory. Molecular synthesis is initiated with and without energetic processing of surfaces, the network in **Figure 1.10** shows the network of reactions involving carbon monoxide

molecule (CO). CO is a simple, non-polar molecule which has a very high abundance in the ISM and the chemical network shows how CO is getting evolved with a surface chemical network.

1.4 Energetic processing of interstellar and planetary ices

Laboratory simulation of energetic processing of icy grain mantles is vital to understand and verify formation pathways of interstellar species and also to quantify the products of interstellar chemical synthesis.

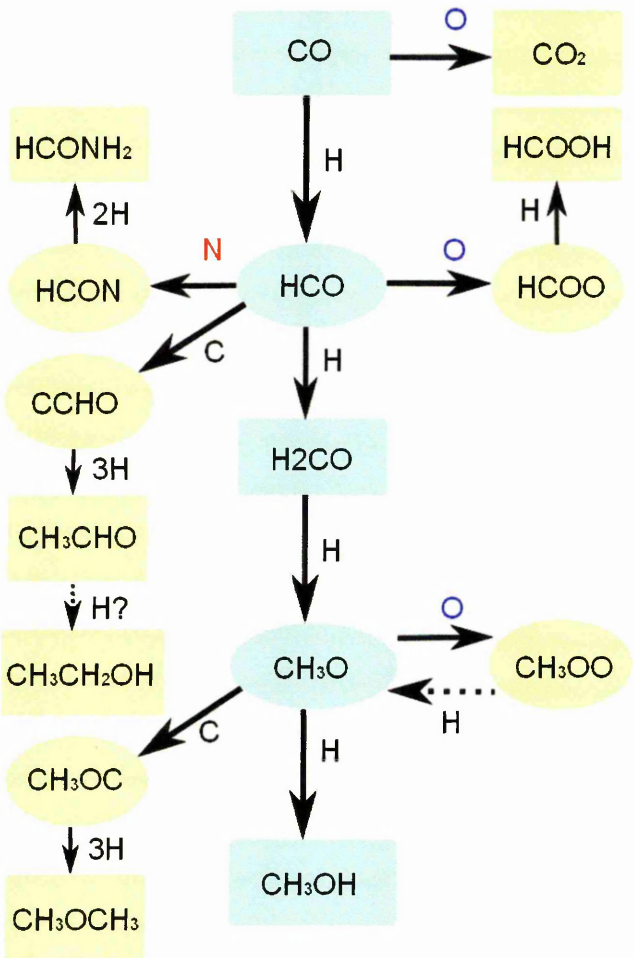

Figure 1.10 Surface chemistry of CO [Tielens 2006]

Astrochemical models and quantum chemical calculations can predict the rate of reaction, barrier height, and probability of alternate pathways, tunnelling, chemical time etc and models can test reactions which are practically impossible to perform under laboratory conditions. However, laboratory experiments are inevitable for astrochemistry; without spectral data from laboratory, detection and confirmation of new species with observation is impossible. Rate coefficients of various reactions measured in laboratory are incorporated into astrochemical models.

Energetic processing such as thermal, ion irradiation, electron irradiation, proton irradiation, photo processing, shock processing etc can result in structural or morphological changes, chemistry, ion implantation, sputtering and desorption of interstellar ice analogues. Sputtering of icy mantle by heavy ions cosmic rays and thermal processing is very important since it is the foremost mechanism which supports the observed abundances of complex organics in gas phase. Cosmic ray induced production of secondary electrons may result in anions [Millar et al. 2007], chemical changes [Herbst and van Dishoeck 2009; Herbst 2005] and charging of the dust and ice surface [Draine and Salpeter 1979]. UV photons drive the chemical synthesis and regulate the chemical structure by photochemical reactions, photo-dissociation and photo-ionization. Photo-dissociated regions (PDRs) are common in the vicinity of young stellar objects. Photons and electrons also contribute towards desorption of icy mantle into the gas phase. Thermal processing alter the morphology and result in desorption of the icy mantle. **Figure 1.8** depicts energetic processing in interstellar ices.

Cosmic rays play an extremely important role in the chemistry of the interstellar medium. (ISM) Cosmic rays are the primary ionization source in the dense molecular cloud regions where the density severely limits the entry of high energy photons. The ions produced by cosmic rays interaction then trigger the chemistry in

such environments via various ion-molecule reactions. The ion-molecule reactions lead to simple and complex molecules detected in the ISM. The low energy (100 MeV) cosmic rays are primarily responsible for ionizing the ISM. The most recent calculation was performed by Webber (1998), who computed an ionization rate of $(3-4)\times10^{-17}$ s^{-1} using a cosmic ray spectrum extrapolated from data taken with the Pioneer and Voyager spacecraft [Webber 1998].

Photoionization and photodissociation also plays a crucial role in the chemical dynamics of the interstellar medium, especially in the Photo-dissociated regions and ionized hot and cold mediums. But photo-induced chemistry is limited by the Lyman edge of 912 A^0, and therefore the influence of photoprocess in dense molecular cloud is dominated by cosmic rays, and shocks. Secondary electrons of energies ranging from 1-5 kev are generated from the interaction of high energy cosmic rays (~ 1 GeV), these secondary electrons, secondary ions and protons are the major drivers of chemical dynamics in the dark clouds.

Icy surfaces of comets, planets, satellites and other astronomical bodies are also subject to energetic processing. Even though interstellar and planetary or cometary ice processing is initiated by the same agents, the synthesis or product evolution will be of a different nature due to the influence of ambient medium and the characteristics of the ices. Planetary ices are thick and dense in nature when compare to their interstellar counterparts and the density of molecules in the ambient space is three or four orders of magnitude higher than that of dark clouds. The thickness and porosity of ice regulates the penetration depth, thereby reducing the amount of matter that can be processed. A large number of complex organic molecules have been identified in comets and meteorites, while the dynamic history of such bodies reveals complex and rich chemistry. Appreciating such processes may reveal the origin of molecules of intelligent life.

1.5 Laboratory Astrochemistry

Interstellar chemical pathways for both gas phase and surface reactions can be simulated under controlled laboratory conditions. Interstellar cloud densities, temperature conditions and energetic sources are simulated to determine the influence of the physical conditions on chemical evolution. Simulating interstellar conditions is extremely changing, since the number density of dark clouds 10^4- 10^8 cm^{-3} correspond to a mean free path of ~10^4 to 10^6 meters. The number density at mean sea level at 300 K is ~ 10^{19} cm^{-3} and to achieve mean free path of the order of 10^3 meters, ultrahigh vacuum (UHV) conditions are required. Dynamic UHV is maintained inside a stainless steel chamber for simulating low density conditions; but even at UHV the chamber has residual gas constituting hydrogen (H_2) and other trace species. It is almost impossible to achieve the exact density conditions of interstellar medium, the best achieved vacuum on earth is maintained at Large Hadron Collider in Geneva and it is of the order of 10^{-14} mbar, still 10^3 times higher than the ISM. The whole range of molecular cloud like temperature conditions can be generated without much difficulty; temperatures from few Kelvin (2.7 K) to 300 K are readily achieved with excellent control over gradients. Time scale or the rate of interstellar reactions is the biggest constraint in the laboratory conditions; interstellar reactions take place over millions of years and with very slow rates. The collision time for two atoms to interact in the ISM is approximately 1 month at 10^4 cm^{-3}, with a life time of 10^7 years [Tielens 2006]; the chemical time in a dark cloud is ~ 10^5 years [Ehrenfreund 2000]. Therefore it is impossible to simulate the reactions at same rate or over interstellar time scale, but quantified reaction rates can be extrapolated and the rate coefficients can be incorporated into accurate chemical models to generate the interstellar reaction time scales.

Various energetic sources are employed to simulate the ISM conditions. The interstellar radiation field composed of cosmic rays, ions, shocks, thermal radiation etc can be simulated in laboratory conditions with high accuracy and control over the flux. Controlled reactions with such sources enable us to quantify the outcome of potential processes in ISM and determine the probability of those reactions predicted by chemical models. Electron guns can simulate cosmic ray induced secondary electrons of energy ranges 1-5 keV, synchrotron sources simulate UV photons from 3-15 eV, a combination of cryogenic fingers and intelligent temperature control system simulate temperature conditions in 10 to 300 K range and proton or ion sources simulate the other interactions.

In addition to gas phase or surface reaction simulation, laboratory studies generate reference spectra; those spectra are invaluable for observational astronomers, and support the detection of new species in the interstellar space. Laboratory based spectral data are in high demand after the commission of sub millimetre wave facilities such as Atacama Large Millimetre Array (ALMA). Laboratory based surface reactions, gas phase studies and spectral data bases fill the gaps in the perspective of chemical evolution of our universe and there by forms an essential part of astrochemistry.

From the observations by ground based millimetre-wave instruments and satellite based observations by Herschel, AKARI, ISO etc has shed light on the distribution of dust and ice in interstellar medium. Till date 178 species has been identified in the ISM, majority of them in gas phase, however, simple molecules such as water, CO, CO_2, NH_3, HCOOH etc were detected in both gas and ice phase [Tielens 2013]. Distribution of dust grains, both silicon and carbonaceous are observed towards SgrB2, and Orion, the distribution of dust is mapped with observing the emission far-IR and millimetre wave region. Ice mantles thickness (including dust

grain) was estimated to be ranging from 0.05 μm to 1 μm [Tielens 2013]. Dusts especially, SiO_2, SiC are used as a probe for investigating shock dynamics [Tielens 2013]. Along with dust, bigger molecules such as polycyclic aromatic hydrocarbons (PAHs), C60 are observed throughout the galaxy [Tielens 2013].

1.6 Structure and aim of this thesis

The chemical complexity, physical conditions and evolution of matter in interstellar medium conditions has been discussed in this chapter. Although more than 160 molecules have been identified in the interstellar space, very little is known about the processes leading to their formation. Regions of the ISM, physical conditions, the inventory of complex and simple species, dust, icy mantle accretion etc are discussed in detail. Energetic processing of icy dust mantles under interstellar conditions and simulation of such processes in laboratory conditions are also discussed. Laboratory simulations are invaluable for appreciating the chemical evolution of the interstellar medium and also to support astronomical observations.

Electromagnetic radiations, interactions of radiation with matter, molecular structure, vibrational and electronic spectroscopy of molecules, surface science and properties of molecules in condensed or ice phase are discussed in Chapter 2.

Details of the experimental methodology used for simulating interstellar conditions in the laboratory are discussed in chapter three. UHV design, mid-IR spectroscopy, synchrotron beamline, VUV spectroscopy, TPD techniques etc are discussed in detail.

The VUV spectroscopy of astrochemically relevant species is presented in chapter four. VUV absorption cross-sections and temperature dependent VUV absorption cross-sections of astrochemically relevant species are dealt with in detail.

The results of electron irradiation and thermal processing of interstellar ice analogues are presented in chapter five. The results of electron irradiation of pure ice films are examined in section 1 and the results of electron irradiation and thermal processing of methanol mixtures are presented in Section 2.

Electron irradiation and simultaneous deposition of interstellar ice analogues are investigated and presented in Chapter 6. Temperature programmed desorption studies of astrochemically relevant species and future challenges are discussed in Chapter 7.

CHAPTER 2

SPECTROSCOPY AND SURFACE SCIENCE

"Physicists are made of atoms. A physicist is an attempt by an atom to understand itself."
- Michio Kaku

2.0 Introduction

The interaction of radiation with matter can reveal various properties of interacting matter such as the elemental composition, its distribution in a medium, the nature of ambient medium around it and physical properties such as kinetic temperature, energy state etc. Radiation emitted or absorbed by matter has its intrinsic imprints and to investigate such interactions, it is crucial to understand the nature of radiation as well as structure and properties of atoms and molecules. This chapter deal with the nature and interactions of radiations with matter and the principles of spectroscopy. Chemical and physical properties of surfaces and spectroscopic methods for analysing surface properties are also discussed in detail.

2.1 Electromagnetic spectrum

The simple harmonic propagation of time-dependent, coupled electromagnetic fields is called electro-magnetic radiation (EM). Electric and magnetic field oscillations are mutually perpendicular and perpendicular to the direction of propagation of the radiation. EM radiation is quantized and the field particles are called 'photons', EM radiation exhibit both wave and particle nature and the field particle or photon has intrinsic spin. In vacuum, photons can propagate with a speed

of 3 x 10^8 m/s and have zero rest mass. Periodic oscillations of electric and magnetic fields can be expressed as a sine function,

$$y = A\sin\omega t \quad = A\sin 2\pi\upsilon t \tag{2.1}$$

$$y = \frac{A\sin 2\pi\upsilon x}{c} = \frac{A\sin 2\pi x}{\lambda}$$

$$y = A\sin 2\pi\bar{\gamma}x \tag{2.2}$$

where A is amplitude of the oscillation, υ is frequency of oscillation; λ is wavelength and $\bar{\gamma}$ is wave number or number of waves per 1 cm, expressed in cm^{-1}.

EM radiation transports energy from a source to a sink as discrete quanta of energy and during transport or interactions, they reflect, refract, scatter, diffract, interfere or polarize. Electromagnetic radiations are classified with respect to the energy of photons and spans from the high energy region of gamma radiation to the very low energy radio region. The collection of all these regions is known as the *electromagnetic spectrum*. **Figure 2.1** shows the various regions of electromagnetic spectrum and respective atomic or molecular interactions with equal amount of energy.

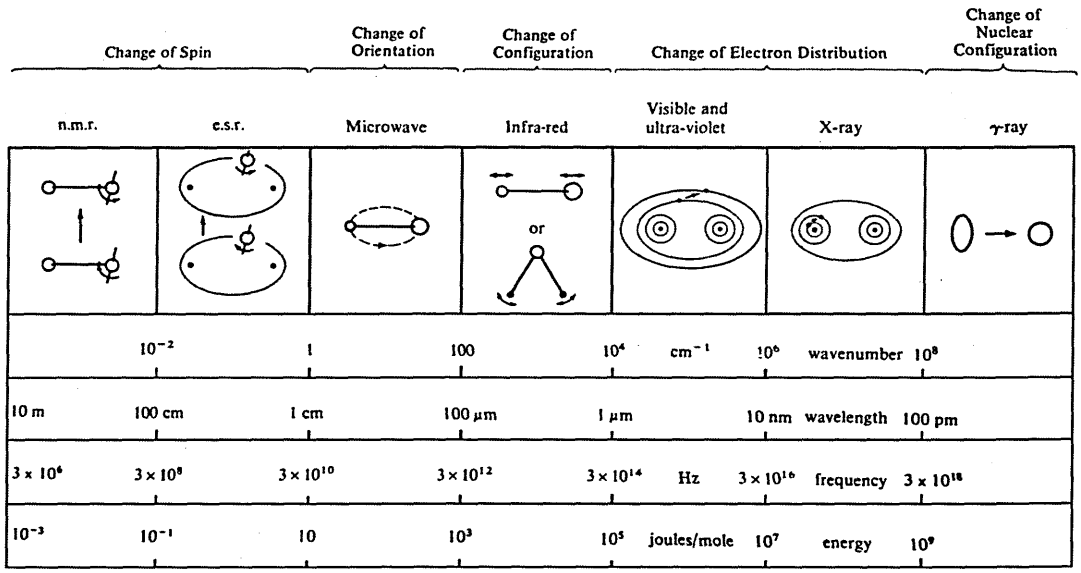

Figure 2.1 Regions of electromagnetic spectrum and respective atomic or molecular interactions [Adapted from Fundamentals' of molecular spectroscopy, Banwell 1995].

2.2 Atoms and molecules

2.2.1 Atomic orbitals and energy levels

The electronic wave function is governed by three elements (a) Physical constants (b) spatial co-ordinates and (c) quantum numbers. There are four atomic quantum numbers, principle (*n*), orbital (*l*), magnetic (m) and spin (s); these quantum numbers and allowed values, and probable orientation of electrons around a nucleus influenced by these numbers are listed in **Table 2.1**.

Table 2.1 The atomic quantum numbers

Quantum No.	Allowed values	Function
Principal, *n*	1, 2, 3.....	Governs the size and energy of the orbital
Orbital, *l*	(n-1), (n-2),....0	Governs the shape of the orbital and the electronic angular momentum.
Magnetic, m	±*l*, (*l*-1), ...0	Governs the direction of an orbital and the electrons behaviour in a magnetic field.
Spin, s	±1/2	Governs the axial angular momentum of the electron.

In addition to these orbital energies (represented by the principle quantum number n), electrons in an atom have discrete orbital and spin angular momenta, (represented by orbital quantum number and spin quantum number respectively). This allows the electronic structure of an atom to be expressed in terms of the number of electrons in each orbital. The *Pauli Exclusion Principle* states that each orbital can contain only one or two electrons, and if there are two electrons in an orbital they must have paired (opposite) spins. The spin quantum number m_s take a value of +1/2 or -1/2 to denote spin up (↑) or spin down (↓). The total angular momentum is represented by *j* and takes the value of (*l*±1/2), depending on whether the spin and orbital angular momenta are in the same direction or if they are opposite.

The orbital quantum number of an electron is combined with the energy level with the form *nl*, with the value for *l* replaced by a letter: *s* for 0, *p* for 1, *d* for 2, *f* for 3 and then alphabetically for higher orbitals. The *p* level consist of three orbitals (p_x, p_y, p_z representing x, y and z co-ordinates with respect to the atom), allowing it to contain six electrons. The *d* level can contain ten electrons in five orbitals. As the atomic number increases, electrons fill up the orbitals in the order of increasing

energy: 1*s*, 2*s*, 2*p*, 3*s*, 3*p*, 4*s*, 3*d*, 4*p*, 5*s*, 4*d*, and onwards. For example carbon has an atomic number 6 and hence has electronic structure,

$$1s^2\ 2s^2\ 2p_x^1\ 2p_y^1\ 2p_z^0$$

Full orbitals contain two paired electrons, one with spin up and one with spin down. However, in general only part-filled orbitals are considered when discussing atomic energy levels. These levels are denoted by term symbols, which summarise the total orbital and spin angular momenta of the atom. Term symbols take the form $^{2s+1}L_J$, where L is the total angular momentum quantum number, S is the total spin angular momentum (and 2S+1 is the multiplicity) and J is the total angular momentum. L and S are formed using the same method; the example equation (2.3) uses l and L. there is potentially a number of possibilities for any combination of angular momenta, but the range of values must remain positive, hence the modulus signs.

$$L=l_1+l_2, l_1+l_2-1 \ldots\ldots |l_1-l_2| \qquad (2.3)$$

In the case of L the same convention is used for expressing orbitals with s, p, d, f notation representing l, but in this case uppercase letters are used (S, P, D, F).

A full calculation of J can be complex when more than one electron is taken into account. However, for atoms with low atomic number (with weak spin-orbit coupling), *Russell-Saunders* coupling scheme can be used, as shown in equation (2.4).

$$J= L+S, L+S-1 \ldots\ldots\ldots |L-S| \qquad (2.4)$$

Combining these, the term symbol for atomic carbon in the ground state can be expressed as $^3P_0$.

2.2.2 Molecular structure and energy levels

Molecular electronic orbitals are made up of overlapping atomic orbitals, and the way in which atomic orbitals combine produces a number of different types of molecular orbital. Overlapping *s* and p_z orbitals (those along the molecular axis) form σ orbitals, the equivalent of atomic *s* orbitals; p_x and p_y orbitals (those perpendicular to the molecular axis) combine to form molecular π orbitals. The presence of a σ bond and one or two π bonds means that a double or a triple bond is formed between nuclei. For some polyatomic molecules (such as methane, CH_4) hybrid bonds are formed from a mixture of an *s* and three *p* orbitals (known as sp^3 hybridisation) to allow the formation of four molecular σ orbitals.

Excitations from these orbitals can take place to higher energy *non-bonding* or anti bonding orbitals. As the name suggests, non bonding orbitals do not contribute directly to the bonding between nuclei, as they are derived from an atomic orbital of only one atom; examples are the lone pairs found in water and ammonia. Anti-bonding orbitals, however, result from destructive interference between atomic orbitals and decrease the overall bond strength between nuclei. Anti bonding orbitals can be caused by over-lapping *s* and *p* orbitals, and are labelled as σ^* and π^*.

Molecular orbitals in homo-nuclear diatomic molecules are also labelled with a parity subscript to denote their behaviour under inversion. This process compares the sign of the electronic wave function at points exactly opposite each other through the central point o the molecule (the centre of inversion). Orbitals which keep the same sign are said to have even parity and are labelled with a subscript *g* for gerade (the German for "even") or orbitals which change have odd parity (ungerade) and are labelled with a subscript *u*.

In the same way as molecular orbitals use Greek characters to distinguish them from atomic orbitals, *molecular term symbols* use upper case Greek characters, but are otherwise constructed in a similar way. Molecular orbital angular momentum is represented by λ and total angular momentum by Λ (Σ, Π, Δ and Φ). However, the parity of the state replaces the total angular quantum number J. The parity of the state is found by treating even and odd orbitals as ± 1 and multiplying: $g \times g = 1 \times 1 = 1$; $u \times u = -1 \times -1 = 1$; $g \times u = 1 \times -1 = -1$. Finally, a '$\pm$' subscript for Σ terms represents the behaviour of the molecular wave function under reflection through the nuclear plane and is calculated in a similar way to parity.

Molecular oxygen has two π electrons with parallel spins and so the ground state term symbol is $^3\Sigma$. For example the two orbitals have even parity, but behave differently under reflection, so the full term symbol is $^3\Sigma_g^-$.

2.2.3 The Born-Oppenheimer approximation

Since it is impossible to solve the Schrodinger equation for molecules exactly, it is necessary to use the *Born-Oppenheimer approximation* to model the energy levels of the molecule. Since the mass of atomic nuclei is a factor of around ~ 2000 larger than the mass of the electrons, the electrons move much faster than the nuclei and so the motions of the electrons can be decoupled from those of the nuclei. This provides a way to separate the electronic vibrational, and rotational motion of a molecule by assuming that they take place independently from one another, such that

$$E_{total} = E_{electronic} + E_{vibrational} + E_{rotational.} \qquad (2.5)$$

The approximation is reasonable for ground state molecules, but breaks down when two electronic states have the same energy. One consequence of the Born-Oppenheimer approximation is the concept of a potential energy surface for nuclear motion created by faster moving electrons. The simplest one dimensional potential energy surface useful for describing any diatomic molecule is the *Morse potential*, represented by equation (2.6) (where D_{eq} is the molecular dissociation energy, a is constant for each molecule, r_{eq} is the equilibrium separation), a Morse potential for a diatomic species is shown in **Figure 2.2.** The actual dissociation energy is slightly lower than this D_{eq} value due to the zero-point vibrational energy ($1/2\ \hbar\omega^2$, where ω is the vibrational frequency) of the bonded nuclei.

$$E = D_{eq}(1-e^{a(r_{eq}-r)})^2 \qquad (2.6)$$

The Morse function shows the potential energy of the molecule as the bond length between nuclei changes. The preferred bond length, r_{eq}, occurs when the potential of the molecule is at its minimum value. If the molecular energy increases by greater than the dissociation energy, the molecule is able to dissociate.

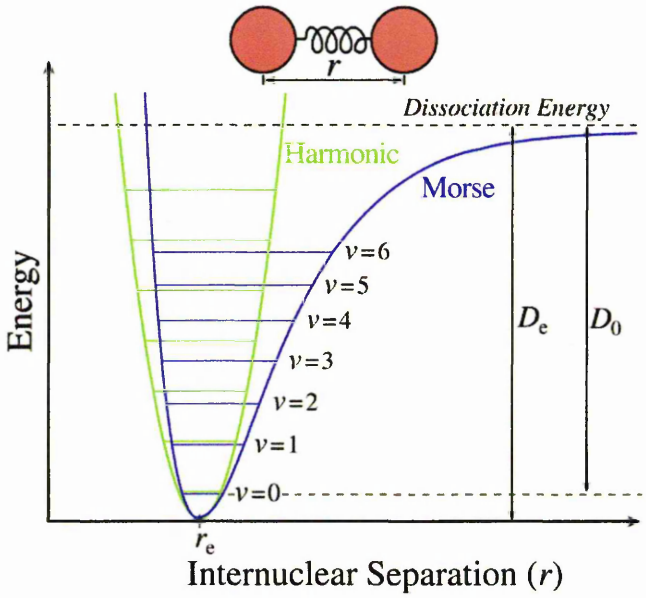

Figure 2.2 The Morse function, representing a molecular potential energy curve [Image adapted from Fundamentals of molecular spectroscopy, Banwell 1995].

2.3 Interaction of matter with radiation and spectroscopy

2.3.1 Molecular transitions

A molecule can absorb energy, generally in the form of quanta of EM radiation i.e. photons and undergo transitions. The excitation can take the form of a rotation or vibration, or an electronic transition, usually from ground state. The possible transitions can be predicted using selection rules and the initial state of the molecule. Knowledge of the nature of the transitions taking place in a molecule provides an understanding of the processes taking place and, in some cases, can help in forming a description of the morphology of a solid phase sample.

2.3.2 Vibrational transitions and IR spectroscopy

There are a number of types of vibration which can take place between molecular nuclei. For a polyatomic molecule of N atoms, there are (3N-5) vibrational modes for linear molecule and (3N-6) vibrational modes for a non-linear molecule. The possible modes can be either symmetric or asymmetric, depending on the physical properties of the processes taking place. The two most common forms of vibration are the stretch and the bend, both of which can occur in symmetric or asymmetric forms. Molecular vibrations can be modelled as simple harmonic oscillators using equation 2.7, with k representing the force constant and the other parameters as defined in section 2.2.3.

$$E = \frac{1}{2}k(r - r_{eq})^2 \qquad (2.7)$$

The vibrations of water molecules are shown in **Figure 2.3**. The three normal modes possible here are the υ_1 symmetric stretch, the υ_2 symmetric bend and the υ_3 asymmetric stretch. The asymmetric bend in water is equivalent to a rotation and so is not included.

The vibrations in carbon dioxide are shown in **Figure 2.4** and include the same three types of vibration; in this case, however, the υ_2 symmetric bend occurs in two directions perpendicular to one another. This is treated as two separate normal modes, although there is no energy difference between the two.

There are a number of electronic selection rules which must be taken into consideration in molecular transitions. For molecules, transitions which are able to occur (allowed transitions) must have: $\Delta\Lambda=0, \pm1$; $\Delta S=0$; $g \leftrightarrow u$; and for Σ states, $+ \leftrightarrow +$ / $- \leftrightarrow -$.

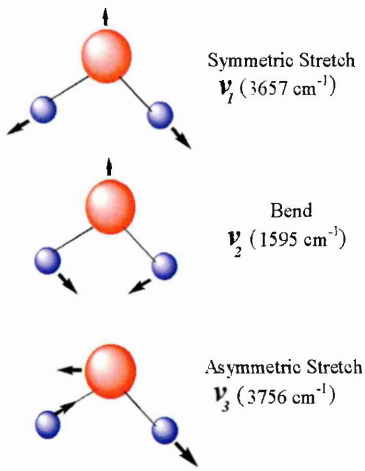

Figure 2.3 Basic modes of vibrations of water molecules

Under many situations, an incident photon will excite an electron to a higher electronic state, subject to these selection rules. There are three cases, however, in which the end result is that the molecule dissociates into two or more fragments. **Figure 2.7** illustrates these possible excitation processes.

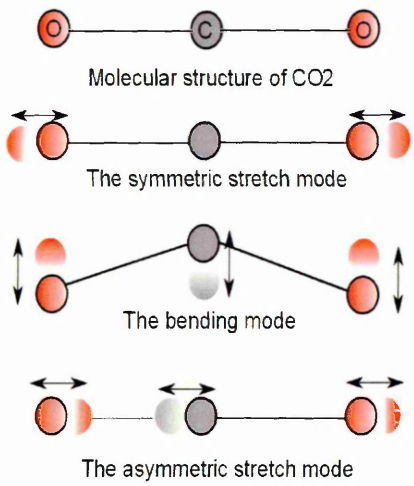

Figure 2.4 Vibrational modes of CO_2, symmetric stretch, bend and asymmetric stretch modes are shown here.

Lower energy infrared photons are only able to induce vibrations in the sample and so produce vibrational spectra, with rotational fine structure in the gas phase. However, such rotational fine structures are absent in the condensed phase due to the

suppression of rotational fine structure due to lack of degrees of freedom in closely packed amorphous solids. An important aspect of vibrational spectroscopy is that the dipole moment of the molecule must change during the vibration for the feature to be observable. This factor rules out a number of important transitions, including most homonuclear diatomic vibrations (such as oxygen and nitrogen) and the υ_1 symmetric stretch of carbon dioxide. In this energy region spectra are often classified by wave-number (in the units of cm^{-1}) in the range of 600-4000 cm^{-1} (0.07-0.5 eV) but conventionally plotted with energy decreasing.

Generally, spectroscopy in this region is carried out using Fourier Transform techniques. Rather than scanning through the entire range, a Michelson interferometer (**Figure 2.5**) is used to generate an interferogram of the sample. A large number of these scans can be acquired rapidly, with more scans providing an enhanced signal-to-noise ratio. Fourier transforms are carried out by a computer to combine the interferograms as they are acquired, forming the complete vibrational spectrum.

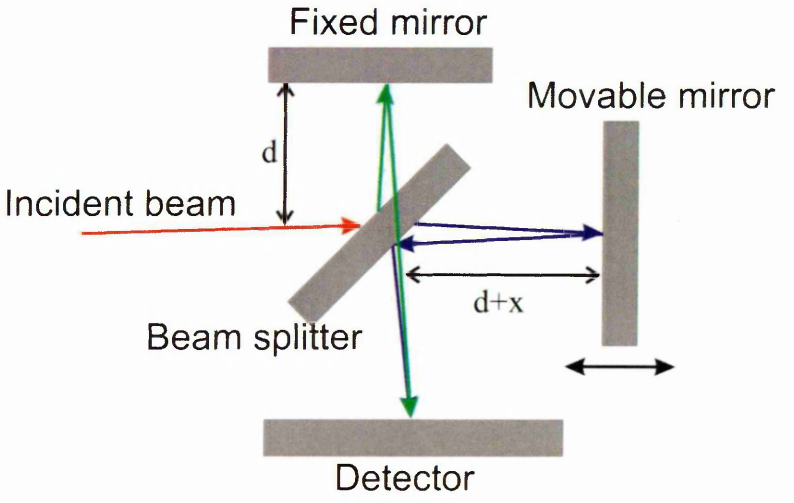

Figure 2.5 Michelson interferometer

Vibrational features for each molecule are identified by their energy. Conventionally, vibrations are labelled by decreasing frequency within their symmetry type. Using water as an example (**Figure 2.3**), the symmetric vibrations are labelled υ_1 and υ_2 for stretching and bending respectively (at 3651.7 cm^{-1} and 1595.0 cm^{-1} in the gas phase) and the anti-symmetric stretch is labelled as υ_3 (at 3755.8 cm^{-1}). Vibrational overtones may also appear in the spectrum due to derivations in the vibrations from simple harmonic motion; these are denoted by $2\upsilon_i$, $3\upsilon_i$ etc.

A sample FTIR spectrum of solid, liquid and gaseous water is shown in **Figure 2.6** with these band assignments. Differences in this solid state spectrum when compared to the gas phase spectrum is described above including the blending of υ_1 and υ_3 bands to form the 3306 cm^{-1} feature and the υ_L vibration features, representing restricted rotations in the solid phase.

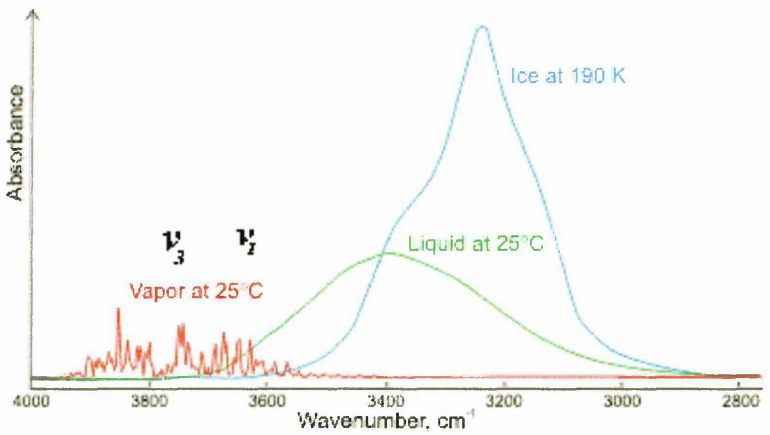

Figure 2.6 Fundamental vibrational features of water in the absorption spectra of gaseous (298 K- red), liquid (298 K- green) and solid (190 K- blue) water.

2.3.3 The Franck-Condon principle

The *Franck-Condon* principle states that, because the nuclei are so much more massive than the electrons, an electronic transition takes place very much faster than the time it takes for the nuclei to respond. The result of this is that the transitions in **Figure 2.7** represented by the vertical lines occur vertically on this diagram from the ground state to the excited state.

For the first of these dissociation processes (**Figure 2.7a**), the internuclear separation of the excited state is greater than the ground state. With the increased internuclear separation the energy of the excited state is greater than the dissociation energy for the molecule and so the molecule may dissociate.

The second case, shown in **Figure 2.7b**, occurs when upper electronic state is unstable. Unlike the other molecular potential curves there is no minimum potential to this state and so the molecule immediately dissociates into fragments when it is excited to this state.

In the third case, the potential energy curves of two different excited states of the molecule intersect (**Figure 2.7c**); this is known as pre-dissociation. For pre-dissociation to take place, one of the curves must have a minimum, and the other must be continuous. If the transition takes place to a vibrational level above or below the intersection point of the two curves, a normal vibrational (and rotational) spectrum will be observed. When the transition is to energy equal to that of the intersection, there is the possibility that the molecule will "crossover" from one potential energy curve to the other and so dissociation will take place. This is also known as a radiation less transfer, as after the initial excitation no further energy absorption or emission takes place.

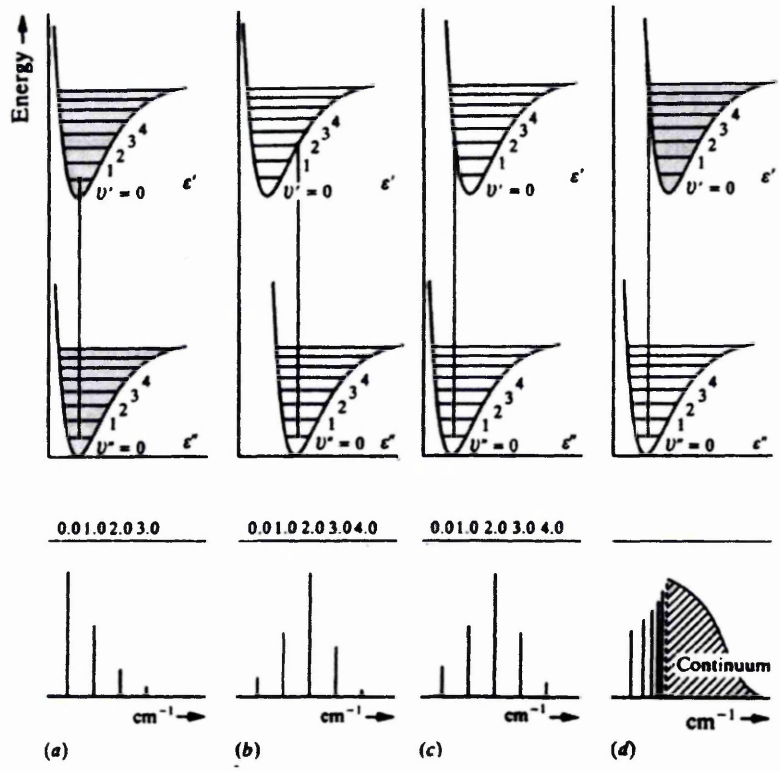

Figure 2.7 The operation principle of Franck-Condon principle [Image adapted from Fundamentals of molecular spectroscopy, C. N. Banwell 1995].

Spectra are produced, in general, by shining light from a continuum source through a sample and measuring the intensity of the transmitted light at a number of discrete points across the continuum. The greater the number of points used, the higher the resolution of the spectrum, defining the level of detail which can be seen.

The three main molecular transitions affecting the spectra of gaseous and solid samples in this work are, in order of increasing energy: rotational, vibrational and electronic. UV photons are required for electronic transitions to takes place, infrared photons are required for vibrational transitions and photons with energies in the microwave region cause rotational transitions. In addition to these transitions, fine structure caused by lower energy transitions is often seen overlaying the main features in UV and IR spectra, especially in the gas phase. Vibrational (and occasionally

rotational) fine structure is observed on electronic spectra and rotational structure can be observed on vibrational spectra.

In this thesis spectra have been collected at UV and IR wavelengths, concentrating on the electronic and vibrational excitations of molecular ices. In each of the UV and IR ranges there are a number of different physical processes taking place which may produce similar features in the spectra. Because of this it is often difficult to assign a specific transition to a spectral feature from its appearance alone and hence theoretical modelling may be required to conclusively assign a feature to a specific transition.

2.3.4 Electronic transitions and UV spectroscopy

The transitions of electrons between orbitals within a molecule can be observed using ultraviolet (UV) photons with energies of a few eV (such as Lyman-α atomic hydrogen excitation with an energy transition of 10.2 eV (121.6 nm). The features seen in electronic spectra often correspond simply to electronic excitations but, if the electron is excited to an anti-bonding orbital, they can also be associated with molecular dissociation. The presence of (or lack of) vibrational fine structure in the electronic spectrum can also provide a great deal of information about the phase or morphology of an ice sample.

Gas phase spectra are dominated by coarse and fine structures, corresponding to vibrational and rotational transitions overlaying the broad electronic transitions. As such, an important aspect of electronic spectroscopy in the gas phase derives from the *Franck-Condon principle* (**section 2.3.3**). The effect of this principle on the electronic structure of molecules is shown in **Figure 2.7**. It is assumed here that

all transitions take place from the lowest vibrational level in the ground state; in practice some transitions occur from higher vibrational levels but the effect is small.

If the internuclear separation remains the same between the electronic states, as in (a), the transition goes to the lowest vibrational level of the excited state, causing this vibrational feature to be the strongest in the electronic spectrum. In (b), there is an increase in nuclear separation from the ground state to the excited state, causing the most likely transition to occur to $\upsilon' = 2$ level. In each of these cases, some transitions will occur to other levels, resulting in a vibrational progression as shown. If there is a much greater internuclear separation between the molecular nuclei in the excited state, as in (c), the most likely transition will be to a higher vibrational level. If the excitation energy is slightly higher than this the molecule will be excited with an energy high enough that it can dissociate, causing a continuum feature to be observed in the spectrum. The continuum is present due to the lack of quantization in the kinetic energy of the dissociated molecular fragments.

In the solid phase, differences in the interactions between molecules can strongly affect the resulting UV spectra. At extremely low temperatures (<10 K) almost all samples solidify into an amorphous structure in which individual molecules have a random orientation (there is no longer long-range-order). Molecular rotation is suppressed and all vibration excitation in the amorphous solid have slightly different energies to each other due to this random orientation, contributing to an overall broadening effect in the vibrational fine structure. As such, the spectra of amorphous solid ices display only the broad electronic transitions and very little or no fine structure. In crystalline solids, molecules are aligned with long-range order, and little or no broadening of the vibrational fine structure takes place. However, the transitions are often not as strong as those observed in gaseous samples.

Another important difference can occur in ices in which hydrogen bonding takes place. Hydrogen bonds between molecules such as water and ammonia lower the ground state energy of each molecule, increasing the energy change in transitions to or from the ground state. This result in an overall blue shift in the electronic spectrum of up to around 2 eV, depend on the strength of hydrogen bonding between molecules.

There are two forms of simple electronic excitation: the valence and *Rydberg transitions*. They are both caused by the promotion of an electron to a higher energy orbital and so produce similar spectral features. However, where as a valence transition involves the promotion of an electron to the valence orbital, In a Rydberg transition the electron is promoted to an orbital with a greater quantum number than any of those occupied in the ground state. In gaseous samples, this does not result in a significant difference, but solid samples, with their smaller intermolecular separation, the larger physical size of the Rydberg state means that they are more susceptible to perturbation than in the gas phase. This can either result in a broadening of vibrational fine structure and a small (~ 0.2 eV) additional blue shift of the spectral band, or the complete suppression and removal of the Rydberg excitation from the electronics spectrum of the ice, depending on the ice being studied.

2.4 Properties of molecules in the condensed phase

2.4.1 Structure of ice films

There are a number of forms in which ices can form. The formation phase depends most strongly on the temperature at which the ice is formed. However, after formation the ice can be processed, either thermally or by photons or cosmic rays, which can affect the structure of the ice.

Molecules impacting on a very cold surface (<10 K) have a very high sticking probability. The low temperature means that once the molecules have physisorbed onto the cold surface they no longer have sufficient energy to move around or rotate on the surface. As further molecules collide with the cold surface they will also stick and be unable to rotate. After some time a complete monolayer will form, made up of a film of randomly oriented molecules. Further molecules will stick to this monolayer, again without sufficient energy after impact to orient themselves with the surrounding molecules. The end result, after enough molecules have collided with the ice surface, is that a multilayer ice film will form, consisting of a random ice matrix, with no long-range order. This ice structure is known as amorphous and is shown in **Figure 2.8**(c), due to random orientation of molecules, this phase is thermodynamically not stable and it is readily processed into other forms.

At higher deposition temperatures molecules can form into one of a number of crystalline phases, including cubic and hexagonal crystalline forms. The exact structure of crystal formed depends on the molecule involved. This phase is characterised by long-range order within the ice, as the molecules have sufficient energy to become aligned with one another on deposition. Schematic representation of this phase is shown in **Figure 2.8 (a)**.

The result of depositing at intermediate temperatures can depend strongly on the molecule involved and, with some molecules; the results of depositing at these intermediate temperatures have caused some confusion as to what structures are formed. Some molecules go directly from amorphous to crystalline phase without a noticeable intermediate phase. Water is known to exist in two distinct amorphous phases before the surface temperature is high enough for crystalline material to form. It is also possible for a distinct intermediate phase to form: one that is neither

amorphous nor wholly crystalline. One example of this intermediate phase is formation of small crystallites, creating a type of poly crystalline material. The interaction of crystallite grains and grain boundaries can cause unexpected effects in the ice which can result in the characteristic spectral features such as excitons.

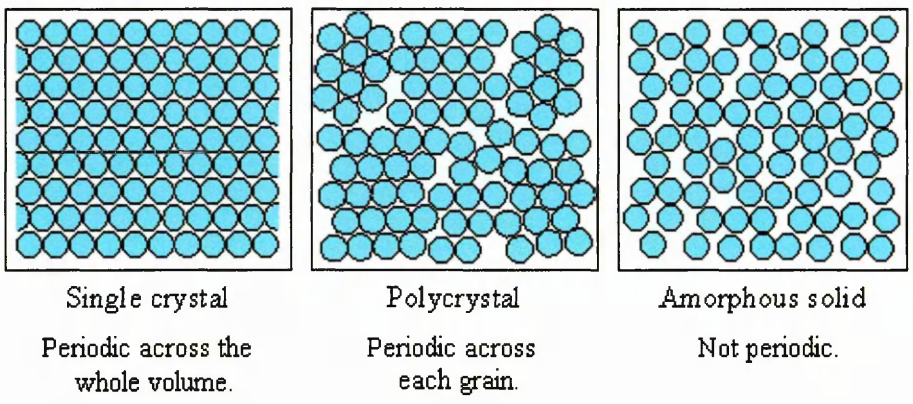

Figure 2.8 Structure of solids (a) Crystalline (b) Polycrystalline and (c) Amorphous

It is well known that annealing water ice film (heating it temporarily from base temperature then re-cooling to "freeze" the changes) results in the modification of the ice film to a cubic crystalline form; continued heating further modifies the ice to a hexagonal crystalline structure [Blake and Jenniskens 2001] other ices are known to behave in a similar way. Intermediate structures formed by annealing, but which are themselves not thermodynamically stable can be referred as metastable. Unfortunately, use of this term in the literature is somewhat inconsistent causing further problems in the understanding of these little studied intermediate phases.

In contrast, energetic particle radiation can have the opposite effect. Crystalline water ice under solar wind and cosmic ray bombardment, for example may revert to an amorphous structure [Jewitt and Luu 2004]. These various factors demonstrate that studies of the morphology of laboratory ice films can be extremely important to our understanding of astrophysical ices.

2.5 Irradiation processes

The three primary forms of irradiation in the interstellar medium are photons (interstellar radiation field), ions (from cosmic rays) and electrons (often produced in irradiation induced chemical reactions). However, the results of irradiation by each of this can be very different.

The first difference is in penetration depth. UV Photons have an optical depth (at which the transmission drops to 37%) of around 0.15 μm in water ice, where as 0.8 MeV protons can pass through 20 μm of similar material [Gerakines et al. 2000]. The effects of such penetration depth depends on types of ice: a cometary or planetary ice is likely to have a thickness of the order of a few metres or kilometres, where as a dust grain mantle may be thinner than the UV photon penetration depth.

In addition, while UV photons are absorbed by a single atom or molecule, ions can interact with a large number of atoms or molecules along their impact path, before eventually undergoing a chemical reaction or implanting into the ice.

2.6 Surface science

Surface science is the study of physical and chemical phenomena that occur at the interface of two phases for example solid–liquid interfaces, solid–gas interfaces, solid–vacuum interfaces, and liquid-gas interfaces. Surface catalysis involves in interstellar chemistry and to understand the chemical pathways involved in gas-solid and solid-solid interactions we need to understand the chemical kinetics of surfaces. Surfaces possess excess energy or energy wells, these potential wells trap molecules and there by play an important role in chemical kinetics. In interstellar chemistry, molecular ice films adsorbed on an interstellar grain mantle enhance the production of complex non-volatile organic molecules therefore the surface mediates the kinetics in

the astrochemical evolution. Adsorption of molecules onto surface is classified according to the energy level of the process; the two principal modes of adsorption are physisorption and chemisorption.

2.6.1 Physisorption and Chemisorption

Adsorption or absorption on a surface takes place when an attractive interaction between a particle and a surface is strong enough to overcome the disordering effect of thermal motion. Physisorption may be described through Van der Waal forces. Physisorptive bonds are characterised by dissociation energies below approximately ~ 50 kJ/mol. Chemisorption occurs when the overlap between the molecular orbitals of the adsorbed particle and the surface atoms permit the formation of chemical bonds, which are characterised by dissociation energies typically exceeding 50 kJ/mol. Chemisorption is often an activated process, *i.e.*, the formation of a chemisorptive bond requires overcoming an activation barrier [Shroeder 2002].

A universal feature of molecular chemisorption is the weakening of intramolecular bonds that often lead to the dissociation of the adsorbed molecule. An important example for activated, dissociative chemisorption is the adsorption of oxygen molecules on most metal surfaces at room temperature. The elementary reaction steps occurring during such a process is summarised in **Figure 2.10** [Shroeder 2002]. The energy barrier, ΔE_{des} for chemisorption is much higher than combined energy barrier contributed by ΔE_{des} of physisorption and activation energy E_{akt}.

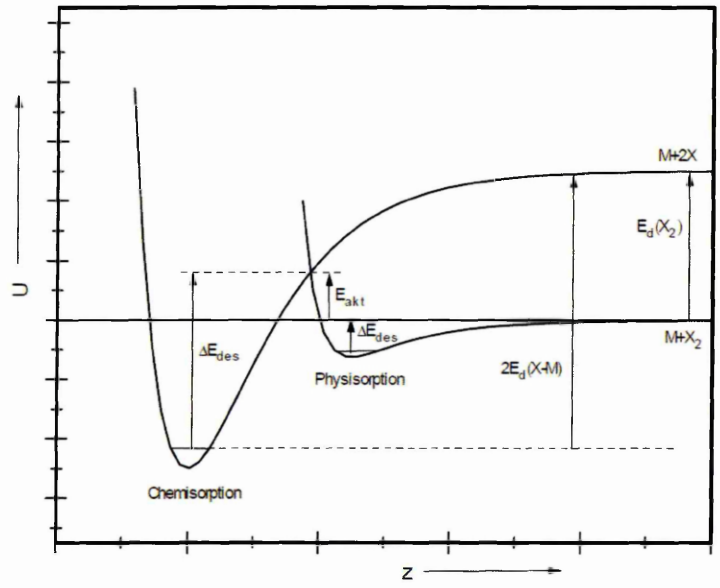

Figure 2.10 Physisorption and chemisorption explained using a potential energy of the surface [Adapted from Shroeder 2002]. ΔE_{des} is the energy barrier for desorption from the surface, ΔE_{des} for chemisorption is much higher than combined energy barrier contributed by ΔE_{des} of physisorption and activation energy Eakt.

2.6.2 The Desorption Process

An adsorbed species present on a surface at low temperatures may remain almost indefinitely in that state. As the temperature of the substrate is increased, however, there will come a point at which the thermal energy of the adsorbed species is such that one of several things may occur: a molecular species may decompose to yield either gas phase products or other surface species, an atomic adsorbate may react with the substrate to yield a specific surface compound, or diffuse into the bulk of the underlying surface, or the species may desorb from the surface and return into the gas phase.

The last of these options is the desorption process. In the absence of decomposition the desorbing species will generally be the same as that originally adsorbed but this is not necessarily always the case. The rate of desorption can be

expressed in terms of number of adsorbed molecules, desorption or activation energy, temperature,

$$R_{des} = -dN/dt = v.N^{x}.e^{\left(-E_a^{des}/RT\right)} \qquad (2.8)$$

where N is number of adsorbed molecules, R- Boltzmann's constant, E_a^{des} is the desorption barrier and υ is frequency factor as shown in **Figure 2.10**.

Phenomena of desorption, both physisorption and chemisorption can be investigated using reflection InfrarRed (IR) techniques or mass spectrometry. Each method has its own advantages and disadvantages, therefore, both techniques are jointly employed in our experiments (in-situ) for higher sensitivity and precision (detailed explanation of the experimental setup is described in chapter 3).

2.6.3 IR Spectroscopy

There are a number of ways in which the IR technique may be implemented for the study of adsorbates on surfaces. For solid samples possessing a high surface area we can employ Transmission IR Spectroscopy (TIRS). This technique is often used for studies on supported metal catalysts where the large metallic surface area permits a high concentration of adsorbed species to be sampled. The solid sample must be IR transparent over an appreciable wavelength range (mid to far IR) [Shroeder 2002].

Diffuse Reflectance IR Spectroscopy (DRIFTS) in which the diffusely scattered IR radiation from a sample is collected, refocused and analysed. This

modification of the IR technique can be employed with high surface area samples that are not sufficiently transparent to be studied in transmission mode.

For studies on low surface area samples (e.g. single crystals) Reflection-Absorption IR Spectroscopy (RAIRS) can be employed, where the IR beam is reflected from the front face of a highly-reflective sample, such as a metal single crystal surface. It can be shown theoretically that the best sensitivity for IR measurements on surfaces is obtained using a grazing-incidence reflection of the IR beam (**Figure 2.11**).

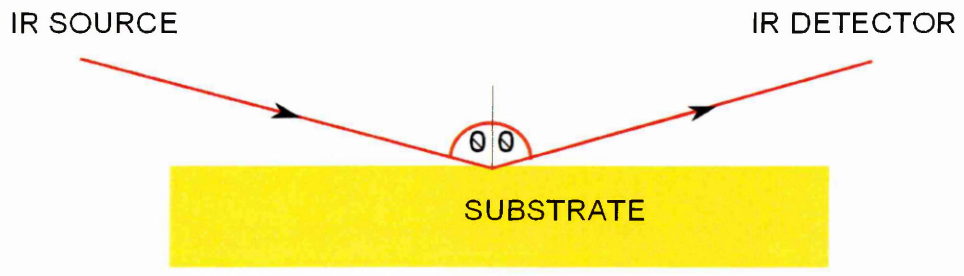

Figure 2.11 RAIRS - the Study of adsorbates on surfaces by Reflection IR Spectroscopy

Furthermore, since RAIRS is an optical technique it is not necessary for such studies to be carried out in vacuum. The technique is not essentially surface-specific, but there is no bulk signal to worry about, the surface signal is readily distinguishable from gas-phase absorptions using polarization effects. A detailed description of the RAIRS experimental setup is presented in chapters 3 and 7.

In case of transmission IR spectroscopy, an IR beam is passed through IR transparent sample and substrate and the signal is collected with highly sensitive LN_2 cooled MCT (A or high-D) detector. One major problem of this technique is that of sensitivity (i.e. the signal is usually very weak due to lesser coverage of adsorbing molecules). Typically, the sampled area is 1 cm^2 with less than 10^{15} adsorbed molecules, with modern FTIR spectrometers, however, such small signals (0.01% -

2% absorption) can still be recorded at relatively high resolution (1 cm^{-1}). We employ transmission as well as RAIRS in our experiments, especially when we use a ZnSe substrate we employ the transmission mode, which helps to identify the chemical changes in the ice films.

IR techniques are significant in terms of surface studies because, the observation of vibrational modes of adsorbates on metallic substrates is subject to the surface dipole selection rule. This states that only those vibrational modes which give rise to an oscillating dipole perpendicular (normal) to the surface are IR active and give rise to an observable absorption band, a schematic representation of this property is shown in **Figure 2.12**. It also needs to be remembered that even if a transition is allowed it may still be very weak if the transition moment is small [Sheppard & Erkelens 1984].

Another technique which can be employed to study a surface is multiple Internal Reflection Spectroscopy (MIR), in which the IR beam is passed through a thin, IR transmitting sample in a manner such that it alternately undergoes total internal reflection from the front and rear faces of the sample.

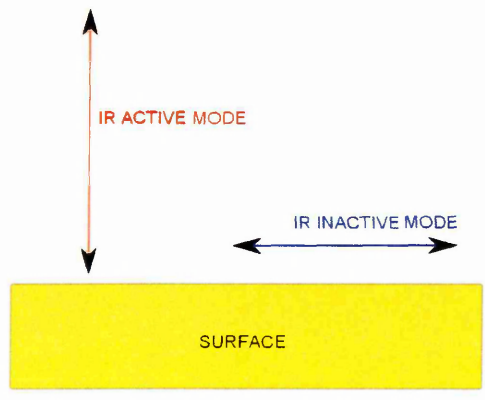

Figure 2.12 Vibrational modes which give rise to an oscillating dipole perpendicular (normal) to the surface (blue) are IR active and give rise to an observable absorption band.

Since at each reflection, some of the IR radiation may be absorbed by species adsorbed on the solid surface – the techniques is also known as Attenuated Total Reflection (ATR).

2.6.4 Temperature Programmed Desorption (TPD)

There are a range of techniques for studying surface reactions and molecular adsorption on surfaces which utilise temperature-programming to distinguish between processes with different activation parameters. Adsorption of one or more molecular species onto the sample surface at low temperature and subsequently heating of the sample in a controlled manner (linear temperature ramp) whilst monitoring the evolution of species from the surface, desorbing back into the gas phase is known as temperature programmed desorption (TPD).

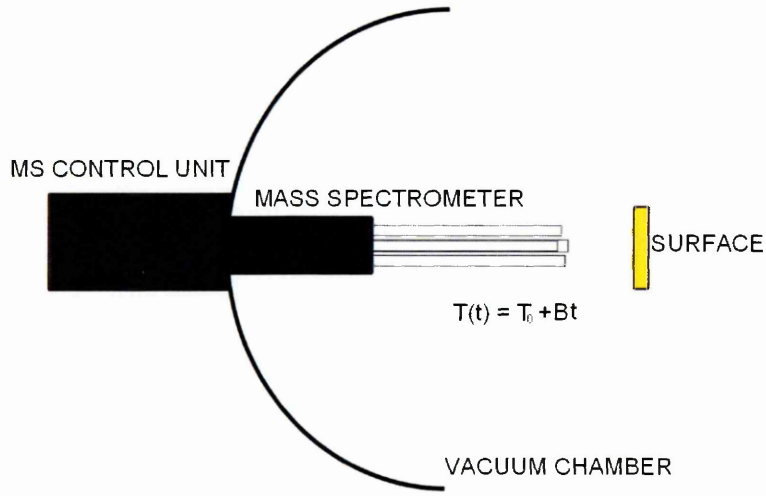

Figure 2.13 Schematic of a TPD experiment with a line-of-sight mass spectrometer alignment.

In our experiment we employ a quadrupole mass spectrometer (QMS) in line-of-sight orientation, and the whole process is carried out under computer control with simultaneous monitoring of a large number of possible products (**Figure 2.13**).

The data obtained from such an experiment consists of the intensity variation of each recorded mass fragment as a function of time / temperature. In the case of a simple reversible adsorption process it may only be necessary to record one signal - that is attributable to the molecular ion of the concerned adsorbate.

Since mass spectrometric detection is used, the sensitivity of the technique is good, with attainable detection limits below 0.1% of a monolayer of adsorbate. The area under a peak is proportional to the amount originally adsorbed sample, i.e. proportional to the surface coverage. The kinetics of desorption (obtained from the peak profile and the coverage dependence of the desorption characteristics) give information on the state of aggregation of the adsorbed species.

The position of the peak (the peak temperature) is related to the enthalpy of adsorption, i.e. to the strength of binding to the surface. One implication of this result is that, if there is more than one binding state for a molecule on a surface (and these have significantly different adsorption enthalpies) then this will give rise to multiple peaks in the TPD spectrum.

2.6.5 Theory of TPD

The rate of desorption of a surface species will in general be given by an expression of the form (equation 2.8),

$$R_{des} = v.N^{x}.e^{\left(-E_a^{des}/RT\right)} \qquad (2.9)$$

where

R_{des} - desorption rate
x - kinetic order of desorption (typically 0, 1 or 2)
E_a^{des} - activation energy for desorption

In a temperature programmed desorption experiment in which the temperature is increased linearly with time from some initial temperature T_0, then

$$T = T_0 + \beta.t \quad \text{and} \quad dT = \beta.dt \tag{2.10}$$

The intensity of the desorption signal is proportional to the rate at which the surface concentration of adsorbed species is decreasing. This problem may also be considered in a quite simple way (**Figure 2.14**), the expression for the desorption signal given in the above equation (2.9) is basically a product of a coverage term (N^x - where N depends on T) and an exponential term (involving both E_a and T).

Initially, at low temperatures $E_a >> RT$ and the exponential term is vanishingly small. However, as the temperature is increased this term begins to increase very rapidly when the value of RT approaches that of the activation energy, E_a.

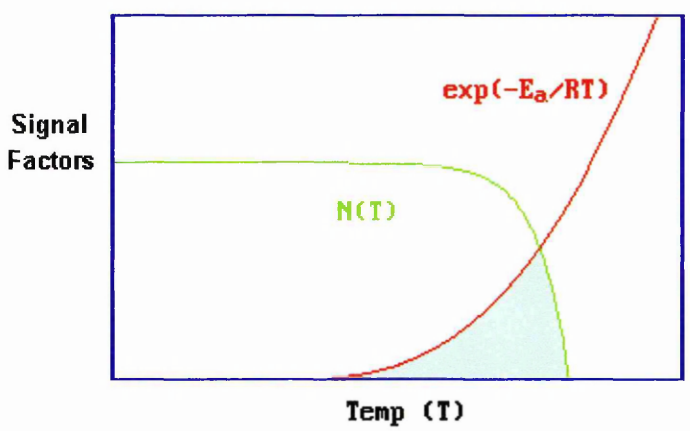

Figure 2.14 The influence of surface coverage on desorption rate [Shroeder 2002]

By difference, the pre-exponential term is dependent upon the coverage, N(T), at the temperature concerned - this term will remain at the initial value until the desorption rate becomes of significance as a result of the increasing exponential term. Thereafter, it will decrease ever more rapidly until the coverage is reduced to zero.

The shaded area is an approximate representation of the product of these two functions, and hence an approximate representation of desorption signal, whereas this illustration may be overly simplistic, it does clearly show why desorption process gives rise to a well-defined desorption peak [Shroeder 2002].

2.7 Conclusion

Atomic and molecular structure, spectroscopic principles, microscopic structure of ice films and surface science principles are described in this chapter. Molecular structure in terms of atomic and molecular quantum numbers, energy levels and energy states expressed in terms of molecular term symbols are discussed. Electronic and vibrational transitions of the molecules and the spectroscopic techniques to study such phenomena have also been presented. Temperature dependent changes in UV and IR spectra of molecules and concepts of absorption cross-section of such molecules in condensed state are also described in this chapter. Finally a section describing surface science and experimental techniques employed to understand the chemical and physical processes on surfaces are described in detail. Special focus is given on techniques such as TPD with line-of-sight mass spectrometer and RAIRs, which are employed in our experiments.

CHAPTER 3

THE EXPERIMENTAL SYSTEMS AND TECHNIQUES

The true method of knowledge is experiment.
- William Blake

3.0 Introduction

The physical and chemical conditions prevalent in the interstellar medium (ISM), and planetary surface maybe recreated in the laboratory, to explore the formation pathways, which leads to synthesis and evolution of complex molecules in such environments. The physio-chemical conditions of diffuse clouds, dense molecular clouds, photo-dissociated regions, proto-stellar envelopes, planetary environments and comets are highly complex. And achieving such conditions in the laboratory is challenging. Molecular clouds are an inventory of large volumes of silicate and carbonaceous dust formed through stellar evolution cycles. These dust grains at an ambient temperature of ~ 10 K act as a catalyst, carrier and a third body in the solid-state/surface reaction pathways. Planetary surfaces, atmospheres, their moons and comets possess high column densities of simple molecules in their environments with temperatures ranging from 50-300 K and can support complex chemical synthesis.

In order to understand the complex chemical synthesis in the ISM, comets and planetary environments, similar conditions are simulated in the laboratory. The laboratory experiments relevant to astrochemical ices focus primarily on the purity of

ice, pressures of 10^{-8}-10^{-10} mbar are necessary to minimize the contamination from the H_2O or CO_2 or other trace gases common in vacuum systems. However, we should note that such laboratory simulations still operate at ~ 10^4 times greater pressure than that in the ISM. Interstellar grain mantle ices and planetary ices are constantly subjected to irradiation sources such as cosmic rays, with energies ranging from GeV to MeV, particles accelerated in magnetic fields, solar wind particles, shocks and UV photons. The primary objective of this project was to study the effect of irradiation of interstellar or planetary ice analogues as a function of temperature, morphology and types of irradiation. An integrated series of experiments were performed at the following laboratories:

1. The Astroices Laboratory, The Open University, UK

2. UV1 beamline, The Institute for Storage rings (ISA), University of Aarhus, Denmark

3. UV-A1 beamline, National Synchrotron Radiation Research Centre (NSRRC), Taiwan

4. The Molecular Physics Laboratory, The Open University, UK

3.1 Ultra-High Vacuum and low temperature in the laboratory

All the experiments were conducted under ultrahigh vacuum conditions (UHV~ $<10^{-7}$ mbar). UHV conditions were achieved by using stainless steel vacuum chambers along with vacuum pumps. All the chambers are made up of 316 LN grade stainless steel, since this grade of stainless steel is best for attaining UHV and to keep clean, moisture less environment for surface experiments. Each chamber was heated

(baked) and pumped to avoid moisture and general environmental contaminants. Turbo molecular pumps with the backing of dry or rotary vane/oil pumps or scroll pumps were used in combination to achieve Ultra High Vacuum (UHV) conditions. Pirani, baratron, and ion gauges were employed to measure the degree of vacuum. All the pressure gauges were calibrated for N_2 and CO_2 at room temperature (298 K). A separate set of calibration/test runs were recorded for pressure measurements at 10 K as well as for special conditions such as residual gas analyzer (RGA) 'ON' or electron gun 'ON' conditions. The vacuum that is created ranges from 10^{-10} to 10^{-8} mbar.

Using compressed high pressure (20 bars) helium gas from a closed cycle cryostat (Sumitomo), the substrate can be maintained at 10 ± 0.2 K. The temperature is measured on the substrate by a high precision silicon diode (Lakeshore) which can measure temperature in the range of 2.7 K to 300 K with ± 0.001 K error factor. Heating is performed carefully by using a resistive heater (e.g. Cartridge heater, flexible Kapton heater etc) located very close to the substrate using an external power supply, this method is followed in all the experiments described in this thesis except for temperature programmed desorption. In temperature programmed desorption experiments, an Intelligent Temperature Controller (ITC 502) is used for precise heating, with precise PID control mechanism. In this way both the temperature and pressure are maintained as low as possible to simulate planetary, satellite and interstellar conditions and to study the chemistry under these conditions.

3.2 Gas dosing

Ice films on a surface (interstellar ice analogues) are achieved by depositing molecular gas onto the cold substrate held at low temperatures (~10 K). The gas line is prepared by baking and pumping thoroughly, this process is necessary to eliminate contamination of gases other than the desired gas for deposition. Normally the gas line is pumped using a backup pump either a dry rotary or scroll pump with molecular sieve. The whole gas line is evacuated to a base pressure of ~ 10^{-3} mbar. A separate pumping line was used to pump the dosing line for introducing molecules into the chamber. Swagelok components with ø 6 mm stainless-steel tubing were used to construct an all metal leak-tight gas line.

In the experiments discussed here mostly pure ice of one molecular composition or binary mixtures of methanol (CH_3OH) or water (H_2O) ice are used. A line diagram of the gas line is shown in **Figure 3.1(a)** where a regulator is used to draw small quantities of gas from pressurised gas lecture bottles. This is then passed into the gas cell or the gas mixing chamber. In order to measure the pressure in the gas line a non-ionising baratron pressure gauge is used. This was either a transducer or capacitance type gauges which measures the absolute pressure independent of the gas used. Normally few mbar quantities of gas are let in to the gas line before they are opened to the UHV chamber. An all metal UHV leak valve which enables very fine gas leak adjustments in quantities of 10^{-6} -10^{-10} mbar of gas is employed to let the molecular gases into the UHV chamber.

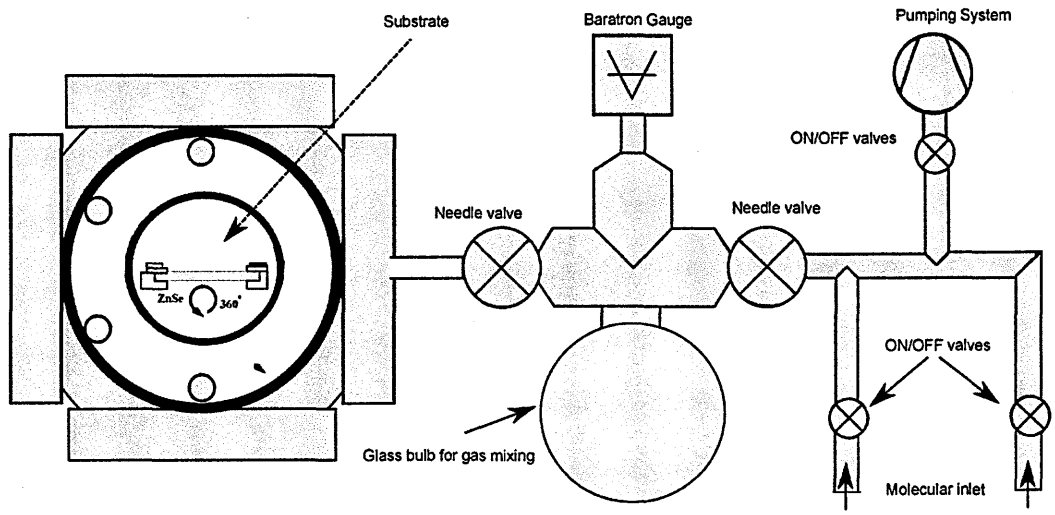

Figure 3.1 (a) Gas dosing system for growing ice films.

Once the substrate was cooled down to low temperatures at UHV pressures then gas deposition can be started in order to obtain molecular ice samples on the cold substrate. There are several methods used for gas deposition and these are discussed in the following sub sections.

3.2.1 Background gas deposition

In this method small quantities of gas are allowed into the UHV chamber containing the cold substrate. The gas inlet nozzle is directed towards the walls of the chamber. Therefore gas molecules entering the UHV chamber are dispersed within the boundaries of the chamber inner walls, when these molecules come in contact with the cold substrate they stick on to the surface. In this way a few layers of molecular ice were formed. In the case of background deposition method, infrared spectroscopy is used in transmission mode; therefore the substrate required a special design to eliminate molecules that could stick on the "opposite side" of the substrate – that side where irradiation was not performed. Therefore, the unirradiated side of the substrate was covered leaving small opening with an extended means for the infrared

beam to pass through the ice. This combination enabled an even deposition of molecules on the front face but reduces the number of molecules being deposited on the back face of the substrate. In this method larger quantities of gas are used for a longer time because only a small percentage of the molecules come into contact with the substrate under vacuum conditions; however a uniform ice surface can be obtained by using this method. All the experiments described in this thesis were conducted by employing this deposition technique.

3.2.1.1 Co-deposition of pre-mixed samples

Ice films of molecular mixtures were prepared by co-depositing premixed samples. Known volumes of individual samples at room temperature were introduced into a glass bulb, in case of liquid samples, vapours were mixed carefully by considering the vapour pressure. For example, sample with less vapour pressure is introduced into the glass bulb by using the ON/OFF valve needle valve arrangement as shown in Figure 3.1(a), after securing the first needle valve (situated before the glass bulb) the second sample with higher vapour pressure is introduced and mixed with the first sample. Then the known volume of gas at a known pressure, measured by Baratron gauge was introduced to UHV chamber by using a high precision all metal leak- valve. Growth of the ice film and the composition of the ice film were monitored by in-situ measurements using a transmission mode FTIR (section 3.2.2).

In case of liquid samples, maintaining the specific mixing ratios only with the volume-pressure-time (period of deposition) were very difficult, therefore we optimized the mixing ratios from column density calculations obtained through the FTIR measurements. And we repeated measurements of volume-pressure-time / column density for individual mixtures at various proportions and used these values to prepare ice films of mixtures with definite proportions.

3.2.2 Direct gas deposition

In this method the gas inlet is targeted directly onto the substrate. The distance between the inlet nozzle and the substrate is optimized to be with in 2 – 3 cm. Also during this type of deposition the substrate is usually placed normal to the inlet nozzle. Therefore those molecules entering the vacuum chamber by opening the gas line-UHV separator valve are directed towards the cold substrate and most of the gas used will form an icy layer over the substrate.

3.2.3 Methods used to quantify the deposition

The gas cell or the gas mixing chamber was prepared with a known quantity of gas. The amount of gas in the gas cell ranges from a few to 100 mbar depending on the sensitivity of the pressure gauge used. The quantity of gas in mbar to be deposited is decided before deposition. Deposition is carried out until the required pressure decrease is recorded in the gas cell. This method can only be used during direct deposition. Usually a reservoir of gas is used in order to have a constant flow rate from the gas cell to the UHV chamber. The main advantage of this method is that it is easy to control the deposition rate of a given amount of gas for either slower or faster deposition. It is found that deposition rate also plays a major role in determining the morphology of the ice. It is also necessary to know the ice thickness in an independent way to compare the quantity of molecules let into the chamber and number of molecules forming ice.

In this method a high precision manually operated UHV leak valve that can let in small amounts of gas was used. The chamber pressure was used as a measurement together with recording the time for deposition. Normally this method is employed in

UHV chambers reading base pressures less than 10^{-10} mbar. However, in our experiments typically a deposition pressure of 10^{-6} mbar was used with deposition time varying from seconds to minutes depending on the thickness of the ice required.

This method has the same advantages as the gas quantity method, explained above, where changing the pressure and the timing for deposition determines either slower or faster deposition. In addition maintaining a constant pressure during deposition ensures a constant flow rate of the gas which eventually relates to a constant deposition rate.

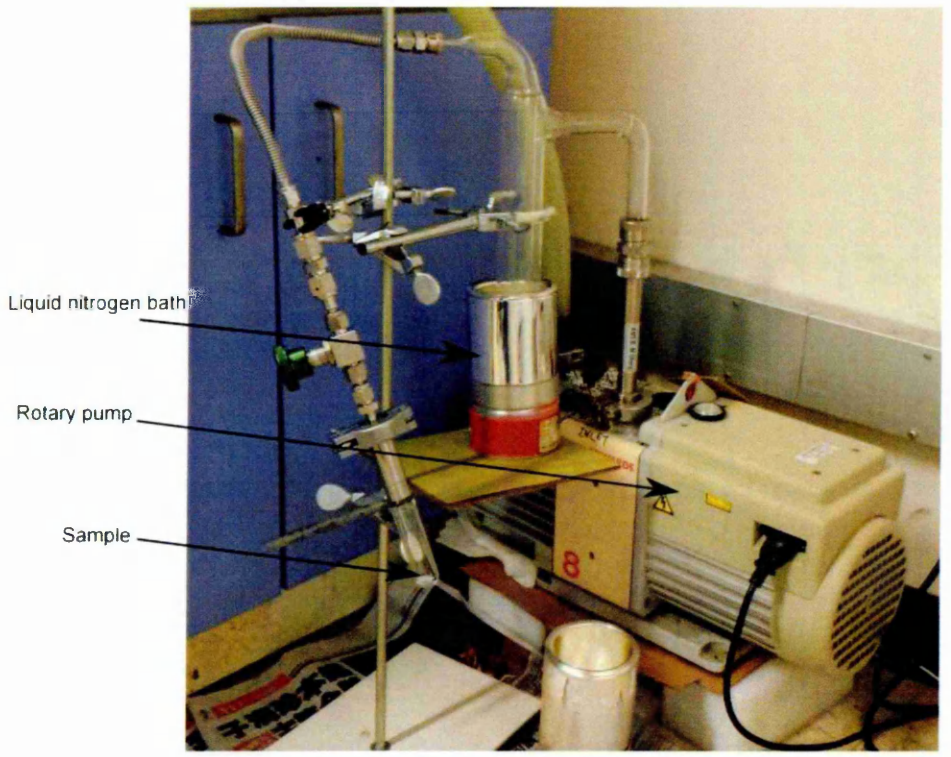

Figure 3.1 (b) the setup used to degas the sample using freeze-thaw-pump cycle

3.3 Monitoring ice thickness

3.3.1 Interference fringes method

A laser beam is used to obtain an interference pattern due to the reflection of light from the ice-vacuum and ice substrate interface. The fringes relate to the

thickness of the ice grown on the substrate. The deposition can be stopped after reaching the required number of fringes for a desired ice thickness (Equation 3.1). Both of the types of deposition described above can use this technique. The main advantage of this method is that it is independent of the type of molecular gas that is used to grow molecular ice. When more than one molecular ice experiment needs to be compared with respect to the sample thickness then this technique can be used to produce approximately the same ice thickness just by measuring the number of fringes, schematic of such measurement is shown in Figure **3.2**.

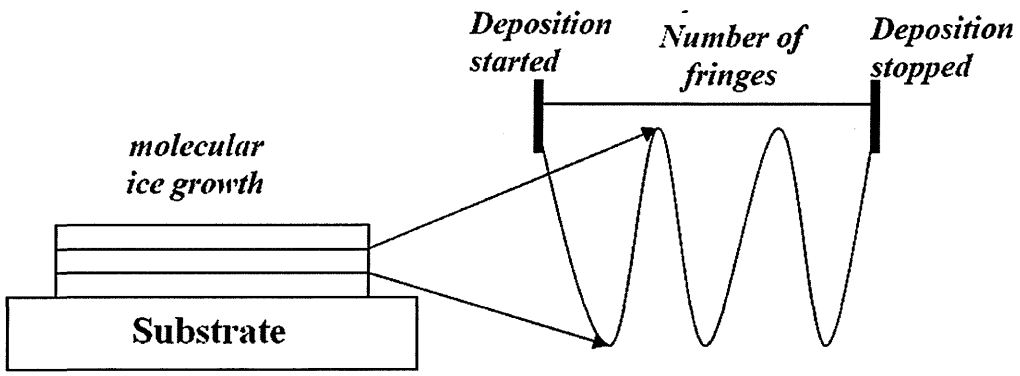

Figure 3.2 Molecular ice growth on a substrate monitored using interference fringes method

The ice thickness, t, can be determined from the following expression,

$$t = \frac{m\lambda}{2n\left(1-\frac{\sin^2\theta}{n^2}\right)^{\frac{1}{2}}} \qquad (3.1)$$

where, λ is the laser wavelength (nm), m is the number of fringes, n is the index of refraction and, θ is the angle of incidence of the laser beam.

3.3.2 Using a real-time infrared spectrum method

This method involves the use of an infrared spectrometer to record an infrared spectrum while depositing gas on to the cold substrate (**Figure 3.3, 3.4**). This method can be applied for both types of gas deposition. As the deposition is carried out, the number of molecules sticking to the substrate increases such that the recorded IR band strength also increases. Deposition is carried out until the desired band strength of a particular molecule is reached, or until a good and clear infrared spectrum is recorded. Deposition can be carried out until bands appear clearly in the spectrum with less noise and deposition is stopped before the bands reach a saturation limit. The advantage of this method is the in-situ visual of the growth of infrared bands due to icy layer formation. In particular while using a mixture of gases this method is very effective to ensure a good infrared spectrum for analysis. The limitation of this method is that it cannot be used for infrared inactive molecules.

The ice thickness can be calculated using equation (3.2). This equation can only be used when oscillations are observed in the infrared spectra due to multiple reflections taking place within the ice.

$$t = \frac{N_{osc}}{2n(\upsilon_0 - \upsilon_1)} \qquad (3.2)$$

where, t is the ice thickness (cm), n is the index of refraction, N_{osc} is the number of fringes or oscillations, (T_0 – T_1) is the wavenumber of the oscillation occurring between T_0 and T_1.

If no oscillations are present in the infrared spectrum then equations (3.3 & 3.4) can be used to calculate the number of molecules in column density (N, molecules/cm^{-2}) and then ice thickness, respectively.

$$N = \frac{\int Area\ under\ the\ curve(Optical\ depth)}{A} \qquad (3.3)$$

where 'A' is integrated IR absorption constant (cm molecule^{-1})

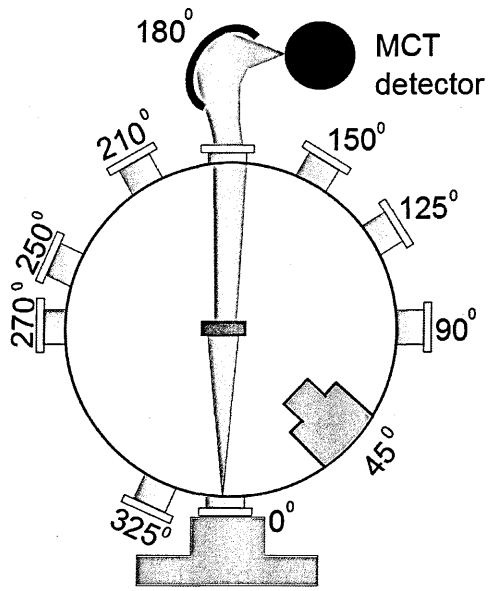

Figure 3.3 Transmission mode InfraRed (IR) spectrometer with an external MCT (LN_2cooled) detector. The substrate can be rotated and placed at various incident angles.

The column density can also be expressed as

$$N = \frac{N_A \rho l}{M} \qquad (3.4)$$

Where N_A is Avogadro's number and ρ is mass density l is the path length or thickness and M is molecular mass.

Research group at INAF (Catania Astrophysical Observatory) uses the interference fringes technique to measure the thickness and 'A' value (Coefficient of

infrared absorption) [Brucato et al. 2006]. 'A' value of methyl formate and benzene was measured by the research group at INAF [Modica and Paulambo, 2011]. A value of formamide, formic acid, acetic acid, methanol and ammonia was measured by Research group at University of Hawaii using the interference fringes technique [Jones et al. 2011]

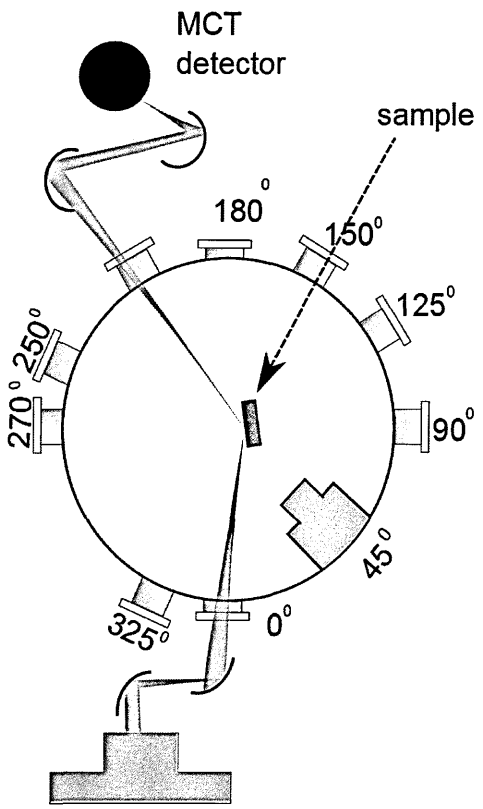

Figure 3.4 Reflection absorption infrared arrangements in an apparatus used for TPD.

3.4 Irradiation sources in the laboratory

To mimic the irradiation environment from cosmic ray particles and accelerated charged particles from planetary magnetospheres we need to use a wide range of irradiation sources and energies. Therefore electrons at various energy ranges (1 keV –5 keV) were used in our experiments to study the molecular formation in the ice mantles. In addition we measured the photoabsorption spectra using synchrotron

radiation (based at the University of Aarhus and NSRRC Taiwan) to explore the spectroscopy and morphology of ices. Electrons with 1 keV energy were used during the experiments at The Open University, The electron beam current ranges between 100 nA to 100 μA.

3.5 Irradiation dose

Since all the irradiation sources were different and a wide range of energies were used to study the chemistry, in order to compare and understand the amount of energy implanted on to the ice by different irradiation sources a common scale has to be used. There are several factors that affect the amount of energy deposited during the irradiation processes including:

- The density and thickness of the ice sample,
- The type of irradiation source (electron, proton or UV photons),
- The energy of the electron, proton or ion used,
- The irradiation beam current and time.

For a given density and thickness this can be obtained for a specified ion and energy. Stopping power is given in eV $Å^{-1}$ or eV cm^{-1} $molecule^{-1}$. The fluence of the irradiation source i.e. the number of electrons or ions incident on the ice sample per unit area. Fluence (electrons or ions per unit area) is dependent on the electron or ion beam current (I_{sample}), irradiation time (t) and area of the sample (a) being irradiated, as given in the following equation:

$$Fluence(electrons\ or\ ions\ cm^{-2}) = \frac{t(s) \times I_{sample}(A)}{e(C) \times a(cm^2)} \quad (3.7)$$

From the product of stopping power and fluence (equation 3.8) a unit of eV molecule^{-1} will be obtained and this is termed as dose. The dose is the quantity that gives a common scale to compare different irradiation source.

Dose = Stopping power x fluence

[eV cm^{-2} molecule^{-1}] x [electrons or ions cm^{-2}] = eV molecule^{-1} (3.8)

Thus the dosage was determined for each irradiation source used and either 16 or 18 amu is used commonly to obtain dose in eV 16 or 18 amu^{-1}. This is obtained by dividing 16 or 18 amu by the molecular mass of the ice under irradiation. For example equation (3.9) shows oxygen (molecular mass = 32) ice irradiation in terms of dose in eV 16amu-1.

Dose = [eV molecule^{-1}] x [16 / 32] = eV 16 amu^{-1} (3.9)

To study the formation kinetics of a new molecule formed by irradiation the temporal growth, i.e. the number of molecules vs. time, is used. However, for low energy ions and electrons (1- 4 keV) the term fluence (ions cm^{-2}) can be used to determine the production of new molecules in terms of column density (molecules cm^{-2}) in order to relate the number of ions implanted and new molecules produced in an unit area. Finally to compare irradiation from different sources at different energies on a molecular ice it is imperative to use the irradiation dose.

3.6 Powder sample deposition

Samples of PAHs and molecules such as glycine exist in powder form at the room temperature. In order to deposit them on to the ZnSe substrate, we designed a UHV sample deposition chamber (**Figure 3.5**), The powder sample is collected in a ceramic crucible and placed on the bottom side of the UHV chamber, a cleaned ZnSe window was placed on a specially prepared OFHC holder with ceramic caps (**Figure**

3.6). After placing the sample and substrate the chamber is closed and pumped down to HV pressures (~ 10^{-7} mbar). Then the pump is turned OFF and the heater is turned on, the temperature can be regulated by an automated heating regulator. The deposition rate is roughly noted by time-pressure method.

Figure 3.5 Sample deposition chamber for powder samples (eg. PAHs and glycine).

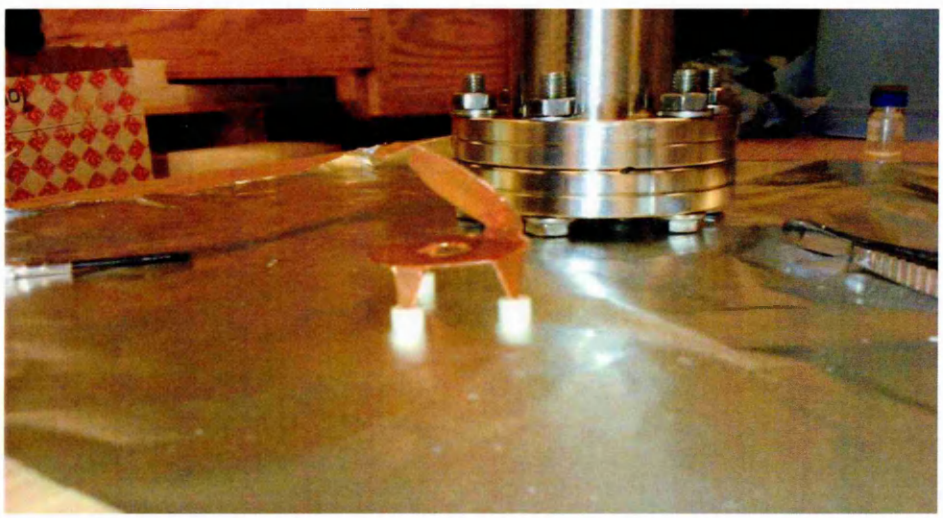

Figure 3.6 Substrate holders with high temperature ceramic legs.

Figure 3.7 Deposited powder samples (Glycine) on ZnSe (left), Glycine after electron processing (right).

The resulted films were removed from the chamber after preparation and stored in a clean-dry environment before inducting into the tip of the cold head (**Figure 3.7**).

3.7 Detecting chemical modifications in the ice

In order to detect the chemical changes induced by the effect of irradiation on a molecular ice a reliable and non destructive detection method needs to be used. Infrared spectroscopy was used as a tool to detect chemical modifications that occur in the ice phase and mass spectrometry was used to analyse the products subliming from the substrate into the gas phase.

3.7.1 Infrared spectrometry

A commercial Fourier Transform InfraRed (FTIR) spectrometer (**Figure 3.7**) using either the transmission (**Figure 3.2**) or reflection absorption mode (**Figure 3.3**) was used to record the infrared spectra of molecules over the Mid-InfraRed (MIR) range, 4000 – 400 cm^{-1}. A Michelson interferometer was used to obtain the interferogram and then by applying a Fast Fourier transform (FFT) mathematical tool a FTIR spectrum is generated.

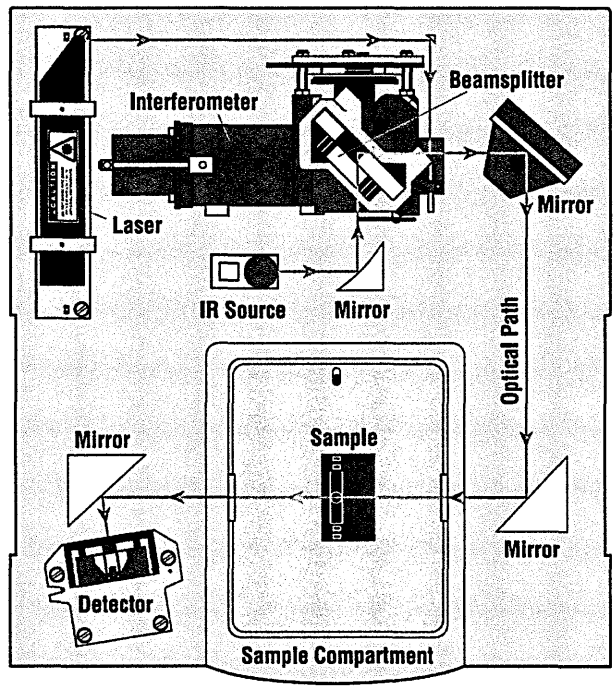

Figure 3.8 Schematic of an FTIR spectrometer (Image credit: Thermo Nicolet)

The MIR range with resolutions from 1 to 4 cm^{-1} was used in all the laboratories where electron, proton and ion irradiation were carried out. A background infrared spectrum of the substrate, kept at low temperature and at UHV, was recorded initially before depositing a molecular gas (**Figure 3.9**). After gas deposition the recorded spectrum was ratioed to the background spectrum (**Figure 3.8**) acquired before deposition.

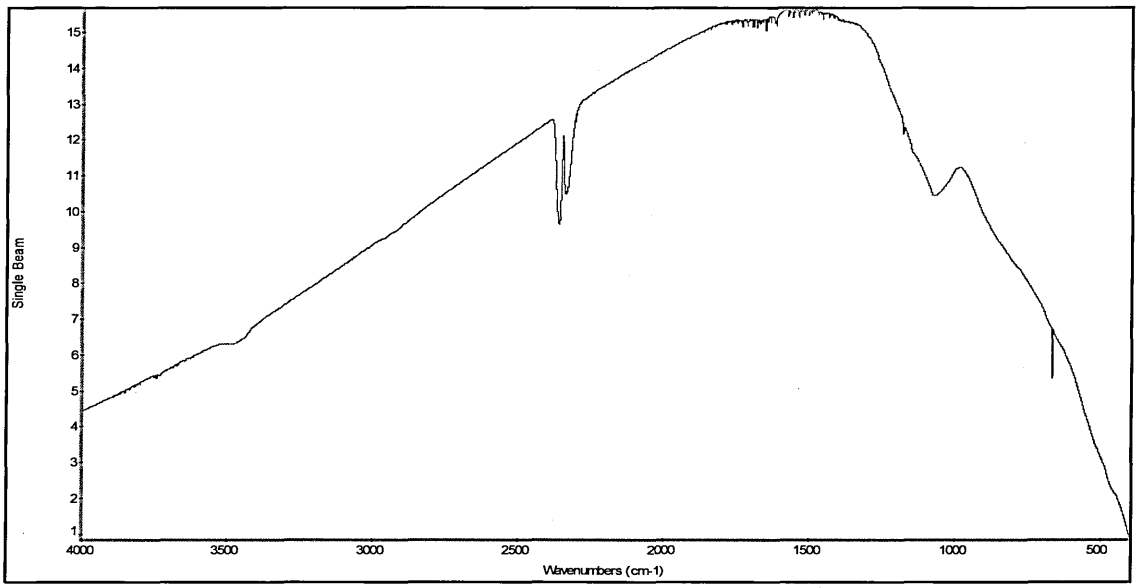

Figure 3.9 A typical background spectrum (4000-400 cm^{-1} region). Absorption at 2350 cm^{-1} is from atmospheric CO_2 and absorption features at 1800, 3400 cm^{-1} is due to ambient H_2O.

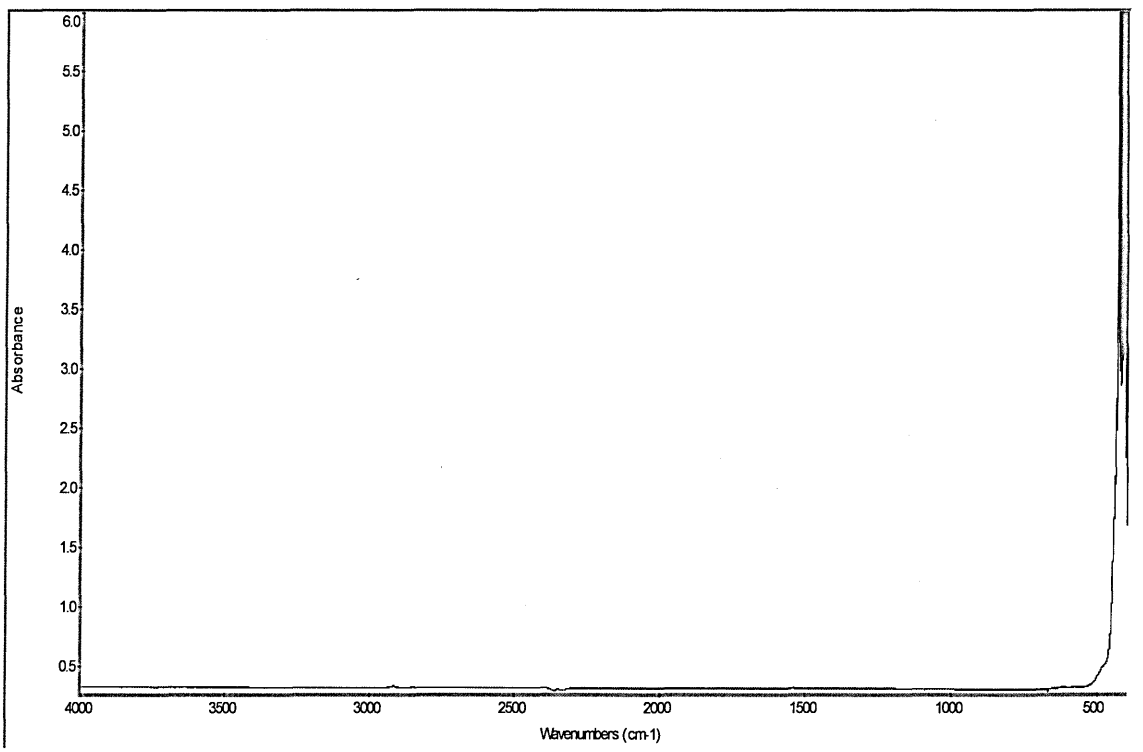

Figure 3.10 FTIR Calibration spectra of ZnSe substrate window in transmission mode with MCT-HD external detector.

In a typical background spectrum (**Figure 3.8**), there are several absorption features which corresponds to ambient medium, absorption at 2350 cm^{-1} is from atmospheric CO_2 and absorption features at 1800, 3400 cm^{-1} is due to ambient H_2O.

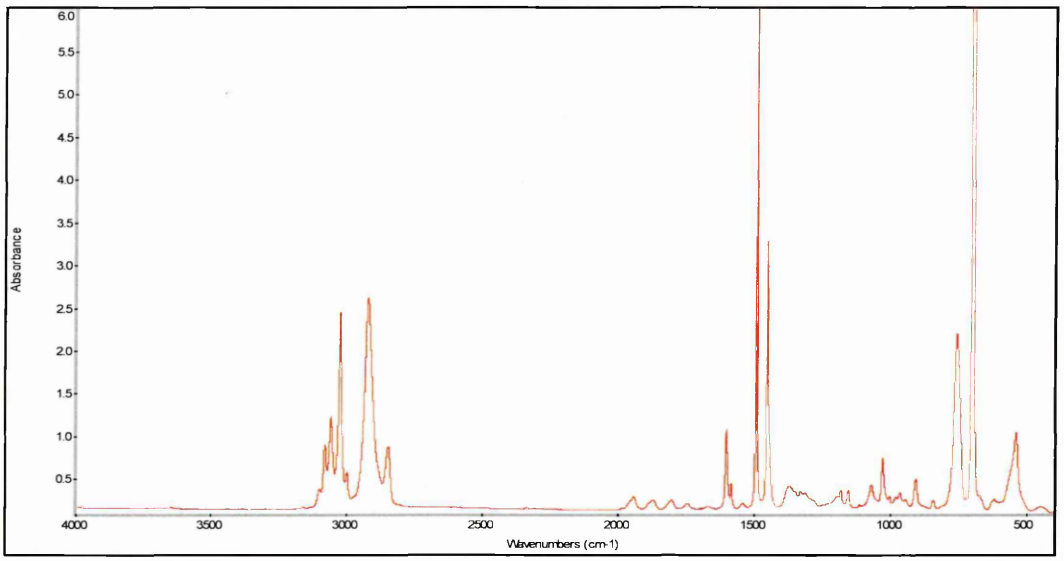

Figure 3.11 FTIR calibration spectra of plolystyrene film in transmission mode with DTGS detector.

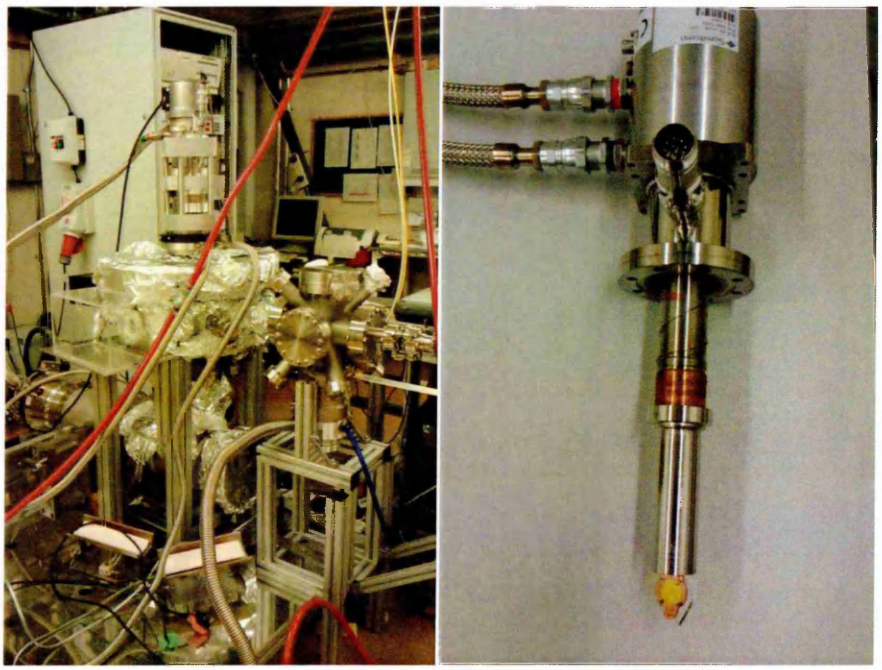

Figure 3.12 (a) Photograph of TPD chamber and (b) Cryostat and cold finger with ZnSe substrate.

Atmospheric corrections can be employed to reduce these contributions, and also by isolating the entire environment from the ambient medium and by flushing the volume by dry air or nitrogen. It is also important to calibrate the spectrometer with a standard polystyrene film and to align the optical bench prior to the actual acquisition. An absorption spectra of a polystyrene film is shown in Figure 3.10, the spectra was collected with the internal triglycine sulphate (TGS) detector, the same procedure was followed for the MCT detector, and the resulted absorption peaks were studied and calibrated against the NIST calibration values [Gupta et al., NIST special publications 1995].

3.7.2 Mass spectrometry

A Quadrupole Mass Spectrometer (QMS) was used in the experiments to record desorbing molecules in the gas phase. These gas phase species were produced as a result of sputtering of the ice film during irradiation or due to ice sublimation during warm-up. A quadrupole mass spectrometer (Hiden Analytical) with minimum detection range of 2×10^{-13} mbar is used to measure the residual gas generated during temperature programmed desorption (TPD) as well as during the electron or UV processing. The QMS is mounted at 90^0 with respect to the substrate window, this ensure the high probability of detection of desorbing molecules along line-of-sight. QMS operates in the range of 1– 200 amu with a mass resolution of 1 amu. Figure 3.13 shows the QMS.

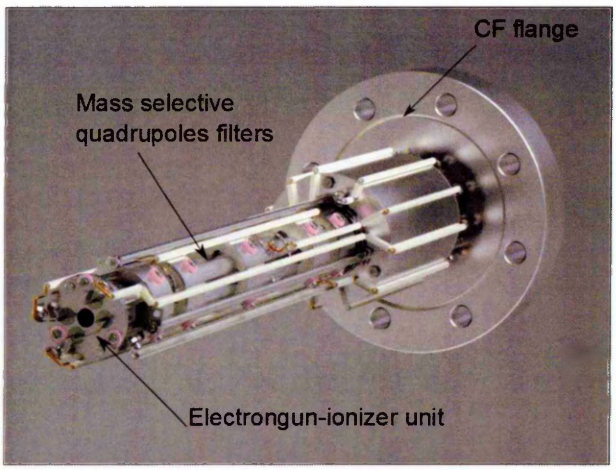

Figure 3.13 Quadrupole mass spectrometer (Residual gas analyser)[Hiden analytical]

3.8 Chemical substrates and windows

To observe the physio-chemical changes in the ice films during electron or thermal processing and TPD experiments, we employed FTIR and VUV spectral techniques. The window materials used for each experiment were carefully selected according to the range of transmission, chemical nature, and refractive index properties of these materials. In addition to windows, transparent materials in mid-IR or VUV regions were also employed as a substrate to deposit ice films (**Figure 3.14**).

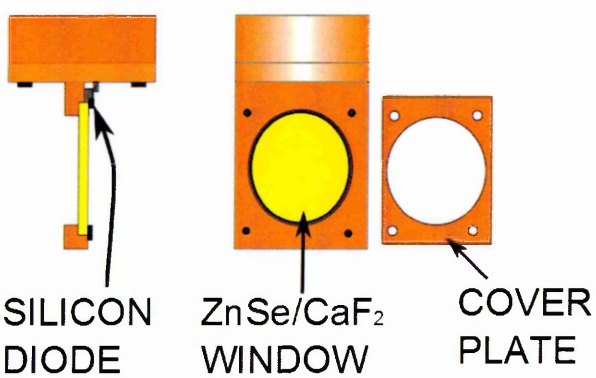

Figure 3.14 Schematic diagrams of substrate holder and substrate windows

Zinc selenide (ZnSe) was used as the substrate material due to good thermal conductivity in comparison with potassium bromide (KBr). In addition ZnSe is chemically inert, whereas KBr is hygroscopic. So, KBr was used as the window material except at CAO, where Silicon (Si) was used as a substrate. Therefore all three infrared transmission windows were used as substrate material and out of which only KBr was used as a window material to hold UHV inside the chamber and atmospheric pressure outside the chamber. For the VUV experiments either magnesium fluoride (MgF_2) or calcium fluoride (CaF_2) was used as a substrate material.

3.9 Astroices portable chamber at The Open University

The experimental astrochemistry apparatus based at The Open University (OU) can simulate irradiation environments down to temperatures of 10 K and pressures of the order of 10^{-10} mbar. **Figure 3.15**, shows a schematic diagram of the portable chamber used in the Astro-ices laboratory at The Open University. The chamber has four ports on each side of the stainless steel chamber. One of which is used for the gas inlet, another used for the electron gun and the other two ports placed on either side are used for the infrared beam to pass through. Potassium bromide (KBr) windows are used in order to have an interface between the UHV (10^{-10} mbar) and atmospheric pressure regions to allow infrared beam to probe the ice. The Zinc Selenide (ZnSe) substrate used inside the chamber is also infrared transparent. As KBr is hygroscopic and ZnSe is chemically inert the later was chosen for depositing the molecular ices.

Using compressed high pressure (20 bar) helium gas from a closed cycle cryostat, the ZnSe substrate was cooled down to ~ 20 K. The substrate was then

rotated towards the gas inlet which was a metal nozzle that extends into the UHV chamber from the gas line (ø ~5mm). After deposition the substrate was rotated towards the IR beam with spot size 15-20 mm (variable aperture) to record spectra of the deposited ice sample. Further rotating the substrate to face the electron beam will expose the ice for irradiation, as in **Figure 3.15**. The diameter of the ZnSe substrate was about ø 20 mm and the electron beam spot size at 1 keV was 20 mm at 4.5 mm from the emission tip of the electron gun (Kimbal Physics EGL-2).

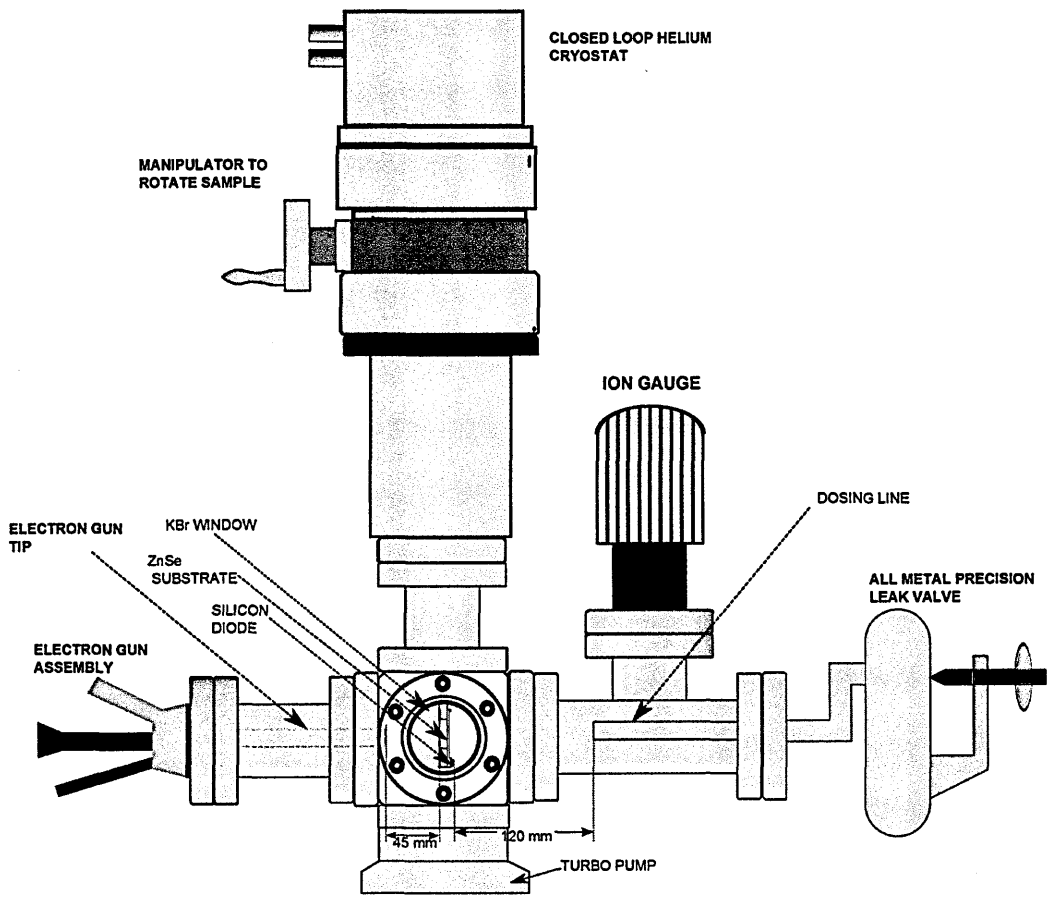

Figure 3.15 Portable chamber at the Open University, used for electron irradiation and VUV spectroscopy, in this configuration chamber is mounted with an electron gun.

Spot size of the electron gun was optimized to 20 mm at the sample by positive grids (+5 V), shape and size of the electron beam at the sample position was

calibrated by using a phosphor screen. The spot size of electron beam of energy 1-5 keV is variable from 5 mm to 50 mm within a working distance of 100 mm (Kimball Physics ELG-2) by varying the spot size. The substrate was also placed at 45^0 angles such that both electron irradiation and IR detection can be performed at the same time. This technique allows the detection and quantification of new molecules with respect to time.

Using resistive heaters the sample could be heated to any desired temperature above the irradiation temperature and a spectrum recorded. Spectral changes, if any, due to a rise in the temperature indicate other chemical changes that take place in the ice. Spectra recorded at different temperatures while heating the substrate allow the sublimation temperature of the ice to be evaluated. The thickness of the ice was selected such that electrons were stopped before the substrate; penetration depth of electrons in the ice films varies with composition and morphology. The penetration depth of electrons (energy- 5 keV) in water ice is ~ 275 nm [Gudipathi et al. 2012].

3.10 Vacuum Ultraviolet spectroscopy

As a continuum source of UV photons, we used the synchrotron irradiation facility based at the University of Aarhus and NSRRC, Taiwan, and recorded the VUV spectra of molecules in the condensed phase. The UV1 beamline provides low photon energy irradiation over wavelengths ranging from 100 – 700 nm but in these experiments only the 120 -320 nm range was used.

The portable chamber at The Open University (Figure 3.15) was modified to perform VUV experiments with the electron gun being replaced by VUV photon line and we used a photomultiplier tube (Hamamatsu) for recording the photo absorption spectra. In this we used calcium fluorite (CaF_2) as substrate, since it has high

transmission range from 109 to 320 nm. Spot size of the VUV beam at ASTRID was 1.5-2 mm at the undulator exit and 2-5 mm at the sample. Spot size of the VUV beam at NSRRC was 0.1-1.0 mm at the undulator exit and 5 mm at the sample. Deposition line, pumping system, cryostat and pressure monitoring systems were as before.

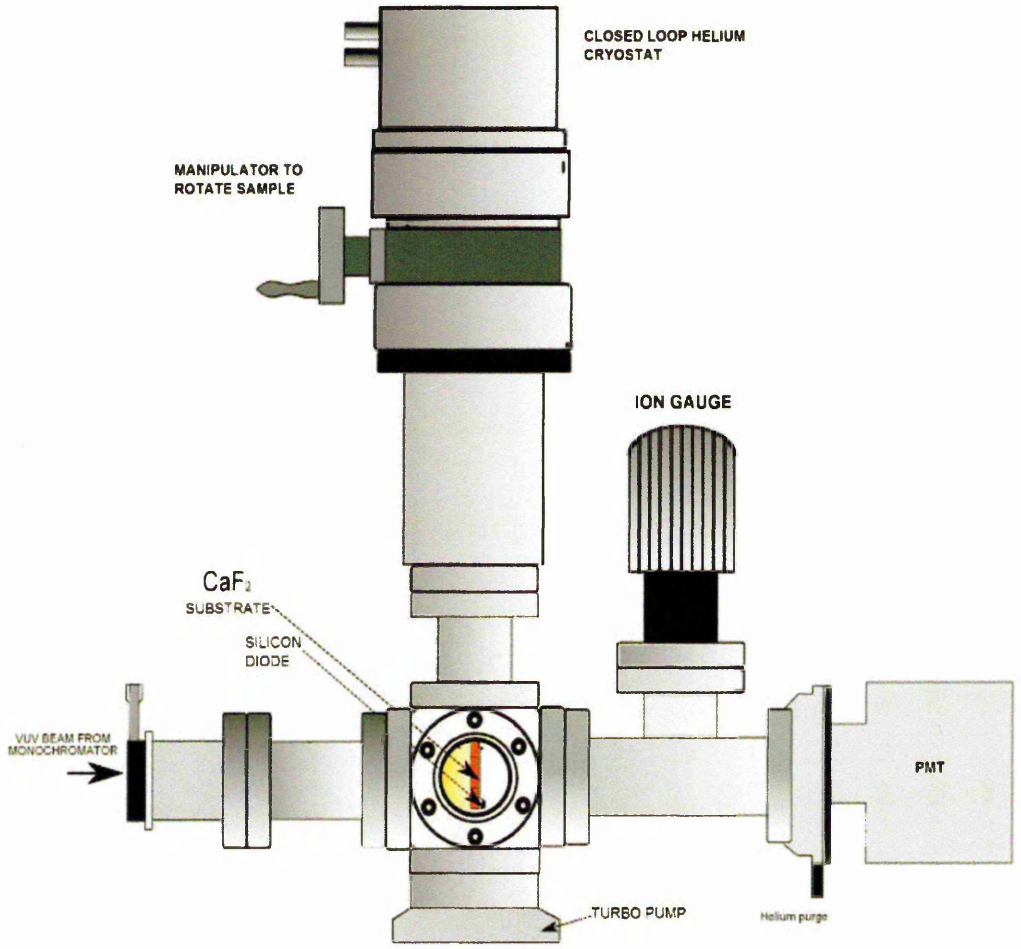

Figure 3.16 Portable chamber modified for VUV spectroscopy measurements at UV-1, (ASTRID) Aarhus.

A helium purge was employed at the PMT end to avoid absorption by atmospheric oxygen, see **Figure 3.16**. A background spectrum with and without CaF_2 substrate was recorded to calculate the absolute absorption. The ice sample was grown on the substrate in the same way as in the electron irradiation experiments, and VUV photoabsorption spectra of the sample was recorded with 1 nm resolution.

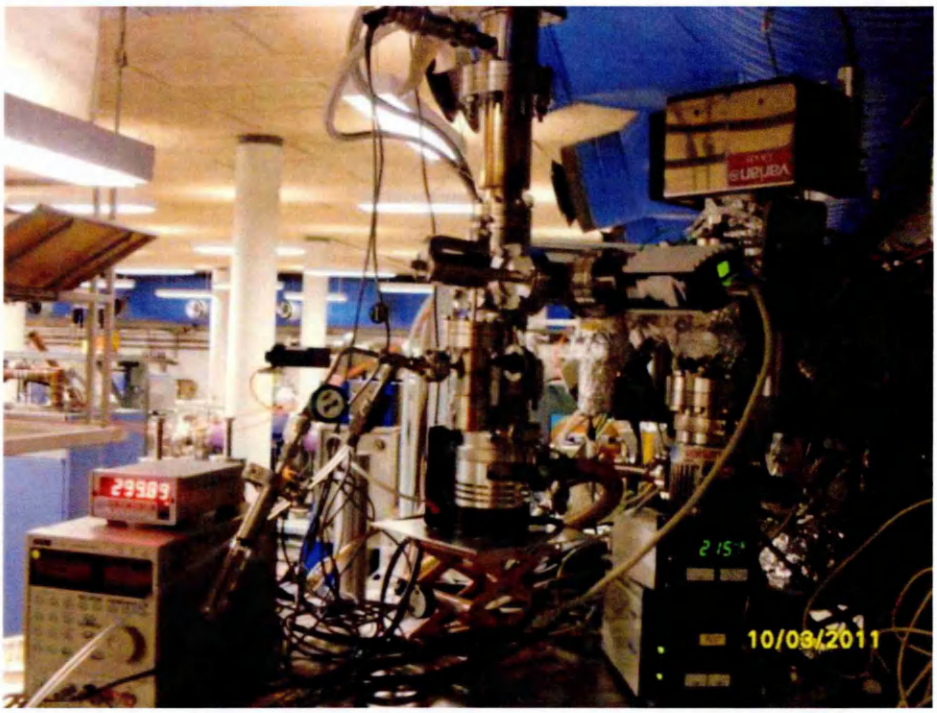

Figure 3.17 Portable chamber mounted on the UV-1 beamline, ASTRID-1

UV-A1 beam line at the NSRRC, Taiwan is a high flux beamline with highly stable beam energy with high precision grating monochromator provides a resolution of 100,000. The procedures described above were also repeated in the NSRRC experiments. Portable chamber integrated with UV1 beamline, ASTRID is shown in **Figure 3.17**. UHV chamber used for VUV experiments at UV-A1beamline, NSRRC is shown in **Figure 3.18**; sample dosing line, cryostat and the PMT arrangements can be noted.

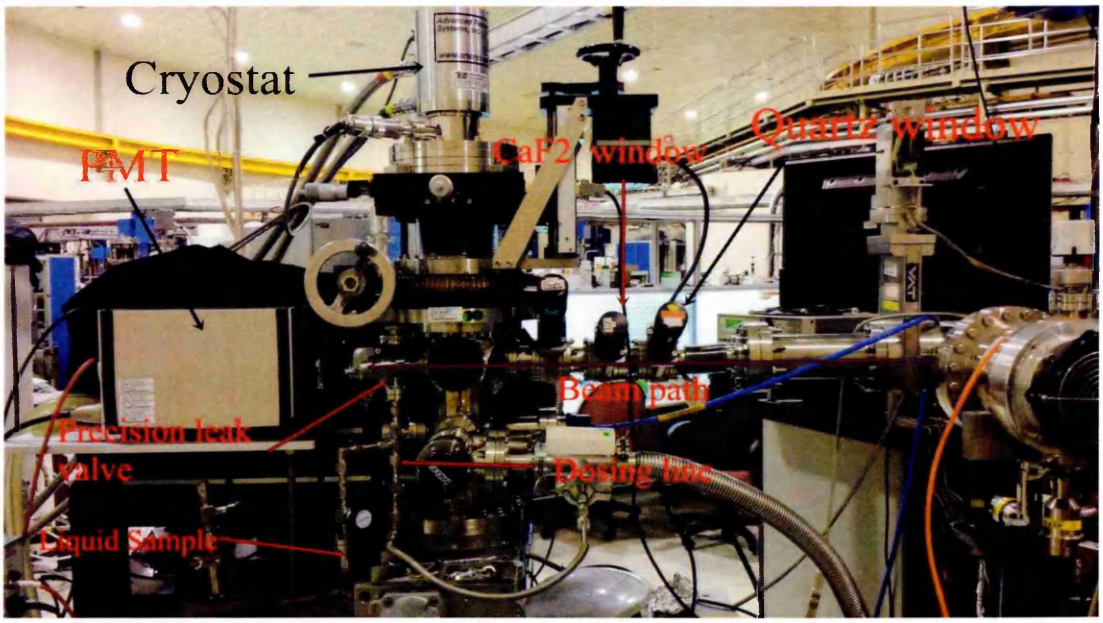

Figure 3.18 VUV experiment chamber at UV-A1 beamline, NSRRC.

The VUV photo-absorption cross-section is calculated from the absorption spectra by using modified Beer-Lambert law,

Ratio of intensity of incident light I_0 to the transmitted light I_t through a medium can be expressed as,

$$A = \ln\left[\frac{I_0(\gamma)}{I_t(\gamma)}\right] \tag{3.5}$$

where A is the absorbance. Therefore absorption cross-section is,

$$\frac{I_t}{I_0} = e^{-\sigma cl} \tag{3.6}$$

where σ is the absorption cross-section, c is the concentration(number density), l is the path length.

A detailed description of synchrotron source is presented in section 3.11.

3.11 Synchrotrons

A synchrotron is a particle accelerator that produces photons (electromagnetic waves) of high flux in the region from infrared through to X-rays. Accelerated charge particle emit electromagnetic radiation, during acceleration a rearrangement of its electric fields is required and this field perturbation, travelling away from the charge at the velocity of light, and radiated in the form of electromagnetic waves.

Accelerated electrons behave similarly; when the source is in motion the properties of the emitted radiation are also different. Radiation from a fast moving particle source appears to the observer in the laboratory as being all emitted in the general direction of motion of the particle. This forward collimation is particularly effective for highly relativistic electrons where most of the radiation is concentrated in a small cone with an opening angle of $1/\gamma$ (some 0.1 to 1 mrad), where γ is the particle energy in units of its rest energy (typically 103 - 104). In synchrotron radiation sources (storage rings) highly relativistic electrons are stored to travel along a circular path for many hours.

Radiation is caused by transverse acceleration due to magnetic forces in bending magnets (forming the circular path) or periodic acceleration in special insertion device magnets like undulators, wiggler magnets and wave length shifters. Radiation is linearly polarized in the plane of acceleration (in most cases the horizontal plane). Elliptical polarization occurs for bending magnet radiation observed from above or below the midplane. The radiation is emitted in pulses of 10 - 20 psec separated by some 2 nsec or longer separation if desired.

Different parts of a storage ring perform different functions, undulator, wiggler, bending magnets etc.

Undulator: The electron beam is periodically deflected by weak magnetic fields. Similar to antenna radiation the particle emits radiation at the wavelength of its periodic motion in the undulator (**Figure 3.19**). To the particle this wavelength is the undulator period length (λp) divided by γ due to relativistic Lorentz contraction. In the laboratory system this wavelength appears to the observer further reduced by another factor γ due to the Doppler Effect. The undulator period length of the order of cm^2s is thus reduced by a factor $\gamma 2$ (106 - 108) to yield short wavelength radiation in the VUV and x-ray regime. The spectral resolution of the radiation is proportional to the number of undulator periods and its wavelength can be shifted by varying the magnetic field. Most radiation is emitted within the small angle of $1/\gamma wNp$.

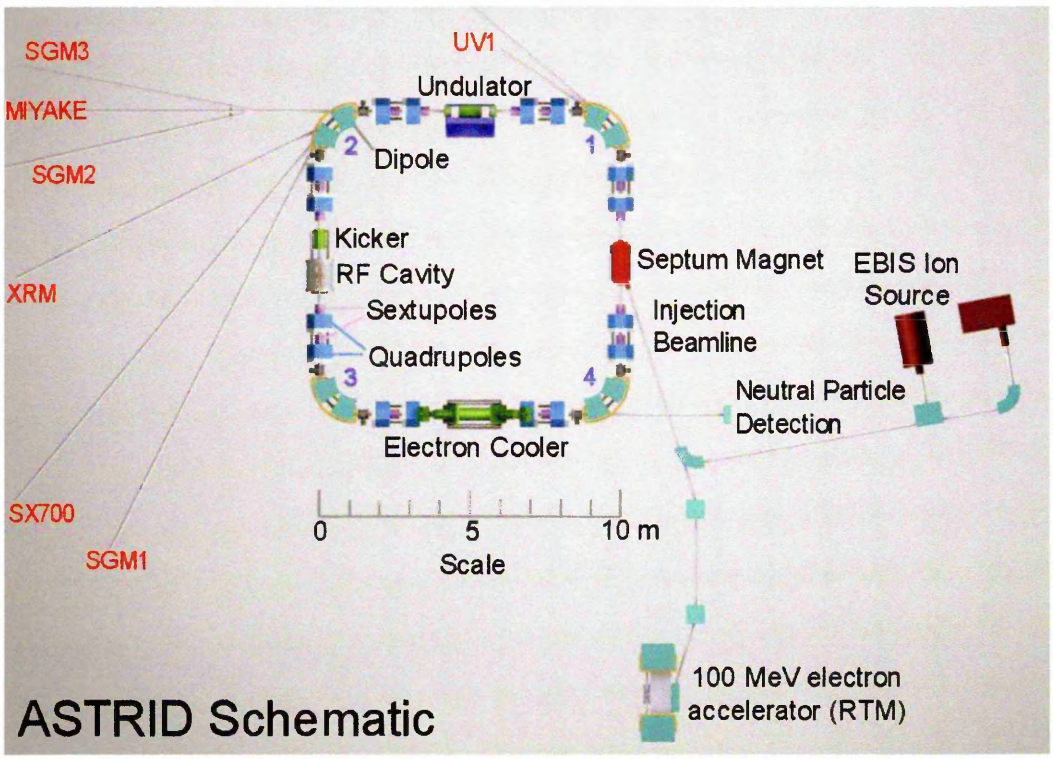

Figure 3.19 Schematic representation of ASTRID synchrotron

Wiggler magnet: Increasing the magnetic field strength causes the pure sinusoidal transverse motion of electrons in an undulator to become distorted due to relativistic effects generating higher harmonics of the single wavelength undulator radiation (**Figure 3.14**). The monochromatic undulator spectrum therefore changes into a line spectrum. For very strong fields many harmonics are generated which eventually merge into a continuous spectrum from IR to hard x-rays. The spectral intensity varies little over a broad wavelength range and drops off exponentially at photon energies higher than the critical photon energy. Compared to bending magnet radiation, wiggler radiation is enhanced by the number of magnet poles and is well collimated within an angle of K/γ, or a few mrad.

Bending magnet: Radiation is emitted tangentially to the orbit similar to a search light while well collimated in the non-deflecting or mostly vertical plane (**Figure 3.14**). The observer at the Experimental station sees radiation from only a small fraction of the circular path which can be described as a piece of a distorted sinusoidal motion. The radiation spectrum is therefore similar to that of a wiggler magnet while the intensity is due to only one pole. Because the geometry of the storage ring is determined by bending magnets, it is not possible to freely choose the field strength and the critical photon energy is therefore fixed.

Wavelength shifter: This magnet consists of a high field central pole and two weaker outside poles to compensate the deflection by the central pole. The field strength can be chosen freely to adjust the critical photon energy and is used in conjunction with superconducting magnet technology particularly in low energy rings to extend the available photon energy to higher value.

3.12 Conclusion

UHV chambers have been modified to integrate with the end station of a VUV beamline to investigate the VUV photoabsorption features of condensed films of astrochemically relevant molecules. The same UHV chamber has been employed to investigate the electron impact studies condensed films of samples of pure and mixed molecules which are both relevant to interstellar medium and planetary surfaces. The electron irradiation experiment was monitored in-situ by a transmission mode FTIR spectrometer. The design, operation and specification of both these systems and accessories, and the procedure to integrate them with the beamline, preparation of ice films, maintaining vacuum and cryogenic conditions etc are also discussed in this chapter.

CHAPTER 4

TEMPERATURE DEPENDENT VACUUM ULTRAVIOLET (VUV) SPECTROSCOPY OF ASTROCHEMICALY RELEVANT MOLECULES

The iron from that meteorite and the iron from our blood have common origin in the core of a star.
- Tyson

4.0 Introduction

Understanding the interaction of vacuum ultraviolet (VUV) photons (50,000 cm^{-1} to 100,000 cm^{-1} or 100 to 220 nm) with molecules is central to determining the electronic state spectroscopy of the molecule. VUV photo-absorption experiments with continuum light sources are one of the best ways to measure high resolution photo-absorption cross-section and photolysis rates [Robin 1974]. As discussed in the first chapter, the interaction of UV radiation and cosmic rays leads to the chemical evolution of the molecular cloud and to understand such changes over the vast spatial and temporal scales of the ISM, we need to construct astrochemical models. In such a model, parameters such as UV absorption cross-section and photolysis rates provide crucial constraints and lead to a better understanding of pathways of complex molecular formation. In addition, laboratory spectra of interstellar ice analogues in the VUV region may be used as a reference for observational astronomy in this spectral window. VUV spectroscopy is an important tool for investigating the morphology of

ice films [A Dawes et al. 2007]. VUV spectra also help to understand the nature of Rydberg transitions by comparing, spectra of a molecule in gas, and condensed phase [Robin 1974]. Since, temperature is the major parameter which drives the morphology of these condensed films; it is also necessary to measure such spectra for several temperatures ranging from 10 K to 200 K. This chapter describes the vacuum ultraviolet photo-absorption spectroscopy of ice films of 12 molecules relevant to astrochemistry and astrobiology.

A detailed description of the experimental setup is described in chapter 3. Experiments were carried out using the ASTRID synchrotron facility at the University of Aarhus in Denmark and the National Synchrotron Radiation Research Centre (NSRRC), Taiwan. The UV1 beamline at Aarhus has a resolving power of 1000 to 5000 achieved by a grating monochromator with 2000 lines/mm and the beam has a typical flux of 2×10^{11} photons /sec. Our experiments were carried out over the range of 120 to 320 nm limited by CaF_2 windows used at the entrance and exit of the target chamber and as the substrate. The 0B1 VUV beamline at NSRRC is a high flux beam line derived from a 1.5 GeV storage ring, the beam is dispersed with a cylindrical grating monochromator (focal length 6 m) which provides excellent spectral resolution around 100,000 and for our experiments the wavelength range was selected between 120 to 350 nm. We used a LiF window as a substrate to grow the ice film and transmission spectra were recorded with a photomultiplier tube (Hamamatsu R-94302) setup.

4.1 The Molecules

Accurate photo-absorption cross-sections are crucial for astrochemical modelling. In this study organic species which are believed to play a major role in interstellar chemistry were chosen, the majority of these molecules being interlinked

by various proposed reaction schemes. The majority of these molecules have already been detected in interstellar space, while the others are potential candidates in forming intermediates leading to detected species and are believed to play a role as precursor to astrochemically and astrobiologically relevant molecules. Even though there are systematic VUV studies of such molecules in gas phase [Robin 1974], very little is know about them in condensed phase and the optical properties of condensed ice films of these molecules are largely unknown.

Table 4.1 List of molecules, regions of ISM where it was detected and the respective column densities are listed in the table.

	MOLECULE		REGIONS IN ISM	COLUMN DENSITY/ cm^{-2}
1	FORMAMIDE $HCONH_2$	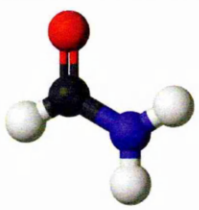	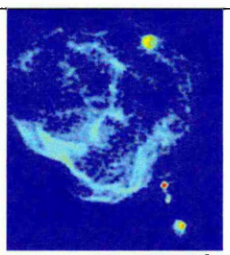 Sgr B2(N)[c]	2.7×10^{13}
2	FORMIC ACID HCOOH	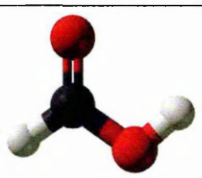	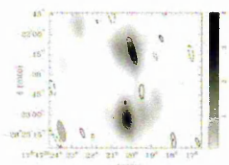 HCOOH in Sgr B2	11.0×10^{15} ICE- 2.4×10^{17} (NGC 7538: IRS 9)
3	METHYL FORMATE $HCOOCH_3$	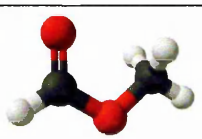	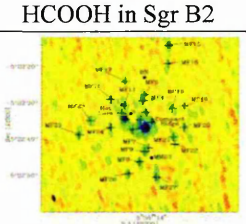 $HCOOCH_3$ in Orion KL	1.6×10^{16}
4	BENZENE C_6H_6	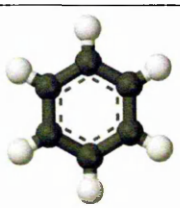	 CRL-618	3.0×10^{14}

5	ALLYL ALCOHOL	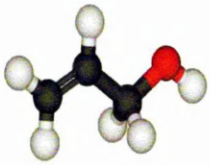	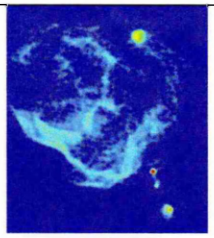 Sgr B2(N)	• Not yet detected • A potential species • Vinyl alcohol detected in SgrB2
6	METHYL ACETATE	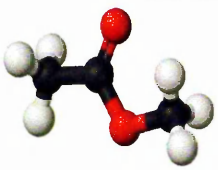	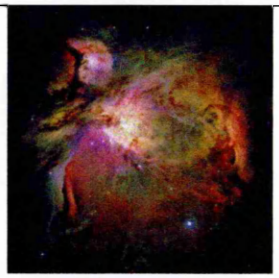 Orion nebula	1.4×10^{15}
7	PROPIONOIC ACID	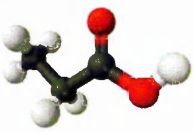	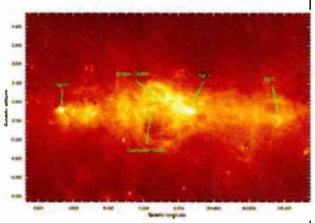 Sagittarius A,B2 and C	Trace amounts
8	OZONE	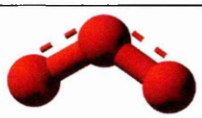	 Martian atmosphere	Trace amounts

4.2 VUV photo-absorption studies of formamide ($HCONH_2$) at 30 K- 160 K

Formamide ($HCONH_2$) is an organic species which is believed to be a precursor, to many of the more complex organic molecules responsible for the origin of life. Formamide is a precursor molecule in the formation of purine and pyrimidine bases [Nguyen 2010] during the course of chemical evolution towards the origins of life. The importance of formamide as a possible pre-biotic precursor has been well known for more than a century, it is also a precursor for sugars and recently, Barks et al. [Barks et al 2010] have shown the production of guanine, adenine and hypoxanthine from UV irradiation of formamide solutions. However, the rate coefficients for the formation of this pre-biotic molecule under ISM conditions are still not known to any certainty.

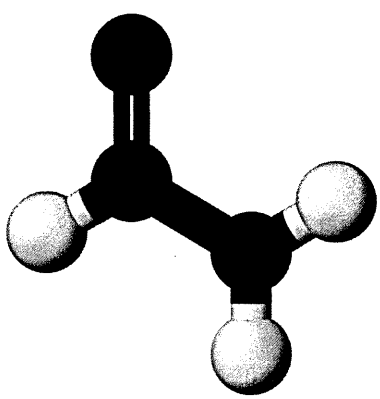

Figure 4.1 Molecular structure of Formamide, $HCONH_2$

Formamide has been observed as a gas phase molecule in many different environments in the interstellar medium, in the long period comet C/1995 O1 Hale-Bopp [Raunier et al. 2004; Requena-Torres et al. 2006], towards several protostars and, tentatively, in the young stellar objects W33A and NGC 7538 IRS9 [Bockelee-Morvan et al. 2000, Schutte et al. 1999] and, most recently, with high abundances in SgrB2 (N) [Halfen et al. 2011].

The molecular structure of formamide is shown in the **Figure 4.1**, and ground state electronic configuration of formamide is

$$(\sigma_8)^2(\sigma_9)^2\ (\pi_1)^2\ (\pi_2)^2(n_0)^2\ (\pi_3)^2$$

Formamide is a good example of the species which exhibit quenching of Rydberg states in the condense phase, [Robin 1974] all the transitions are repeated in the condense phase, but the Rydberg transitions are quenched and shifted towards higher energy region. In order to calibrate the film thickness we used the infrared transmission spectrum and determined the line of sight column density of molecules in the film by using modified Beer-Lamberts equation and integrated absorption value (A) of formamide from the literature. Detailed description of the spectral analysis is described in section **4.2.1.**

Formamide (99.5% Sigma Aldrich) was degassed through a freeze (using liquid nitrogen at 77 K)-thaw-pump cycle for three times, and then introduced into the UHV chamber through an all metal gas line system (Swagelok) with a high precision leak valve (range ~ 10^{-10} to 10^{-5} mbar). Deposition pressure was maintained at 1 x 10^{-6} mbar (1 Langmuir) and the vapour was deposited (background deposition) for 30seconds on to a CaF_2 window maintained at 30 K and positioned to face the deposition line. We continued the deposition process ten times and made the ice film of desired thickness. An FTIR spectrum (transmission mode) of the ice film in mid-IR region (4000 cm^{-1} to 400 cm^{-1}) with a resolution of 1 cm^{-1} was recorded at every deposition (Figure 4.2), sample was kept normal to the IR beam and the absorption spectrum was prepared for the quantitative analysis. The spot size of the IR beam and the size of the CaF_2 window were aligned and calibrated in such a way that, ø = 20

mm of the window material is entirely scanned by the IR beam. A recorded FTIR spectrum of condensed formamide at 30 K is shown in **Figure 4.2.**

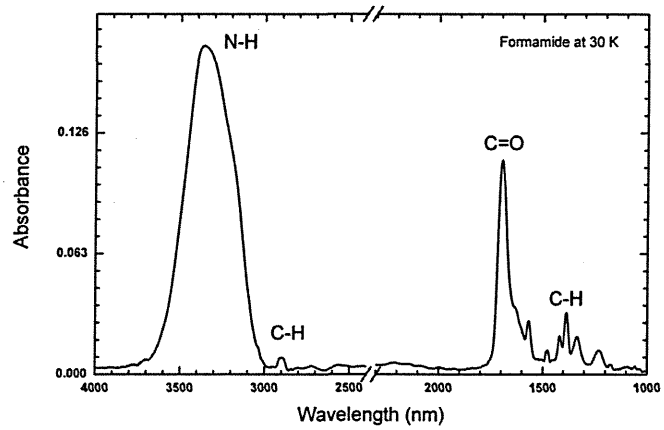

Figure 4.2 Absorption spectrum of condensed formamide at 30 K.

The reported density of formamide ice from the literature is, $\rho = 0.937$ g cm^{-3} [Brucato et al. 2006] and integrated infrared band absorption value, $A = 0.68 \times 10^{-17}$ cm mol^{-1} at 1688 cm^{-1}. Using the 'A' value and density, the column density of the molecules in the film (using equations 3.3 and 3.4) was found to be 1.46×10^{17} molecules/cm^2, and the film was ~ 116.75 ±.5 nm thick.

4.2.1. Results and discussion

VUV photo-absorption studies of formamide in gas phase have been studied extensively [Gingell et al. 1997, Robin 1974] in contrast there are few condensed phase studies, the valence transitions in the gas phase was identified as V_1 and Q bands, and there is an additional transition W from the non-bonding orbital.

From the gas phase VUV studies and calculations it is evident that formamide can undergo the following transitions,

Singlet transitions of formamide	Triplet transition of formamide
W $^1(n_0 \rightarrow \pi_3^*)$ [$E_{max} \approx 5.80$ eV]	**$^3(n_0 \rightarrow \pi_3^*)$**
V_1 $^1(\pi_2 \rightarrow \pi_3^*)$ [$E_{max} \approx 7.40$ eV]	**$^3(n_0 \rightarrow 3s/\ 3\pi_2 \rightarrow 3s)$**
R_1 [$E_{max} \approx 7.71$ eV]	**$^3(\pi_2 \rightarrow \pi_3^*)$**
R_2 [$E_{max} \approx 6.35$ eV]	**$^3(\pi_1 \rightarrow \pi_3^*)$**
Q $(^1\pi_1 \rightarrow \pi_3^*)$ [$E_{max} \approx 9.20$ eV]	

Figure 4.3 shows the VUV photoabsorption cross-section of condensed formamide at 30 K and valence transitions are labelled as V_1 and Q.

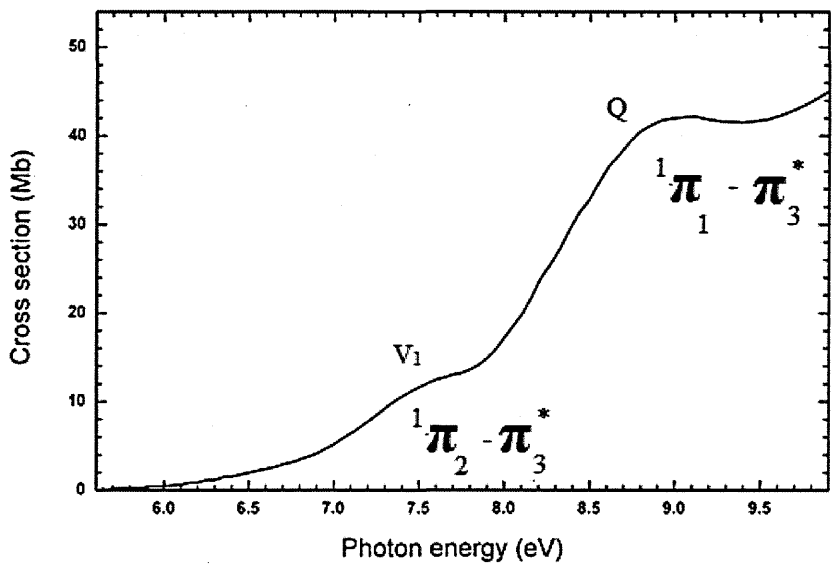

Figure 4.3 Photo-absorption cross-sections of condensed (30 K) formamide.

Figure 4.4 depicts the comparison of gas (298 K) and condensed (30 K) spectra of formamide and from the comparison we can elucidate the quenching

behaviour of the Rydberg transition of R_1 and R_2 band and the Q band has been slightly shifted towards the higher energy region.

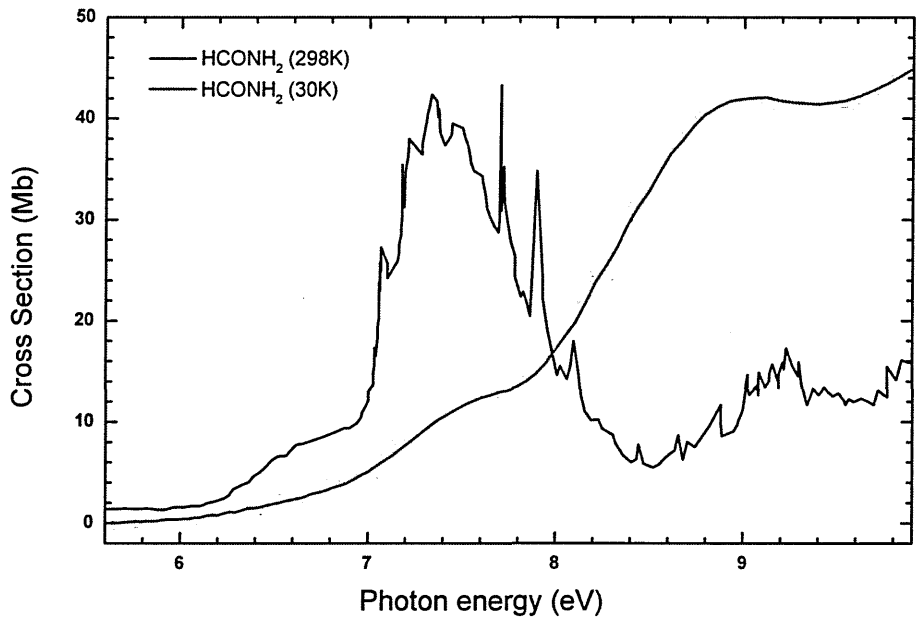

Figure 4.4 Comparison of photo-absorption cross-sections of gas (black) [Gingell et al. 1997] and condensed (30 K) formamide.

From the VUV spectra **(Figure 4.4)** in case of valence transition V_1 it is evident that there is a shift towards the higher energy region and it is in good agreement with the earlier studies reported by M. B. Robin [Robin 1974], V_1 band in gas phase (peaking around 7.40 eV) has been shifted to 7.47 eV and the Q (9.20 eV) transition has shifted to lower energy region at 8.92 eV, and this exhibits the predicted behaviour, and strictly follows Rydberg formula [Robin 1974]. Shift in the valence transitions arise because of the intra-molecular interactions of formamide in the condensed form, formation of hydrogen bonded clusters of formamide may also contribute towards such effects. At 30 K formamide ice film is mostly composed of dimers rather than the monomers [Ladell 1954; Mardyukov et al. 2007], due to the

dipole moment it readily forms dimers and these dimers are stable at lower temperatures. To investigate the effects of thermal induced effects of absorption the ice was warmed and studied at each step of warming.

The sample was warmed at a rate of 5 K/ minute and spectra were reordered at several different temperatures 30 K, 60 K, 90 K, 120 K, 150 K and 160 K. The spectra are shown in Figure 4.5.

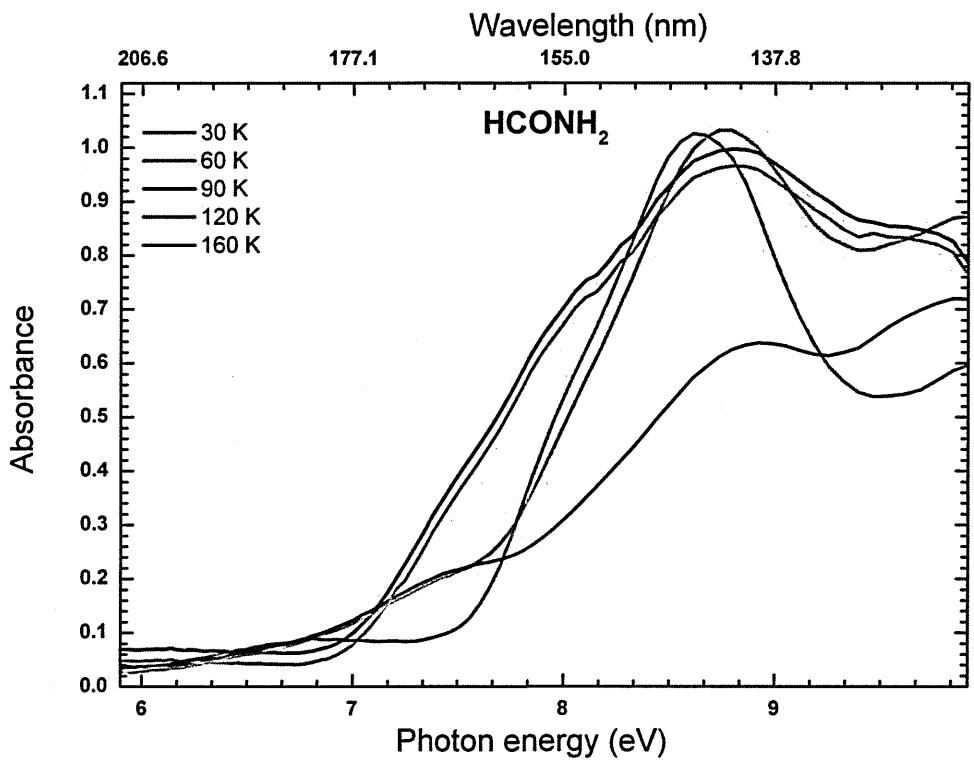

Figure 4.5 Temperature dependent variations in the absorption spectra of condensed formamide deposited at 30 K. Absorption spectra at 30, 60 90, 120 and 160 K are shown here.

With warming, V_1band at 7.47 eV started to shift towards lower energy region and the intensity of this band has diminished considerably, spectra at 160 K shows that the V_1 band has shifted to region below 7eV and intensity of the Q band has increased prominently. Therefore the changes indicated by the spectrum at 160 K are ascribed to the formation of a polycrystalline ice film of formamide. These temperature induced morphological changes in the VUV spectra of formamide ice

films are in well agreement with the recent studies reported by Sivaraman et al. [Sivaraman et al. 2013(a)], the phase changes observed in the VUV spectra are in good agreement with the FTIR (160 K phase change) studies [Sivaraman et al. 2013(b)].

4.3 VUV photo-absorption studies of formic acid (HCOOH) at 30 K

Formic acid (HCOOH) is the simplest carboxylic acid, which includes carbonyl doubly-bonded oxygen and a hydroxyl group (OH) on the same carbon atom (**Figure 4.6**). Being oxygen rich and a precursor to many biologically important species, formic acid is expected to play a vital role in astrochemistry and astrobiology [Liu et al. 2001; Bennett et al. 2011]. Gaseous HCOOH was initially detected in the interstellar medium by Zuckerman et al in 1971, and the gas phase signature of HCOOH has since been identified towards several star forming regions [Liu et al. 2001; Ikeda et al. 2005; Bottinelli et al. 2004], towards hot cores [Liu et al. 2001], the galactic centre [Requena-Torres et al. 2006], in the comet Hale-Bopp and in chondritic meteorites [Crovisier et al. 2004; Rodgers et al. 2001]. HCOOH has also been detected both in gas and condensed phase towards hot molecular cores [Schutte et al. 1999; Ikeda et al. 2005]. The observed column density of formic acid towards various sources in ISM is listed in Table 4.2, and it is observed that the abundance of the solid formic acid is a factor of $\sim 10^4$ higher than that of gaseous formic acid in high-mass star-forming regions [Schutte et al. 1999; Remijan et al. 2004].

Table 4.2 Observed relative fractional abundance of formic acid towards various regions of ISM

Source	HCOOH Column density, N (cm^{-2})	Phase
Sgr B2 N-LMH[1]	11.0×10^{15}	Gas
W51[1]	18.0×10^{15}	Gas
G327.3-0.6[6]	8.5×10^{13}	Gas
W33A[9]	7.8×10^{17}	Ice
NGC 7538: IRS 9[1]	2.4×10^{17}	Ice

Formation of formic acid by solid state pathways [Ioppolo et al. 2011], by energetic processing such as UV and cosmic ray interaction [Bennett et al. 2011] and gas phase processes have been confirmed through experiments and astrochemical models [Garrod et al. 2006; Park et al. 2006].

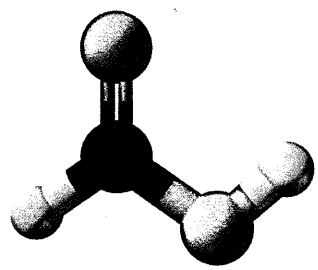

Figure 4.6 Molecular structure of formic acid

It is very likely that gaseous and solid HCOOH coexist in the same region of ISM, so to understand the condition for gaseous and solid state co-existence of formic acid, further spectroscopic investigations of condensed formic acid over VUV and mid-IR region is essential. IR spectroscopic studies of gaseous [Marechal 1987], liquid [Chapman 1956] and condensed [Gadermann 2007] phase formic acid have been investigated [Bisschop et al. 2007]. VUV photo-absorption studies of gaseous [Leach et al. 2002] HCOOH have also been investigated thoroughly, but there are no reported photo-absorption cross-section studies of condensed formic acid. Photo-absorption cross-sections in condense phase incorporate constraints in various astrochemical models and provide a better understanding of reactions involving formic acid as an intermediate and precursor. Therefore measuring high resolution photo-absorption cross-sections of formic acid in condense phase is essential. And in addition, our FTIR studies are dedicated for investigating thermally induced morphological variations of condensed HCOOH ice films of astrochemical interest.

In order to calibrate the film thickness we used an Infrared band calibration technique. We deposited 1 x 10^{-6} mbar of purified sample (freeze-thaw-pump) of formic acid vapours (99.9% Sigma Aldrich) for 300 seconds onto a CaF_2 window maintained at 30 K. A transmission mode FTIR spectrum of the ice film was then recorded normal to the IR beam. All the experiments were repeated with a CaF_2 window as substrate material and in the same chamber with unaltered volume and pressure conditions.

The integrated absorption constant of formic acid is A = 1.5 x 10^{-17} cm molecule^{-1} at 1717.5 cm^{-1}(normal to the beam) and density of formic acid ice is 1.22 g cm^{-3} [Bisschop et al. 2007]. By substituting the area under the curve measured from the recorded spectra, 'A' value and density in equation (3.5) and (3.6), we can estimate the column density and thickness of the film. The column density of molecules in the prepared ice was found to be N = 11.628 x 10^{17} molecules/cm^2 and the thickness of the film was ~ 157± 4 nm.

4.3.1 Results and discussion

The VUV spectrum of formic acid recorded at 30 K was found to have strong absorption from 107 nm – 180 nm (11.6 – 6.9 eV) with three peaks at 134 nm, 152 nm and 165 nm (**Figure 4.7**). The VUV photo absorption spectrum of formic acid in the condensed phase is in good agreement with that of gas phase literature values of S. Leach at al. 2002, absorption starts around 6.89 eV and increases monotonically towards the end of the spectrum and there are two absorption maxima in this region and both are repeated as in the gas phase.

The first broad band peaks at 8.05 eV and there is an absorption maximum towards the end of the spectra at 9.1 eV. Both of the maxima correspond to the

transition of formic acid and they are in good agreement with the literature values [Leach et al. 2002].

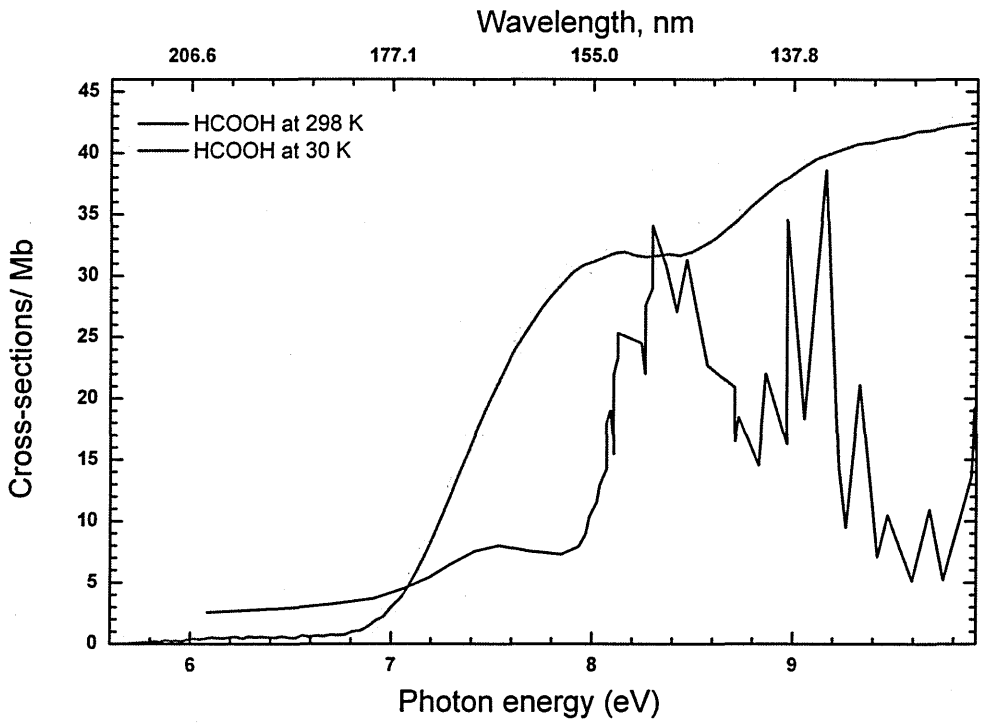

Figure 4.7 Comparison of VUV photo-absorption cross-sections of gaseous formic acid (black) versus solid formic acid (red)

Even though there are no vibrational features in the VUV spectra of condensed formic acid, the temperature induced changes are readily visible from the shift in the position of absorption maxima of two transitions. By annealing the sample from 30 K to 90 K, and recording spectra at every step of heating, we found that there is no significant change in the absorption criteria and no addition spectral features are observed. However, by further increasing the temperature we recorded a spectrum at 120 K, and it showed a single broad peak (peak centre ~140 nm) containing weak structures in the 150 – 120 nm region (**Figure 4.8**). The region between 180-120 nm was observed to gain intensity, whilst the broad structure also found to be more profound in the spectrum recorded at 120 K and 145 K. At 145 K, the peak in the 140

– 150 nm region intensified and also shifted to ~ 139 nm whereas the structure at 160 nm was found to gain intensity and shifted towards higher energy region (157 nm), **Figure 4.8** The sample was then cooled back to 30 K and a spectrum recorded at this temperature found to be similar to the spectrum recorded at 145 K.

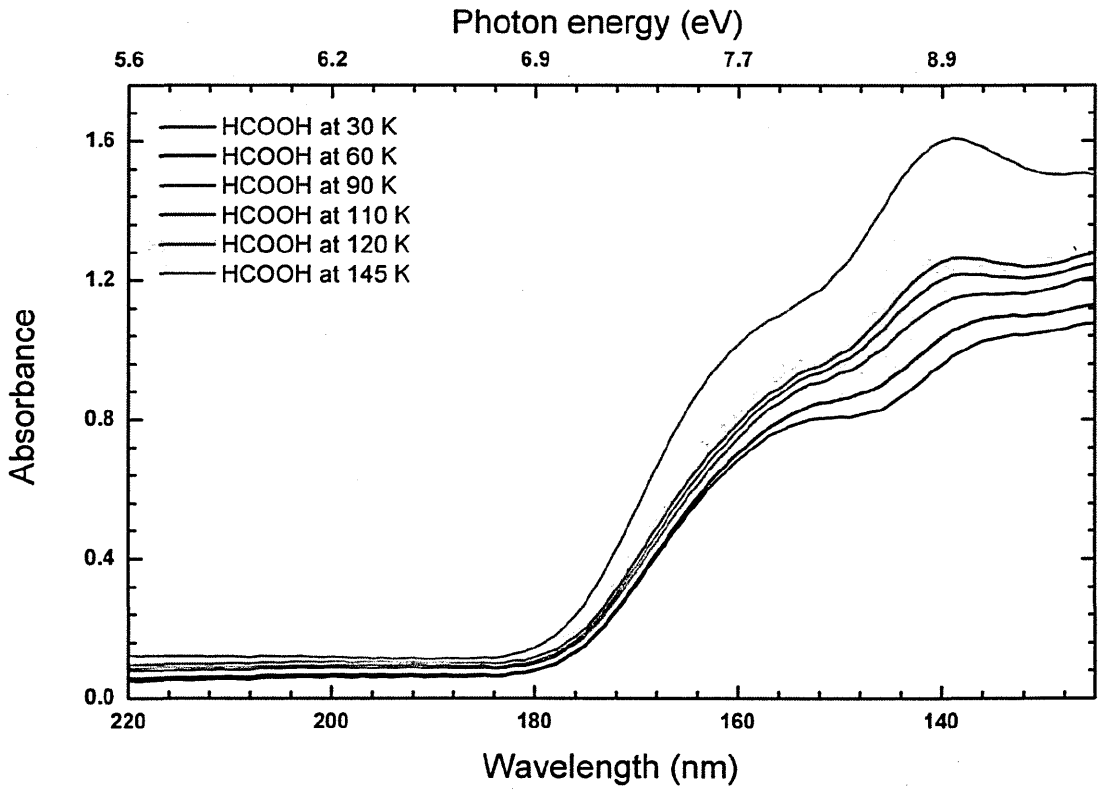

Figure 4.8 Temperature effects of condensed formic acid from 30 K to 145 K .

When the temperature is lowered to 30 K, the general features remain similar to the high temperature spectrum. Upon subsequent heating to 150 K features shown in the spectrum 145 K were retained. And above 180 K the ice film starts to sublimates but there are no characteristic changes exhibited after the crystallisation. Thus, the changes in the ice matrix structure, after heating, are irreversible.

4.4 VUV photo-absorption studies of methyl formate ($HCOOCH_3$) at 30 K – 100 K

Methyl formate, or methyl ester of formic acid ($HCOOCH_3$) is one of the most abundant molecules observed towards the hot cores [Horn et al. 2004] and it is an isomer of acetic acid (CH_3COOH), a third structural isomer, glycolaldehyde ($HCOCH_2OH$), with the same composition is the first observed sugar in the ISM [Hollis et al. 2000].

Table 4.5 Observed relative fractional abundance of methyl formate, acetic acid and glycolaldehyde towards various sources

Source	$HCOOCH_3$ N (cm^{-2})	CH_3COOH N (cm^{-2})	$HCOCH_2OH$ N (cm^{-2})
G34.3+0.2[26]	1.6×10^{16}	1.2×10^{15}	2.3×10^{13}
W51[29]	$9 \pm 6 \times 10^{17}$	1.7×10^{16}	4.5×10^{14}
Sgr B2 N-LMH[30]	1.5×10^{17}	6.1×10^{15}	2.1×10^{13}
G327.3-0.6[45]	5.13×10^{17}	-	3.7×10^{13}

Molecules containing the methyl group ($-CH_3$) play a crucial role in the formation of complex hydrocarbons in the molecular cores, especially species such as methyl formate, acetic acid and glycolaldehyde which are highly abundant towards SgrB2 (N-LMH) [Pedelty 2003]. Methyl formate has been detected towards SgRB2 (N) by Brown et al in 1975 [Brown et al. 1975], and since then it has been detected towards high and low mass star-forming regions [Friedel et al. 2012], towards protoplanetary nebula [Remijan 2005] and in comets [Crovisier 2004; Rodgers 2001], both cis and trans form of methyl formate has been identified in ISM [Cole 2012]. The column density of methyl formate in SgrB2 (N-LMH) is 1.1×10^{-17} cm^{-2} [Liu 2001], and it is observed that methyl formate is the most abundant species among its isomers. Column density of these molecules toward SgrB2 is estimated as 1.1×10^{17}

molecules cm^{-2} for methyl formate [Liu 2001], 5.9 x 10^{13} molecules cm^{-2} for glycolaldehyde [Ellder 1980] and 6.1 x 10^{15} molecules cm^{-2} for acetic acid [Churchwell 1980]. The unusual abundance of methyl formate in this region is still unexplained. Current astrochemical models both in the gas and solid state have not yet been able to explain this observed abundance, since there remain gaps in our knowledge of cosmic ray interactions with methyl formate in both gaseous and solid phase. Therefore for understanding the complexities which leads to unusual abundance of methyl formate, a detailed investigation of photo-absorption of condensed methyl formate in VUV and mid-IR region is essential. Methyl formate ice films were prepared from a purified sample (99.9% Sigma Aldrich) by following the same vapour deposition technique and maintaining the physical conditions in the previous VUV experiments.

4.4.1 Results and discussion

The molecular structure of methyl formate is shown in **Figure 4.9**, methyl formate exhibit C_s symmetry in its ground electronic state and the corresponding symmetry elements are A' and A". Calculated ground state of methyl formate is $X^{'A'}$ and transitions of methyl formate in gas phase are $\pi^*_{CO} \leftarrow n_{O,}$ 13 a'(5.87 eV), $\sigma^* \leftarrow n_{O,}$ 13 a'(7.48 eV) and $\pi_{CO}^* \leftarrow \pi_{CO,\ 3\ a"}$ (8.37 eV) [Nunes et al. 2010].

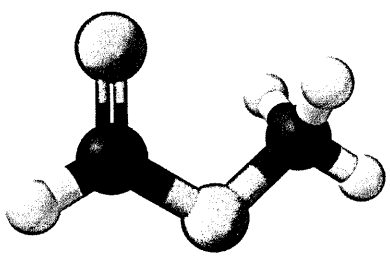

Figure 4.9 Molecular structure of methyl formate

All transitions (**Figure 4.10**) are repeated in the condensed phase, however quenching effect due to molecular interactions in condense phase perturb the system and effects in the absence of Rydberg transitions [Robin 1974].

Transmission mode FTIR spectra of that sample normal to the beam at 1 cm^{-1} resolution were recorded. The reported density of methyl formate ice is $\rho = 0.901$ g cm^{-3} [Modica and Palumbo 2010] and integrated infrared band absorption value $A = 4.77 \times 10^{-17}$ cm mol^{-1} at 1720 cm^{-1}[Modica and Palumbo 2010].

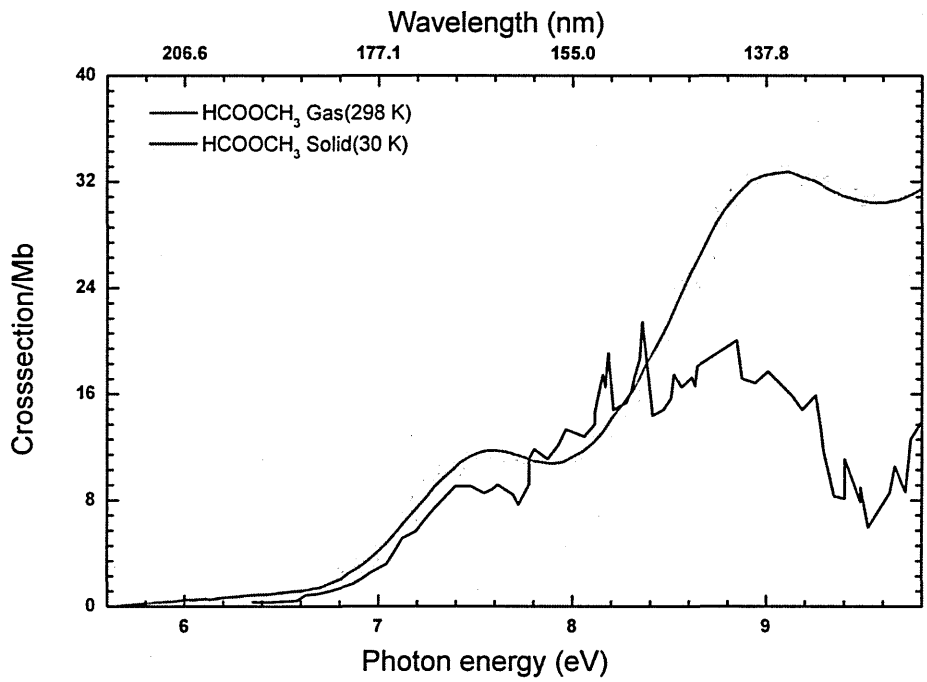

Figure 4.10 Comparison of photo-absorption cross-sections of gaseous (black) and condensed (30 K-red) methyl formate

By repeating the above mentioned calculations, column density of the molecules in the film was found to be 4.84×10^{17} molecules cm^{-2}, and the film was 123.62 ± 0.7 nm thick.

In this study we have recorded VUV photo-absorption spectra of a thin ice film of methyl formate at 30 K, over the range of 120 to 220 nm with a step size of 1

nm. These spectra may also be compared with gas phase VUV studies reported by Y. Nunes et al. [Nunes et al. 2010]. Except for the vibrational induced transitions, all the bands in the gas phase are repeated in the condensed phase. With the peaks at 7.56 eV and 8.96 eV being shown to be at the same position and the cross-section values in the solid phase are in good agreement with those in the gas phase.

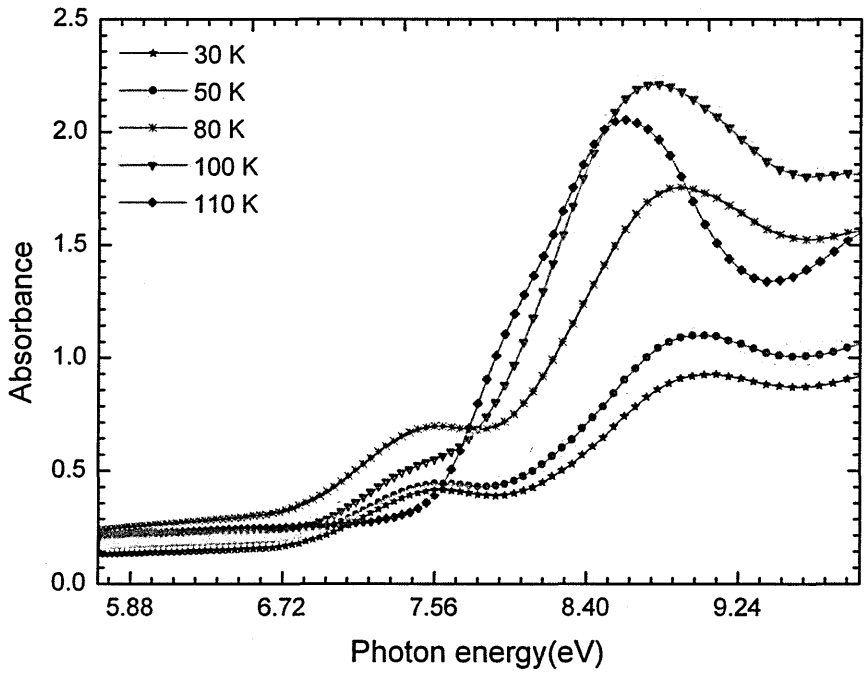

Figure 4.11 Temperature effects of condensed methyl formate, amorphous to crystalline transition of methyl formate at 110 K is shown here.

Temperature induced morphological changes in methyl formate ice recorded over VUV region are shown in **Figure 4.11** (5 eV- 10 eV), during the transition from amorphous to polycrystalline phases, the absorption near 7.56 eV is gradually red slightly shifted and at crystallization the absorption feature was completely suppressed. The second peak at 9.04 eV (30 K) also exhibits red shift and became enhanced and forms a broad but relatively sharp peak at 8.61 eV. Overall absorption intensity decreased with the increase in temperature, but the area under the curve

remained the same, this confirms the effect is not due to photon induced chemistry or photo-desorption effects, but due to the thermally induced morphological changes. The temperature of transition observed 110 K is in good agreement with the FTIR studies as well as reported value in literature [Nunes et al. 2010].

4.5 VUV photo-absorption studies of Benzene (C_6H_6) at 30 K-135 K

Benzene, the fundamental building block of polycyclic aromatic hydrocarbons (PAHs) plays a crucial role in the astrobiological evolution of interstellar space [Kim 1985] and by being the precursor of PAHs, which also act as a nucleation site [Coustenis et al. 2003] for smaller molecules. PAHs species are assigned to 30 % of the contribution of carbon to the galaxy, and benzene has been detected towards proto planetary nebulae, H II- regions, etc [Wong et al. 2003]. Together with PAHs, benzene has been linked to the unidentified infrared bands (UIR) observed in the range of 3-14 μm (3300-700 cm^{-1}) and diffuse ISM bands [Bruston 1994; Wu et al. 2000] in interstellar space and it is an important intermediate in various chemical networks. Benzene has been detected towards proto planetary nebulae CRL 618, [Cernicharo et al. 2001] Table 3 shows the regions of interstellar medium where benzene has been detected

In addition to interstellar space benzene has been detected in planetary atmospheres, other bodies in solar system and in exo-planets, it is one of the heaviest hydrocarbons ever identified in the giant planets' atmospheres. It has been detected in the north polar auroral region of Jupiter [Kim 1985] and in the stratospheres of Jupiter and Saturn [Kim 1985] as well as in Titan's atmosphere [Coustenis et al. 2003].

Benzene and substituted benzenes as well as toluene were observed in laboratory experiments reproducing the photochemistry of Titan [Tran 2005]. Models of the atmospheres of Jupiter, Saturn, and Titan now include benzene in their photochemistry scheme [Lebonnois 2005; Wong 2003]. The accurate knowledge of the photo-absorption cross section of such species is required for those modelling studies. The needs for laboratory spectroscopic data to study organic chemistry in planetary atmospheres were highlighted in recent studies [Bruston 1994; Shindo 2001; Wu et al. 2000].

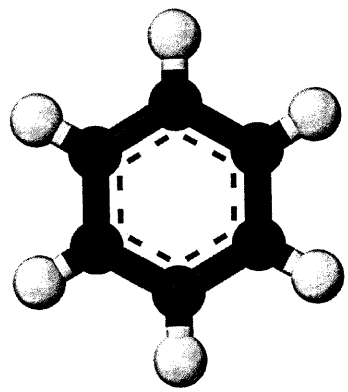

Figure 4.12 Stick and ball model molecular structure of benzene (C_6H_6)

The photo-absorption cross-section of benzene is very important for testing various astrochemical models involving benzene and other PAHs, and benzene as an intermediate. UV and VUV absorption of benzene in vapour and liquid has been thoroughly studied by various groups [Robin 1974 and references there in]. And the UV absorption of benzene in 260 nm is very well known, the UV absorption spectrum of benzene is attributed to the S1 (1B2u)'S0 (1A1g) electronic transition [Steinfeld, 1974, references therein]. It is the lowest singlet system of the molecule and is electronically forbidden but vibrationally induced. Therefore the vibronic features are prominent in case of pure benzene in gas phase; the dominant vibronic progression is

designated 610 nm and involves n_1, the symmetrical ring-breathing vibration. This band becomes more allowed and therefore more intense as the D6h symmetry is broken [Steinfeld, 1974], but in this work the focus has been given to photo-absorption studies from 120 nm (~10 eV) - 320 nm region. And the phase changes induced by thermal processing are confirmed through FTIR studies (Figure 4.16).

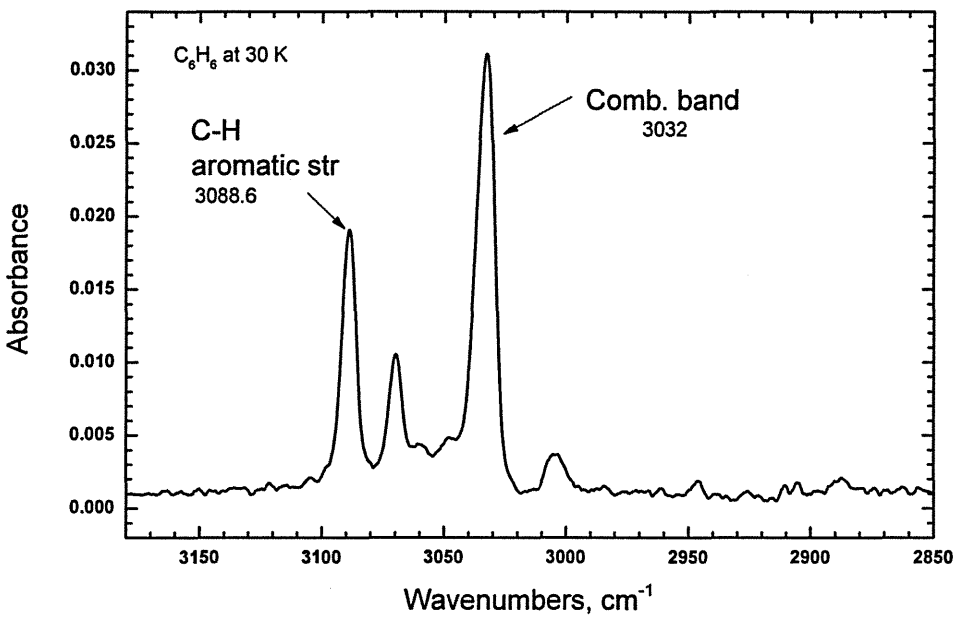

Figure 4.13 Fourier transform infrared spectra of benzene ice film at 30 K

The reported density of benzene ice is $\rho = 0.874$ g cm^{-3} [Strazzulla and Baratta, 1990] and integrated infrared band absorption value $A = 0.17 \times 10^{-17}$ cm mol^{-1} at 3032 cm^{-1}. Using the 'A' value and density, the line of sight column density of the molecules in the film was found to be 4.87×10^{17} molecules/cm^2, and the film was ~ 103 ± 8 nm thick.

Benzene (Sigma Aldrich 99.0%) ice films were prepared using benzene samples from a glass bulb, purified through freeze-pump cycle using liquid nitrogen at 77 K. Samples were introduced into the UHV chamber at a rate of 1×10^{-6}

mbar (1 Langmuir) through an all metal leak valve, Swagelok component gas line and deposited (background deposition) on to a CaF_2 substrate maintained at 30 K for 10 seconds and the cycle was repeated 8 times and prepared an ice film of the desired thickness. VUV absorption spectrum of the formed ice film was recorded over a range of 120 to 220 nm at 1 nm resolution, since the condensed phase of the molecule does not exhibit sharp absorption peaks this resolution is convincing for these types of studies. By using Beer-Lambert's relation (equation 3.4 & 3.5) we calculated the absorption cross-section of the condensed benzene.

4.5.1 Results and discussion

The molecular structure of benzene is shown in **Figure 4.12**, benzene is a highly symmetric molecule and its symmetry group is D_6h. Electronic spectra of benzene in gas phase have been thoroughly studied and reviewed by Dunn et al. [Dunn et al. 2000], A moderately intense band correspond to the $A_{1g} \rightarrow B_{1u}$ singlet transition starts at about 215 nm and has a quite diffuse structure (**Figure 4.14**), this band is in agreement with that observed in vapour and liquid phases [Steinfeld, 1974]. Broad band with peak at 6.65 eV is also assigned to the valence transition [Dunn et al. 2000]. Vibrational transitions are not prominent in the 120-220 nm window, but are exhibited in the lower energy regions 220-320 nm (**Figure 4.14**). Absorption features at 243.8 nm, 249.6 nm, 253.2 nm, 255.4 nm, 258.6 nm and 261.6 nm are ascribed to vibronic structures. Vibronic features are prominent in case of pure benzene in gas phase and they are also visible in the higher wavelength region even in the condensed phase.

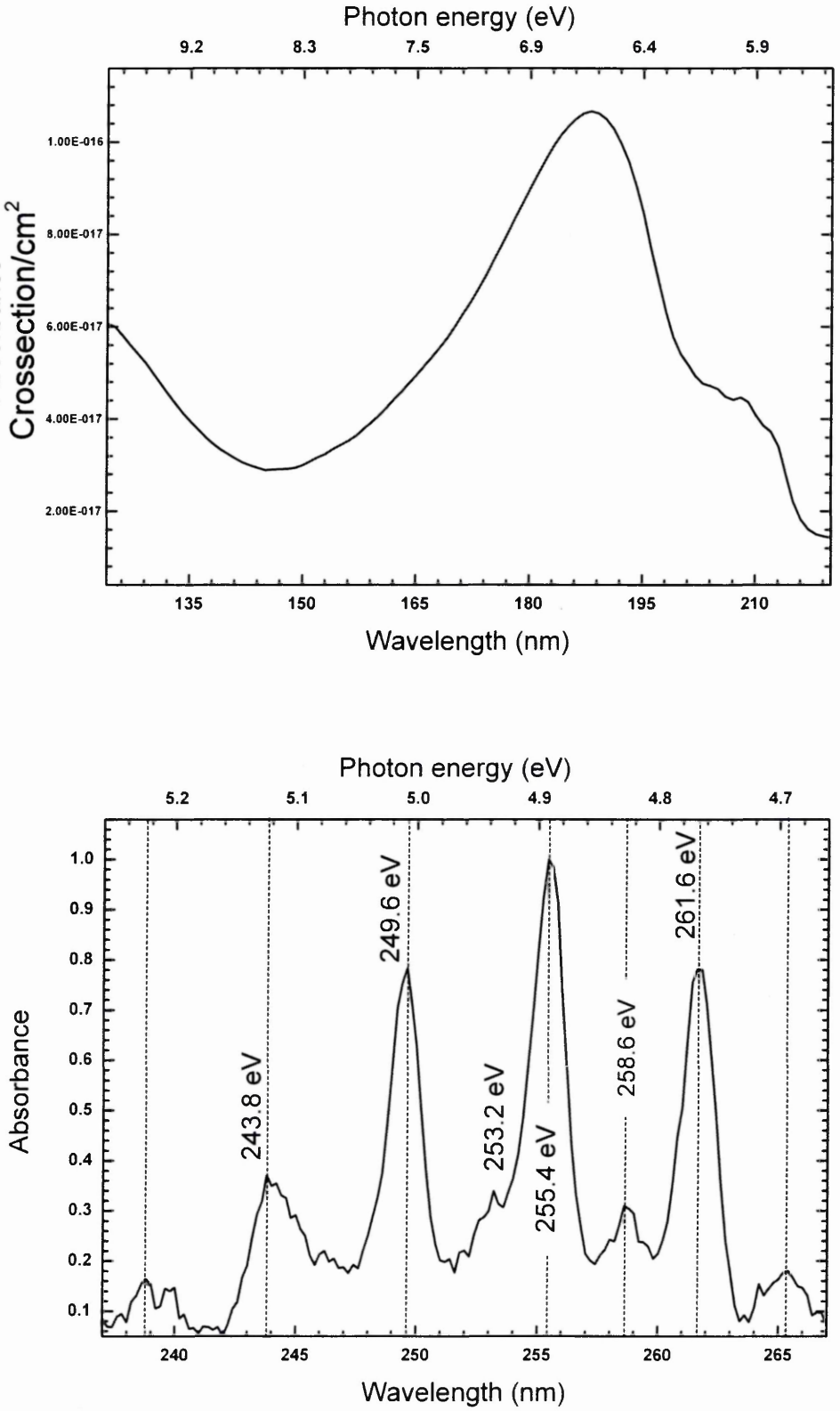

Figure 4.14 Photo-absorption cross-sections of benzene ice film at 30 K, region from 120 to 220nm (top), absorption features of benzene in the region 220 to 270 nm (bottom)

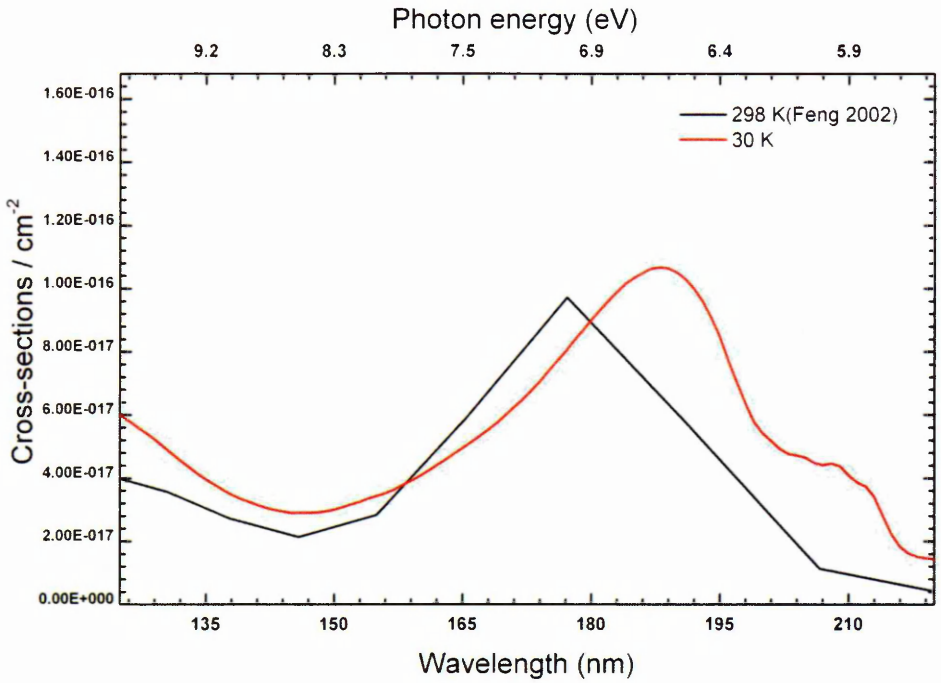

Figure 4.15 Comparison of photo-absorption cross-sections of gaseous benzene (black) [Feng et l. 2002] versus solid benzene (red)

A shift in the peak position is observed for the condensed phase benzene, there is a slight shift for the 178 nm peak towards the lower energy region and the cross section in gas phase was not at good resolution to compare the absorption in the region 200 to 220 nm, it is evident that there are fine structures believed to be from vibrational features which is noted at 6.12 eV, 5.91eV and 5.89 eV respectively.

After recording the spectra at 30 K the sample was warmed (at a rate of 5 K/ minute) until sublimation. A spectrum is recorded at every stage of warming and the resulted spectra at 30 K, 40 K, 50 K, 80 K, 120 K and 135 K are shown in **Figure 4.16**. From the absorption spectra at different temperatures it is evident that the morphological changes have profound influence in the absorption features of benzene in condensed phase.

At 40 K a broad absorption feature is appeared at 8.84 eV, and started to grow as the warming progress.

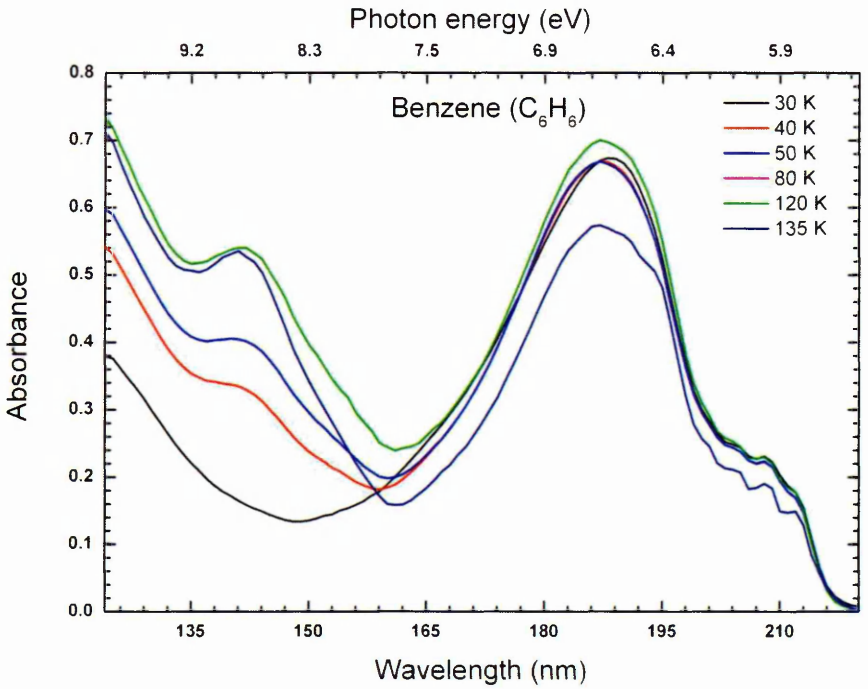

Figure 4.16 Temperature dependent variation in solid benzene, amorphous to crystalline transition of benzene at 120 K is clearly observed, spectra at 30, 40, 50, 80, 120 and 135 K are shown here.

During warming from 30 K, there is an overall increase in the intensity of absorption features at 8.84 eV and 6.65 eV. Changes occurring at 30 K, 40 K, 50 K, 80 K, 120 K and 135 K are shown in **Figure 4.16**. At 135 K there is profound change in the intensity as well as absorption pattern in case of both the valence transitions. And it is attributed to the phase change of benzene from amorphous to polycrystalline at that temperature. And this value (135 K) is in good agreement with the FTIR studies we have conducted, in a separate experiment with ice of similar thickness.

4.6 VUV photo-absorption studies of allyl alcohol (CH_2CHCH_2OH) at 30 K-155 K

Allyl alcohol is simplest among allylic alcohols, even though it has not been detected in the interstellar medium; it is believed to be an important precursor to vinyl alcohol, ethylene oxide, acetaldehyde (isomers) and vinyl alcohol and its isomers which have been detected toward Sagittarius B2N. Therefore allyl alcohol is a potential candidate in interstellar chemistry leading to aldehydes and allylic alcohols. In our experiment we have recorded VUV absorption spectra of condensed allyl alcohol

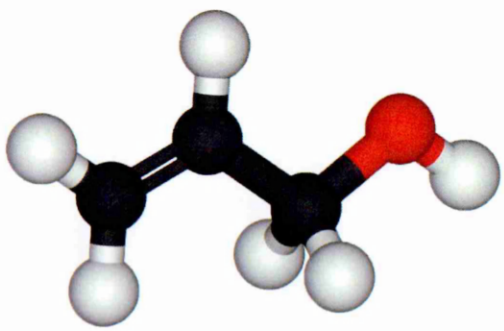

Figure 4.17 Stick and ball model molecular structure of allyl alcohol

4.6.1 Results and discussion

Allyl alcohol (Sigma Aldrich 98.5%) vapour from a glass bulb, cleared through freeze-pump cycle using liquid nitrogen at 77 K, was introduced into the UHV chamber at a rate of $1x10^{-6}$ mbar (1 Langmuir) through an all metal leak valve, Swagelok component gas line and deposited (background deposition) on to a CaF_2 substrate maintained at 30 K for 10 seconds and for every deposition we recorded a VUV spectrum from 120 to 320 nm the cycle has been repeated 12 times (we calculated and plotted the absorbance to make sure that the absorption is below the

saturation value)and prepared a thin ice film. VUV absorption spectrum of the finally formed ice film was recorded over a range of 120 to 220 nm at 1 nm resolution, since condensed phase of the molecule does not exhibit sharp absorption peaks this resolution is convincing for these types of studies. In the case of allyl alcohol, there are no reported studies of its condensed phase, therefore we were unable to calculate the photoabsorption cross-section values since 'A' value was unavailable.

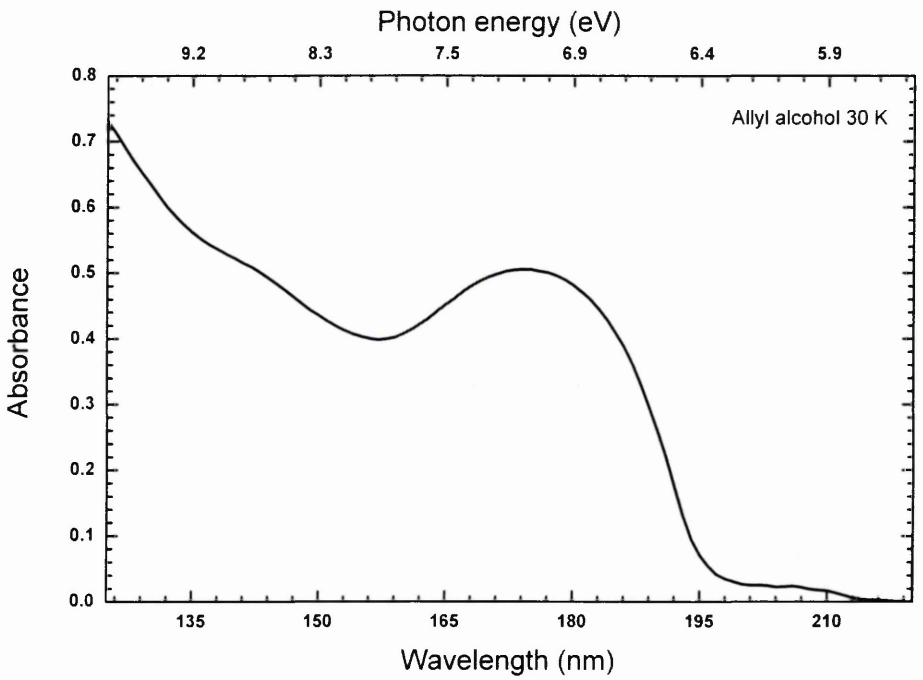

Figure 4.18 VUV Photo-absorption spectra of allyl alcohol ice film at 30K

Absorption features of allyl alcohol begins around 5.895eV and progresses up to the end of the spectral region under study (**Figure 4.18**). There are two broad maxima in the region and one peak at 7.1 eV and the second at higher energy region towards 8.94 eV. There are no reported studies of allyl alcohol and this is the first reported photo-absorption study of this molecule in this region. we were not able to confirm the absorption peaks with references available in literature, but the trend of

absorption is in good agreement with that of other allylic alcohols (vinyl alcohol) [Robin 1974].

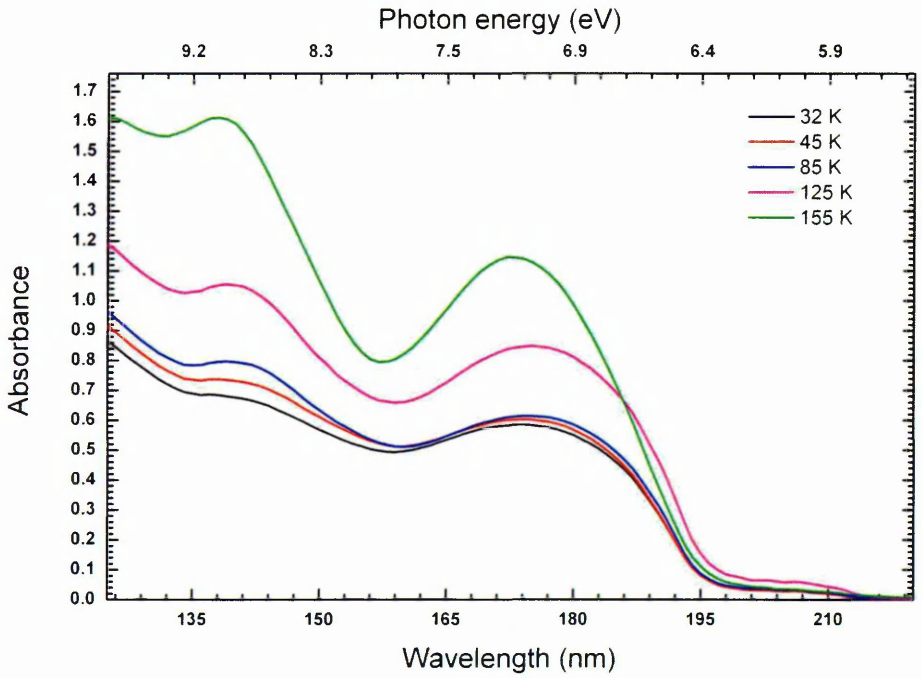

Figure 4.19 Temperature dependent VUV spectra of allyl alcohol, 32 K to 155 K.

After recording the photo-absortion spectra at 30 K, the ice film was warmed up to sublimation (at a rate of 1 K/ minute). Absorption spectra were recorded at every step of warming and the resulted spectra at 32 K, 45 K, 85 K, 125 K and 155 K are shown in **Figure 4.19**. There are no changes during warming except increase in intensity of absorption for both band transitions at 7.1 eV and 8.94 eV. A phase change of allyl alcohol is evident from the shift in absorption peak at 7.1 eV, this peak has shifted towards the higher energy region at 155 K, the transition started around 130 K and it has been confirmed with the FTIR features in a separate study. The peak at 9.1eV is sharpened during this transition and desorption of allyl alcohol started around 164 K and all the sample was desorbed by180 K

4.7 Temperature dependent VUV Photo-absorption studies of Methyl acetate (CH_3COOCH_3) at 10 K – 150 K

First identification of methyl acetate, CH_3COOCH_3, in the ISM was reported very recently [Tercero et al. 2013]. Identified in the Orion, methyl acetate is considered to be the most abundant non cyclic isomer of $C_3H_6O_2$ [Tercero et al. 2013]. To date there has been no VUV and IR spectroscopic data available for this molecule in conditions similar to those of the ISM dust grain ice mantles. Also there has been little or no information present towards the formation or dissociation of this molecule at similar conditions. However, the formation mechanisms are expected to be from other molecules such as, but are not limited to, methyl formate, acetic acid and methanol. Here we present the first VUV and IR spectra of methyl acetate ices using laboratory simulations of ISM dust grain ice analogues.

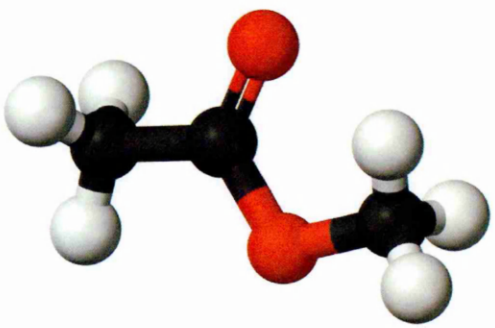

Figure 4.20 Molecular structure of methyl acetate

Methyl acetate (CH_3COOCH_3) is possibly synthesized through multiple reaction pathways from molecules previously detected in hot cores, most notably from acetic acid and methanol via esterification. Esterification, beyond the formation of methyl formate, has not yet been observed in the ISM.

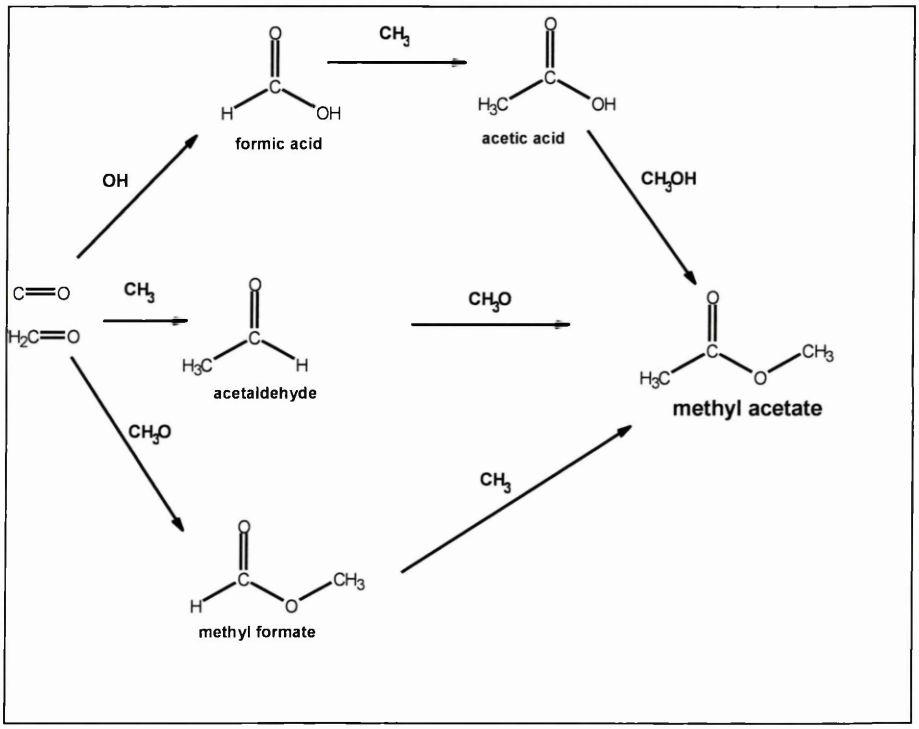

Figure 4.21 Proposed interstellar reaction schemes which lead to methyl acetate in ISM

The above shown reaction mechanism (**Figure 4.21**) has not yet been observed or attributed to chemistry in the ISM. But this mechanism could also help to explain the unusually high observed abundances of methyl formate. Structural isomers Acetic Acid: Glycolaldehyde: Methyl Formate = ~ 1: 0.5: 26 within LMH (Large Molecular Heimat in Sgr B2) [Tielens 2006]. Methyl acetate could be formed through photolysis pathways via acetaldehyde or methyl formate (both found in the ISM, see below). Of particular interest is the possible esterification reaction of methanol and acetic acid (also present in the ISM).

4.7.1 Results and discussion

Experiments for recording VUV spectra of methyl acetate reported in this paper were all carried out at the National Synchrotron Radiation Research Center

(NSRRC), Taiwan. VUV photons from the beamline were focused on to a lithium fluoride (LiF) window, kept at 10 K, enclosed in a vacuum chamber at pressures on the order of 10^{-8} mbar. Further details on the experimental setup can be found in our earlier publication [Lu Chen et al. 2008]. The vapour from methyl acetate (99.5%, Sigma Aldrich) liquid sample was allowed to form a uniform film of methyl acetate to grow on the LiF substrate. Spectra (110 – 240 nm; 11.3 – 5.2 eV) were accumulated before and after deposition to obtain the incident (I_0) and transmitted (I_t) intensities from which absorbance spectra are calculated, using the Beer-Lambert law.

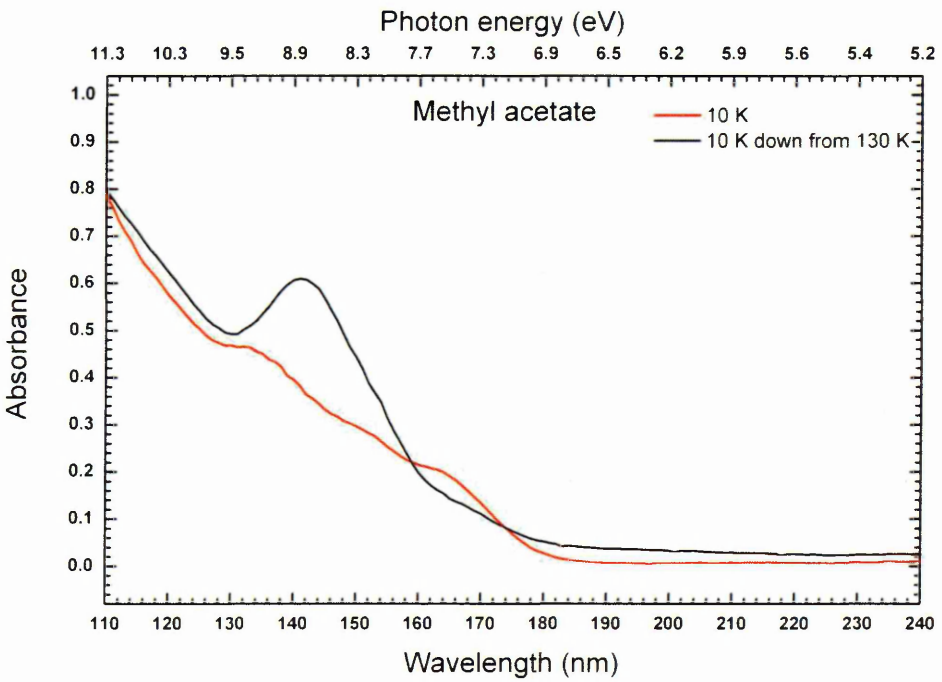

Figure 4.22 VUV photo-absorption spectra of methyl acetate at 10 K and annealed film at 130 K

Spectra were recorded by annealing the sample at several higher temperatures, which include 30 K, 75 K, 90 K, 100 K, 120 K, and 130 K, until sublimation of the sample. The minimum wavelength cut off is determined by the window material used. For the spectra presented in this paper, a LiF window was used as both the entrance

and substrate window. Thus the minimum wavelength for which reliable data could be acquired was 107 nm.

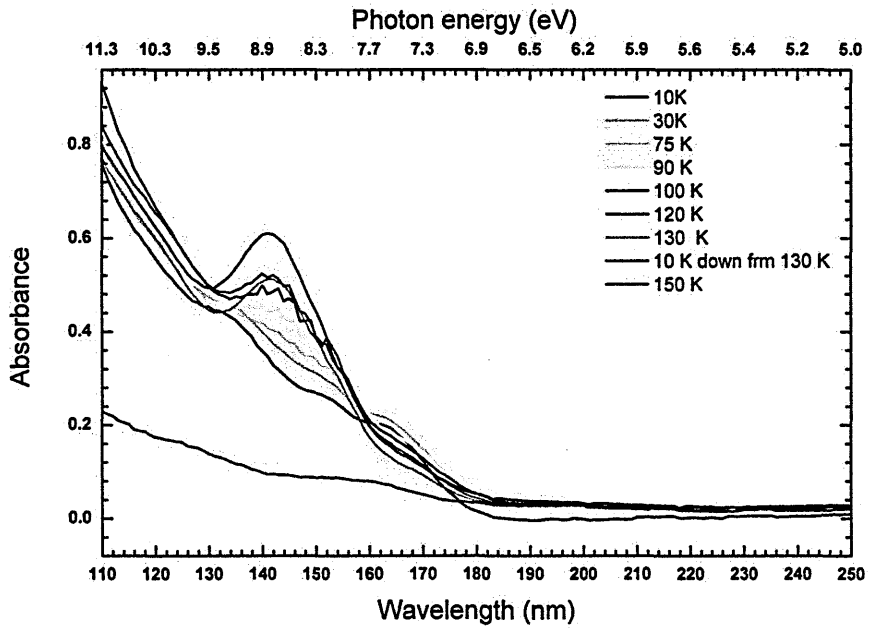

Figure 4.23 Temperature dependent variations in VUV photoabsorption spectra of methyl acetate

VUV spectra recorded at 10 K was found to have strong absorption from 107 nm – 180 nm (11.6 – 6.9 eV) with three peaks at 134 nm, 152 nm and 165 nm (**Figure 4.22**). A spectrum recorded at 30 K, by annealing the sample from 10 K to 30 K, was found to be similar to the spectrum at 10 K. However by further increasing the temperature and a spectrum recorded at 75 K was found to develop as one broad peak (peak centre ~146 nm) containing structures in the 131 – 160 nm regions. This region was observed to gain intensity whilst the fine structure was also found to be more profound in the spectrum recorded at 100 K. At 120 K, the peak in the 131 – 160 nm region intensified and also shifted to ~ 142 nm whereas the fine structure was found to diminish and then smoothened at 130 K (Figure 4.21). The sample was then cooled back down to 10 K and the spectrum recorded was found to be similar to the spectrum

recorded at 130 K before cooling down (**Figure 4.23**). Spectrum recorded at 150 K, by re-annealing the methyl acetate ice back to higher temperatures, was observed to be very less intense.

From the VUV spectra recorded by re-cooling the sample to 10 K from 130 K the phase change from amorphous to crystalline form was found to be irreversible. Therefore, those spectra obtained at 10 K and 15 K, by re-cooling the crystalline sample, were indeed the crystalline VUV and IR spectra of methyl acetate ice at lower temperatures, respectively. The intensity variation of the spectra recorded at even higher temperatures indicates that the methyl acetate ice sublimes above 140 K and below 150 K. New structures observed in the 131 nm – 160 nm region of the VUV spectra recorded from 75 K – 110 K, just before phase change, might correspond to the reorientation of molecules altering the density of the ice upon annealing. Such rearrangement before crystallization may have an effect on the mobility of atoms or molecules that may be trapped in methyl acetate ices, exposed to irradiation. Our spectra can be used to identify and interpret the morphology of methyl acetate ices in different regions of the ISM. Also from the sublimation temperature of methyl acetate ices we can understand that it can sustain and contribute to chemical changes in the icy mantles of dust grains until 140 K.

4.8 Temperature dependent VUV Photo-absorption studies of propionic acid (propanoic acid, CH_3CH_2COOH) 10 K-140 K

Propanoic acid (CH_3CH_2COOH) has been identified in ISM and also in cometary bodies [Tielens 2006]. It is an important intermediate of many carboxylic acids and recent experiments shown that propionic acid is an intermediate of highly abundant species like methyl formate and methyl acetate. The below figure depicts the various proposed reaction schemes of propionic acid in ISM,

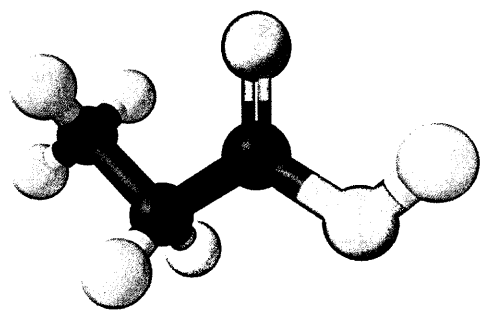

Figure 4.24 Stick and ball model of propionic acid

The gas grain interaction in a hot core like region may readily engage in such a pathway and lead to the efficient formation of CH_3COOH and CH_3CH_2COOH, this mechanism gives an insight into the formation of methyl formate and its isomers in hot cores. In order to understand such gas-grain interaction simultaneous with UV and thermal processing of grain mantle, we need spectroscopic and morphologic information of such ices. Temperature dependent VUV absorption spectrum of methyl acetate is very crucial for investigating the existence of such chemical pathways.

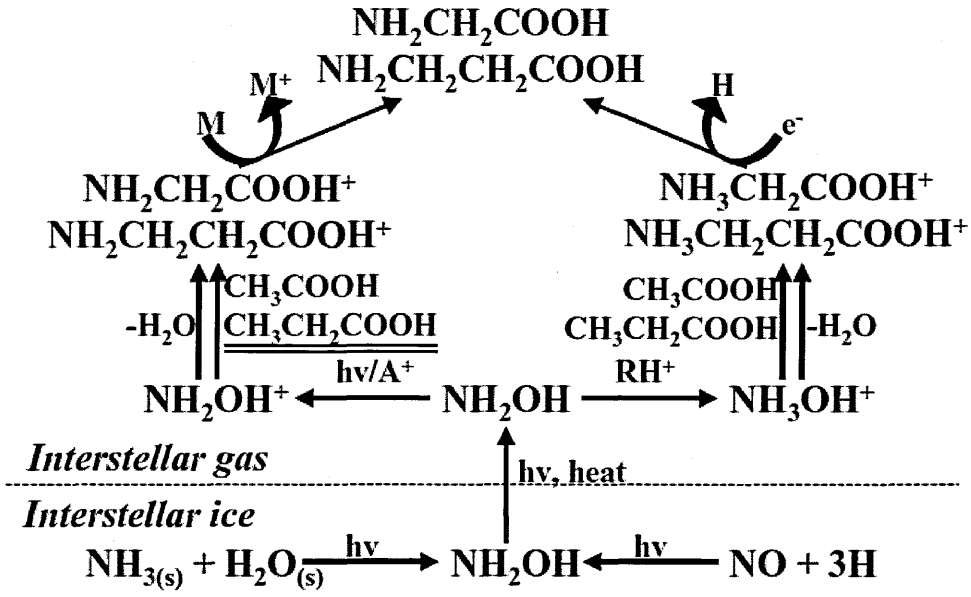

Figure 4.25 Proposed formation pathways of interstellar Glycine (NH_2CH_2COOH) with propionic acid (CH_3CH_2COOH) as an intermediate.

Propionic acid (99.0%) vapour from a glass bulb, degassed through freeze-pump cycle using liquid nitrogen at 77 K, was introduced into the UHV chamber at a rate of $1x10^{-6}$ mbar (1 Langmuir) through an all metal leak valve and Swagelok component gas line and deposited (direct deposition) on to a LiF substrate maintained at 10 K for 120 seconds and prepared an ice film of desired thickness ~ 485 nm (In-situ absorption measurements allowed us to have a control on maintaining the thickness and to keep the absorption below saturation level). VUV absorption spectrum of the formed ice film was recorded over a range of 110 to 320 nm at 0.5 nm resolution.

4.8.1 Results and discussion

The photo-absorption spectra of propionic acid recorded in the 110-250 nm region exhibits (**Figure 4.26**) two broad features peaking at 10.4 eV and 8.2 eV. Both the features are broad and ascribed to the valance band transitions. Gas phase studies of propionic acid at these wavelengths are absent and therefore characterization of the peaks were difficult. Further studies are needed for the detailed characterization of absorption peaks of propionic acid in this region.

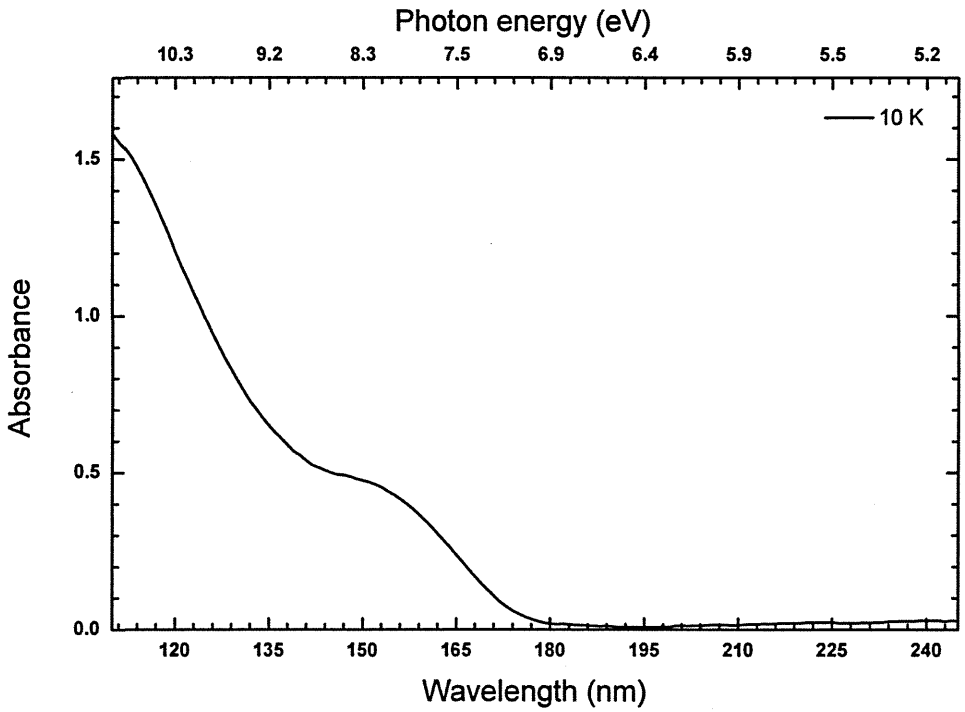

Figure 4.26 VUV photo-absorption spectra of propionic acid at 10 K

After recording the photo-absorption spectra at 10 K, the ice film was warmed until sublimation and spectra were recorded at each step of heating. There were no changes in the absorption pattern during heating, spectra recorded at 10 K, 50 K, 110 K, 130 K and 140 k are shown in **Figure 4.27** There are changes at 10 K, 50 K and

110 K but at 130 k there is a slight change in the intensity of absorption for the 8.2 eV feature, this feature has shifted towards the higher energy region and peaked around 8.45 eV.

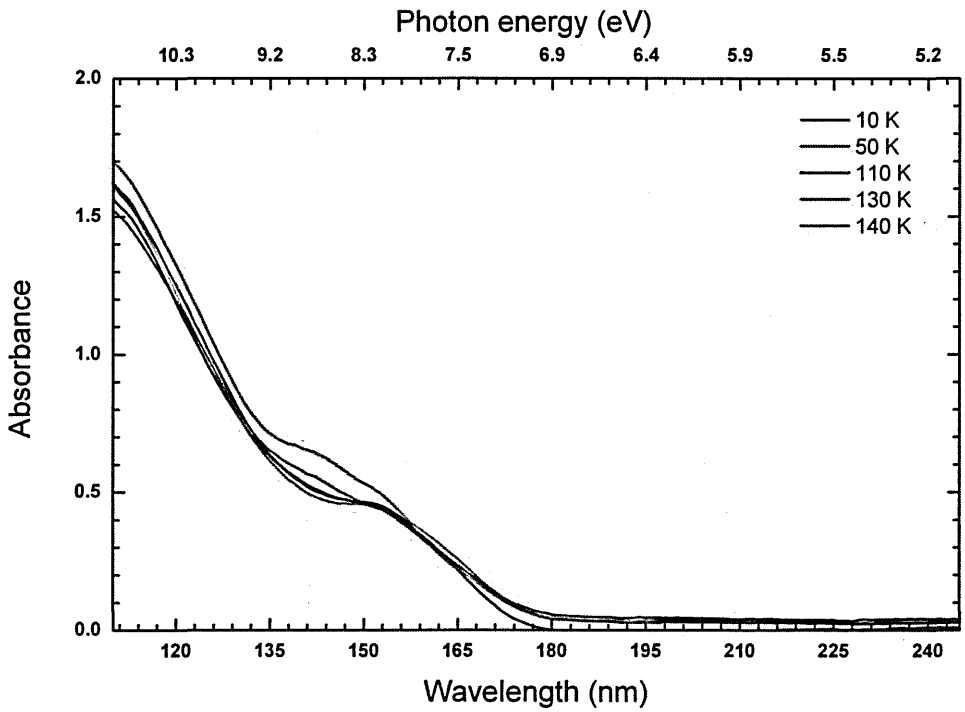

Figure 4.27 Temperature dependent variations in VUV photo-absorption spectra of propionic acid

And this change is ascribed to the phase change of propionic acid ice film from amorphous to polycrystalline. This transition temperature, 130 K, has been confirmed through separate FTIR studies of propionic acid ice films with variable thicknesses.

4.9 Temperature dependent VUV Photo-absorption studies of ozone at 10 K

Ozone is an important constituent of Earth's stratosphere and Hartley (1881) observed that O_3 during photo dissociation absorbs UV light strongly between 200 - 320 nm, radiation which is extremely damaging to life so ozone acts as the Earth's 'UV filter [Okable 1978]. Ozone has been detected in the interstellar medium [Tielens and Hagen 1982 and references therein]. Condensed O_2 (highly abundant in molecular clouds) on grain mantles of interstellar dust grains are continually processed by galactic cosmic rays and interstellar UV field and this process leads to chemical changes in such ices and formation of ozone. Experimental evidences of such processes are reported recently by 5 keV electron irradiation studies of pure oxygen ice, [Bennett et al. 2005; Sivaraman et al. 2010] and UV processing of pure oxygen and CO_2 ices.

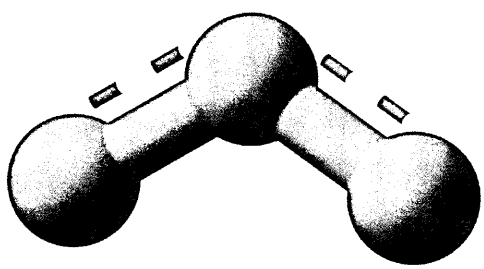

Figure 4.28 Stick and ball model molecular structure of ozone (O_3)

In the search for habitable worlds using molecules and their absorption spectra, ozone (O_3), is regarded a prime molecule among the list of biomarker molecules that are selected to find signatures of life elsewhere in the Universe.

Beyond the Earth's atmosphere, O_3 was first identified in the Martian atmosphere using the Hartley Continuum and dedicated space missions were carried out to map the O_3 seasonal variation in the Martian atmosphere. Please note that spectroscopy for O_3 identification strongly depended on the Hartley band (220 nm – 320 nm), which was used in identifying the molecule in various satellites, such as Ganymede, Europa, Dione and Rhea, of the Solar System icy bodies.

Table 4.10 Reported peak positions in the VUV spectra of gaseous and solid ozone [Mason et al 2005; Johnstone et al. 1992].

Feature	O_3- 10 K This work (eV)	O_3- 298 K (Johnstone et al.) (eV)	O_3- 298 K (Mason et al.) (eV)
1	4.806	4.89	4.86
2	6.457	-	-
3	-	7.04	7.25
4	-	8.76	8.80
5	9.0499	9.30	9.31
6	-	10.17	10.21
7	10.8758	10.59	10.59
8	-	11.07	11.1

For preparing ozone, pure oxygen (99.99%) vapour from a lecture bottle was introduced into the UHV chamber at a rate of $1x10^{-6}$ mbar (1 Langmuir) through an all metal leak valve, with Swagelok component gas line and deposited (background deposition) on to a LiF substrate maintained at 10 K for 130 seconds (background deposition, detailed description of the experiment is discussed in the chapter 3). After the deposition we recorded a VUV spectra to ensure that there are no impurities in the system **Figure 4.29**, the oxygen film at 10 K has been irradiated with VUV photons 120 nm for one hour (60 minutes) and the spectra of the resulted film is recorded and we found that it is a mixture of oxygen and ozone, or ozone trapped in an oxygen matrix. We checked for possible contaminants like NO_2, CO_2 etc and for this reason

we recorded a spectrum at high resolution in whole range, 110 to 320 nm, and we found that there are no contaminants in the film, **Figure 4.29**, we annealed the resulted film up to 48 K and recorded a spectrum at this temperature, **Figure 4.30**, ensured that all oxygen has been desorbed and enhanced formation of ozone. We cooled back to 10 K and recorded high resolution (0.2 nm) spectrum of pure ozone, the resulted spectrum is shown in **Figure 4.31** (we calculated and plotted the absorbance to make sure that the absorption is below the saturation value).

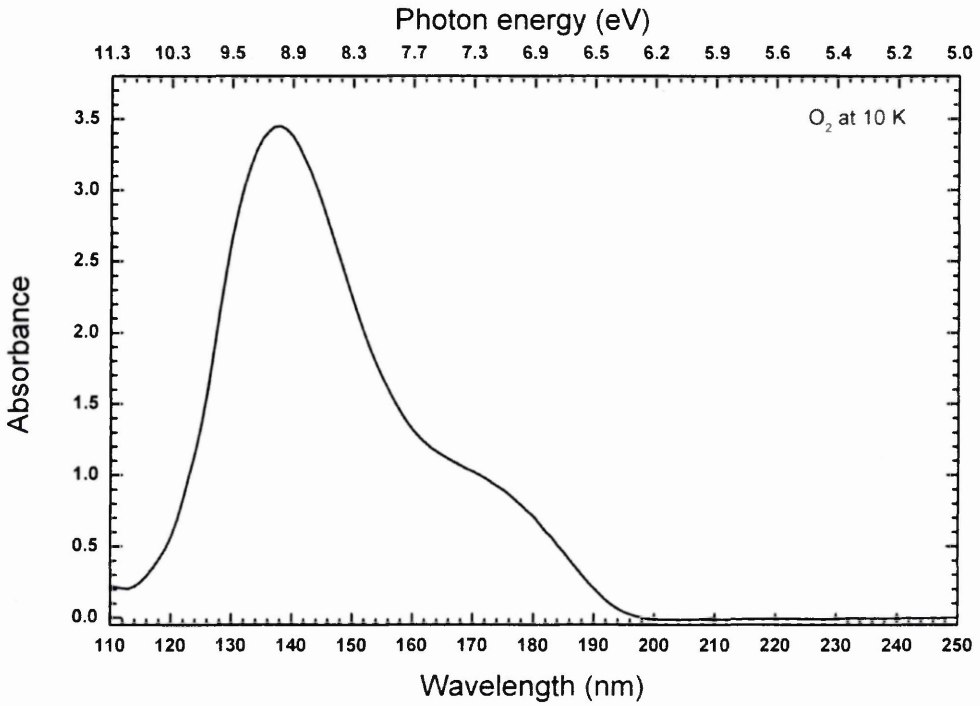

Figure 4.29 Photoabsorption spectra of pure oxygen at 10 K (condensed onto CaF_2)

Spectra recorded after irradiation was found to have two bands on either side of the O_2 spectra at 115 nm and 245 nm. By annealing the irradiated ice to 47 K more than the sublimation temperature of O_2 the substrate was found to contain O_3 where all of O_2 was found to have sublimed off the ice and this in good agreement with the previous experiments carried on similar O_2 ices using 5 keV electron irradiation followed by warm up [Sivaraman et al. 2007]. Little decrease in intensity at both the

115 nm and 245 nm bands observed in the spectra recorded at 47 K which was due to O_3 molecules that were lost while O_2 rapidly sublimes off whilst heating the substrate. We found the spectrum recorded at 47 K to be the pure amorphous O_3 spectrum which may be compared to the gas phase photoabsorption spectra of O_3 (**Figure 4.32**). By re-cooling to 10 K from 47 K we found a very small shift in the band position. Spectrum recorded at 55 K was found to be much different to those spectra recorded at low temperatures and we interpret this to the phase change from amorphous to the crystalline phase of solid O_3. Moreover after the phase change, the 110 nm – 175 nm region in the absorption spectra closely resembles VUV spectra of solid H_2O (**Figure 4.33**).

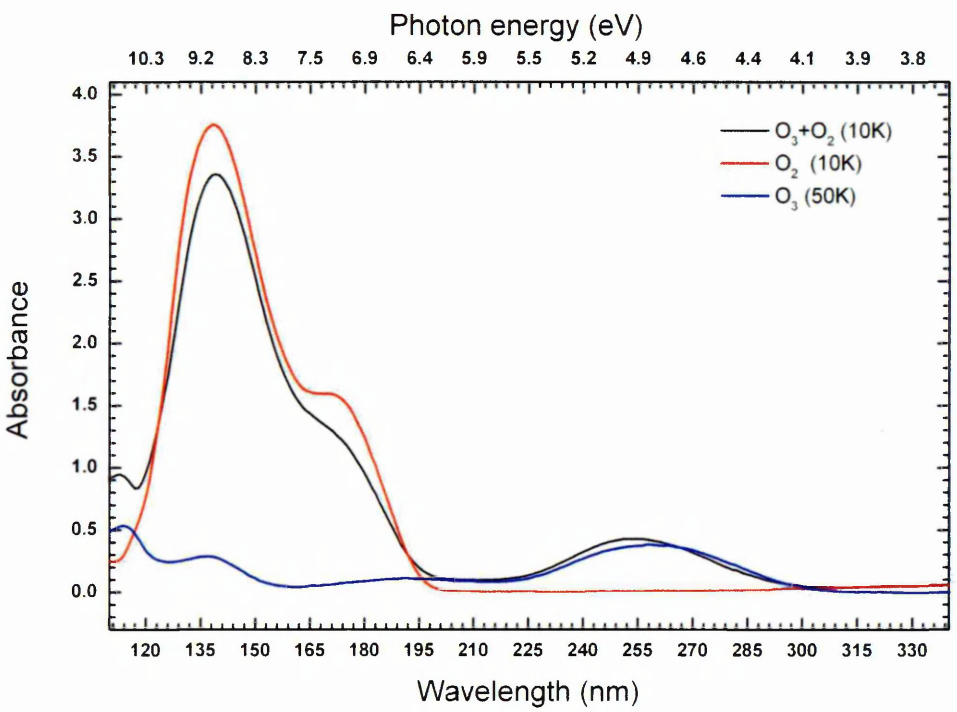

Figure 4.30 Photoabsorption spectra of pure oxygen at 10 K (red) before irradiation, photo-processed (120 nm) oxygen ice at 10 K (black), photo-processed ice annealed to 50 K (blue)

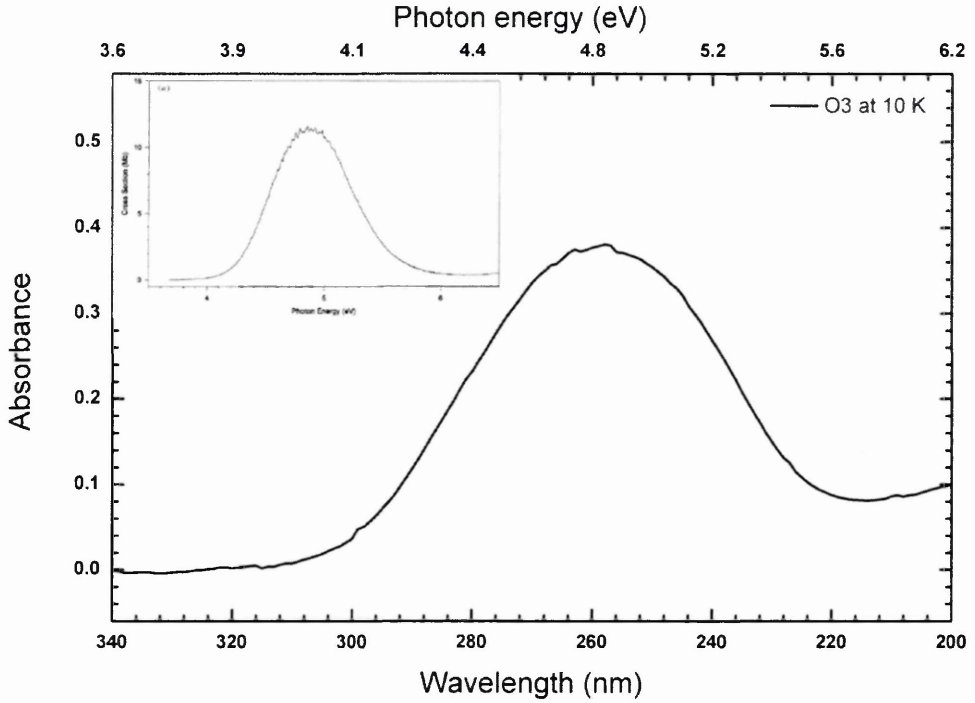

Figure 4.31 Absorption spectra of condensed ozone in 300 to 220 nm region (Hartley band). Inset, Hartley absorption exhibited by ozone in the gas phase.

From the crystalline O_3 spectra recorded at 55 K we found that the Hartley band to be less intense to that observed in the amorphous ice at 47 K (**Figure 4.31**). Further annealing the ice to higher temperatures, up to 100 K in 10 K steps with subsequent recording of VUV spectra at every 10 K interval clearly showed the disappearing Hartley band in the crystalline O_3. Earlier experiments using infrared (IR) spectroscopy has reported most of the O_3 to sublime off the surface at 70 K however this depends on the detection limits in the IR because mass spectroscopy contains signatures of O_3 molecules subliming of until 100 K [Jones et al. 2014]. However, given the higher absorption cross section in the VUV region we are able to observe O_3 molecules that are still left in the surface by recording O_3 spectra even at higher temperatures. Spectral comparison between the amorphous and crystalline O_3 showed that the photoabsorption in the Hartley band is very strong when the molecule

is present in the amorphous form and a phase change to pure crystalline form had reduced absorption (**Figure 4.32** & **4.33**) in the Hartley band region.

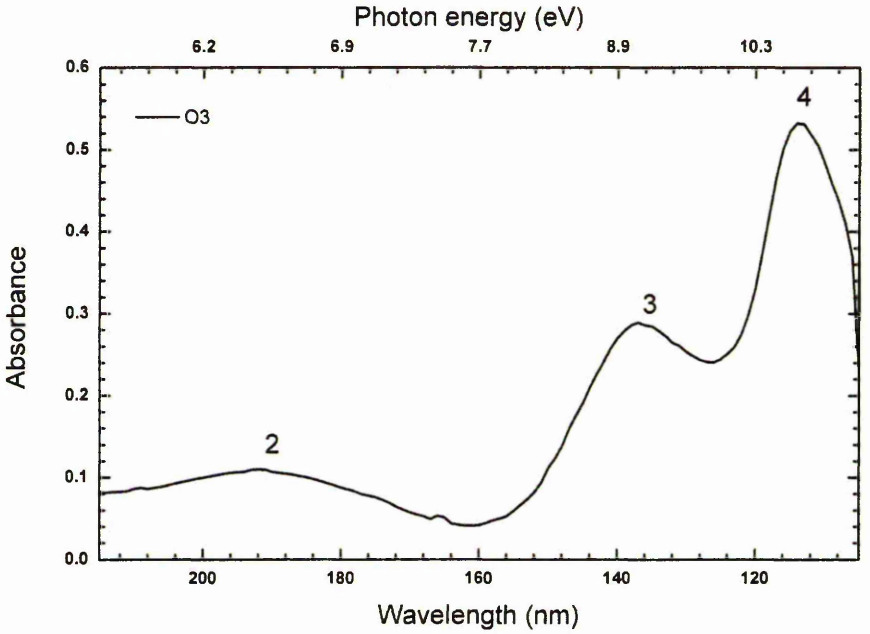

Figure 4.32 VUV photoabsorption spectra of condensed Ozone from 250 to 110 nm

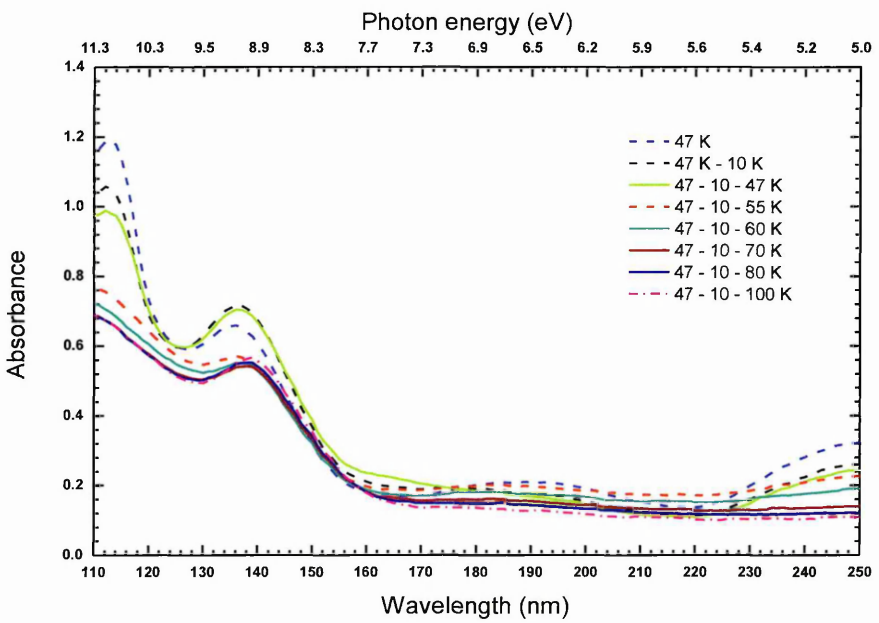

Figure 4.33 Temperature dependent VUV absorption spectra of Ozone

Our results supports the O_3 detection, so far, made in the icy satellites using the Hartley band to be in the amorphous phase, like O_3 present in combination with

H_2O, CO_2 etc, as reported in those identifications. When O_3 turns to pure crystalline form and present in an environment where temperatures are $\geq$ 70 K the crucial photoabsorption at the Hartley band is either found to be less intense or absent when compared to those absorptions present from 110 – 170 nm at similar temperatures.

4.10 Conclusion

Temperature dependent VUV photo-absorption spectra of various molecular ices were recorded. The VUV photo-absorption cross-section for some of these molecules at 10 K was calculated and in addition, temperature dependent absorption of these molecular ices from 10 K to sublimation temperatures investigated in detail. The majority of the samples exhibit changes in absorption behaviour during the phase transformation, therefore spectra in VUV region are an excellent tool for investigating morphology of molecular ice films.

It is difficult to distinguish the individual features of electronic transitions in condensed- amorphous ice spectra, but condensed phase electronic spectra can reveal the strength of hydrogen bonding as well as influence of intermolecular interactions. Rydberg transitions are suppressed in all the cases; however molecules do not follow the same pattern of transition in condensed phase. Hydrogen bonding is one of the major factors affecting the shift in an electronic transition from gas to solid phase; in the case of formamide it is observed that there is a considerable blue shift (~2 eV) in terms of Rydberg transitions and a surprising change in the transitions due to the molecular interactions in the condensed phase.

The VUV spectrum of condensed ozone presented in this thesis is unique as it is the first VUV spectra of pure condensed ozone. An ice film of ozone was synthesized from pure oxygen and then annealed to form pure ozone ice matrix, the

condensed phase spectra of ozone also reveals the nature of Hartley band in condensed phase. Indeed our results confirm the existence of O_3-O complex formation and ozone dimer formation in ozone matrix discussed by Sivaraman et al. 2006.

Temperature dependent variations in VUV spectra of methyl acetate and dimethyl ether are also reported for the first time. Gas phase spectra of the molecules have been analysed but the changes in absorption with annealing of methyl acetate and dimethyl ether ice is not well understood. The works presented in this thesis provide an overall understanding of behaviour of molecular ice films of formamide, methyl formate, formic acid, methyl acetate, propionic acid, benzene and ozone in VUV region. In addition, temperature dependent VUV spectra of simple molecules such as benzene (C_6H_6), methyl formate ($HCOOCH_3$), formic acid (HCOOH), allyl alcohol and formamide ($HCONH_2$) are investigated and results are presented in this chapter.

The photo-absorption cross-sections of the molecules in condensed phase presented in this chapter can be used to measure the photo-ionization and photo-dissociation rates of these molecules in interstellar medium. Photo-absorption spectra can be used as reference spectra for astronomers who observe in VUV window, therefore these spectra helps to identify the signatures of such species in condensed phase. The photoabsorption cross-sections can be incorporated into astrochemical models, most of the existing astrochemical models are using gas phase cross-section, to account for the condensed phase kinetics and contributions from the surface kinetics it is important to include photo-chemistry of condensed phased species. Therefore the results presented in this chapter are very important for improving the current astrochemical models and to address the future challenges. Our cross-section data and phase transition spectra are incorporated into OU based VAMDC website

and it's freely available to all researchers (also available from http://ipc.iisc.ernet.in/astroices/searchmolucule.php).

CHAPTER 5

ELECTRON IRRADIATION OF PURE AND MIXED FILMS OF INTERSTELLAR ICE ANALOGUES

All that glisters may not be gold,
but at least it contains free electrons
- John Desmond Bernal

5.0 Introduction

Investigation of electron driven processes in the laboratory is vital for determining the role of cosmic ray interactions in the interstellar medium. Electron irradiation and thermal processing of interstellar ice analogues of simple organic molecules are discussed in this chapter. Thermal processing of pure and mixed ice analogues are also discussed in detail.

5.1 Electron irradiation and temperature dependent infrared spectroscopy of condensed formamide ($HCONH_2$) ice films.

Formamide ($HCONH_2$) or methanamide is an amide of formic acid, formamide is the simplest molecules with an amide or peptide bond (**Figure 5.1**), and it plays a vital role as an intermediate and precursor in several astrochemical reaction pathways [Rubin 1971]. Formamide has been identified towards Sgr B2 (N) [Halfen et al. 2011], solar system bodies and also in comets [Raunier et al. 2004; Requena-Torres et al. 2006].

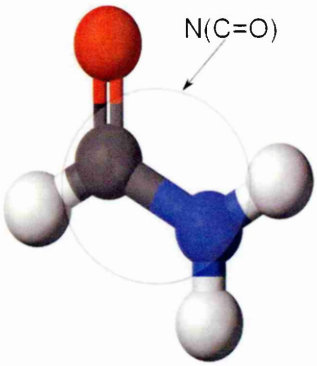

Figure 5.1 Molecular structure of formamide (HCONH2), N(C=O) peptide link is highlighted.

The presence of an amide bond and its simple nature make it a suitable molecule to investigate its irradiation chemistry and to appreciate the survival probabilities of amide species in interstellar conditions. Galactic cosmic rays constitute of high energy protons (GeV) which when under interactions with interstellar dense clouds result in the cascade of secondary electrons of energy in the rage of 1-5 keV [Jones et al. 2011]. To simulate such cosmic ray interactions of icy grain mantles, we employ a flood mode electron gun. For electron irradiation experiments the existing portable apparatus was modified to house a commercial electron gun (from Kimball Physics, USA), which generates electrons of energy 1-2 keV with 1 to 100 μA of emission current, a detailed description of the electron irradiation apparatus is given in section 3.9.

5.1.1 Preparation of the ice film

Experiments were carried out using The Open University astrochemistry apparatus (section 3.9). Using a closed cycle helium cryostat the sample substrate was cooled down to 30 K while the apparatus was maintained at 7.5 x 10^{-10} mbar pressure. A chemically inert and mid-infrared (2-25 μm) transparent Zinc Selenide (ZnSe) window was used as the substrate onto which $HCONH_2$ (99.5 % Sigma Aldrich) was deposited at 30 K. Electron irradiation was carried out for 60 minutes at an energy of 1keV and 10 μA current. An FTIR spectrometer operating in transmission mode with an external MCT-HD detector was employed to record spectra in-situ, during, before and after irradiation processes.

5.2 Electron irradiation

Upon electron irradiation of amorphous $HCONH_2$ three new peaks were observed at 2140 cm^{-1}, 2165 cm^{-1} and 2342 cm^{-1}, these correspond to CO, OCN and CO_2, respectively. Warming up the irradiated sample was found to release the trapped CO when the ice temperature reaches around 110 K, with subsequent loss of CO_2 at about 140 K but the presence of OCN^- was observed until 225 K. However, the dissociation pathway that leads to such new products, upon keV electron irradiation, need to be deduced.

The formation of OCN^- and CO from $HCONH_2$ can take place by the removal of H atoms (dehydrogenation) for OCN and a subsequent removal of N from OCN yielding CO. In a 200 keV H^+ irradiated $HCONH_2$ ice a band corresponding to N_2O was observed in the IR spectra suggesting the presence of nascent N and O atoms to be available upon irradiation [Van Broekhuizen 2004].

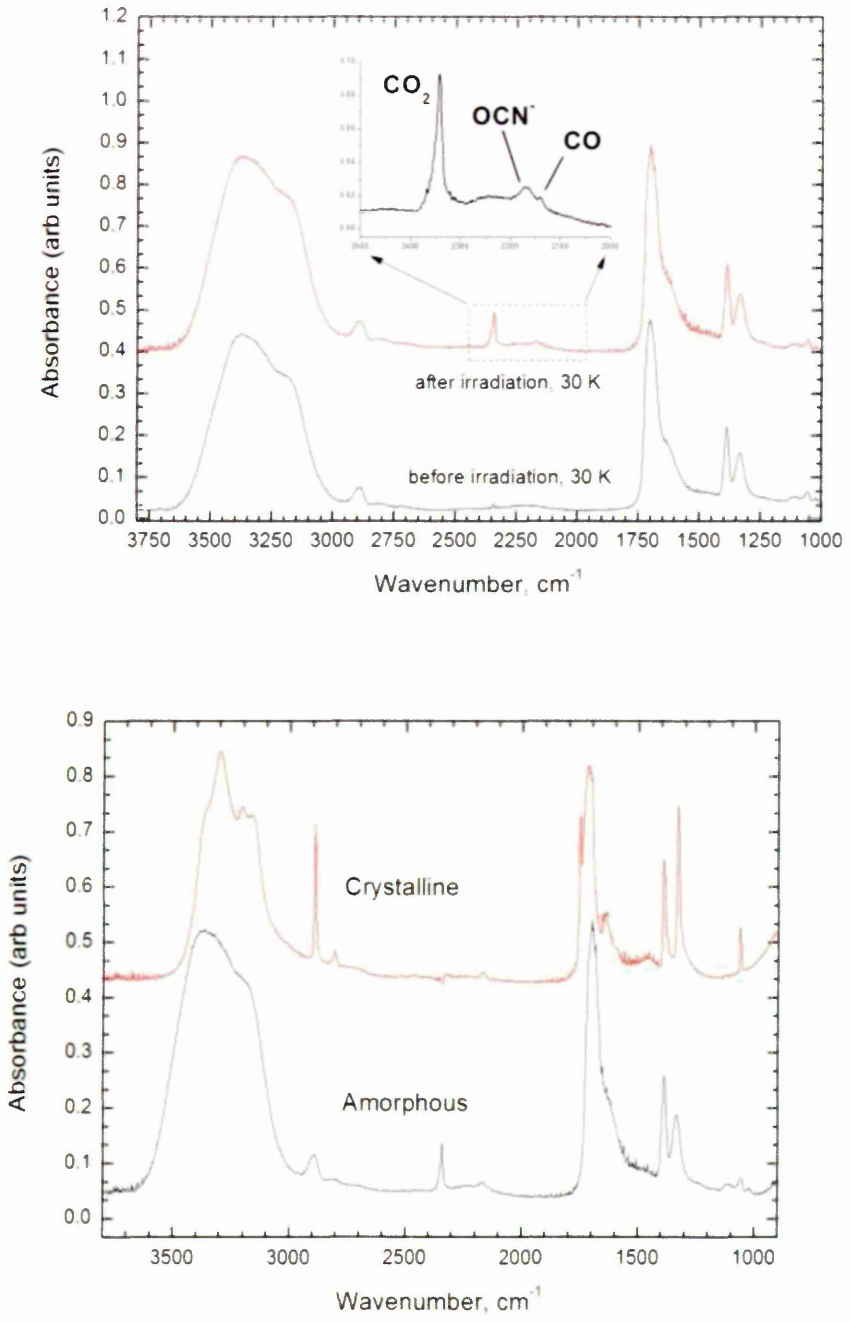

Figure 5.2 (a) Infrared absorption spectra of solid formamide at 30 K before and after 1 keV electron irradiation, (b) amorphous and crystalline formamide at 30 K and 195 K.

However, dehydrogenation from $HCONH_2$ molecule may leave behind HNCO or HOCN. Earlier experiments using electron irradiation on HNCO and HOCN had demonstrated the formation of OCN^- and CO in the solid phase [Mason et al. 2006; Sivaraman et al. 2013; van Broekhuizen 2004].

Another dissociation pathway leading to CO from $HCONH_2$ is possible together with the formation of NH_3. This could be the preferred pathway for CO formation even though NH_3 was not spectroscopically identified in our spectra but this could be due to band overlap from NH_2 asymmetric and symmetric stretching vibrations occurring from $HCONH_2$. For making CO_2, the formation pathway follows the addition of O to CO. Interestingly if such a formation mechanism occurred then CO molecules have to provide both the reactants in producing CO_2 molecules, for which the CO has to further dissociate to supply O atom. The amorphous nature of the ice formed suggests 'cage effect' to play a role in the formation of CO_2 from $HCONH_2$ where dissociated atoms become available from electron irradiation. However more experimental simulations along with theoretical calculations will help towards a complete understanding on the formation pathways of new products from electron induced dissociation of frozen $HCONH_2$ molecules.

Dissociation pathways

OCN

$$HCONH_2 \rightarrow HNCO + H_2 \quad (5.1)$$

$$HNCO \rightarrow OCN^- + H^+ \quad (5.2)$$

CO

$$OCN \rightarrow CO + N \text{ (Dissociative recombination)} \quad (5.3)$$

$$HCONH_2 \rightarrow CO + NH_3 \quad (5.4)$$

5.2.1 Thermal processing of condensed $HCONH_2$

IR spectra recorded at 30 K indicated that the ice formed is an amorphous formamide ice, **Figure 5.2**, and the band peak positions observed, Table 5.1, were in good agreement with previous experiments. Upon gradual warming, up to higher temperatures, the infrared spectral changes suggesting a phase change has occurred around 165 K. This phase change is confirmed by spectra recorded at 195 K clearly indicating a fully crystalline formamide ice to be present on the ZnSe substrate. The spectral changes observed before phase transition from amorphous to crystalline form were linked to changes between conformers of formamide dimers.

To appreciate the structural changes in $HCONH_2$ during thermal processing, a separate experiment was conducted. $HCONH_2$ ice film was synthesised by following the same procedure as in the electron irradiation experiment. Then the ice film was thermally processed until its sublimation at a 5 K/minute step, an FTIR spectrum was recorded at every stage of thermal processing and the processes was repeated for film of three different thicknesses to investigate the effect of thickness.

At 30 K (Figure 5.3(a)) a broad band was observed from 3800 to 2944 cm^{-1} with two peaks positioned at 3372 cm^{-1} and 3179 cm^{-1} corresponding to the vibrational modes υ_1 and υ_2 , respectively. Five other fundamental bands were observed at 2895 cm^{-1}, 1698 cm^{-1} , 1628 cm^{-1}, 1386 cm^{-1}, and 1334 cm^{-1}corresponding to the υ_3, υ_4, υ_5, υ_6 and υ_7 modes, respectively (Table 5.1).

Table 5.1 Observed band positions of $HCONH_2$ at 30 K

Peak positions (cm^{-1})			Mode	Assignment
30 K	20 K[1]	20 K[2]		
710	-	685	?	NH_2 twisting
836	-	841	?	NH_2 wagging
1022	-	-	?	CH out of plane bend
1056	-	1068	?	
1117	-	1134	?	NH_2 rocking
1172	-	1142	?	
1226	-	-	?	
1334	1328	1333	υ_7	CN stretch
1386	1388	1388	υ_6	In plane CH bending
1628	1631	1661	υ_5	In plane NH_2 scissoring
1698	1708	1704	υ_4	CO stretch
2895	2881	2891	υ_3	CH stretch
3179	3181	3217	υ_2	Symmetric NH_2 stretch
3372	3368	-	υ_1	Asymmetric NH_2 stretch

[1] Brucato J.R., Baratta G.A., Strazzulla G., A&A 455 (2006) 395–399; [2] Torrie B.H., Brown B.A., J. Raman Spectrosc. 25 (1994) 183–187.

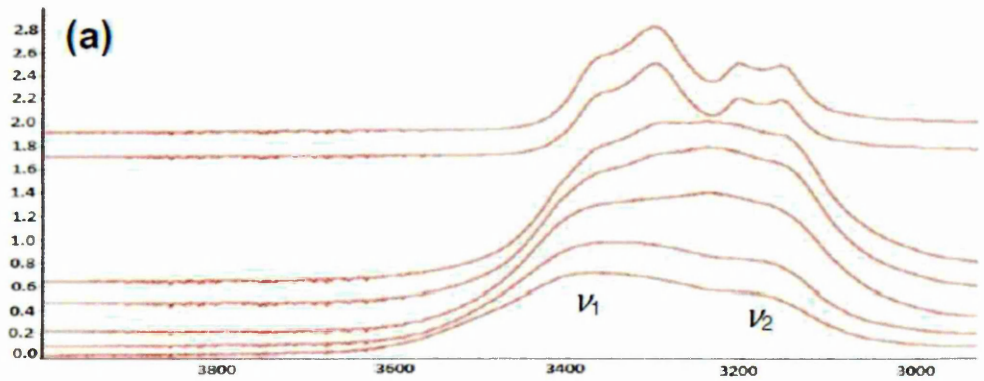

Figure 5.3 (a) Infrared spectra of a condensed molecular formamide ice recorded at 30 K, 90 K, 155 K, 165 K, 185 K, 200 K and 210 K, stacked from bottom to top, respectively.

All the bands are in good agreement with those observed previously [13,15] but four more bands were observed at 1172 cm^{-1}, 1117 cm^{-1}, 836 cm^{-1} and 710 cm^{-1} (Figure 5.3(e)) bands that were also observed by Torrie and Brown [Torrie and Brown 1994] albeit in a 20 K formamide ice.

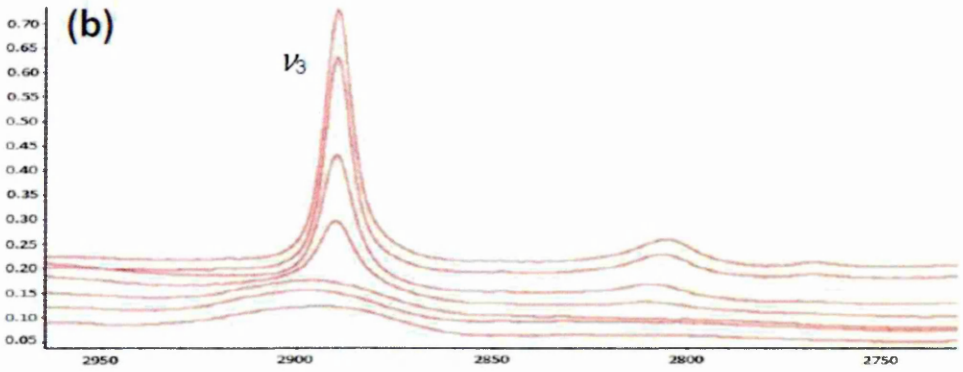

Figure 5.3 (b) Infrared spectra of a condensed molecular formamide ice recorded at 30 K, 90 K, 155 K, 165 K, 185 K, 200 K and 210 K, stacked from bottom to top, respectively.

In our spectra, three bands at 1022 cm^{-1}, 1056 cm^{-1} and 1226 cm^{-1} were observed for the first time at low temperatures (**Figure 5.3**(e)). The two bands observed in the region 1065–1040 cm^{-1} in solid formamide at 108 K, by Itoh and Shimanouchi [Itoh and Shimanouchi 1972], were assigned to the CH out of plane bend, therefore the bands observed at 1056 cm^{-1} and 1022 cm^{-1} in our spectra at 30 K were also assigned to the CH out of plane bend (Table 5.1). The 1226 cm^{-1} band was also reported to be present in the matrix isolation studies of formamide [Rasanen 1983]. Comparing the spectra obtained at 30 K with the spectra recorded at 77 K by King [King 1971] we found that (**Figure 5.2**) the formamide at 30 K is an amorphous phase of $HCONH_2$ ice.

5.2.2 Infrared spectra of formamide recorded during warm-up (30–210 K)

(a) NH_2 asymmetric stretch. The broad band observed at 3372 cm^{-1}, is assigned to the NH_2 asymmetric stretch mode. Upon annealing the sample this band red shifted to 3360 cm^{-1} (at 70 K) and to 3351 cm^{-1} at 90 K. The band position then remains unchanged until 140 K when the band was observed to shift again to 3328 cm^{-1}. At

155 K, when a phase transition occurs this band was observed at 3329 cm^{-1}, with an additional peak appearing at 3377 cm^{-1} (**Figure 5.3**a).

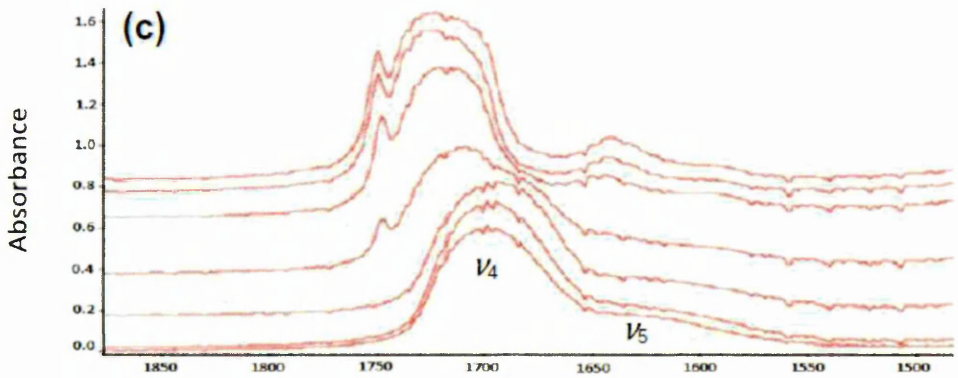

Figure 5.3 (c) Infrared spectra of a condensed molecular formamide ice recorded at 30 K, 90 K, 155 K, 165 K, 185 K, 200 K and 210 K, stacked from bottom to top, respectively.

A further 10 K increase in the sample temperature showed another new peak centered at 3296 cm^{-1}. It must be noted that at 165 K all the three peaks are very clear resolved. Shifts in the band positions due to further heating up to 210 K are listed in Table 5.2. A new peak centre at 3242 cm^{-1}, was observed only at 180 K.

(b) NH_2 symmetric stretches: The broad band observed in the 30 K sample at 3179 cm^{-1} is assigned to the NH_2 symmetric stretch. In contrast to the asymmetric band there is no shift in the band position until the sample was heated to a temperature of 155 K at which temperature the band was observed to shift to 3146 cm^{-1} (**Figure 5.3**a). The υ_2 band intensity also grew when the sample is heated from 30 to 140 K. Between 165 and 175 K, only a small shift in the band was observed but at 210 K the band was observed to have shifted to 3156 cm^{-1} (**Figure 5.2**a).

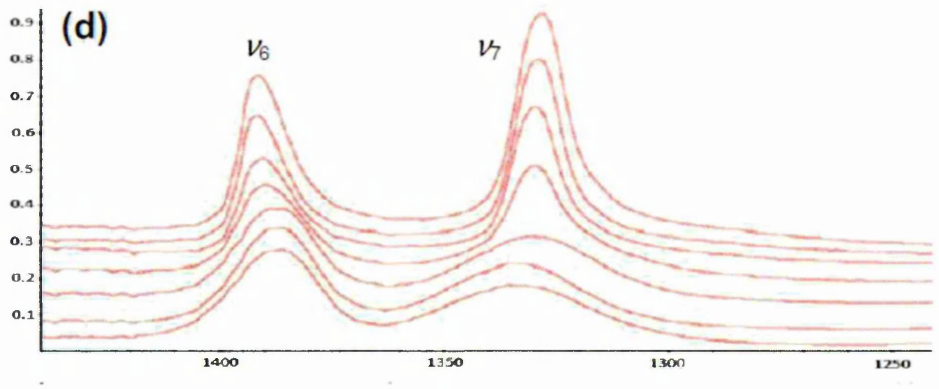

Figure 5.3 (d) Infrared spectra of a condensed molecular formamide ice recorded at 30 K, 90 K, 155 K, 165 K, 185 K, 200 K and 210 K, stacked from bottom to top, respectively.

(c) CH stretch: The band observed at 2895 cm^{-1} in the 30 K sample, is ascribed to the CH stretching mode of the formamide molecule. There is no major change in the band position until the ice temperature reaches 165 K (**Figure 5.3**b) when the band was centered at 2890 cm^{-1} and a new band was observed at 2811 cm^{-1} . No major band shift was observed during warm up the sample from 165 up to 210 K, where the band was observed at 2889 cm^{-1} (Figure 5.3b). Table 5.2 presents the shift in CH stretch band position while the sample is annealed from 30 to 210 K. The spectra recorded at 170 K revealed another new band at 2769 cm^{-1} (Figure 5.3b) which we assign to an overtone or combination band.

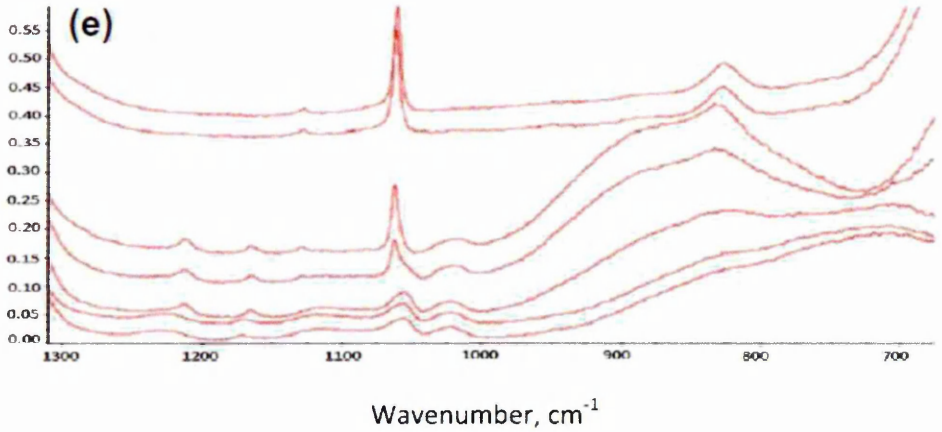

Figure 5.3 (e) Infrared spectra of a condensed molecular formamide ice recorded at 30 K, 90 K, 155 K, 165 K, 185 K, 200 K and 210 K, stacked from bottom to top, respectively.

(d) CO stretch: The band observed at 1698 cm^{-1} in the 30 K sample, is ascribed to the CO stretching in the formamide molecule. There is no shift in the band position until the sample was heated to 165 K, where the band was observed at 1711 cm^{-1} together with a new shoulder at 1747 cm^{-1}. The 1711 cm^{-1} band shifted to 1719 cm^{-1} at 170 K, whereas the shoulder was observed at 1748 cm^{-1} (**Figure 5.3**(c)). Both the bands remain unchanged until approximately 200 K where the bands were observed at 1725 cm^{-1} and 1750 cm^{-1}, respectively.

(e) NH_2 scissoring: The band observed at 1628 cm^{-1} in the 30 K sample, the υ_5 band (fundamental) is ascribed to the in plane NH_2 scissoring mode. Annealing the sample from 30 K to higher temperatures and recording the infrared spectrum showed a red shift in the peak to 1621 cm^{-1} , at 165 K (**Figure 5.3**(c)). In addition a new band at 1677 cm^{-1} was observed, similar to the NH_2 asymmetric stretching region where new bands appeared at the same temperature. At 170 K both the bands were observed to have shifted to 1594 cm^{-1} and 1645 cm^{-1} respectively and at 210 K they were observed at 1599 cm^{-1} and at 1641 cm^{-1}.

(f) CH bending: The band observed at 1386 cm^{-1} in the 30 K sample is ascribed to the in plane CH bending mode. There is no significant change in the band position until the temperature reaches 165 K where the band was found to be centered at 1390 cm^{-1} (**Figure 5. 2**d). No major band shift was observed by further heating the sample up to 210 K, (**Figure 5.5**a&b). Table 5.2 shows the small shifts in the band positions due to in plane CH bending while the sample is annealed from 30 to 210 K.

Table 5.2 Observed peak positions in the infrared spectra of solid formamide at different temperatures.

30 K	70 K	90 K	105 K	119 K	130 K	140 K	155 K	165 K	170 K	175 K	180 K	190 K	201 K	210 K	210-30 K
710	710	710	710	710	710	710	710								
836	836	836	836	836	836	836	836	830	830	830	830	830	827	827	840
								890	890	890	890				
1022	1022	1022	1022	1022	1022	1022	1022	1019	1018	1018	1018				
1056	1056	1056	1056	1056	1056	1056	1055	1062	1062	1062	1062	1062	1061	1061	1065/1069
1117	1117	1117	1117	1117	1117	1117	1117								
													1128	1127	1134
1172	1172	1172	1169	1169	1169	1168	1166	1165	1165	1165	1165				
1226	1226	1226	1226	1226	1226	1226	1213	1213	1213	1213	1213				
1334	1334	1334	1334	1334	1334	1334	1334	1330	1330	1330	1330	1330	1329	1329	1315/1332
1386	1386	1386	1386	1386	1386	1386	1386	1390	1389	1389	1389	1389	1392	1391	1392
1628	1628	1628	1628	1628	1628	1628	1628	1621	1594	1594	1594	1594	1596	1599	1600
								1677	1645	1645	1645	1645	1642	1641	1655
1698	1698	1698	1698	1698	1698	1698	1698	1711	1719	1719	1719	1719	1725	1722	1719
								1747	1748	1748	1748	1748	1750	1750	1748
									2468	2468	2467	2467	2467	2465	2472
															2705
															2742
									2769	2769	2769	2767	2767	2767	2771
								2811	2810	2810	2808	2809	2806	2805	2813
2895	2896	2896	2896	2896	2896	2896	2896	2890	2890	2890	2890	2890	2890	2889	2891
															3139
3179	3179	3179	3179	3179	3179	3179	3146	3149	3149	3145	3151	3154	3155	3156	3174
3372	3360	3351	3351	3351	3348	3328	3239	3236	3234	3210	3205	3204	3204	3204	3204
											3242	-	-	-	-
							3377	3296	3298	3295	3295	3299	3300	3301	3290
								3377	3374	3371	3363	3366	3367	3365	3356

(g) CN stretch: At 30 K the band observed at 1334 cm^{-1} is ascribed to the CN stretch in the formamide molecule. The peak position of the CN stretch region remained unchanged until 165 K where the recorded spectrum showed the peak to have shifted to 1330 cm^{-1} (**Figure 5.3**d). Upon further heating to 210 K no significant shift in the band position was observed (**Figure 5.5**a and **Table 5.2**).

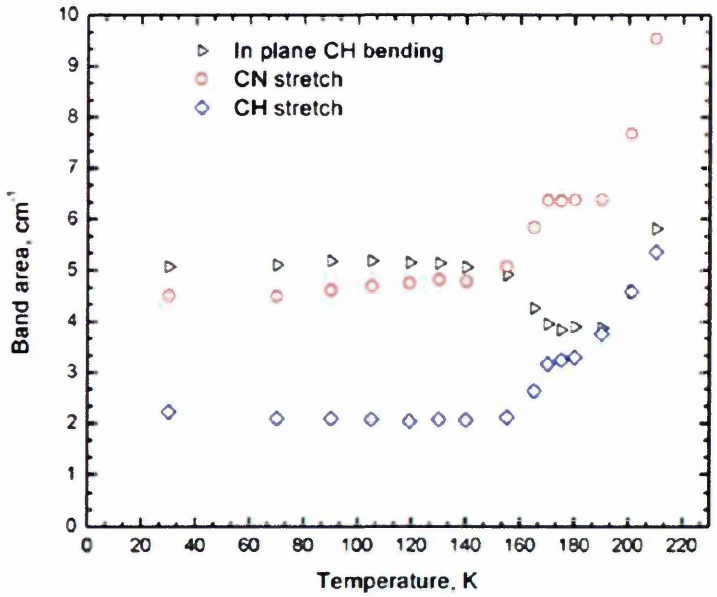

Figure 5.4 Shows the integrated band area of CN (υ_7), CH (υ_3) stretching and in plane CH bending (υ_6) vibrations of formamide as a function of temperature.

(h) Other NH_2 and CH vibrations: The bands observed at 710 cm^{-1} and 836 cm^{-1} in the 30 K solid were assigned to the NH_2 twisting and wagging vibrations [Torrie and Brown 1994 ;Itoh and Shimanouchi 1972], respectively. The bands at 1117 cm^{-1} and 1172 cm^{-1} were assigned to the NH_2 rocking vibration [Itoh and Shimanouchi 1972]. The 710 cm^{-1} band disappeared in the spectra recorded at 165 K whereas the 836 cm^{-1} band was found be at 830 cm^{-1} and at 827 cm^{-1} at 165 K and 210 K respectively (**Figure 5. 3**e). Interestingly a new band, at 890 cm^{-1}, appeared in the spectra at 165 K which remained until 180 K. The 1117 cm^{-1} band was not observed in the spectra at 165 K whereas around 200 K a band appeared at 1128 cm^{-1}. Spectra recorded at 165 K also revealed a new band appearing at 2811 cm^{-1} which, on heating to 210 K shifted to 2805 cm^{-1} (**Figure 5.3**b). It is important to note that the band observed at 2811 cm^{-1} and shifted to 2805 cm^{-1} under the action of increasing temperature matches with the υ_5 fundamental of $N{=}NH_2$ band observed in a formamide synthesis experiment at 12 K using varied concentrations of CO and NH_3

[Jones et al. 2011]. The observed band shift with respect to the increase in NH_3 concentration by Jones [Jones et al. 2011] was analogous to the shift observed in our experiment as a function of temperature. Two more bands at 1022 cm^{-1} and 1056 cm^{-1} were also observed at 30 K, which correspond to the CH out of plane bend [Itoh and Shimanouchi 1972] in the formamide molecule. Upon annealing the sample to higher temperatures, the 1022 cm^{-1} band remained unshifted until 165 K where it was observed to shift slightly to 1019 cm^{-1} and the band disappeared in the spectra recorded at 190 K. However, the other band at 1056 cm^{-1} was observed to shift to 1062 cm^{-1} at 165 K and was observed at 1061 cm^{-1} up until 210 K (Figure 5.5a). Infrared spectra after re-cooling (30 K), it is interesting to compare the spectra acquired at 30 K, just after sample deposition, with the spectra of a sample that had been annealed to 210 K, and then cooled to 30 K. The spectra recorded at 30 K, after re-cooling the sample from 210 K, matches with the crystalline formamide spectra recorded at 77 K, by King [King 1971], and the spectrum recorded at 20 K, by Khanna et al. [Khanna et al. 2002], after re-cooling the annealed sample. While cooling down to 30 K from 210 K, the infrared spectra recorded revealed several new bands and shifts in those known band peak positions. The region corresponding to the NH2 asymmetric (υ_1) and symmetric stretch (υ_2) were observed to have five bands at 3139 cm^{-1}, 3174 cm^{-1}, 3204 cm^{-1}, 3290 cm^{-1} and 3356 cm^{-1}. The m3 fundamental band was observed at 2891 cm^{-1}. The region 2820–2460 cm^{-1}, was found to contain five peaks centered at 2813 cm^{-1}, 2771 cm^{-1}, 2742 cm^{-1}, 2705 cm^{-1} and 2472 cm^{-1} (Figure 5.3a).

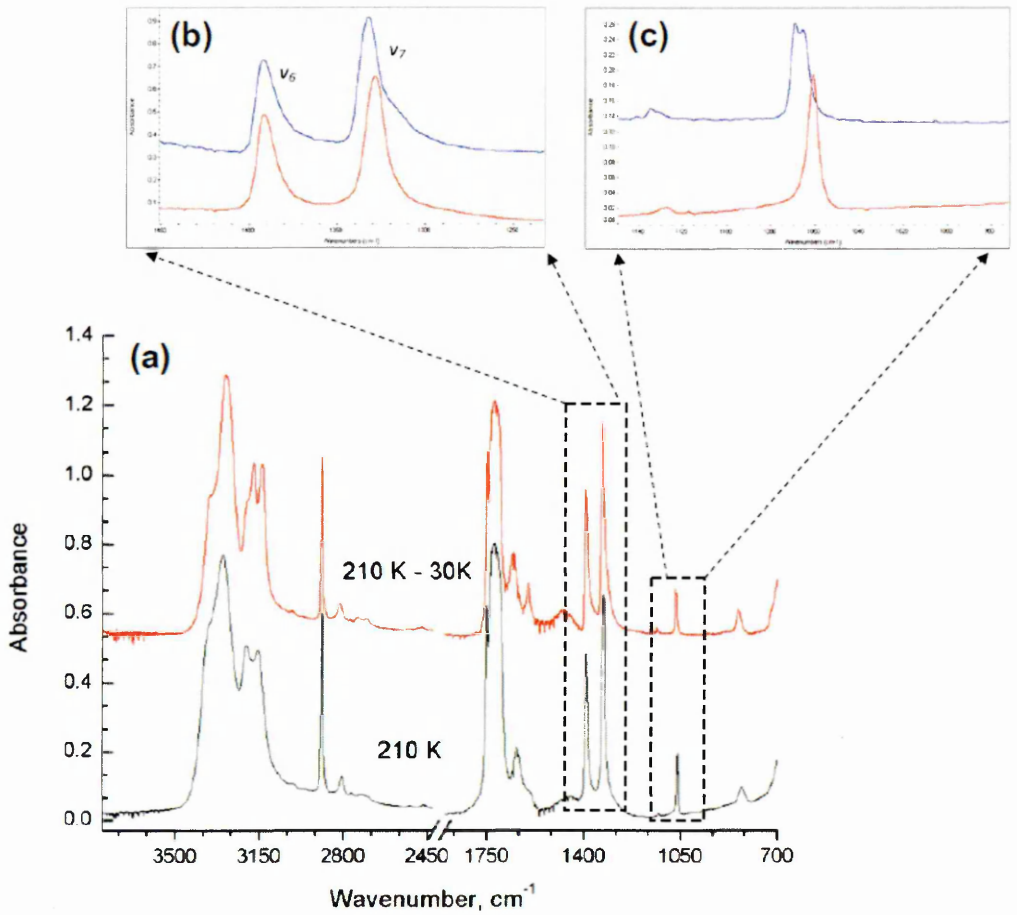

Figure 5.5 Infrared spectra of the sample annealed to 210 K and then re-cooled to 30 K.

The υ_4 fundamental region that corresponds to the CO stretch was observed to contain two bands; one at 1719 cm^{-1} and the other at 1748 υ_3 cm^{-1}. Likewise, two peaks at 1600 cm^{-1} and 1655 cm^{-1} were observed in region that corresponds to the in-plane NH_2 scissoring vibration. The υ_6 fundamental band, corresponding to in plane CH bending, was observed at1392 cm^{-1}, and the υ_7 fundamental, corresponding to the CN stretch, was observed at 1332 cm^{-1} with an additional shoulder band at 1315 cm^{-1} (Figure 5.5b). The other bands observed at 1134 cm^{-1}, 1069 cm^{-1} and at 840 cm^{-1} were found to be a good match to the 20 K data (Table 5.1) reported by Torrie and Brown [Torrie and Brown 1994]. In our spectra the band at 1069 cm^{-1} appeared as a doublet with a peak at 1065 cm^{-1} (Figure 5.3c).

Analysis of IR spectra of formamide at higher temperatures (210 K) appear to show the integrated areas of the CH and CN stretching vibrations (Figure 5.4) increasing. As additional formamide molecules were not added to the sample while heating this suggests that the increase in the peak intensity whilst warming up the sample, this may be due to the formation of dimers or higher aggregates (polymer) formed from formamide association. However, the changes in infrared band intensities with respect to temperature cannot be neglected and the extent of such contributions can be estimated using theoretical calculations, which is beyond the scope of this experimental paper. The crystal structure of solid formamide has been determined [Ladell 1954] to be a collection of centro-symmetric (C2h) dimers. Matrix isolation studies coupled with quantum chemical calculations have shown the presence of four possible energetically stable formamide dimers; Dimer A, B, C and D, and also a less stable dimer, Dimer E [Mardyukov et al. 2007]. Matrix isolation studies have also revealed the formation of these dimers in various proportions depending on the matrix prepared (either Xenon or Argon), on the sample preparation and the sample temperature. The presence of such dimers was experimentally observed in the infrared spectra, using 0.5 cm^{-1} resolution, with the identification of the characteristic vibrations for formamide dimers occurring in the NH_2 and CO vibrational regions [Mardyukov et al. 2007]. In the present work it was hard to distinguish these peaks in our spectra due to our limited 2 cm^{-1} resolution. However, even for a pure formamide sample, the existence of dimers at different temperatures and the interchange to other dimer forms suggest that strong dimer formation is likely to happen while annealing the sample.

While comparing the crystalline formamide spectra at 210 K and the spectrum recorded after re-cooling to 30 K we found the phase change was irreversible (Table

5.2 and Fig. 5.5). The shifts observed in the band positions after the phase change may be due to the interaction between (i) formamide monomers forming dimers and/or (ii) formamide dimers forming polymers. Experimental evidence [Jones 2011; Grim et al. 1989] suggests that the absence of formamide monomer signals in the mass spectrum at higher temperatures might be due to formamide aggregates being formed. Such rearrangement of dimers due to annealing may have contributed to the changes observed in the spectra. Indeed a significant change in the proportions of different formamide dimers would have taken place when solid formamide turns from amorphous to crystalline by annealing.

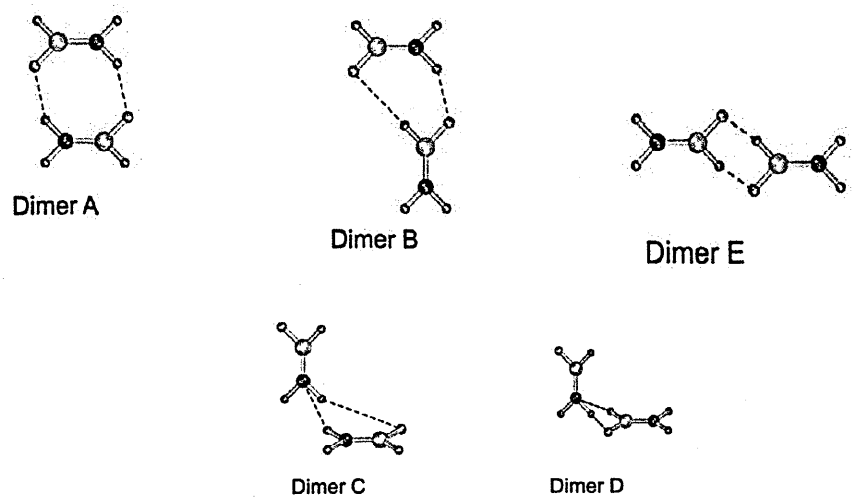

Figure 5.6 Dimers of solid formamide [Adapted from Mardyukov et al. 2007].

In fact spectral changes observed by annealing the solid formamide sample from 30 up to 210 K, may be due to both (i) the molecular aggregation taking place within the ice by converting monomers to dimers or even to polymers [Sivaraman et al. 2013] and (ii) the proportion of the dimers (Dimer A–D) that may vary as a function of temperature [Sivaraman et al. 2013]. This claim is supported by the experimental identification of dimers in the crystalline [Ladell 1954] and amorphous [Mardyukov et al. 2007] solid formamide and the absence of formamide monomer

mass spectrometry signatures at higher temperatures [Sivaraman et al. 2013]. Warming up the sample to 300 K we found that all formamide or the dimers/ polymers had sublimed and left no residue on the substrate. Further evidence for dimer formation arises from calculation of the ice density. The column density of formamide present in our sample at 30 K was calculated using the A_{obs} value of 4.7 x 10^{18} cm molecule^{-1} [Brucato et al. 2006] for the 2895 cm^{-1} (υ_3, CH stretch), from which the column density was estimated at about 4.7 x 10^{17} molecules cm^{-2}. Using the A_{obs} values of 6.8 x 10^{18} cm molecule^{-1} and 8.5 x 10^{18} cm molecule^{-1} [Brucato et al. 2006], for the band at 1386 cm^{-1} (υ_6, in plane CH bending) and 1334 cm^{-1} (υ_7, CN stretch), the column density was estimated to be about 7.4 x 10^{17} molecules cm^{-2} and 5.3 x 10^{17} molecules cm^{-2}, respectively. Thus the estimated column density obtained therefore lay between 4.7 and 7.5x 10^{17} molecules cm $^{-2}$.

5.3 Electron irradiation and temperature dependent infrared spectroscopy of condensed ice films of acetic acid (CH_3COOH).

Acetic acid is a highly abundant organic acid detected towards Sgr B2 (N) [Lass 2011]. Abundance ratio of acetic acid and its structural isomer methyl forte in Sgr B2 is an unresolved problem. According to the observations ratio of column density of $CH_3COOH/HCOOCH_3$ in Sgr B2 (N) is ~ 0.02 [Modica and Palumbo 2011]. Presence of all structural isomers of acetic acid, i.e. methyl formate and glycol aldehyde through laboratory synthesis is confirmed molecular cloud and CH_3COOH has been synthesised in laboratory through electron irradiation of CH_3OH and CO mixture [Sivaraman et al. 2013]. In this study we investigated the survival characteristics of pure CH_3COOH films with 1 keV electrons; in addition to that we quantified the electron destruction cross-section and rate of destruction of CH_3COOH

ice during electron processing are reported. The rate of evolution of products during and after electron irradiation at 30 K is investigated. And the effect of thermal processing is discussed in detail.

Using the astrochemistry apparatus (section 3.9) at The Open University, an ice film is formed through back ground deposition of pure acetic acid sample (98.00 %, Sigma-Aldrich) condensed on to the ZnSe substrate maintained at 28 K. In order to calibrate the film thickness and to quantify the column density, all procedures described above for formamide experiment is repeated for acetic acid ice. The resulted ice film of acetic acid was ~ 324 ± 20 nm thick and had a column density of ~ 5.2 x 10^{17} molecules cm^{-2} with respect to 'A' value = 4.0 x 10^{-18} cm $molecule^{-1}$ [Bennett and Kaiser 2007]. Absorption spectrum of acetic acid at 28 K is shown in Figure 5.7, and infrared absorption features are listed in table 5.3.

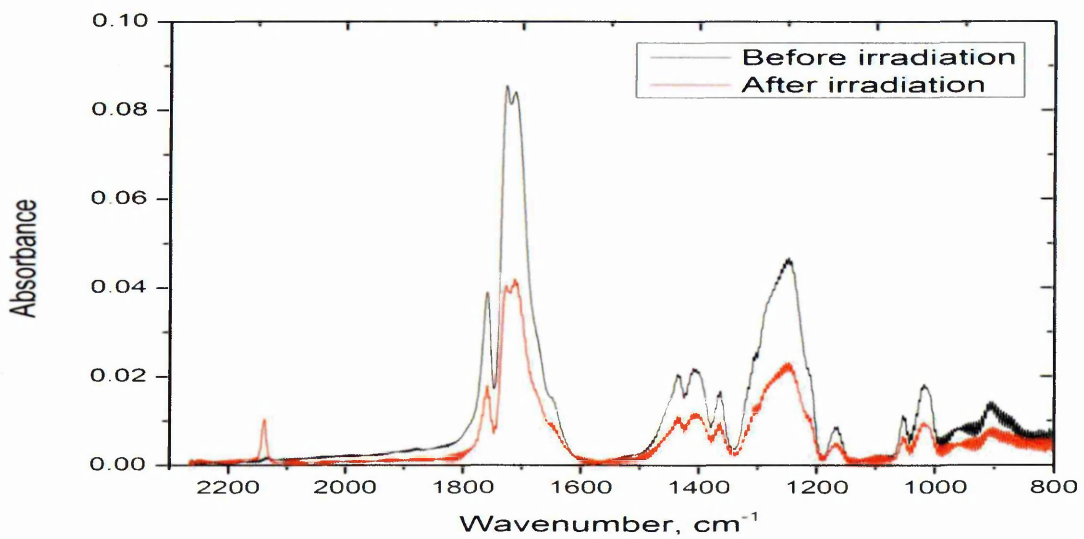

Figure 5.7 Absorption spectra of acetic acid at 28 K. Spectrum of acetic acid before (black) and after (red) irradiation, region 2300-800 cm^{-1} is shown here.

The ice film was processed with electrons of energy 1keV at 10 μA for 60 minutes. A transmission mode FTIR spectrum was recorded after every 5 minute

intervals of irradiation at normal incidence to the ice film. After electron processing the sample was kept undisturbed for 30 minutes and monitored by recording FTIR spectra, and then the sample was heated in 5 K/minute steps. An FTIR spectrum was recorded at every stage of thermal processing and continued until the sublimation temperature of CH_3COOH ice.

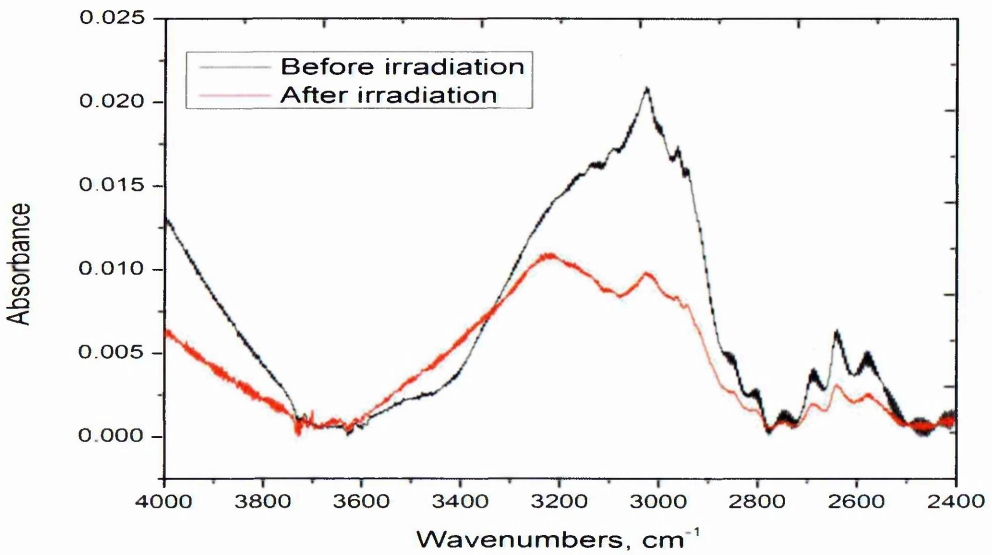

Figure 5.8 Absorption spectra of acetic acid at 28 K. Spectrum of acetic acid before (black) and after irradiation, region 4000-2400 cm^{-1} is shown here.

5.3.1 Electron irradiation

From the Figures 5.7 and 5.8 it is evident that the acetic acid ice deposited at 28 K is amorphous and posses infrared absorption features due to OH stretching at (υ_1) 3562.17 cm^{-1}, CH_3- str at 3084 cm^{-1}, CH_3- str cm^{-1} 2937.08 , C=O str at 1759.12 cm^{-1} , CH_3- deform at 1436.8cm^{-1} and 1364.2 cm^{-1}. In addition to this there is a C-O stretch feature at 1168.21 cm^{-1} and CH_3 rock feature at 969.13 cm^{-1}. All the features in this study are consistent with the values in literature [Lass et al. 2011]. This particular study was focused on survival probability of CH_3COOH versus $HCOOCH_3$, in this

thesis only the result of the destruction characteristics of CH_3COOH is presented. An investigation of survival probability of methyl formate during electron processing is planned for the future.

Table 5.3 Observed infrared bands and assignments

Mode of vibration	Band position **This work** (cm^{-1})	Band position (cm^{-1}) [1, 2]
OH str	3562.17	3583
CH_3-str	3084.96	3051
CH_3- str	2937.08	2944
C=O str	1759.12	1788
CH_3-deform	1436.80	1430
CH_3- deform	1364.17	1382
OH bend	1251.93	1264
C-O str	1168.21	1182
CH_3 rock	969.13	979
CC str		847
CH_3 d-stretch	2978.56	2996
CH_3 rock	1052.96	1048

1. Lass et al. 2011; 2. Modica and Palumbo 2011

Electron processing results in the dissociation of bonds in CH_3COOH, it is clearly evident from the reduction of absorption intensity of C=O stretch and OH bend features.

Figure 5.9 and **5.10** shows the destruction characteristics of CH_3COOH, in case of C=O (most prominent feature), it is observed that up to nine minutes of irradiation the destruction rate was very high and this corresponds to dissociation of the C=O bond in acetic acid.

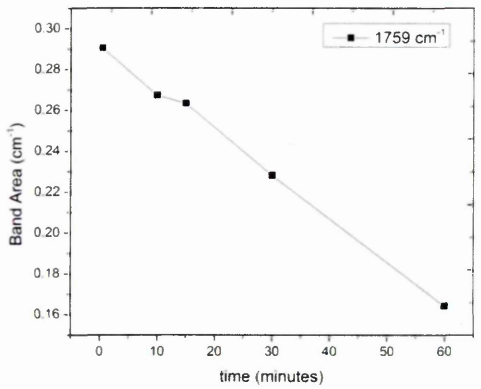

Figure 5.9 Destruction of OH feature (at 1759 cm^{-1}) during electron irradiation of CH_3COOH

However, later on the nature of processing changes and dissociation characteristics reduce considerably and sputtering dominates. Even though it is not possible to quantify and resolve the individual contributions from each process, it is clear that there is a larger contribution from sputtering.

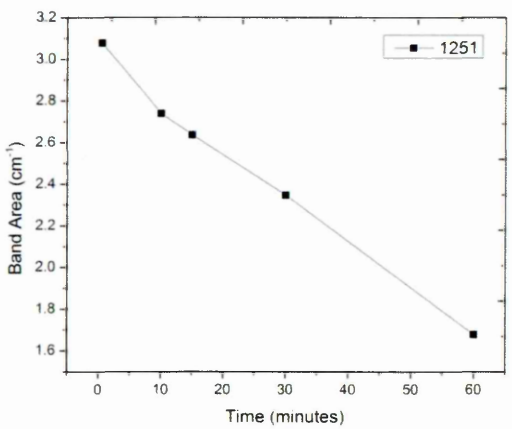

Figure 5.10 Destruction of C=O feature (at 1251 cm^{-1}) during electron irradiation of CH_3COOH

The initial column density of CH_3COOH was ~ 5.2 x 10^{17} molecules cm^{-2}; this column density was reduced to 8.6 x 10^{16} molecules cm^{-2} after 60 minutes of irradiation. In the first ten minutes of irradiation, reduction of overall column density

of CH_3COOH was below 5 %, however there was bond breaking, which is clearly evident from the production of CO, shown in Figure 5.11. CO production can happen through the following pathways

$$CH_3COOH \rightarrow CO + CH_3OH \qquad (5.8)$$

This process is the reverse processes of formation of CH_3COOH from methanol CO surface reactions. This pathway of CO formation is highly efficient and results is large amount of CO. Amount of CO produced through this processes is equivalent to 0.3 % of total mass of CH_3COOH.

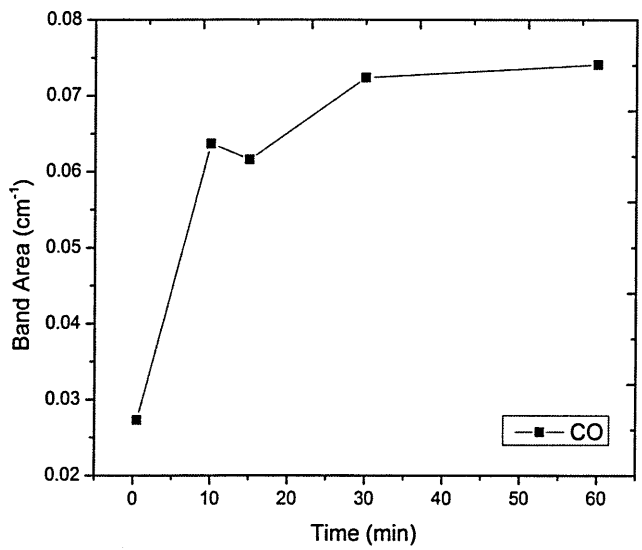

Figure 5.11 Production CO (at 2137 cm^{-1}) during electron irradiation of CH_3COOH at 28 K

Destruction rate of CH_3COOH strongly follows the energy profile and flux of electrons. And survival probability of CH_3COOH is low when compared to that of $HCOOCH_3$, since the bond destruction rate was high. The rate of sputtering due to electron interaction is equal for both $HCOOCH_3$ and CH_3COOH, but electron impact bond dissociation of CH_3COOH is high. By column density calculations of newly formed products reveal that ~50% of sputtered mass is sputtered as CH_3COOH (i.e. more disintegration than $HCOOCH_3$), with FTIR spectra it is impossible to confirm

these observations but from the earlier astrochemical models and quantum chemical calculations these results are valid. The destruction rate of CH_3COOH and production of products (CO) are strictly following the proposed pathway of equation 5.8, and this concludes that CH_3COOH is a stable molecule in ISM like environment. However, $HCOOCH_3$ is the most stable of the $C_2H_4O_2$, this hypothesis was tested by our experiments on electron irradiation of methyl formate, which are discussed in section 5.4.

5.3.2 Thermal processing of CH_3COOH

A pure CH_3COOH ice film was prepared by following the same procedure of the electron irradiation experiment and this unirradiated CH_3COOH film was thermally processed at 5 K/minute steps. An interesting set of changes were observed during the heating procedure. Films of various thickness were processed at separate experiments to investigate the effect of thickness, but we found that thickness play very little or no influence in these changes.

During annealing the C=O feature at 1759 cm^{-1} started to shift towards lower wavenumber regions, at 115 K the feature shifted to 1750 cm^{-1} and eventually started to bifurcate. At 110 K this feature transformed into two separate and sharp bands at 1763 and 1703 cm^{-1}, these peaks are assigned to C=O stretch. In the same fashion, above 115K, broad-weak absorption bands due to CH_3 deformation at 1436 and 1364 cm^{-1} undergo splitting and results in sharp well resolved peaks. The band at 1436 bifurcates and forms two sharp peaks at 1458 and 1454 cm^{-1}. The band at 1364 cm^{-1} bifurcates to 1439 and 1436 cm^{-1}, and the broad feature at 1387 cm^{-1} started to evolve above 90 K and shifted towards higher frequency region to form a relatively sharp feature at 1391 cm^{-1}. Strong absorption at 1251 cm^{-1} due to the OH stretch is

stable throughout the annealing process, even though there is no shift in the peak position of the major band at 1251cm^{-1}the peak is sharpened and evolved into a broad sub feature, which peaks around 1221 cm^{-1}.

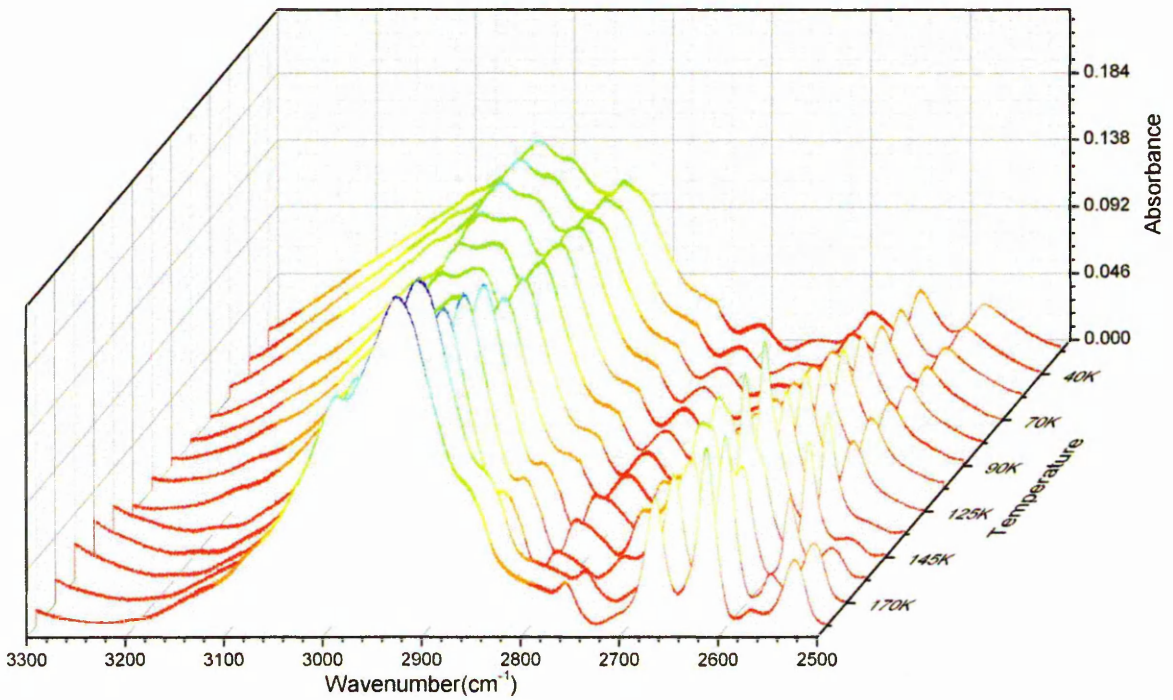

Figure 5.12 Thermal processing of CH_3COOH ice film. Amorphous CH_3COOH ice at 28 K was annealed until sublimation (Region 3300-2500cm^{-1}). Absorption features at 40 K, 70 K, 90 K, 125 K, 145 K, 170 K and 177 K are shown here.

Absorption features due to CH_3 rock at 969 cm^{-1} and 847 cm^{-1} (this feature was absent in the amorphous ice but later emerged during annealing) also split and results in two sharp bands at 957 cm^{-1}, 929 cm^{-1} and 850 cm^{-1} and 828 cm^{-1} respectively. These features are assigned to the CH_3 rock and C-C stretch motions [Katon 1978].

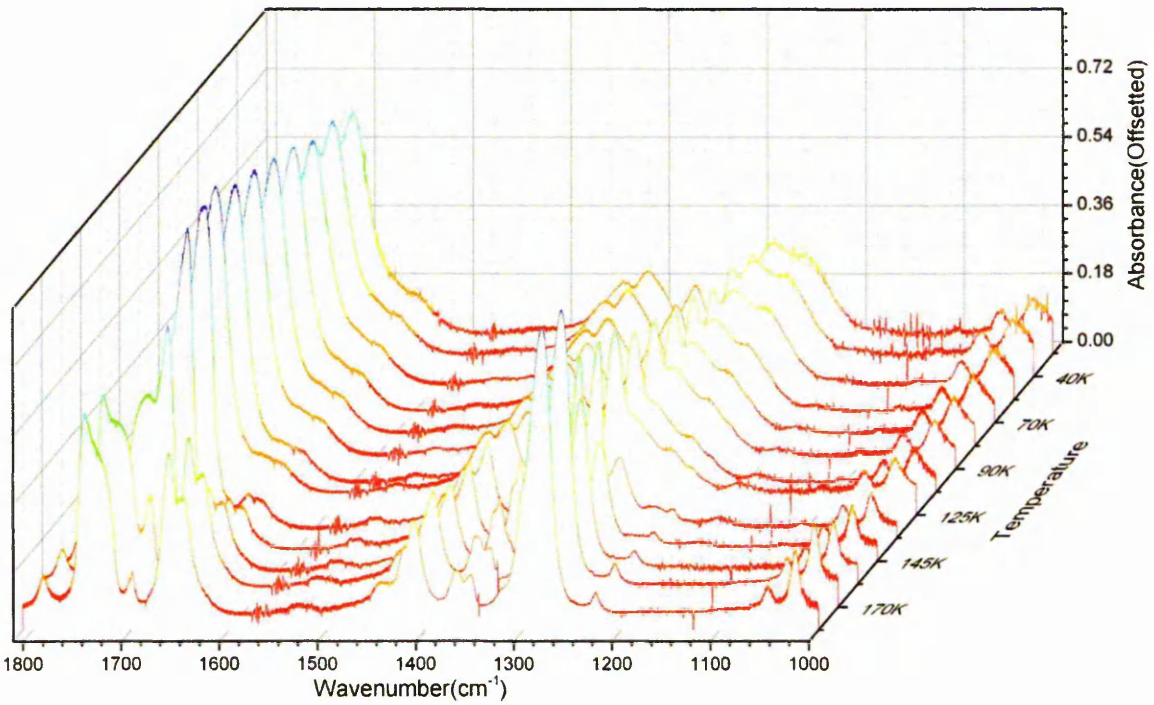

Figure 5.13 Thermal processing of CH_3COOH ice film. Amorphous CH_3COOH ice at 28 K was annealed until sublimation. Absorption features at 40 K, 70 K, 90 K, 125 K, 145 K, 170 K and 177 K are shown here.

The annealed sample was cooled back to 30 K to confirm the stability of the crystalline features in the spectra. When the temperature is lowered to 30 K, the general features remain similar to the spectrum at 177 K. Successive annealing of the sample to 160 K exhibit the same behaviour, and all the spectral features shown by spectrum 160 K are retained. Upon subsequent heating above 180 K, the ice film starts to sublimates, but there are no characteristic changes exhibited after the phase transition. Therefore, the phase change in the ice film is irreversible.

5.4 Electron irradiation and temperature dependent infrared spectroscopy of condensed methyl formate ($HCOOCH_3$) ice films.

Methyl formate is an ester of acetic acid and it is one of the most abundant species observed towards Sgr B2 (N) [Plekan et al. 2012]. Abundance ratio of acetic acid and its structural isomer methyl formate in Sgr B2 is an unresolved problem. To investigate this problem and to confirm and $HCOOCH_3$ has been synthesised in laboratory through electron irradiation of CH_3OH and CO mixture [Sue et al. 2000]. In this study I investigated the survival characteristics of pure $HCOOCH_3$ films with 1 keV electrons; in addition to that we quantified the electron destruction cross-section and rate of destruction of $HCOOCH_3$ ice during electron processing. The rate of evolution of products during and after electron irradiation at 30 K was also investigated and the effect of thermal processing discussed in detail.

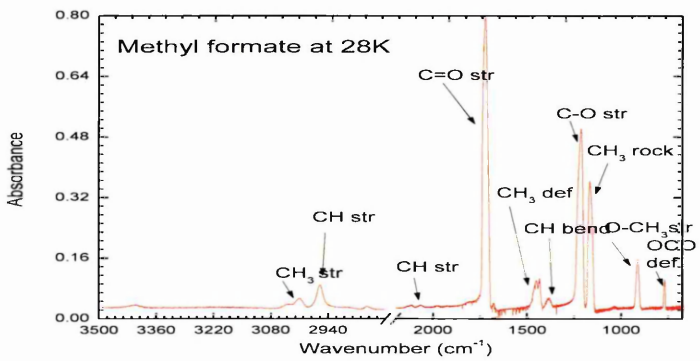

Figure 5.14 $HCOOCH_3$ ice film at 28 K. Characteristic infrared absorption features are marked in the spectrum.

From the absorption spectrum of $HCOOCH_3$ ice film (**Figure 5.14**) it is evident that the $HCOOCH_3$ at 28 K is amorphous and posses infrared absorption features due to OH stretching at (υ_1) 3402.17 cm^{-1}, CH_3- str at 3038 cm^{-1}, CH_3- str cm^{-1} 3010.26 , C=O str at 1724.75 cm^{-1} , CH_3- deform at 1450.62 cm^{-1} and 1434.77 cm^{-1}.

In addition to this there is a C-O stretch feature at 1212.59 cm^{-1} and CH_3 rock feature at 1167.19 cm^{-1}, O-CH_3 stretch at 910 cm^{-1} and OCO deformation at 769 cm^{-1}. All the features in this study are consistent with the values in literature [Goncharov et al. 2005]. This particular study was focussed on survival probability of $HCOOCH_3$versus CH_3COOH in interstellar medium, therefore, the work presented in this thesis mainly focus on the destruction characteristics of the $HCOOCH_3$ ice film.

Table 5.4 Observed band positions of methyl formate ($HCOOCH_3$)

Band position **This work** (cm^{-1})	Assignment	Characterization	Modica et al.	
			Band position (cm^{-1})	Band strength **A** (cm/ molecule)
3038.74	υ_1	CH_3 str	3038	
3010.26	$\upsilon_2, \upsilon_{13}$	CH_3 str	3010	
2959.43	υ_3	CH str	2960	
1724.75	υ_4	C=O str	1720	4.77×10^{-17}
1450.62	υ_6	CH_3 def	1450	
1434.77	υ_{14}	CH_3 def	1435	4.94×10^{-18}
1381.83	υ_7	CH bend	1383	
1212.59	υ_8	C-O str	1210	2.80×10^{-17}
1167.19	υ_9	CH_3 rock	1164	1.62×10^{-17}
910.78	υ_{10}	O-CH_3 str	910	3.79×10^{-18}
769.64	υ_{11}	OCO def	768	1.01×10^{-18}

Figure 5.15 (a) and (b) shows the destruction characteristics of $HCOOCH_3$; in case of C=O (most prominent feature), it is observed that up to 12 minutes of irradiation the destruction rate was very high and this corresponds to dissociation of bonds C=O bond in methyl formate. Electron processing results in the dissociation of bonds in $HCOOCH_3$, it is clearly evident from the reduction of absorption intensity of C=O stretch and OH bend features.

However, later on the nature of electron interaction changes considerably and as a result dissociation characteristics reduces and sputtering dominates. Even though

it is not possible to quantify and resolve the individual contributions from each process, it is clear that there is large contribution from sputtering.

The initial column density of $HCOOCH_3$ was ~ 3.2 x 10^{18} molecules cm^{-2}, this column density has reduced to 2.8 x 10^{17} molecules cm^{-2} after 60 minutes of irradiation. Unlike acetic acid, methyl formate follows a different pattern of destruction and the destruction rate is exponential and converges to an asymptote. In the first ten minutes the destruction rate of C=O feature was 8% of the overall destruction. Sputtering dominates the process, however, there was also bond breaking, which is clearly evident from the production of CO, shown in figure 5.15(d). CO production can happen through the following pathways

$$HCOOCH_3 \rightarrow CO + CH_3OH \qquad (5.8)$$

This process is the reverse processes of formation of $HCOOCH_3$ from methanol CO surface reactions. Amount of CO produced through this processes is equivalent to 0.2 % of total mass of CH3COOH.

Destruction rate of $HCOOCH_3$ strongly follows the energy profile and flux of electrons. And survival probability of $HCOOCH_3$ is low when compared to that of CH_3COOH, since the bond destruction rate was high. Rate of sputtering due to electron interaction is equal for both $HCOOCH_3$ and CH_3COOH, but electron impact bond dissociation of $HCOOCH_3$ is high. By Column density calculations of newly formed products reveal that 60% of sputtered mass is sputtered as $HCOOCH_3$ (i.e. more disintegration than CH_3COOH), with FTIR spectra it is impossible to confirm these observations but from the earlier astrochemical models and quantum chemical calculations these results are valid. In addition, current observations it is evident that abundance of $HCOOCH_3$ is very high in the molecular clouds and it support our findings. Destruction rate of $HCOOCH_3$ and production of products (CO) are strictly

following the proposed pathway (equation 5.8), and this concludes that $HCOOCH_3$ is a highly stable molecule in ISM like environment. By comparing these result with that of CH_3COOH is found that $HCOOCH_3$ is sputtered at a faster rate than CH_3COOH. It is either due to the tendency of CH_3COOH to form hydrogen bonds, since CH_3COOH forms hydrogen bonds, the molecules are likely to stay together in clusters and dissociates during electron irradiation. Still, the rate of destruction of acetic acid is less compared to many other organic species of its class. Unless like acetic acid, the tendency to form hydrogen bonds for methyl formate is very less. But, porosity of methyl formate ice is less when compare to that of acetic acid ice, therefore we conclude that morphology of such ice plays a vital role in determining the survival rate of such molecular ice films.

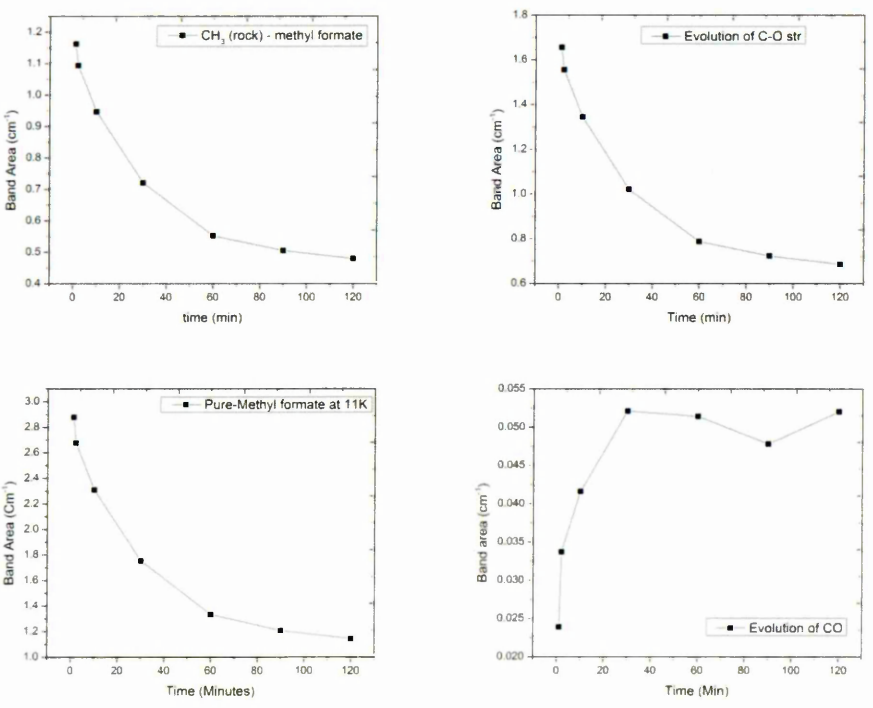

Figure 5.15 Evolution of methyl formate during electron irradiation. Destruction of CH_3 rocking(a) region, $CO_{stretch}$ (b), OH stretch (c), and formation of carbon monoxide (d)

5.4.1 Electron irradiation of crystalline methyl formate

Pure methyl formate (99.5%) vapours are physisorbed onto a ZnSe substrate maintained at 30 K, and the sample was annealed to 115K to synthesise a crystalline methyl formate, the transition temperature of $HCOOCH_3$ is 110 K and the annealed sample was cooled down to 30 K. We found that all the spectral features are stable and we started to irradiate the crystalline sample of methyl formate with 1keV electrons at 10μA flux.

Electron processing of crystalline $HCOOCH_3$ ice film results in the dissociation of bonds in $HCOOCH_3$, but at a lesser rate than for amorphous film, as is clearly evident from the reduction of absorption intensity of C=O stretch and OH bend features.

In case of crystalline ice the sputtering rate is less, however appreciable amounts of CO are produced as a result of the irradiation. The destruction rate of $HCOOCH_3$ follows the energy profile and flux of electrons, but the rate of destruction is less due to the compact nature of the ice.

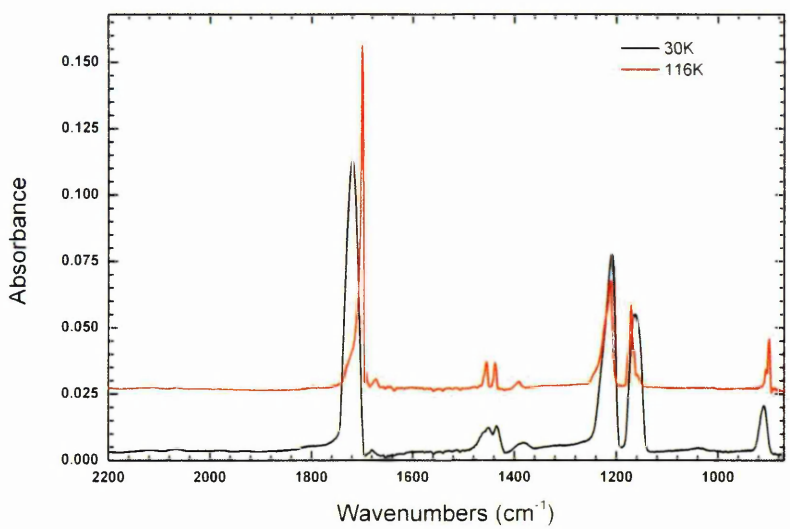

Figure 5.16 An $HCOOCH_3$ ice film at 30 K (black-amorphous) and 116 K (red).

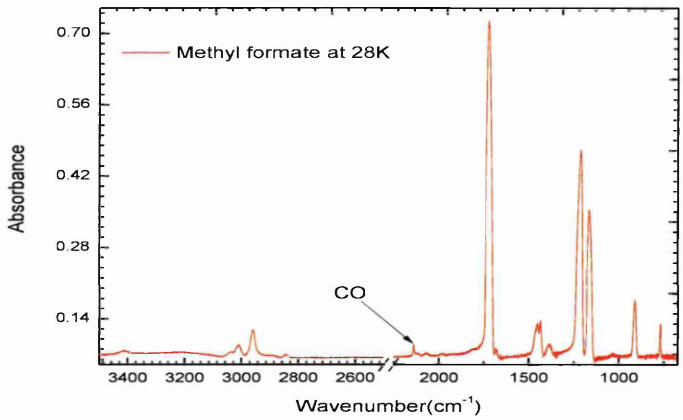

Figure 5.17 CO production from electron processed $HCOOCH_3$ ice film.

From the initial and final column density it is evident that only 10% of original film was processed. **Figure 5.19** show the production of CO from $HCOOCH_3$ and **Figure 5.18** shows the evolution of $HCOOCH_3$ and CO. The rate of destruction of crystalline CH_3COOH ice film is less compared to the amorphous but this experiment support the earlier results, thereby helps to quantify the survival probability of less porous crystalline $HCOOCH_3$.

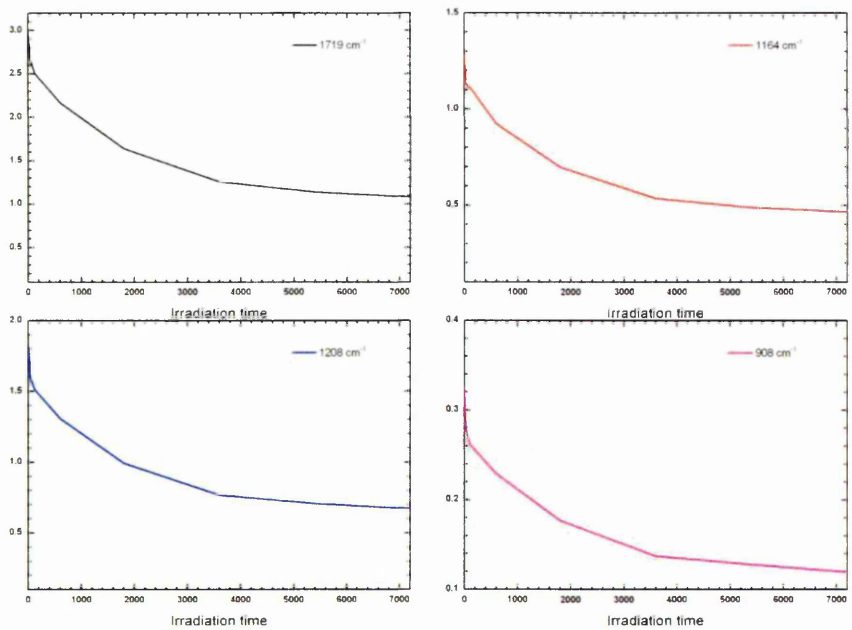

Figure 5.18 Evolution of methyl formate during electron irradiation. Destruction of CH_3 rocking (a) region, $CO_{stretch}$ (b), OH stretch (c), and CH_3 rock (d).

Destruction rate of methyl formate by electrons (energy range 300 to 1000 eV) is less when compared to the sputtering. A large amount of the sample was sputtered at all energies and fluxes. CO formation from the crystalline ice strongly depends on porosity and phase of pure methyl formate ice and even at higher electron flux, formation rate of CO is insignificant when compare to the rate of formation of CO from amorphous porous ice.

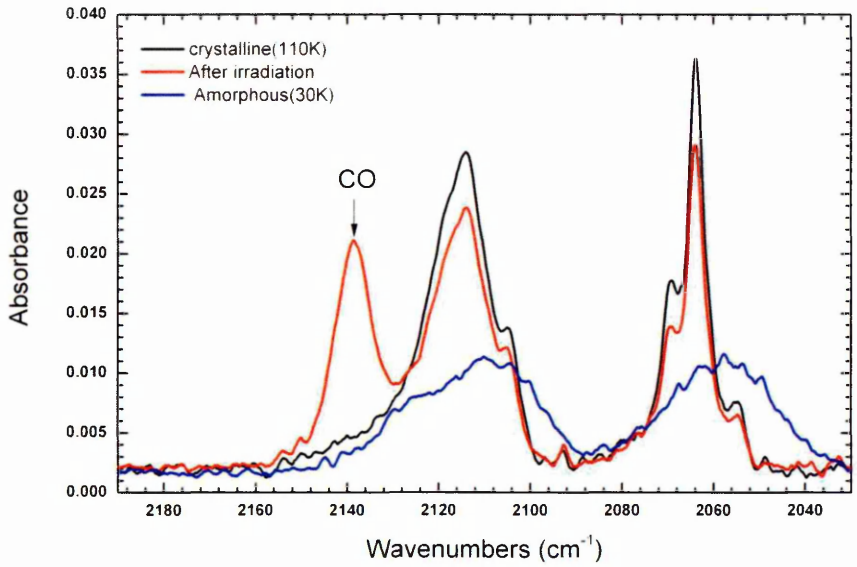

Figure 5.19 Generation of CO from electron processed crystalline $HCOOCH_3$ ice film.

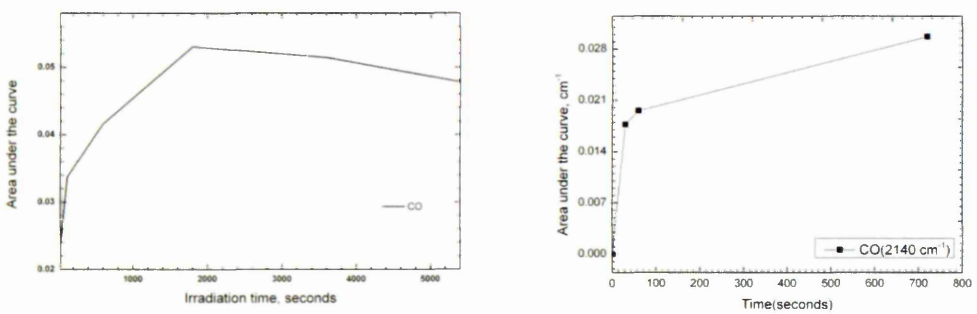

Figure 5.20 Synthesis and evolution of CO from electron processed amorphous $HCOOCH_3$ ice film (left) and amorphous $HCOOCH_3$ ice film (right). The column density of the product was normalized with respect to the thickness of both ice films.

5.4.2 Thermal processing of methyl formate ($HCOOCH_3$)

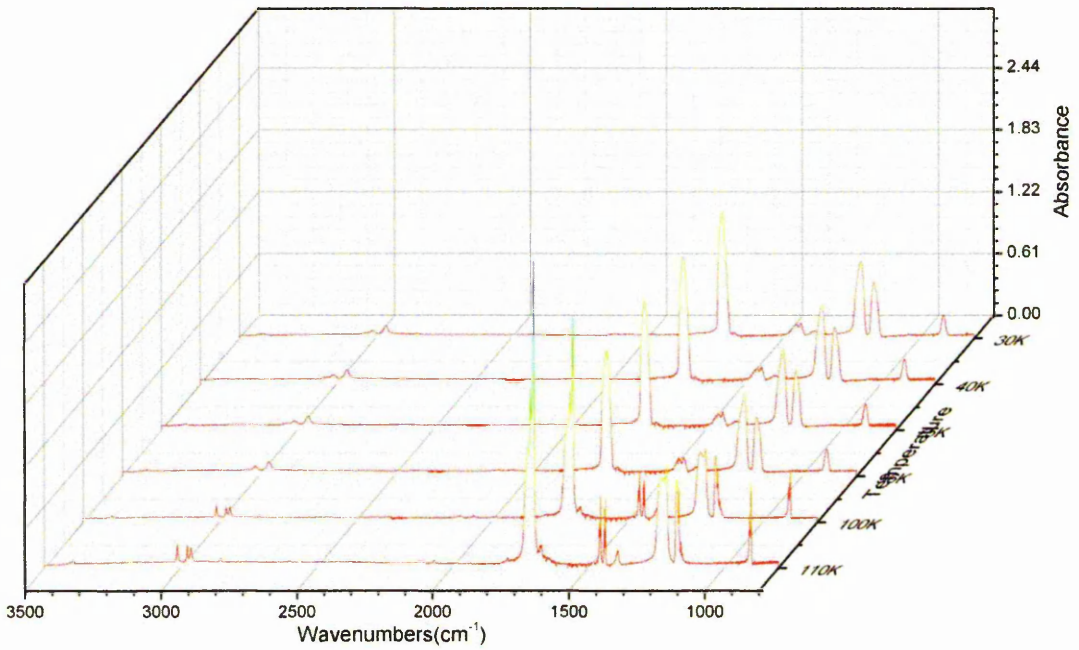

Figure 5.21 Thermal processing of $HCOOCH_3$ ice film. Amorphous $HCOOCH_3$ ice at 30 K was annealed until sublimation. Absorption features at 35 K, 45 K, 70 K, 90 K, 100 K, and 110 K are shown here.

An un-irradiated methyl formate ice film was heated at a rate of 5 K/ min until the sublimation and FTIR spectra were recorded at every step of heating. The FTIR spectrum of $HCOOCH_3$ is rich in absorption features (Figure 5.21 and 5.22), Table 4 reports the main infrared absorption features of methyl formate at 30 K. A broad peak at 3038 cm^{-1} is due to the CH_3 stretching (υ_1), and adjacent peaks at 3010 cm^{-1} and 2959 is assigned to CH_3 ($\upsilon_{2,}\upsilon_{13}$) and CH stretching ($\upsilon_3$) respectively. O-C=O back bone of $HCOOCH_3$ exhibit three strong bands at 1724 , 1212 and 1167 cm^{-1}, 1724 cm^{-1} is due to the C=O (υ_4) stretching vibration and the other two strong bands at 1212 and 1167 cm^{-1} are due to the C−O (υ_9) stretching vibration and the CH_3 (υ_{10}) rocking vibration respectively. The double peak at 1435 and 1450 cm^{-1} is due to the CH_3 (υ_6,

υ_7) deformation. The band at 1381 cm^{-1} is due to C-H (υ_8) bending motion. The two sharp bands at 910 and 768 cm^{-1} are attributed to the O–CH_3 stretching (υ_{11}).

The ice spectrum display features of both form I and form II methyl formate [Katon et al. 1978], even though the ice film shows all absorption features of form II, in addition to absorption features at 1167 cm^{-1} and 1212 cm^{-1}, attributed to form I are also present in our observations. Therefore the resulted film is confirmed as cis-methyl formate ice film [Macoas et al. 2003], which incorporates the absorption features of both form I and form II. Such films of cis-methyl formate has the capability to generate spontaneous electric field of magnitudes $>10^8$ V/m [Plekan et al. 2012].

During annealing the C=O feature at 1724 cm^{-1} started to shift towards lower wavenumber regions, at 95 K the feature shifted to 1720 cm^{-1} and eventually started to bifurcate. At 110 K this feature transformed into two separate and sharp bands at 1710 and 1700 cm^{-1}, these peaks are assigned to C=O stretch. In the same fashion, above 95K, broad-weak absorption bands due to CH_3 deformation at 1450 and 1435 cm^{-1} undergoes splitting and results in sharp well resolved peaks. The band at 1450 bifurcates and forms two sharp peaks at 1458 and 1454 cm^{-1}. The band at 1435 bifurcates to 1439 and 1436 cm^{-1}, a broad feature at 1387 cm^{-1} started to evolve above 90 K and shifted towards higher frequency region and form a relatively sharp feature at 1391 cm^{-1}. Strong absorption at 1211 cm^{-1} due to the C-O stretch is stable throughout the annealing process, even though there is no shift in the peak position of the major band at 1211 $cm^{-1}$the peak is sharpened and evolved into a broad sub feature, which peaks around 1231 cm^{-1}. The feature at 1165 cm^{-1} trifurcates and results in a broad feature at 1174 cm^{-1} and a sharp absorption at 1165 cm^{-1} and 1159 respectively. Absorption features due to O-CH_3 stretch at 910 cm^{-1} and 768 cm^{-1} also

split and results in two sharp bands at 905 cm^{-1}, 899 cm^{-1} and 775 cm^{-1} and 768 cm^{-1} respectively.

Table 5.5 Temperature dependent changes in peak positions of methyl forate

30 K Amorphous	50 K	80 K	100 K	110 K Crystalline
3038	3038	3040	3052	3053
3010	3010	3010	3011	3011
			2975	2975
2959	2959	2960	2961	2961
				2918
				2900
1724	1724	1722	1710	1710
				1700
			1458	1458
1450	1450	1450	1454	1454
			1439	1439
1435	1435	1435	1436	1436
1387	1386	1385	1391	1391
			1231	1231
1211	1211	1211	1211	1211
			1174	1174
1165	1165	1165	1165	1165
			1159	1159
910	910	909	905	905
			899	899
			775	775
768	768	768	768	768

These features are assigned to the in plane and out of plane O-CH_3 stretch [Katon et al. 1978]. Changes in the peak positions of methyl formate during annealing are listed in the Table 5.5 The annealed sample was cooled back to 30 K to confirm the stability of the crystalline features in the spectra. When the temperature is lowered to 30 K, the general features remain similar to the spectrum at 145 K. Successive annealing of the sample to 150 K exhibit the same behaviour, and all the spectral features shown by spectrum 145 K is retained. Upon subsequent heating above 180 K, the ice film starts to sublimates, but there are no characteristic changes exhibited after the phase transition. Therefore, the phase change in the ice film is irreversible.

5.5 Thermal processing of un-irradiated Formic acid (HCOOH)

The FTIR absorption spectrum of HCOOH ice at 30K is shown in Figure 5.22 Complete assignments [Chapman 1956] of these peaks are given in the Table 5.6. The broad feature at 3047 cm^{-1} is due to the OH stretching mode (υ_1) and the absorption feature at 2950 cm^{-1} is the result of the CH stretch and in vapour this feature is present at 2943 cm^{-1}, but due to overlap between the OH region, this feature is not clearly observed. Adjacent overlapping features at 2752 and 2582 cm^{-1} are due to the OH stretching mode (υ_1).

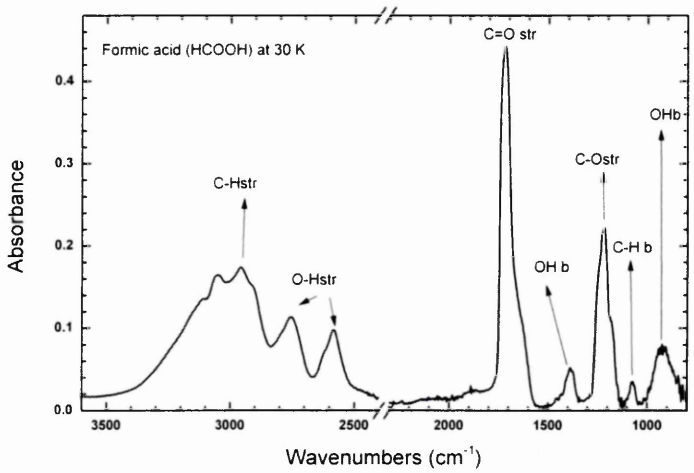

Figure 5.22 Absorption spectra of condensed formic acid at 30 K

Organized dimers and long chains of HCOOH generate various effects in absorption features in this region [Sivaraman et al. 2013; Holtzberg et al. 1953]. The broad, strong absorption feature at 1714 cm^{-1} is from (C=O) stretch (υ_3) and this band is important in astrophysical interest [Bisschop et al. 2007], the OCO back bone generate a feature at 1211 cm^{-1} from the C–O stretch(υ_6). The bending modes are

present of which νB(CH) and νB(OH) at 1073 cm^{-1} and 930 cm^{-1} (9.3 and 10.8 μm), respectively, are out-of-plane.

Table 5.6 Peak positions of condensed formic acid ice film at 30 K

Peak position cm^{-1} (this work)	Assignment	Characterization	Peak position cm^{-1}	A values cm $molecule^{-1}$
			Reference 2	
3047	υ_1	OH stretch		
2950	υ_2	CH stretch		
2750	υ_1	OH stretch		
2580	υ_1	OH stretch		
1703	υ_3	C=O stretch		
1651	υ_3	C=O stretch		
1389	υ_4	CH bend		
1303	υ_5	OH bend		
1212	υ_6	C-O stretch	1224	1.50×10^{-17}
1073	υ_8	CH bend	1073	1.62×10^{-17}
	Out of plane			
932	υ_5	OH bend		
	Out of plane			

The temperature evolution of the HCOOH features in the 3500 -900 cm^{-1} ranges is shown in **Figure 5.23** and changes in the corresponding peak positions are given in Table 5.7 Most features are broad and consist of multiple components at 30 K. Above 100K absorption features due to (C=O), (C-O) stretch and (CH) bend at 1703, 1212, and 1375 cm^{-1} split into two components.

Table 5.7 Shift in the IR band positions of condensed methyl formate during annealing

Peak positions(cm^{-1})				
30 K **Amorphous**	50 K	80 K	100 K	110 K **Crystalline**
3038	3038	3040	3052	3053
3010	3010	3010	3011	3011
			2975	2975
2959	2959	2960	2961	2961
				2918
				2900
1724	1724	1722	1710	1710
				1700
			1458	1458
1450	1450	1450	1454	1454
			1439	1439
1435	1435	1435	1436	1436
1387	1386	1385	1391	1391
			1231	1231
1211	1211	1211	1211	1211
			1174	1174
1165	1165	1165	1165	1165
			1159	1159
910	910	909	905	905
			899	899
			775	775
768	768	768	768	768

The splitting of the (C=O) and (C–O) bands are due to the out-of-phase and in-phase motions of different HCOOH molecules within the same chain, out-of-phase motions absorb higher frequencies, when compared to the in-phase motions[Chapman 1956, Holtzberg et al. 1953].

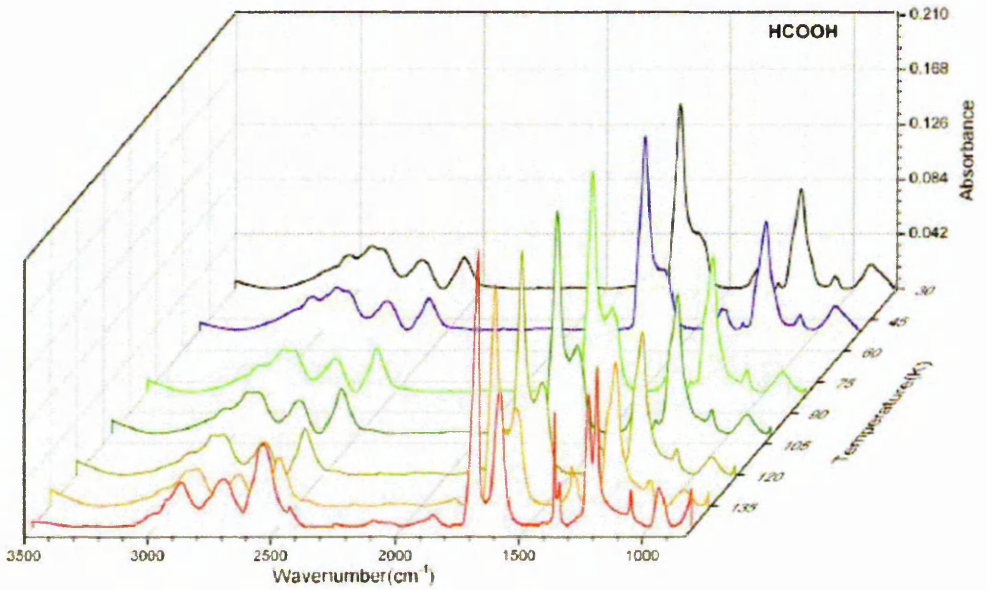

Figure 5.23 Temperature induced morphological changes of formic acid at 30 K, 50 K, 80 K, 100 K, 115 K, 135 K and 145 K respectively.

Features due to in-plane bending modes of OH and CH forms a convolved band at 30 K, but it is clearly observed that this band bifurcates and forms two separate peaks, at higher temperatures. The structure of crystalline formic acid has been investigated by X-ray diffraction [Holtzberg et al. 1953], calculation and modelling [Bowman et al. 2001] and hence the splitting of these absorption features are assigned to conversion of HCOOH dimers to HCOOH organized in chains [Cyriac and Pradeep 2005; Flakus 2006]. The long chain like structure of formic acid [Holtzberg et al. 1953] is shown in Figure 5.7, infrared bands in the region 3100 to 2400 cm^{-1} reveals the nature of ice film, upon deposition, the bands at 2956, 2752 and 2582 cm^{-1} were broad and convolved, and due to combination of dimer and organized aggregates of dimers, above 90 K aggregates and dimers reorganize to form long polymerised chain of formic acid with an orthorhombic unit cell structure [Holtzberg et al. 1953]. Absorption bands in 3100 to 2400 cm^{-1} region evolves with temperature,

above 90 K intensity of absorption increases considerably and this confirms the amorphous to crystalline transition.

5.6 Electron irradiation and temperature dependent infrared absorption studies of condensed (NO) ice films.

5.6.1 Introduction

Nitric oxide (NO) is an important gaseous species in terrestrial atmosphere and plays a key role in ozone depletion chemistry [Sivaraman et al. 2008]. It also plays a key role in acid rain and smog formation [Sivaraman et al. 2008]. NO is a stable free radical (open shell electronic structure), the molecular structure, and possible pair formation pathways of nitric oxide is shown in Figure 5.24. NO plays an important function in human body as a nitrogen regulator in nervous system [Sivaraman et al. 2008]. Oxides of nitrogen are very common in terrestrial atmosphere, in addition, NO has also been detected in interstellar medium towards- Sgr B2 [Liszt et al. 1978], and in OMC-1Cold dark cloud (L134N) [Liszt et al. 1978].

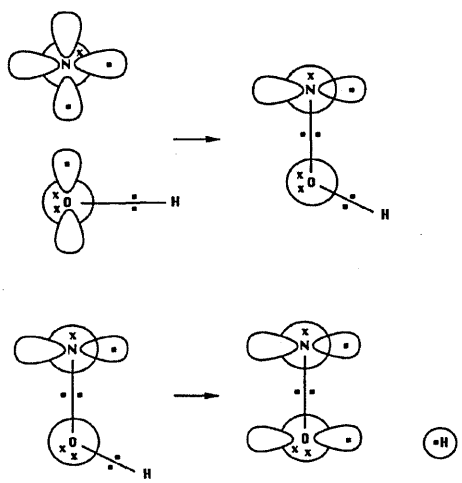

Figure 5.24 Formation of nitric oxide (NO) in ISM and its radical nature [Figure adapted from Prasad et al. 1980].

Experiments were carried out using astrochemistry apparatus at The Open University (section 3.9). Using closed cycle helium refrigeration the sample substrate was cooled down to 30 K while the apparatus was maintained at 8.0 x 10^{-10} mbar pressure. A chemically inert and mid-infrared (2-25 μm) transparent Zinc Selenide (ZnSe) window was used as the substrate onto which NO (99.98 % Fisher Scientific) was deposited at 11.5 K. Electron irradiation was carried out for 60 minutes at an energy of 1keV and 10 μA current. An FTIR spectrometer operating in transmission mode with external MCT-HD detector was employed to record spectra in-situ, during, before and after irradiation processes.

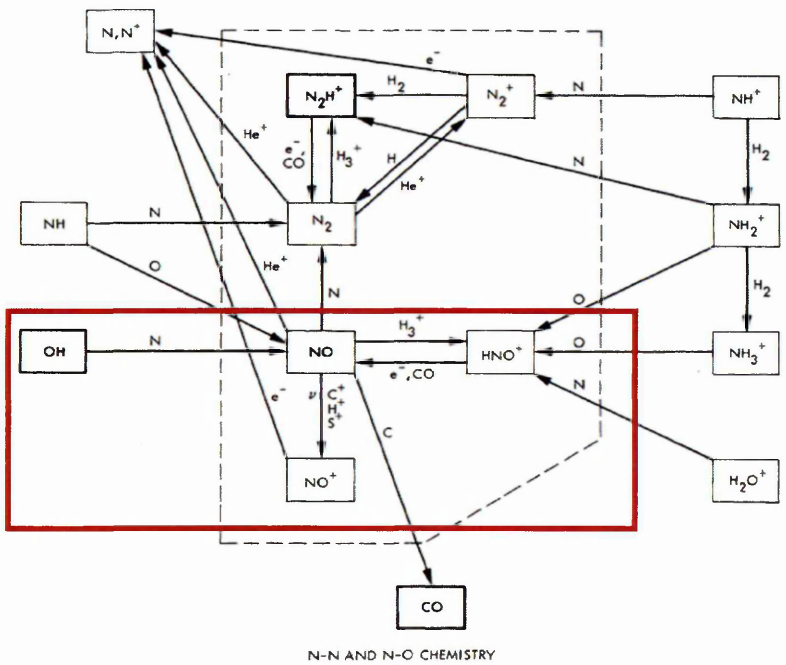

Figure 5.23 Nitrogen chemistry in ISM; formation and evolution on NO through interaction with ion-molecule reactions and neutral-neutral reactions in gas phase is shown in figure [Prasad and Huntress 1980].

The most probable interstellar formation pathway of NO is through gas phase neutral-neutral or ion-molecule reactions shown in Figure 5.22 and 5.23, as being a free radical NO can undergo several oxidation reactions and either transform to higher oxide forms such N_2O, NO_2, N_2O_2 etc or NO^+ ion or disintegrate into stable molecules

such as N_2. The evolution pathways on NO is crucial for the balance of nitrogen in interstellar environments, it is very important in terms of a diagnostic tool in cloud cores [2] since nitrogen species remain in gaseous phase even at very low temperature conditions (~10 K).

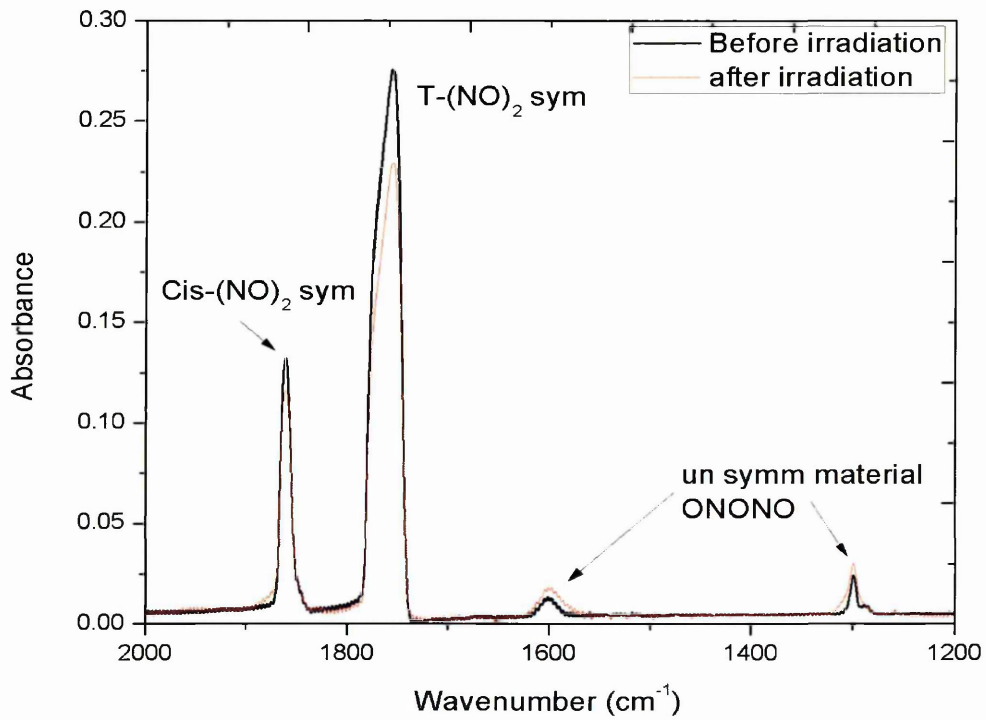

Figure 5.24 Absorption spectra of nitric oxide (NO) at 11.5 K. Spectrum before (black) and after (red) electron irradiation with all characteristic absorption features are shown here.

In order to observe this ion chemistry, we need to maintain laboratory temperature conditions below 20 K, since above this temperature the radicals gain energy and 'hop' through the ice surface and disintegrate to components. Charging of ice surface also plays a vital role. The probability of forming radicals and ions from NO is thus very high and to observe significant chemical changes we should investigate them under stable conditions. All NO experiments were carried out at

temperatures below 11.5 K. Since N_2 is an IR inactive species we notice the change through the availability of signature through the presence of nascent N and O atoms to be available upon irradiation.

Gas phase evolutionary pathways of NO are listed here,

$$NO + NH_2 \rightarrow N_2 + H_2O \quad (5.9)$$

$$NO + H^+ \rightarrow NO^+ + H \quad (5.10)$$

$$NO + S^+ \rightarrow NO + S \quad (5.11)$$

NO can also be formed through gas-grain interactions [5] and path ways such as the following are potential sources of nitrogen species in PDRs and hot cores [2].

$$NH + O \rightarrow NO + H \quad (5.12)$$

$$HNO + e \rightarrow H + NO \quad (5.13)$$

$$HNO^+ + CO \rightarrow HCO^+ + NO \quad (5.14)$$

$$HNO^+ + N_2 \rightarrow N_2H^+ + NO \quad (5.15)$$

5.6.2 Electron irradiation

Absorption spectra of NO at 11.5 K show (Figure 5.24) characteristic absorption due to cis-$(NO)_2$ and trans-$(NO)_2$ and high dimer formation in NO lead to both cis and trans forms. Absorption peaks due to ONO and NO features are also depicted in the spectrum.

Electron irradiation of NO deposited at 35 K does not yield any significant chemical change in the spectra. Other than reduction in the intensity of peaks, due to electron induced desorption (very low rates), no other changes are noticed. We

irradiated the sample for additional 60 minutes to monitor and understand the electron fluence effect, but it is observed that there were no significant chemical changes even after the second round of irradiation. In the second round of experiments NO was deposited onto ZnSe maintained at 11.5 K to ensure the stability of radicals.

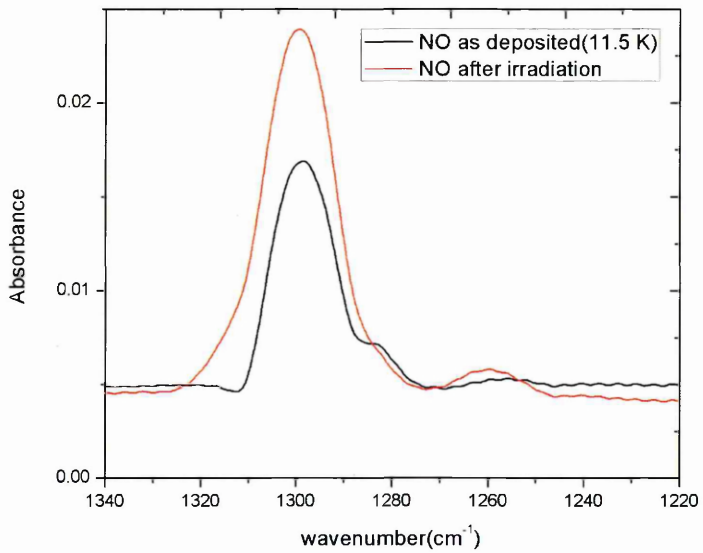

Figure 5.25 Formation of N_2O from electron processed NO ice film at 11.5 K

In contrast upon electron irradiation of amorphous NO at 11.5 K three new peaks were observed at 2228 cm^{-1}, 1872 cm^{-1} and 1740 cm^{-1}, these correspond to N_2O, N_2O_3 and N_2O_5, respectively. Further peaks at 1591 cm^{-1} and 1641 cm^{-1} N_2O_3, and N_2O_4 respectively. Warming up the irradiated sample was found to release the trapped NO_2 when the ice temperature reaches around 50 K, with subsequent loss of NO at about 60 K and the presence of N_2O_4 was observed until 120 K. However, the dissociation pathway that leads to such new products, upon keV electron irradiation, need to be deduced.

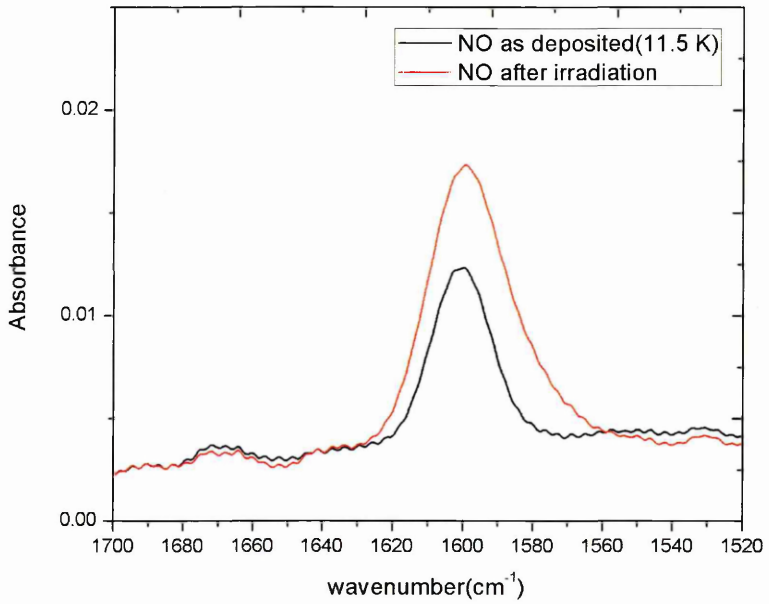

Figure 5.26 Formation of N_2O_4 from electron processed NO ice film at 11.5 K.
Due to the weak bond between N–N in the $(NO)_2$ dimer provides a source for NO monomers.

Atomic oxygen reacts with the NO monomer to produce NO_2 and NO_2 is efficiently converted into heavier molecular products by further reaction with NO, and hence results in products such as

$$NO + O \rightarrow NO_2 \qquad (5.16)$$

$$NO_2 + NO \rightarrow N_2O_3 \qquad (5.17)$$

$$2NO_2 \rightarrow N_2O_4 \qquad (5.18)$$

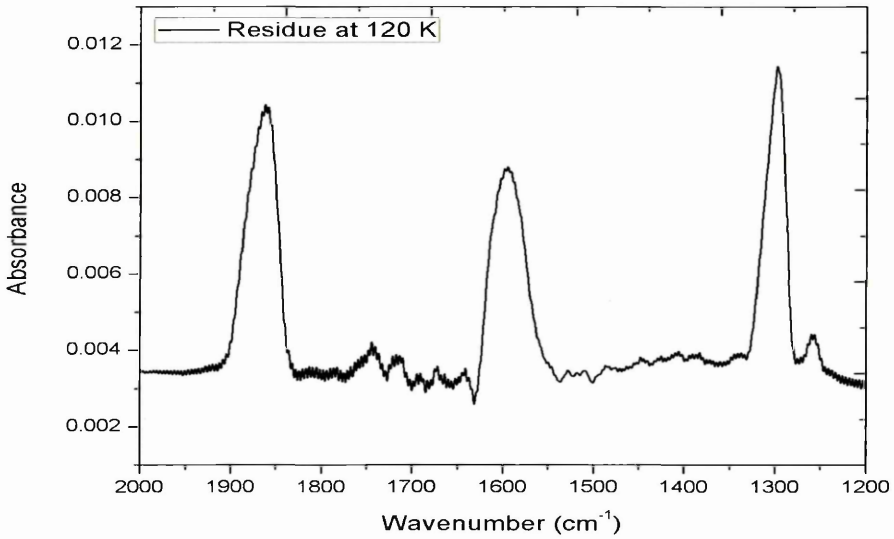

Figure 5.27 Residue of electron processed NO ice. Significant amount of residue at 120 K consist of higher oxides such as N_2O, N_2O_4, N_2O_5 etc.

The experiment was repeated for various thicknesses to check the effect of secondary electron production from the interface of substrate and sample. But it is observed that the same products are observed irrespective of the sample thickness.

Table 5.8 Band positions of newly formed species during and after electron processing of NO ice.

Products Band position(cm^{-1})	Assignments (Molecule)	References
2228	N_2O	1
1872	N_2O_3	1
1741	N_2O_5 or N_2O_4	2
1591	N_2O_3	1
1641	N_2O_4	1
1305	N_2O_3	1
1260	N_2O_4	1
1295	N_2O_3	1

1; Fateley 1959; 2. Sivaraman et al. 2008

The electron processed ice film was processed thermally to investigate the effect of external perturbation on to an ion rich ice, and it is observed that there are significant changes. The product evolution during the thermal process is shown in **Figure 5.27** and **5.30** and all the observed peak positions are listed in the table 5.8.

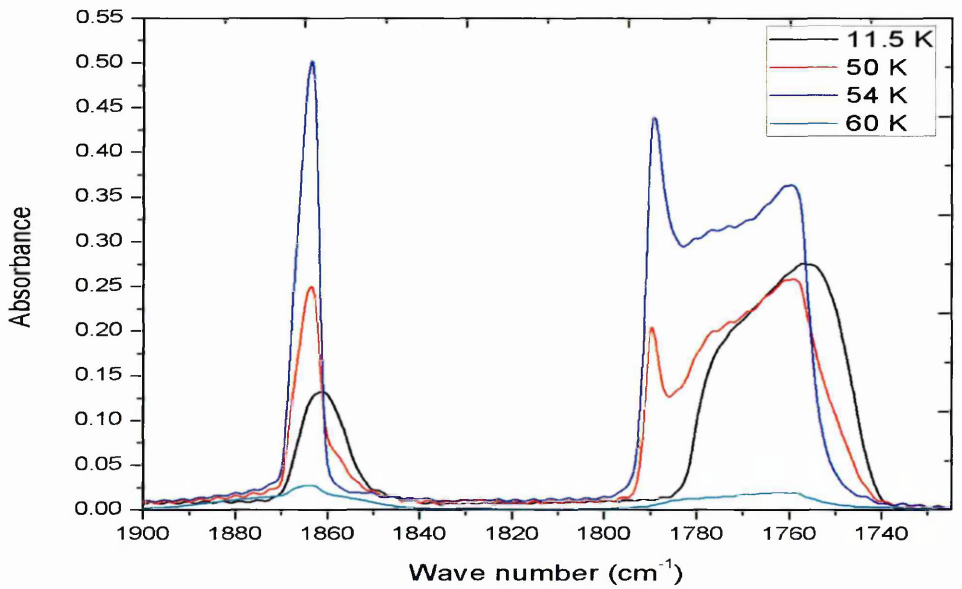

Figure 5.28 Thermal processing of electron irradiated amorphous NO ice.

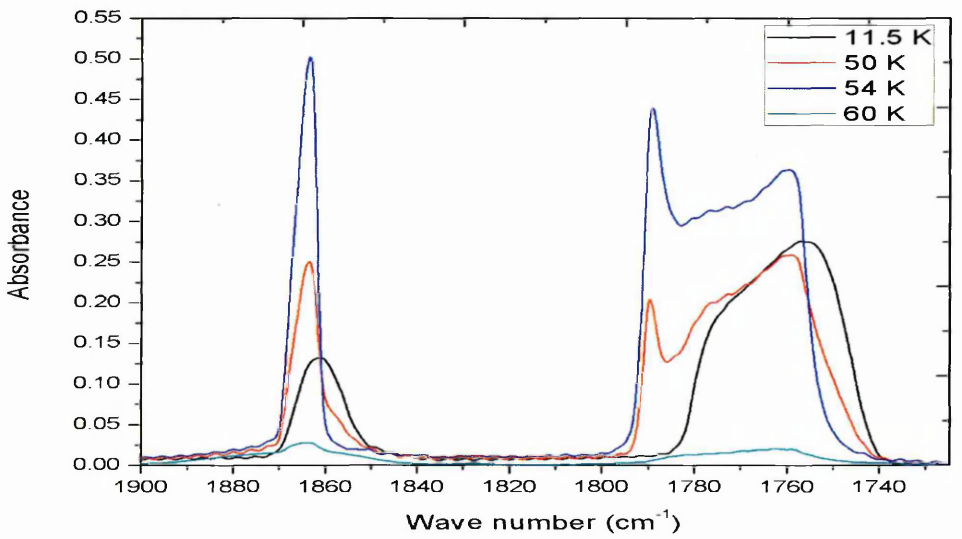

Figure 5.29 Amorphous to crystalline transition of NO ice film.

N_2O_5 is the heaviest molecule that was observed and a possible formation pathway is through O_3 formation [Sivaraman et al. 2008].

$$2NO_2 + O_3 \rightarrow N_2O_5 + O_2 \qquad (5.19)$$

However in our experiment we didn't observe the O_3, this may be due to the fact that products follow a specific pattern and as shown in Figure 5.30, dimers of NO interact and form NO_2, and N_2O_2, later leading to the higher oxides of nitrogen.

Electron irradiation of crystalline NO ice is also investigated under the same conditions. Even though the ice was compact, it is observed that the same products are formed; however the production rate and amount of products were significantly less compared to the amorphous ice experiments.

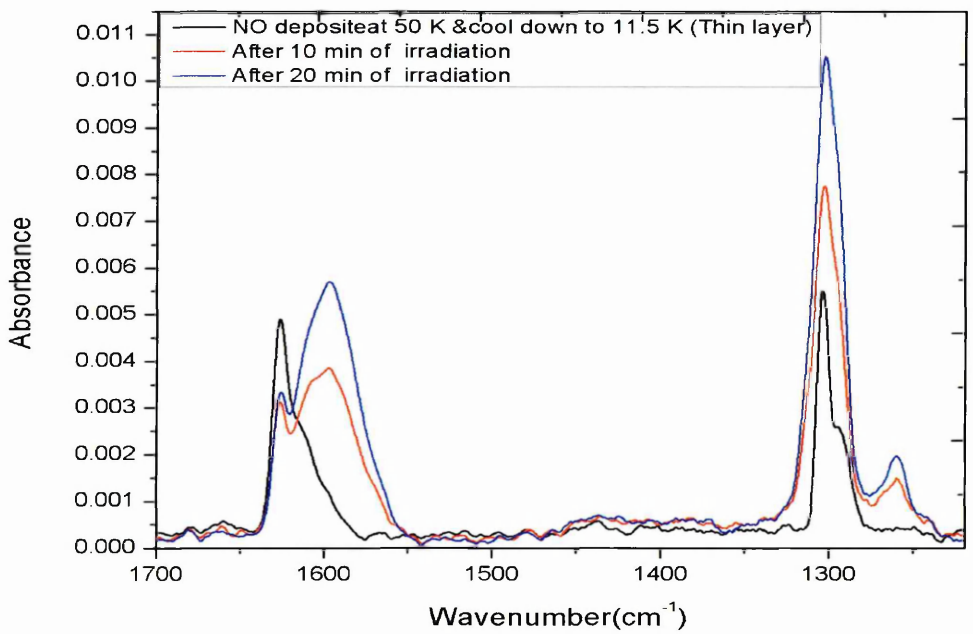

Figure 5.30 Production of NO_2 and N_2O from NO ice film (deposited at 50 K and maintained at 11.5 K) during 1 keV electron irradiation.

Temperature processing of un-irradiated NO ice was carried out to find out the phase transition temperature of this ice. It is found that during warm-up it is found that ice is stable and maintains its amorphous nature until 30 K and started to change slightly after that, between 35 and 40 K the transition begins and started to crystallise. Crystalline structure is stable until 60 K and beyond this temperature ice starts to sublimates and desorbs from the surface.

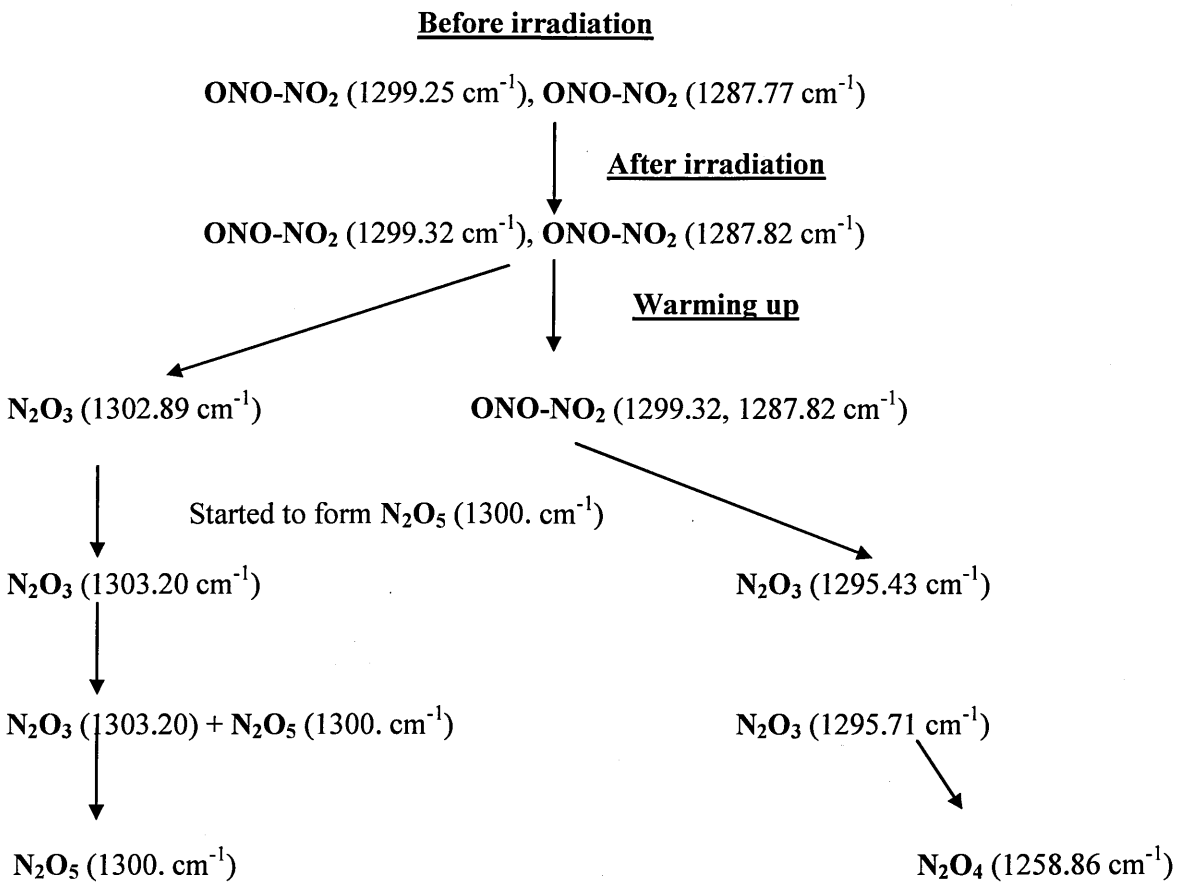

Figure 5.31 Evolution of $ONO-NO_2$ during the irradiation and thermal processing of NO ice films

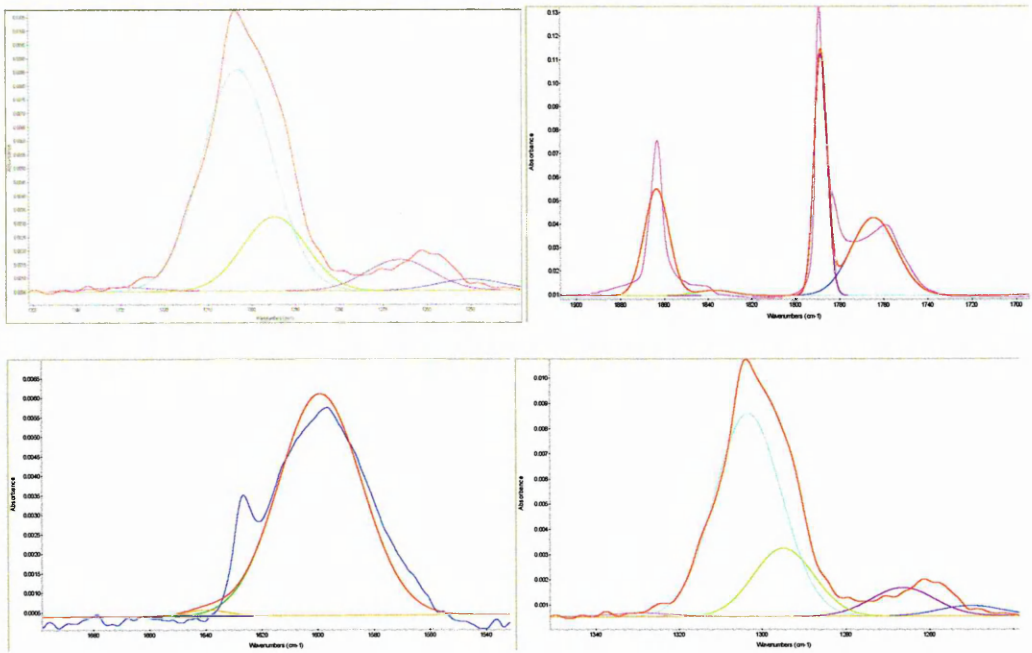

Figure 5.32 (a) Gaussian fit of newly observed peaks in NO ice films.

Table 5.9 Effects of thermal processing on pure, unirradiated NO ice film.

Before Irradiation	After Irradiation	11.5 K	20 K	35 K	40 K	60 K	70 K	80 K	100 K	120 K
2234	2234	2234	2234	2234	2238	2239	2244	2244	2244	
1861	1861	1861	1861	1863	1864	1864	1864	1864	1864	1864
1755	1755	1755	1755	1758	1759	1762	1762	1762	1760	1758
				1790	1787	1787	1786	1785	1785	1785
					1841	1841	1841			
								1596	1600	1600
2234	2234	2234	2234	2234	2238	2239	2244	2244	2244	2244
1861	1861	1861	1861	1863	1864	1864	1864	1864	1864	1864
								1303	1304	1306
								1296	1295	1296
								3509	3509	3509
								2581	2581	2581

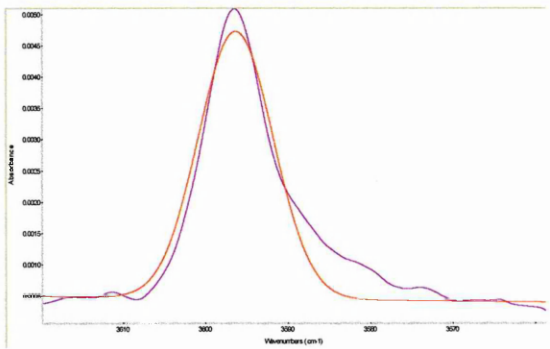

Figure 5.32 (b) Gaussian fit of newly observed peaks in NO ice films.

Table 5.10 Parameters of Gaussian fits for newly formed peaks in NO ice spectrum.

	Peaks position (cm^{-1})	Area Linear (Gaussian)	Area (G-L)	Area None (Gaussian)	Area Constant (Gaussian)	Area Quadratic (Gaussian)	Area Cubic (Gaussian)
1	1863.702	0.4960	0.6465	1.2409	0.5247	0.4907	0.4936
2	2233.411		0.1169				
3	1827.799		0.658	0.3010	0.0672		0.0213
4	1266.338	0.214					
5	1294.922	0.493					
6	1303.352	0.1625					
7	1599.045	0.2101					
8	1639.777	0.0030					
9	3596.299	0.0484					

Electron irradiation of a 11.5 K sample of NO ice has been shown to generate a rich chemistry with the synthesis of large number of nitric oxides from N_2O up to N_2O_5 being formed from intermediate product such as NO, NO_2 and O_2. Surface formation routes of oxides of nitrogen and other nitrogen bearing species is very efficient. Nitrogen oxides can further react with CO and H_2O and form complex organic molecules through grain surface processes.

5.7 Methanol mixtures

Preliminary results of electron irradiation of pre-mixed co deposited mixtures of methanol based ice films are discussed in this section. To investigate the influence of methnol in interstellar ices, and to verify the chemical pathways that is mediated by methanol or non-polar molecules it is necessary to perform such experiments. H_2O is the major component of all observed interstellar ices [Tielens 2006] but CH_3OH also

play a vital role in such chemistry, being polar in nature water has specific ways of forming and associating with other molecules, to understand the influence of polar and non-polar chemistry in ISM it is necessary to investigate the energetic processing of methanol based ice films.

5.7.1 Electron irradiation and temperature dependent infrared spectroscopy of condensed mixture of CH_3OH+NO [1:1] ice films

Using the astrochemistry apparatus (section 3.9) at The Open University, a 1:1 mixture of CH_3OH and NO was prepared and deposited through back ground deposition. Pure CH_3OH (99.5 %, Sigma-Aldrich) and CO_2 (99.99%) was premixed in a clean glass bulb, and this premixed vapour introduced into the UHV chamber through a precision leak valve system at 1 Langmuir rate. The vapour was allowed to condense on to the ZnSe substrate maintained at 28 K. All procedures described for pure ice film synthesis is also repeated again to calibrate the film thickness and to quantify the column density. A ~ 347 ± 25 nm thick ice film was created and it corresponds to a column density of ~ 6.3 x 10^{18} molecules cm^{-2}.

This ice film was processed with electrons of energy 1keV at 10 μA for 60 minutes. A transmission mode FTIR spectrum was recorded after every 5 minute interval of irradiation at normal incidence to the ice film. After electron processing the sample was kept undisturbed for 30 minutes and monitored by recording an FTIR spectra, then the sample was subsequently undergone thermal processing at 5 K/minute steps. An FTIR spectrum was recorded at every stage of thermal processing and continued the processed until the sublimation temperature of CH_3OH+NO [1:1] ice.

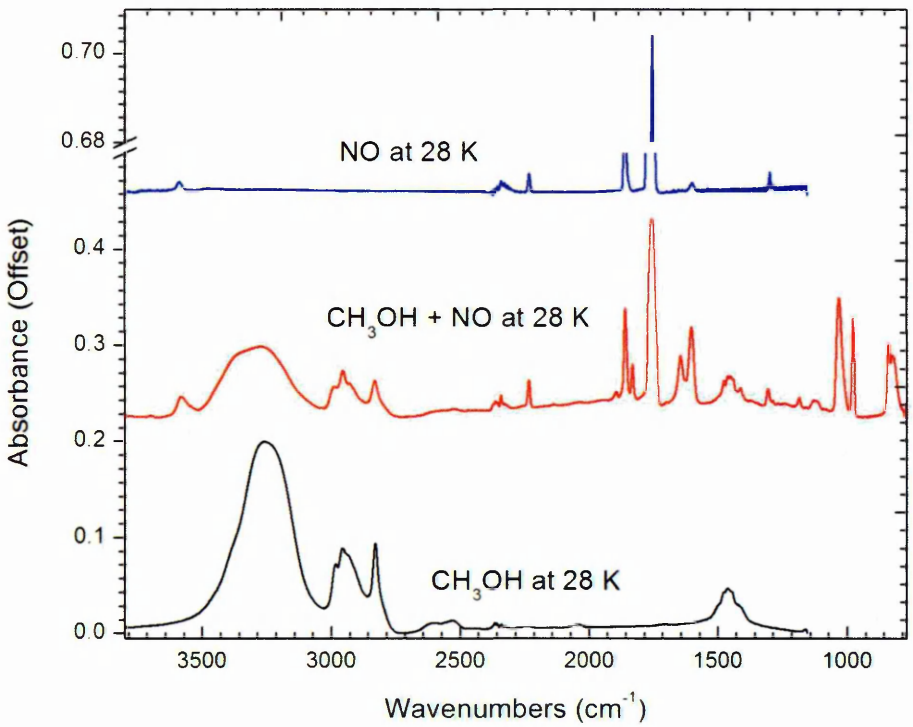

Figure 5.33 Absorption spectra of pure NO ice film at 28 K, CH_3OH+NO [1:1] ice film at 28 K and, pure ice film of CH_3OH at 28 K.

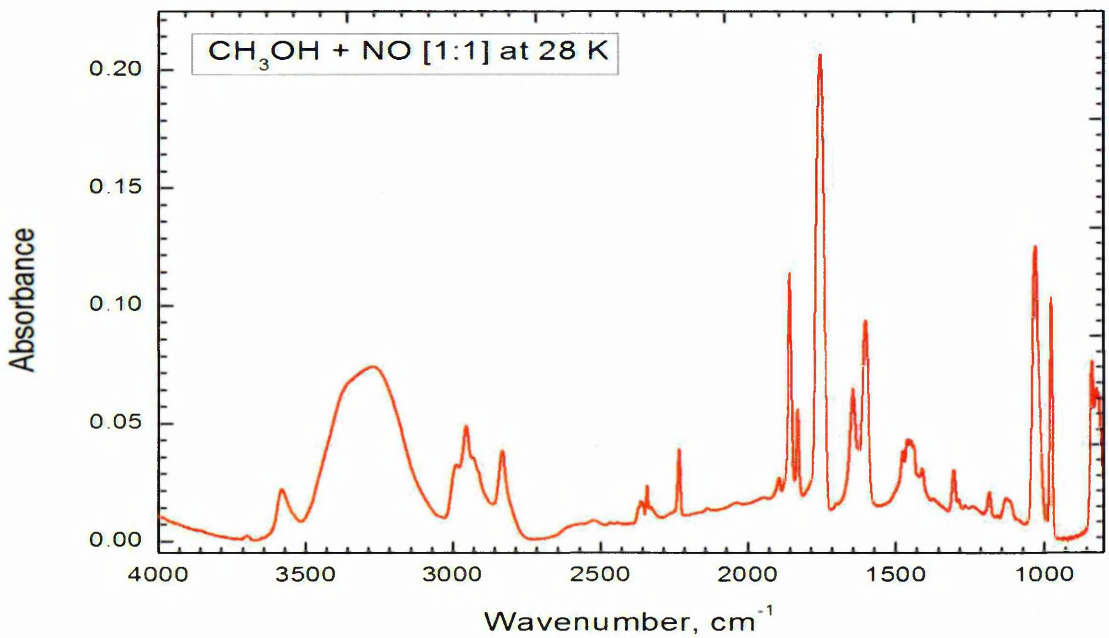

Figure 5.34 Absorption spectra of electron processed CH_3OH+NO [1:1] ice film at 28 K

An absorption spectrum of irradiated ice film is shown in Figure 5.33. Upon electron irradiation of amorphous CH_3OH+NO [1:1] ice at 28 K three new peaks were observed at 3585 cm^{-1}, 3491 cm^{-1} and 2343 cm^{-1}, these correspond to CHN, HNO_2 and $C_2N_2O^+$ respectively [50,51,52]. Further peaks at 2234 cm^{-1}, 1861 cm^{-1}, 1776 cm^{-1}, 1755 cm^{-1} and 1299 cm^{-1} assigned to C_2N_2O, and HNO_3, N_2O_3, NO_2, N_2O_5 and N_2O_4 respectively. In addition there are three more peaks with less intensity, at 1286 cm^{-1}, 2044 cm^{-1} and 1043 cm^{-1} assigned to N_2O_3, C_2O and O_3 respectively. The newly observed peaks are listed in table 5.11.

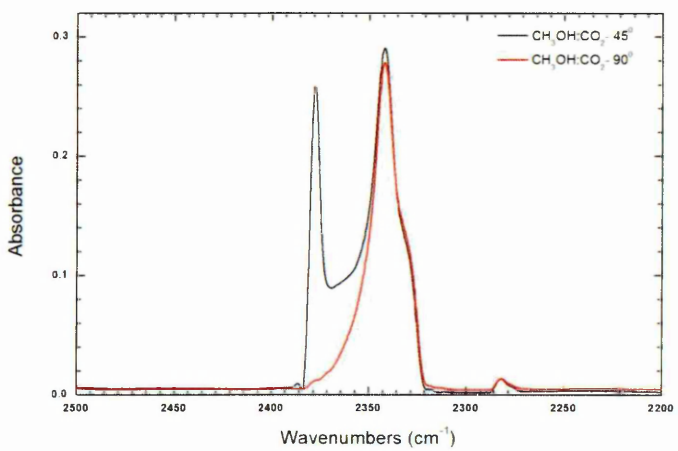

Figure 5.35 Absorption spectra of electron processed CH_3OH+NO [1:1] ice film at 28 K. The longitudinal and transverse mode of CO_2 is clearly observed at 45^0 and 90^0 degrees.

Evolutions of newly formed products with irradiation time are shown in Figures 5.40 and 5.41. CO at 2141 cm^{-1} is a major product of the process; efficiency of production of CO from CH_3OH+NO is high when compared to CO production from irradiation of pure CH_3OH. Production of C_2O at 2044 cm^{-1} is also noted, C_2O is synthesized at an exponential rate and it is stable throughout the irradiation process (Figure 5.39).

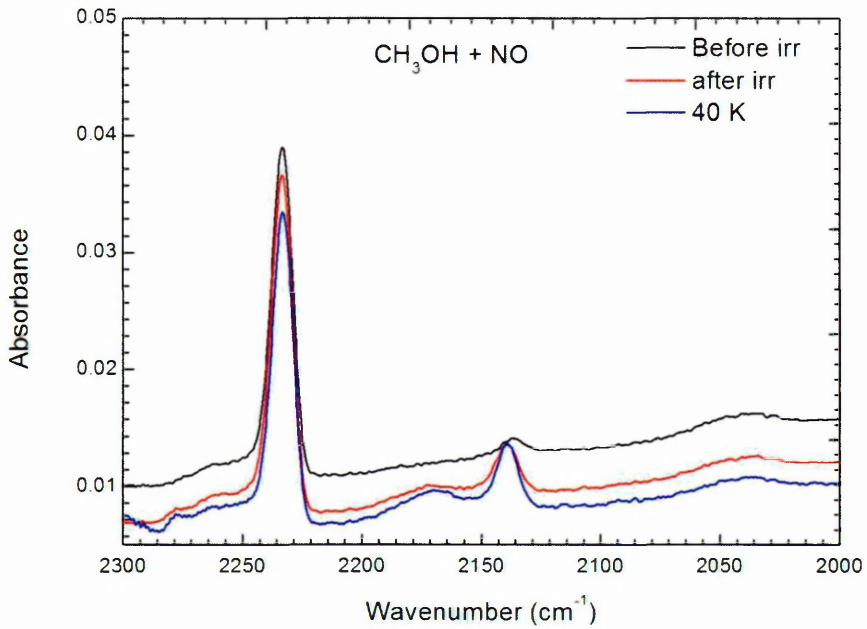

Figure 5.36 Absorption spectra of electron processed CH_3OH+NO [1:1] ice film at 28 K. The longitudinal and transverse mode of CO_2 is clearly observed at 45^0 and 90^0 degrees.

Other important product is O_3, peak at 1043 cm^{-1}, evolution of O_3 is complex when compared to the other products (Figure 5.41). Column density of O_3 increases until 40 minutes and then decreases to wards the end of irradiation process; after the electron processing of the ice film, observed amount O_3 is stable. Reduction of O_3 may due to the electron impact dissociation or due to further reaction with oxides of nitrogen. Products which are oxides of nitrogen follow liner rate of production and the destruction rte of major components in terms of reduction of areas under the IR absorption peaks are shown in Figure 5.39.

Table 5.11 Band assignments of products after electron irradiation of CH_3OH+ CO_2 [1:1] ice films.

Products Peak positions (cm^{-1})	Peak position in reference spectra [1, 2, 3,4,5] (cm^{-1})	Assignments
3585.93	3583	CHN
3491.65	3591	HNO_2
2343.20	2345	$C_2N_2O^+$
2234.06	2233	C_2N_2O
2044.77		C_2O
1861.01	1861	t-$(NO)_2$
	1861	N_2O_3
	1861	ONO-NO_2(D)
1776.45	1776.3 (υ_5 Stretching)	c-$(NO)_2$
1755.73	1752	N_2O_5 or t-$(NO)_2$
	1757	N_2O_4
1601.06	1601	HNO_3
	1596 (υ_2)	N_2O_3
1299.46	1299	ONO-NO_2(D)
	1298	t-HONO
1286.87	1290	ONO-NO_2(D)
	1291	ONO-NO_2(D)
1043.57		O_3
1318	1318	$^{14}NO_2$
1298	1298	N_2O_3

1. Sivaraman et al. 2008; 2. Lapinski et al. 2001; 3. Jamieson et al. 2005; 4. Fateley et al. 1959

Due to several overlapping peaks of nitrogen oxides it was difficult to resolve the components. Gaussian fitted peaks of such species are shown in **Figure 5.37**. All the peaks are fitted for best fit parameters and the column density of all the significant products are quantified and studied.

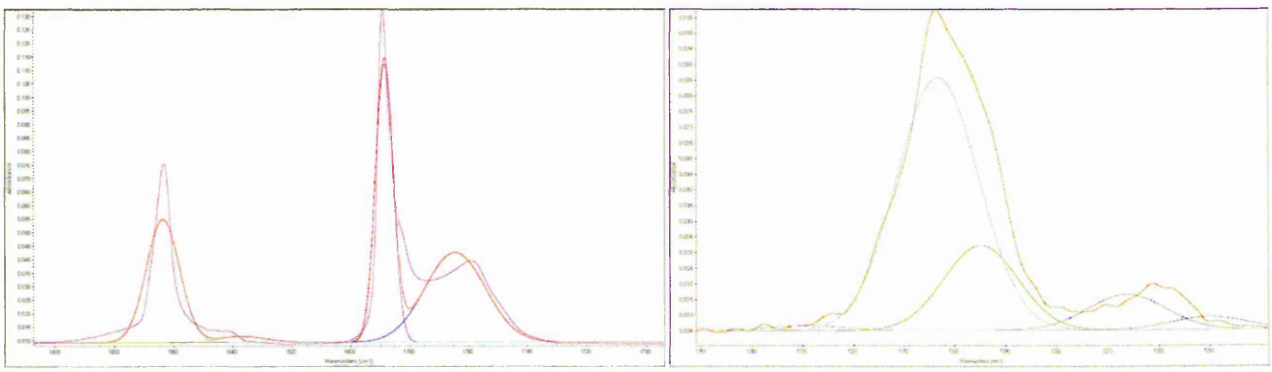

Figure 5.37 Gaussian fits of newly observed peaks in the electron processed CH_3OH+NO [1:1] ice film.

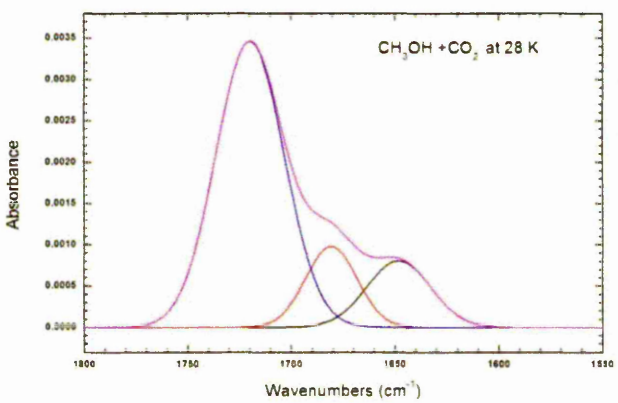

Figure 5.38 Gaussian fits of H_2CO peaks in the electron processed CH_3OH+NO [1:1] ice film.

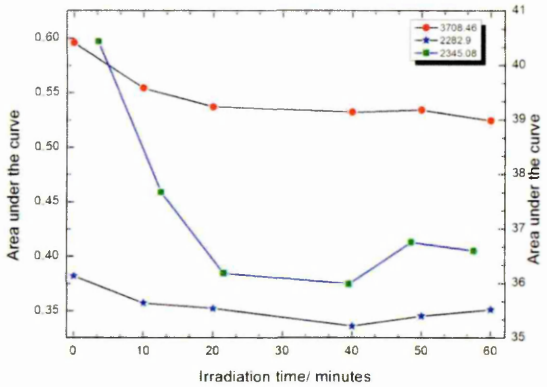

Figure 5.39 Evolution of characteristics peaks of CH_3OH+NO [1:1] with electron processing.

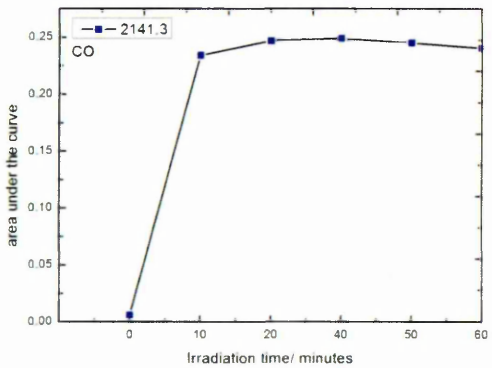

Figure 5.40 Production of CO with electron processing of CH_3OH+NO [1:1] ice film.

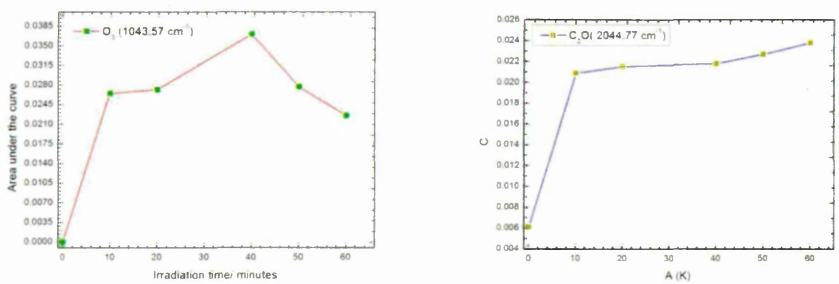

Figure 5.41 Production of O_3 and C_2O with electron processing of CH_3OH+NO [1:1] ice film.

Warming up the irradiated sample was found to release the trapped O_3 when the ice temperature reaches around 50 K, with subsequent loss of NO at about 60 K abut N_2O_5 and all other newly formed species were stable until 130 K. However above 160 K the majority of nitrogen oxide species disappears and the carbon species

and HNO_2, HNO_3 remain. HNO_2 is stable until 180 K and all the residues except C_2O and HNO_3 sublimate above 200 K.

5.8 Conclusions

Electron processing of condensed ice films of pure and binary mixtures of simple molecules provides an insight into the electron driven chemistry in interstellar medium. In this thesis competition between different channels of electron driven processes are investigated and verified.

Solid formamide was prepared by depositing gaseous formamide onto a substrate cooled to 30 K. Infrared spectra were recorded after deposition and showed several peaks of an amorphous formamide ice. Annealing the sample to higher temperatures revealed several spectral changes and the emergence of several new bands. The shifts observed in the NH_2 asymmetric and symmetric stretching vibrations were much larger than shifts observed in the other vibrations. However, all the vibrational modes were observed to have shifted in the spectra recorded at 165 K which indicated a phase change in the sample between 155 and 165 K. Changes in the spectral signature of NH_2 vibrations (υ_1, υ_2 and υ_5) were observed until 210 K. The spectra recorded by re-cooling the annealed sample to 30 K, showed the phase change to be irreversible. The spectral changes that took place before and after the phase transition may be attributed to the association of formamide monomers to form dimers (and polymers) and also the rearrangement between formamide dimers under the action of temperature. Therefore both morphological changes as well as the rearrangement between formamide dimers have taken place in the solid formamide ice that was deposited at 30 K and annealed to 210 K. Such morphological changes may

also occur when formamide ice is processed in the interstellar medium and star forming regions either by shock or local heating, changes that may be identified by the new telescopes (e.g. ALMA).

Electron irradiation of formamide resulted in formation of OCN^-, H_2CO, CO, CO_2 etc. Our study resulted in the proposing of a new pathway of formation of OCN^-. And the thermal processing of irradiated and unirradiated formamide ice revealed the complex nature of morphology of formamide ice and revealed the formation of dimers and other confirmers.

Electron irradiation and thermal processing of methyl formate and acetic acid was investigated to understand the discrepancy of observed abundance of these species in the ISM. It was observed that methyl formate is highly stable in interstellar conditions due to the morphology of the ice film as well as due to the molecular interactions between the molecules. Therefore survivability of condensed methyl formate is high compared to that of its structural isomers.

Electron irradiation of nitric oxide was investigated under different temperature conditions to understand the influence of the formation and stability of radicals in such systems. Irradiation at 30 K and 11.5 K produced entirely different results and is attributed to the influence of radicals. Several set of oxides of nitrogen are formed as a result of electron processing. However, the absence of O_3 was noted, in these studies compared to earlier work. Thermal evolution of newly formed products were also studied, thermal processing of an unirradiated nitric oxide sample reveals the phase transformation. The transition temperature of nitric oxide ice was determined to a high degree of accuracy.

Electron irradiation of amorphous CH_3OH+NO [1:1] ice at 28 K resulted in the formation of species such as CHN, HNO_2 and $C_2N_2O^+$ C_2N_2O, HNO_3, N_2O_3, NO_2,

N_2O_5 N_2O_3, C_2O and O_3. On further processing the irradiated sample results in the thermal evolution of these products in methanol ice matrix. Thermal evolution of such species from ice surface is crucial to understand the chemistry of PDRs and hot molecular cores in which icy grain mantle subjects to heating due to the presence of a parent star.

CHAPTER 6

ELECTRON IRRADIATION AND SIMULTANEOUS DEPOSITION OF $CH_3OH + NH_3$ (1:1) MIXTURES

6.0 Introduction

Cosmic rays with energies in the range of GeV to MeV when interacting with dust and molecules in a dense molecular cloud can generate a cascade of secondary electrons with energies in the range of 1-5 keV [Lafosse 2009; Huang and Pohl 2008]. The resultant secondary electrons can influence the physio-chemical balance of the molecular clouds by various electron driven processes, both in gas and solid phase [Mason et al. 2014]. Cosmic rays of medium and high energies can penetrate deep into the dense molecular clouds and ionize the ambient region through collisional excitation, collisional dissociation, secondary photon interactions, secondary electron driven processes etc [Prasad and Tarafdar 1983].

The temperature (~10 K) and density ($10^4 - 10^8$ cm^{-3}) in the molecular clouds are favourable to the existence of icy mantles on interstellar dust grains (0.1-1 μm). The interaction of cosmic ray driven secondary electrons with such grain mantles synthesise complex organic molecules which eventually desorb off the surface or follow a cycle of desorption-re-accretion-dissociation-recombination and eventually enrich the clouds chemical structure. Due to the high density and shielding, complex, relatively big organic molecules have a high probability of survival and during the evolution cycle of the cloud, these molecules relocate and regenerate and transform into more complex, highly stable, nonvolatile species.

In this chapter, the effect of electron processing of a pre-mixed co-deposited CH_3OH: NH_3 (1:1) ice films are compared with the simultaneous irradiation and deposition of the same molecular mixture. This investigation was initiated to understand the pathways of formation of nitrogen bearing molecules in dense clouds. The products formed in the ice films during the interaction of the molecular gas ((1:1) CH_3OH: NH_3) and an electron beam while being physisorbed onto the substrate are compared with products formed when the respective ice film was processed with electrons. Different electron flux/fluence conditions were explored and electron destruction cross-sections, rate of formation and destruction of products and temperature dependent evolution of the products etc measured.

6.1 Experiments

Experiments were carried out using the Astrochemistry ices apparatus at the Open University, UK. Physical conditions in the interstellar medium were recreated by maintaining UHV and cryogenic conditions in the experimental chamber (pressures in the range of ~5 x 10^{-10} mbar and a temperature of 10 K). A detailed description of the experimental system is described in **section 3.9** of this thesis. A transmission mode Fourier Transform InfraRed (FTIR) spectrometer with an MCT-A type external detector was used for in-situ monitoring of the ice film. A pre-mixed CH_3OH (99.95% Sigma-Aldrich) and NH_3 (99.0% BOC), 1:1, mixture was introduced into the chamber through a precision leak valve arrangement and an ice film was grown by the background deposition technique. The vapour was introduced at a rate of 1 x 10^{-6} mbar for 300 seconds and deposited onto a ZnSe ~ ø 20 mm (mid-IR transparent) substrate. Transmission mode FTIR spectra with IR beam both normal and 45^0 to the substrate were recorded before and after deposition and the spectrum was used to estimate the column density and thickness of the film using a modified

Beer-Lambert law and measured 'A' value (integrated infrared absorption value) for such an ice mixture [Leiden data base].

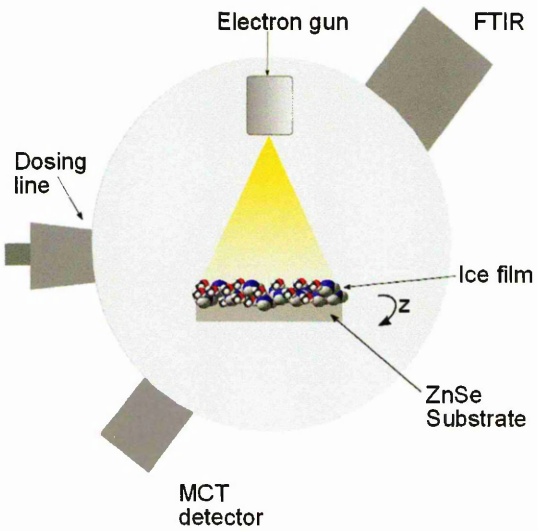

Figure 6.1 A schematic representation of apparatus used for electron irradiation of premixed, co-deposited CH_3OH+ NH_3 (1:1) ice films with 1 keV electrons.

In one set of experiments the deposited ice film was processed by a 1 keV electron beam aligned at 90^0 to the substrate for 50 minutes. The distance between the electron gun and the substrate is 50 mm and the measured spot size of the electron beam at that distance is ~ ø 20 mm. FTIR spectra were recorded *in situ* at 5 minute intervals throughout the irradiation process the acquisitions time of one spectrum (256 scans) at 2 cm^{-1} resolution is 4.2 minutes, after irradiation the ice was kept undisturbed for 60 minutes and subsequently heated (at a rate of 5 K/min) up to sublimation, FTIR spectra being recorded at every step of heating. A schematic diagram of the experimental setup is shown in **Figure 6.1**. Similar experiments were conducted with pure ice films of NH_3 (99.0% BOC) and CH_3OH (99.95% Sigma-

Aldrich), by strictly following the exact procedure with similar conditions using the same experimental setup.

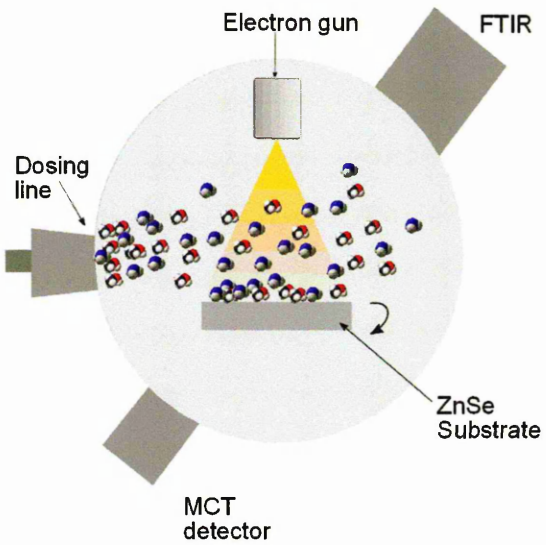

Figure 6.2 A schematic representation of the apparatus used for electron irradiation and simultaneous physisorption of a premixed CH_3OH+ NH_3 (1:1) mixture.

In a separate experiment the CH_3OH+ NH_3 (1:1) mixture was introduced into the same chamber at a lower rate ~1 x 10^{-7} mbar for 3000 seconds, and during the deposition, a 10 μA electron beam with energy 1 keV aligned normal to the ZnSe substrate. In this management the incoming molecules interacted with electrons before being subsequently physisorbed onto the ZnSe substrate maintained at 10 K. A schematic representation of the setup used for simultaneous deposition-irradiation experiment is shown in **Figure 6.2**. FTIR spectra was recorded *in situ* throughout the irradiation-deposition process and after the simultaneous irradiation-deposition procedure, the ice film formed on the substrate was kept undisturbed for 60 minutes and subsequently heated (at a rate of 5 K/min) up to sublimation, FTIR spectra was recorded at every step of heating. The probabilities of ion-molecule interactions and electron-molecule interactions, both in ice and gas phase are highly probable in this experiment, electrons ionize a fraction of molecules in the chamber and these ions can

interact with molecules in the gas phase, or by physisorbed onto the substrate and involve in ion-ion or ion-molecule interaction on a surface. In addition to the ionic processes, the physisorbed molecules on the substrate are subjected to interactions with incoming electrons. Comparing and combining both simultaneous and direct electron interactions can elucidate the influence of such processes in interstellar medium.

6.2 Pre-experimental simulations

6.2.1 Penetration depth of electrons in the ice films (CASINO simulations)

Pre-experimental simulations were conducted by using CASINO, a Monte-Carlo simulation program to predict the penetration depth of electrons in solids and electron interactions in solid film or film supported by a substrate [Hovington et al. 1997]. The average penetration depth of 1 keV electrons in a solid methanol film of 200 nm thickness was found to be 27 nm (see **Figure 6.3**).

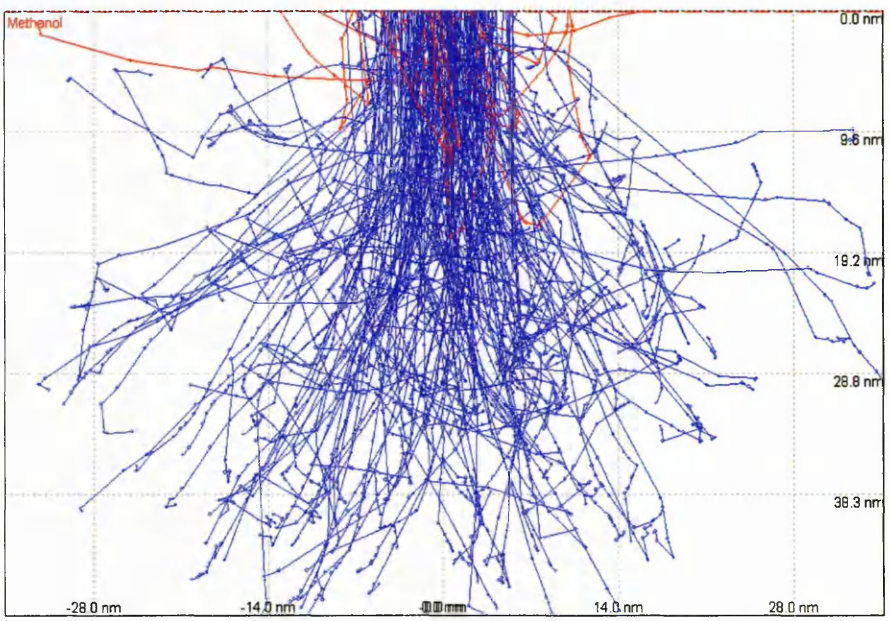

Figure 6.3 CASINO simulation results of 100nm thick methanol film with 100 electrons OF energy 1 keV is shown here.

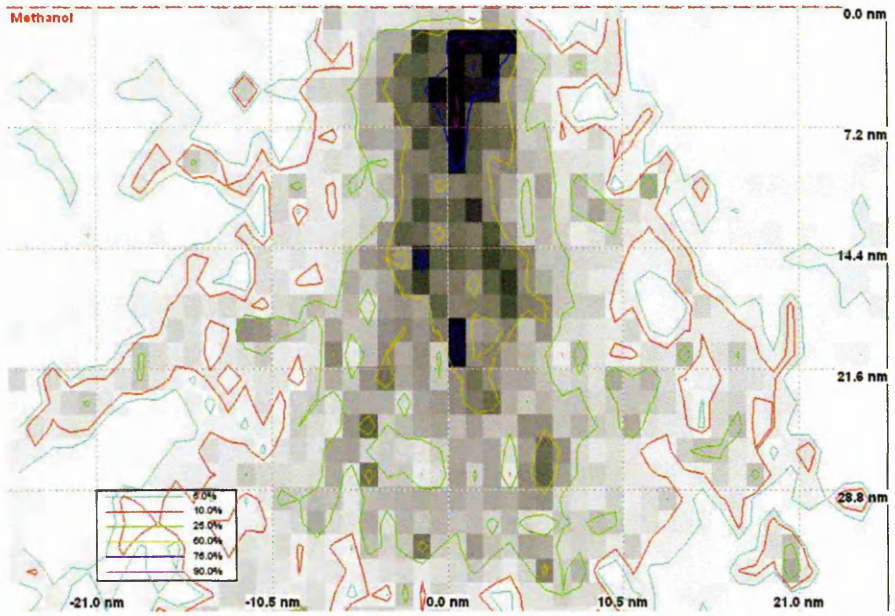

Figure 6.3(b) CASINO simulation results of 100nm thick methanol film with 1 keV electrons, the energy distribution of the electron interaction is shown.

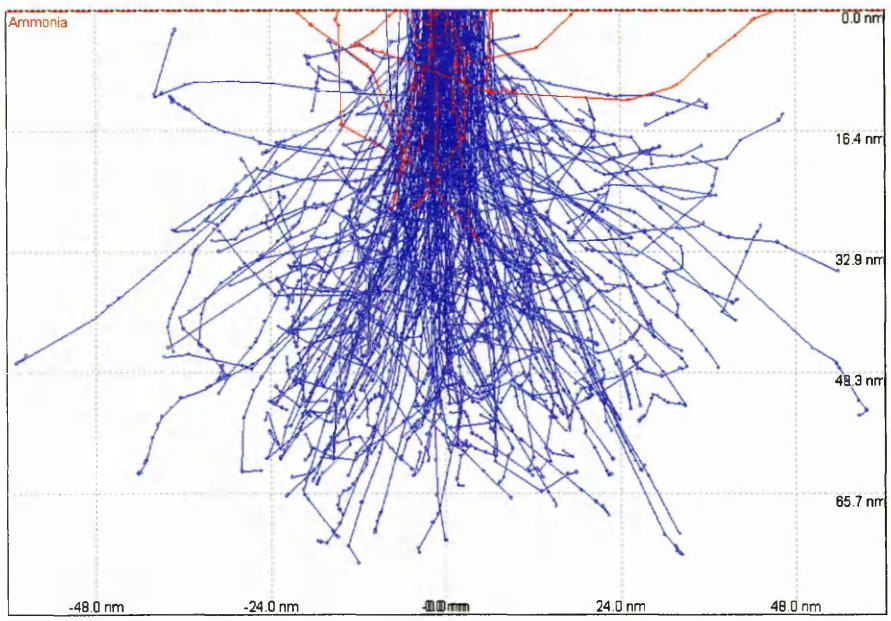

Figure 6.4 CASINO simulation results of 100nm thick ammonia ice film with 100 electrons of energy 1 keV electrons is shown here.

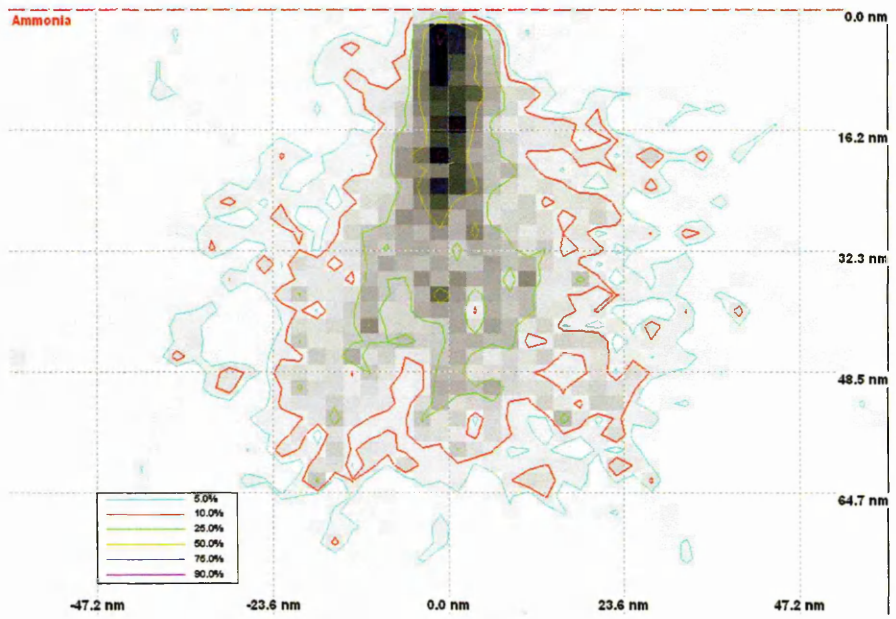

Figure 6.4(b) CASINO simulation results of 100nm thick ammonia film with 1 keV electrons, the energy distribution of the electron interaction is shown.

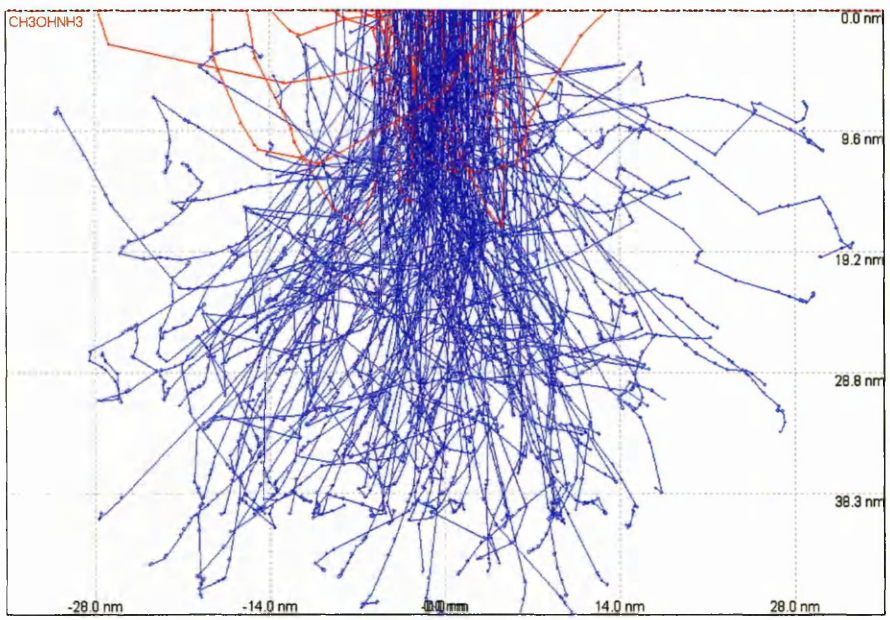

Figure 6.5 CASINO simulation results of 100 nm thick methanol + ammonia (1:1) ice film with 1 keV electrons is shown here.

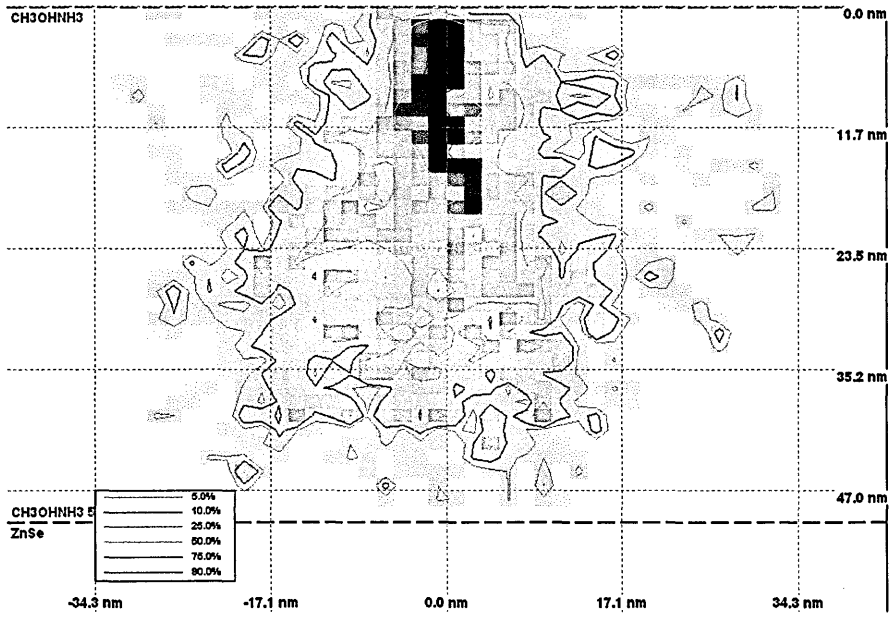

Figure 6.5(b) CASINO simulation results of 100nm thick methanol-ammonia film with 1 keV electrons, the energy distribution of the interacted electrons are shown.

The penetration depth of electrons in 200 nm thick solid film of ammonia is found to be 39 nm (see **Figure 6.4**).

The formation of backscattered secondary electrons from the ZnSe substrate was presented by generating a thin film (~50 nm) of pure CH_3OH, NH_3 and the mixture (CH_3OH+NH_3 (1:1)). The results of simulation of electron irradiation of a homogeneous-isotropic CH_3OH+NH_3 (1:1) ice film of 200 nm thickness show that, 1 keV electrons with spot size of ~10 nm can penetrate 41 ± 5.0 nm (Figure 6.5). Simulations with layer specified samples such as methanol on top of ammonia or vice versa were also conducted. The penetration depth of 1 keV electrons is reduced considerably in a layer deposition, the average penetration depth of a bi layer CH_3OH on NH_3 (200 nm thick) solid film is ~37 nm.

6.3 Electron irradiation of interstellar CH_3OH + NH_3 (1:1) ice films

The absorption spectrum of a co-deposited CH_3OH+NH_3 (1:1) ice film (**Figure 6.6**(c)) is compared with the spectrum of pure CH_3OH (**Figure 6.6**(b)) and pure NH_3 (**Figure 6.6**(a)) ice films, deposited at 10 K. Peak positions in the absorption spectrum of pure CH_3OH and NH_3 ice films and CH_3OH+NH_3 (1:1) ice film at 10 K are summarised in **Table 6.1**. All the fundamental vibrational bands of pure CH_3OH and NH_3 are also present in the mixture, most of the features are overlapping, however, fundamental features are prominent and distinguishable; in Figure 6.6 (c) the band at 1030 cm^{-1} (υ_8) is assigned to C=O stretch (CH_3OH); there is a slight shift of 5 cm^{-1} (with respect to the (υ_7) band at 1125 cm^{-1} of pure CH_3OH) in case of fundamental (υ_7) band at 1130 cm^{-1}, bands due to CH_3 deformation of methanol (υ_{10}, υ_4) is repeated at 1461 cm^{-1} and 1478 cm^{-1} respectively. The strength of the hydrogen bonds between two NH_3 molecules is ~13 kJ mol^{-1} [Bennett et al. 2011] and that of CH_3OH is 27 kJ mol^{-1} [Boyd and Boyd 2007] (in gas phase), since both the species are polar, H-bond formation between single molecules and clusters are highly probable and results the shift in the peak positions of the mixture. A band at 1496 cm^{-1} is assigned to ($\upsilon_8 + \upsilon_{12}$) combination, the bands at 2239 cm^{-1} and 2527 cm^{-1} are assigned to a combination of ($2\ \upsilon_{11}$ /$2\ \upsilon_7$) and ($\upsilon_6 + \upsilon_{11}$) respectively. From the spectrum of the mixture, **Figure 6.6**(c)), it is evident that there are neutral interactions between CH_3OH and NH_3 and this gives rise to a new peaks at 1711 cm^{-1}, which correspond to HNO_3 (N=O stretch) [Guillory and Bernstein, 1975]. A surface can support catalysis even in the absence of energetic sources and such interactions triggered by excess surface energy contributions result in new products.

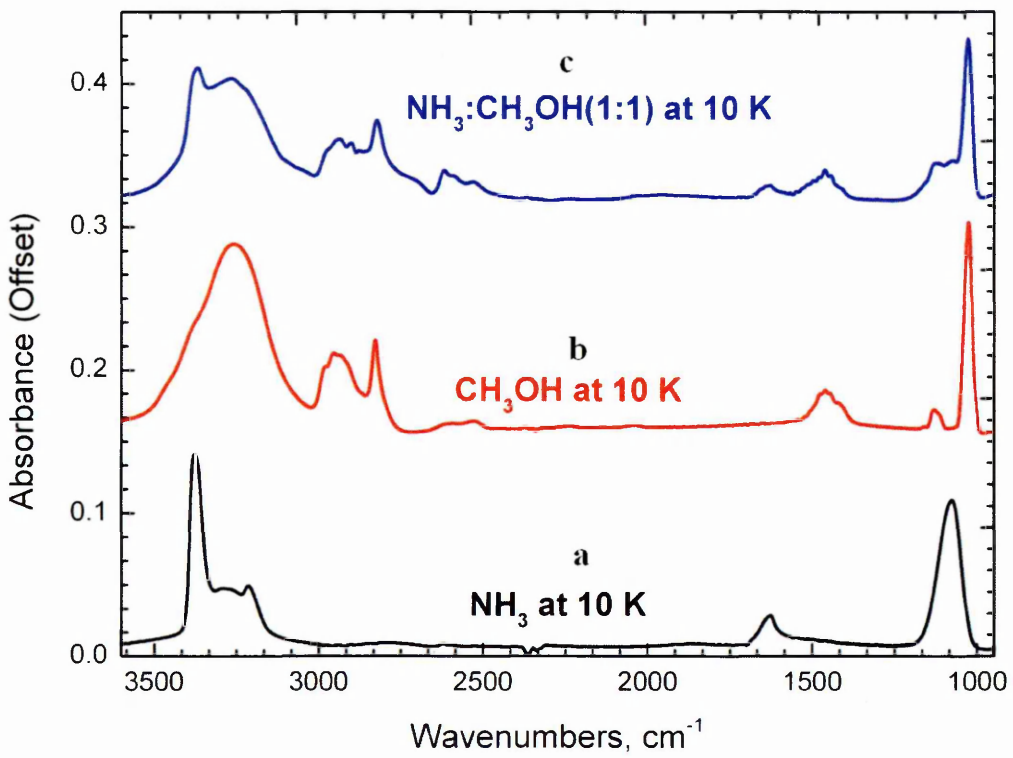

Figure 6.6 FTIR spectra of pure NH_3 (a), pure CH_3OH (b), and pre-mixed, co-deposited NH_3+CH_3OH (1:1) (c) ice films on ZnSe at 10 K.

The absorption spectrum of a pre-mixed co-deposited ice film of CH_3OH+NH_3 (1:1) mixture is shown in **Figure 6.7 (a)**, and a spectrum of the same ice film after 60 minutes of irradiation with 1 keV electrons of a 10 μA beam is shown in **Figure 6.7 (b)**. Upon electron processing, several new products are formed, the major products being CO at 2136 cm^{-1}, CO_2 at 2345 and H_2CO at 1721 cm^{-1} and CH_4 at 1304 cm^{-1}.

These results may be explained by the following reactions, methanol can photo-dissociate into CO and H_2CO by the following channels [Kuo 2007 and references therein],

$$CH_3OH \rightarrow CO + 2H_2 \text{ (Dissociation threshold: 0.8865 eV)} \qquad 6.1$$

$$CH_3OH \rightarrow H_2CO + H_2 \text{ (Dissociation threshold: 0.93234 eV)} \qquad 6.2$$

Electron impact dissociation can also happen through the similar channel and result in the production of CO, CO_2 and H_2CO, which are the major products observed. CH_4 may also form through the following pathway [Bennett et al. 2007],

$$CH_3OH \rightarrow CH_4 + O \qquad 6.3$$

In addition to these simple species, complex organic molecules are also synthesized in the process, C_2H_5OH at 1045 and 1084 cm^{-1}, $HCOOCH_3$ seen at 1443 and 1461cm^{-1}, CH_2CHO at 1546 cm^{-1}, CH_2CHOH at 1631 cm^{-1}, C_2H_6O 2823 cm^{-1}, and $C_2H_4O_2$(cis, trans) at 2879 cm^{-1}.

N-bearing organic species were also observed after the electron irradiation of the mixture, N-bearing products such as CN_2, CH_3NO, CH_3N, were observed with peak positions at 1117 cm^{-1}, 1565 cm^{-1} and 3265 cm^{-1} respectively. Further peaks at 2263 cm^{-1}, 908 cm^{-1} was assigned to CHNO, and HNO_3, respectively. Nitrogen oxides were also synthesized in trace amounts, ONO-NO_2 at 1825 cm^{-1} and $(NO)_2$ at 1778 cm^{-1}.

Table 6.1 Peak positions of ice films of CH_3OH, NH_3, CH_3OH+NH_3 (1:1) and simultaneous irradiation and deposition of CH_3OH+NH_3 (1:1) at 10 K.

CH_3OH		NH_3		CH_3OH+NH_3(1:1) mixture	
Peak positions (cm^{-1})[1]		Peak positions (cm^{-1})[2]		Peak positions (cm^{-1})[1, 2, 3]	
				900	HNO_3[3]
1029	υ_8, CO stretch			1030	CH_3OH
		1076	υ_2, symmetric deformation	1073	NH_3
1130	υ_7			1125	CH_3OH
1458	υ_{10}, CH_3 deformation			1461	CH_3OH
1472	υ_4, CH_3 deformation			1478	CH_3OH
1496	υ_8+ υ_{12}			1496	CH_3OH
		1511		1512	NH_3
		1546		1547	NH_3
		1626	υ_4,degenerated deformation	1631	NH_3
				1640	?
				1658	?
				1688	?
				1711	HNO_3[4]
		1723		1726	NH_3
1733				1744	CH_3OH
1749				1755	CH_3OH
		1768		1768	NH_3
1773					
		1785		1784	NH_3
2239	2 υ_{11} /2 υ_7			2234	CH_3OH
2527	υ_6 + υ_{11}			2324	CH_3OH
				2532	CH_3OH
		2622		2620	NH_3
2828	υ_3 CH_3 stretch			2826	CH_3OH
		2943		2938	NH_3
2955	υ_9 CH_3 stretch			2951	CH_3OH
		3213	υ_1, symmetric stretch		NH_3
3261	υ_1			3267	CH_3OH
		3289	υ_1 or 2υ_4		NH_3
		3377 (S)	υ_3,degenerated stretch		NH_3
3588				3572	CH_3OH
3608	OH stretch			3595	CH_3OH

[1]W. Zheng, R.I. Kaiser, 2007; [2]Guillory and Bernstein, 1975; [3]Chen, Lo, et al., 1992;

All these products and the respective peak positions of the newly formed products after electron irradiation of the ice film of CH_3OH+NH_3 (1:1) mixture are summarised in **Table 6.2**. Strongly overlapping features were resolved by Fourier de-convolution method and the area under the curve was determined by curve fitting. The calculated column densities of the products are listed in **Table 6.3**.

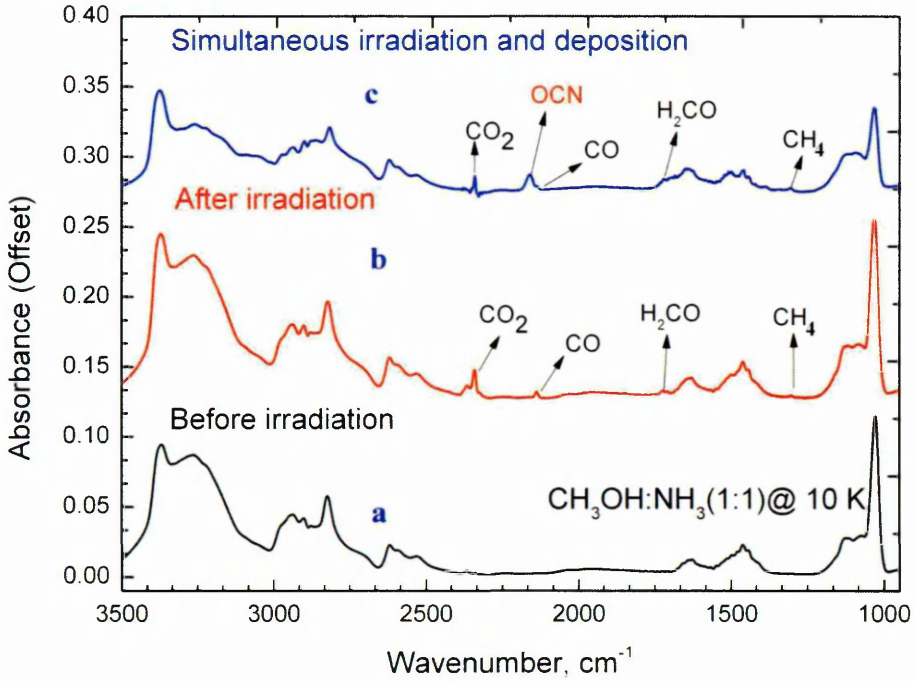

Figure 6.7 Absorption spectra of pure pre-mixed co-deposited NH3:CH3OH (1:1) ice films before (a) and after (b) electron irradiation at 10 K; (c) simultaneous electron irradiation and deposition of NH3:CH3OH (1:1) mixture at 10 K.

Earlier studies by S. Jheeta et al. [Jheeta et al. 2013] has reported the formation of formamide ($HCONH_2$) by electron irradiation of same ice mixture, however, in our experiment we didn't observe any formation of $HCONH_2$.

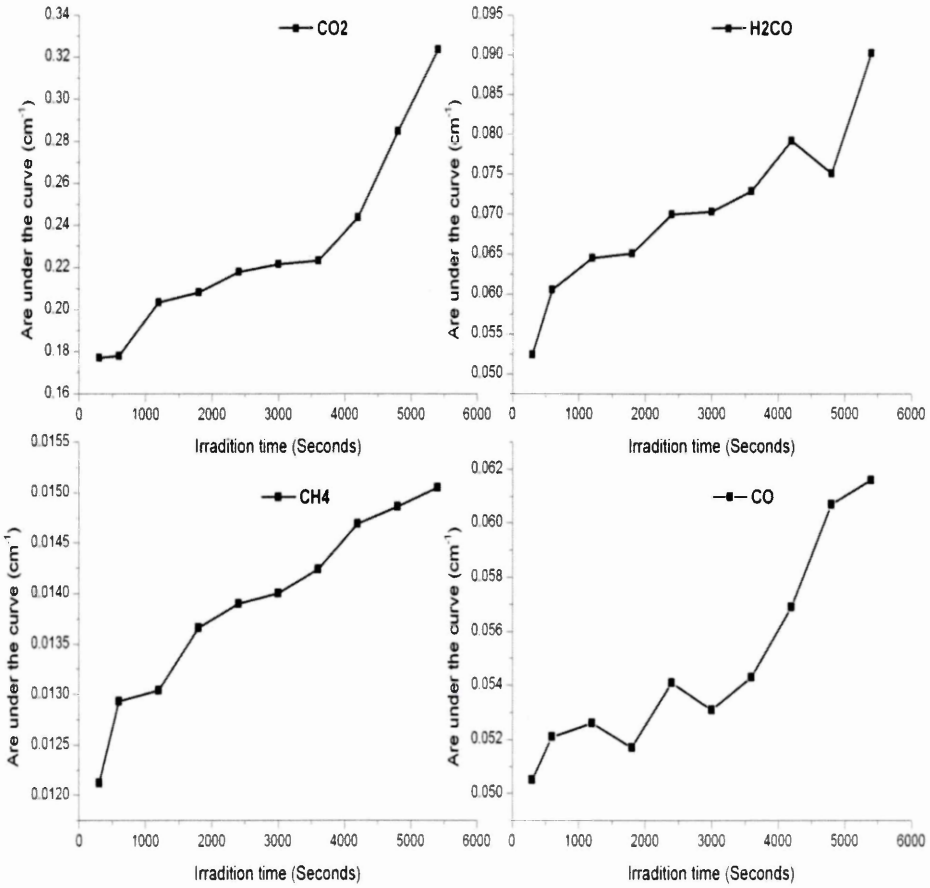

Figure 6.8 Evolution of products during ninety minutes of electron irradiation of pure CH_3OH with 1 keV electrons at 10 K.

Other probable/predicted products which we didn't observe in our experiment are the NH_4^+ ion (at 1488 cm^{-1}), formic acid (HCOOH), the cyanate ion (OCN^-) and CNO. According to the earlier studies, Bossa et al. [Bossa et al. 2008], suggested that it may be due to the fact that NH_4^+ ion is being rapidly removed from the system. The OCN^- ion may be formed from the following reactions:

$$HNCO + NH_3 \rightarrow NH^+_4 + OCN^- \qquad 6.4$$

or through the electron impact dissociation of $HCONH_2$. As mentioned above the absence of $HCONH_2$ implies the absence of formation of OCN^-, in addition absence of NH^+_4 ion through reaction 6.4 also underlines the absence of a reaction channel leading to OCN^- or OCN. The formation of OCN^- after simultaneous irradiation-deposition of NH_3:CH_3OH (1:1) is compared with the electron irradiation result of NH_3:CH_3OH (1:1) and is shown in **Figure 6.9**.

The column density of CO formed after 60 minutes of electron irradiation of ice film of NH_3:CH_3OH (1:1) mixture is estimated to be 9.42×10^{14} molecules cm^{-2}; it is almost equivalent to the amount of CO (8.17×10^{14} molecules cm^{-2}) produced after 60 minutes of electron irradiation of a pure CH_3OH ice film. The evolution of CO, CO_2, H_2CO and CH_4 during electron processing of pure ice film of CH_3OH is shown in **Figure 6.8**. All the products such as CO, CO_2, H_2CO and CH_4 were strictly following the same trend also the in case of processing of NH_3:CH_3OH (1:1) mixture.

The column density of CH_4 (1304 cm^{-1}), CO_2 (2342 cm^{-1}) and H_2CO(1726 cm^{-1}) formed after 60 minutes of electron irradiation of NH_3:CH_3OH (1:1) mixture is estimated to be 1.57×10^{15} molecules cm^{-2}, 7.90×10^{14} molecules cm^{-2} and $9.56 \pm 0.23 \times 10^{14}$ molecules cm^{-2} respectively. In addition to that, 1.34×10^{15} molecules cm^{-2} of C_2H_5OH (1045 cm^{-1}) was also synthesized.

Table 6.2 Products of electron (1 keV) irradiation of pre-mixed, co-deposited $CH_3OH + NH_3$ (1:1) and simultaneous irradiation and deposition of $CH_3OH + NH_3$ (1:1).

Simultaneous		**Premixed-co deposited**		References
Peak positions (cm^{-1})	Products	Peak positions (cm^{-1})	Products	
851	NO_3 or O_3			1,2
909	HNO_3	908	HNO_3	2
1031	$HCOOCH_3$			3
1047	C_2H_5OH	1045	C_2H_5OH	3
1085	C_2H_5OH	1084	C_2H_5OH	3
1121	CN_2, C_2H_4O	1117	CN_2	3
1304	CH_4	1304	CH_4	3
1339	$HCONH_2$			4
1363	NO_2^+			2
1386	$HCONH_2$			4
1420	CH_5N			5
1443	$HCOOCH_3$	1443	$HCOOCH_3$	3
1459	$HCOOCH_3$	1461	$HCOOCH_3$	3
1478	NCN			5
1488	NH_4^+			5
1497	H_2CO	1496	H_2CO	3
1508	NH_3^+			5
1521	NH_3^+			5
1529	CH_2CHO			3
1538	CH_2CHO			3
1545	CH_2CHO	1546	CH_2CHO	5
1556	H_2NCO			3
		1565	CH_3NO	4
1570	$N_2H_3^+$			5
1625	CH_2CHOH			5
		1631	CH_2CHOH	5
		1639	R_2C=CHR	6
1647	R_2C=CHR			
		1679	?	
1684	?			
1693	$HCONH_2$			4
1705	HOONO			
1720	H_2CO	1721	H_2CO	3
1768	HCOOH			
1781	c-$(NO)_2$	1778	c-$(NO)_2$	1
1800	$NCCN^+$, HCCN, HCN^+			6
1825	ONO-NO_2(D)	1825	ONO-NO_2(D)	1
1845	N_2O_3	1848		1
1918	CNO			

1943	$NCCCCN^+$			20
		1950	C_2O	3
2161	OCN^-			
		2136	CO	3
2278	CHNO	2263	CHNO	
2535	CH_2NH^+	2533	CH_2NH^+	6
2621	H_3	2620	H_3	
2817	C_2H_6O	2823	C_2H_6O	5
2862	$C_2H_4O_2$(c, t),			5
		2879	$C_2H_4O_2$(c, t)	5
2900	C_2H_5N	2902	C_2H_5N	7
2937	C_3H_7N	2938	C_3H_7N	8
3262	CH_3N	3265	CH_3N	9

1. Fateley 1959; 2. Jamieson et al 2005; 3. Bennett et al. 2007 4. Brucato et al. 2006 ; 5. Shimanouchi 1972; 6. Sivarman et al 2013; 7. Yu and Duxbury, 1992 8. Jurgen. Hinze and Curl 1964; 9. Hamada et al. 1984

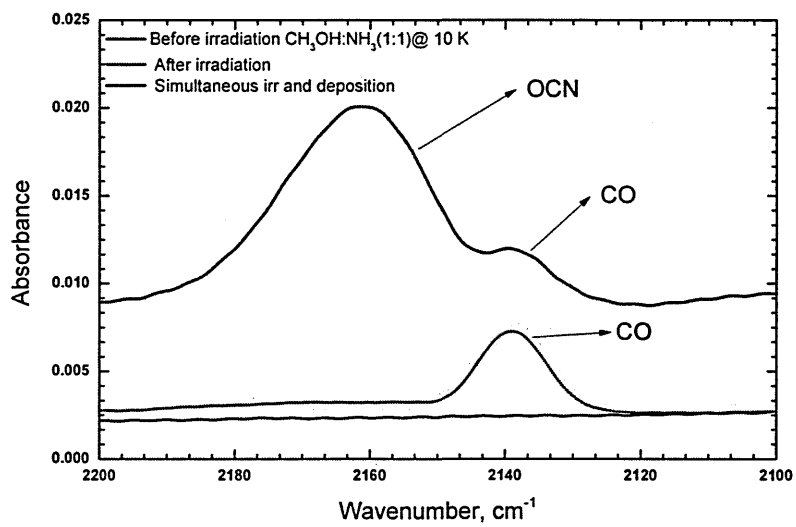

Figure 6.9 Production of CO after 50 minutes of electron irradiation of an NH_3:CH_3OH (1:1) ice films at 10 K and production of CO and OCN after 50 minutes of simultaneous electron irradiation and deposition of NH_3:CH_3OH (1:1) mixture at 10 K.

Almost 18 % (of the initial column density) of CH_3OH molecules were destroyed as a result of the irradiation i.e. a reduction in column density of CH_3OH (1031 cm^{-1}) from 1.81×10^{17} molecules cm^{-2} to 1.5×10^{17} molecules cm^{-2}. Estimated values of column densities and integrated absorbance ('A' values) values used for calculation and references are listed in **Table 6.3.**

6.4 Simultaneous irradiation and deposition of a CH_3OH+NH_3 (1:1) mixture

The FTIR spectrum recorded after simultaneous electron irradiation and deposition of $CH_3OH:NH_3$ (1:1) mixture is shown in **Figure 6.7 (c)**. In comparison to the electron processing of a co-deposited ice film of $CH_3OH:NH_3$ (1:1), simultaneous irradiation and deposition exhibits a richer chemistry and as a result the number of products formed through this processes is larger than the simple irradiation of condensed ice film. The product yields formed during simultaneous processing-deposition and ice film processing are listed in **Table 6.2.** New absorption peaks corresponding to CO at 2140 cm^{-1}, CO_2 at 2345 cm^{-1}, CH_4 at 1304 cm^{-1} and H_2CO at 1721 cm^{-1} are observed after 60 minutes of irradiation.

Complex organic molecules were also synthesized in the process, ethanol (C_2H_5OH) at 1085 cm^{-1}, C_2H_4O at 1121 cm^{-1}, methyl formate ($HCOOCH_3$) at 1443 and 1461cm^{-1}, formaldehyde (H_2CO) at 1497 cm^{-1}, CH_2CHO at 1546 cm^{-1} and 1538 cm^{-1}, CH_2CHOH at 1625 cm^{-1}, formic acid (HCOOH) at 1768 cm^{-1}, C_2H_6O at 2817 cm^{-1}, and $C_2H_4O_2$ at 2862 cm^{-1} were observed in the spectrum. Products formed after simultaneous irradiation-deposition of $CH_3OH:NH_3$ (1:1) are labeled in the spectrum **(Figure 6.10)**.

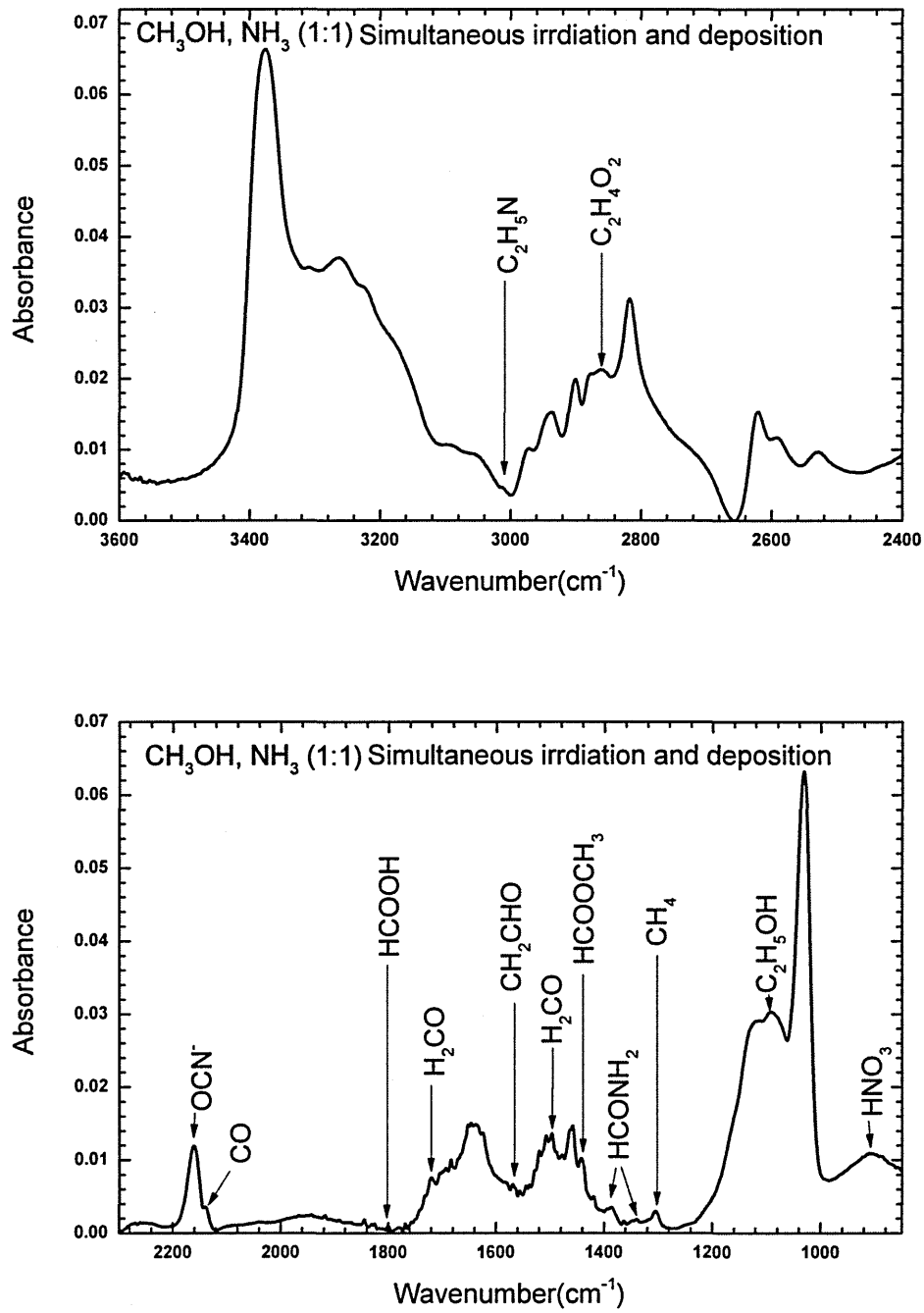

Figure 6.10 Products formed after 3000 seconds of simultaneous electron irradiation and deposition of NH_3+CH_3OH (1:1) mixture at 10 K; top 3600-2400 cm^{-1} region and bottom 800-2300 cm^{-1} region.

In addition to these hydrocarbons, a large variety of N-bearing organic species were also synthesized, C_2H_5N at 2902 cm^{-1}, CH_3N at 3262 cm^{-1} and CHNO at 2263

cm^{-1} were observed along with NCCCCN at 1950 cm^{-1} and CN_2 at 1117 cm^{-1}, $HCONH_2$ 1339 cm^{-1}, 1386 cm^{-1} and 1693 cm^{-1}. Trace amounts of gaseous $(NO)_2$ at 1778 cm^{-1} and ONO-NO_2 (dimer) at 1825 cm^{-1} were also observed.

Several intermediate ions such as NH_4^+ at 1488 cm^{-1}, NH_3^+ at 1508 cm^{-1}, HCN^+ at 1800 cm^{-1}, OCN^- at 2161 cm^{-1}, $N_2H_3^+$ at 1570 cm^{-1}, CH_2NH^+ at 2533 cm^{-1} and CH_3CNH^+ at 2938 cm^{-1} (gas phase value) were also observed.

A peak at 851 cm^{-1} can be assigned to NO_3 and this implies that the probability of formation of O_3 as an intermediate in this reaction is high, although we didn't observe ozone in the final spectrum.

O_3^+ also has a characteristic absorption at 850 cm^{-1}, therefore it is evident that this absorption is either due to NO_3 or O_3^+, in either case, the formation of O_3 is essential.

As discussed in the earlier section, CO, HCO, H_2CO may form through reactions 6.1, 6.2 and the following path ways,

$$CH_3OH \rightarrow H_2CO + 2H/H_2 \qquad 6.5(a)$$

$$H_2CO \rightarrow HCO + H \qquad 6.5(b)$$

$$HCO \rightarrow CO + H \qquad 6.5(c)$$

$$H_2CO \rightarrow CO + 2H/H_2 \qquad 6.5(d)$$

Electron impact dissociation of CH_3OH can liberate H_2CO and H_2, upon further processing H_2CO dissociates and liberates a hydrogen atom to form HCO as an intermediate (6.5 (b)), HCO further dissociates and forms CO. CO can also be formed from H_2CO directly (6.5 (d)).

Three of the most important nitrogen containing compounds formed were: CHNO, (2278 cm^{-1}), OCN^- (2161 cm^{-1}) and $HCONH_2$ (1339 cm^{-1}, 1386 cm^{-1}). CHNO may have been formed from the combination of NH_2 radical (product of NH_3

dissociation) with CO (formed from CH_3OH). $HCONH_2$, NH_4^+ and OCN^- were absent in the electron processing of the ice film but these molecules are synthesized in the simultaneous irradiation-deposition experiment. The following reaction pathways are the most probable route by which HNCO and $HCONH_2$ are synthesized from CH_3OH and NH_3

$$CH_3OH \rightarrow CH_4 + O \quad 6.6$$

$$NH_3 \rightarrow NH_2 + H \quad 6.7$$

$$NH_2 + CO \rightarrow HNCO + H \quad 6.8$$

$$HCOOH + NH_3 \rightarrow HCONH_2 + H_2O \quad 6.9$$

and

$$CH_3OHCO + NH_3 \rightarrow HCONH_2 + CH_3OH \quad 6.10$$

In case of simultaneous electron irradiation and deposition, a considerable quantity of OCN^- is produced; the column density of OCN^- formed after 3000 second of processes is estimated to be 1.2 x 10^{15} molecules cm^{-2}. In case of direct ice processing, OCN^- (**Figure 6.10** region 2200-2100 cm^{-1}) was absent and therefore it is confirmed that the pathways of formation in simultaneous electron irradiation and deposition processes are fundamentally different from those of the pre-deposited ice processing. According to reaction 6.4, both NH_4^+ and OCN^- may form from HNCO and NH_3, HNCO is confirmed as a product in this experiment. OCN^- can also form through electron impact dissociation of $HCONH_2$. Since the presence of $HCONH_2$ is confirmed, this pathway should be taken into account, this dissociation channel is in agreement with our previous results of 1 keV electron irradiation of pure ice films of $HCONH_2$ [Sivaraman et al. 2014].

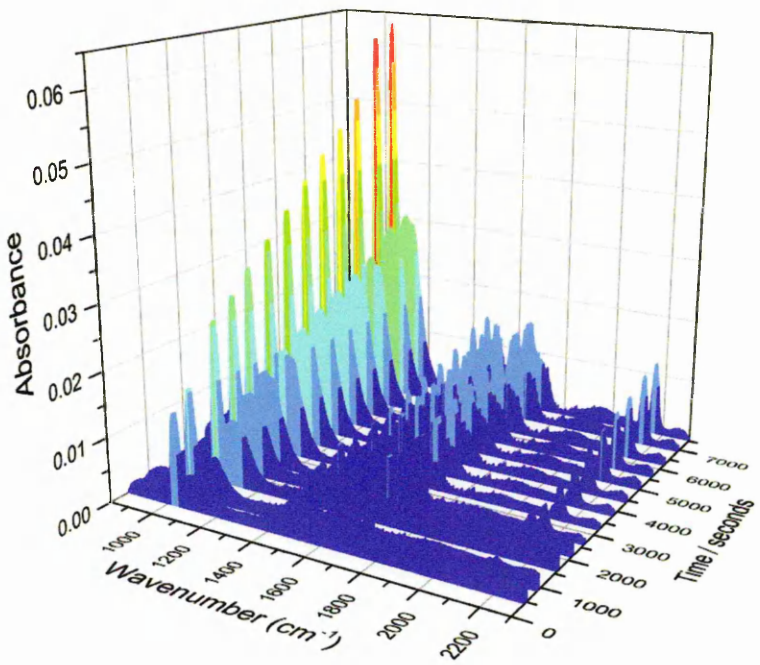

Figure 6.11 Evolution of products with irradiation time for the simultaneous electron irradiation and deposition of NH_3:CH_3OH (1:1) mixture at 10 K, 800-2300 cm^{-1} region.

Therefore we conclude that the major route of formation of OCN^- is through electron impact dissociation of $HCONH_2$, $HCONH_2$ is formed in the gas phase [Sivaraman et al. 2014] physisorbed onto the surface and there it is dissociated to form OCN^-. The second route $HNCO + NH_3 \rightarrow NH^+_4 + OCN^-$, is a subsidiary, but it is a direct surface formation route of OCN^-. The product evolution of simultaneous electron irradiation and deposition of NH_3:CH_3OH (1:1) is shown in **Figure 6.11** (800-2300 cm^{-1}) and **6.12** (3600-2400 cm^{-1}).

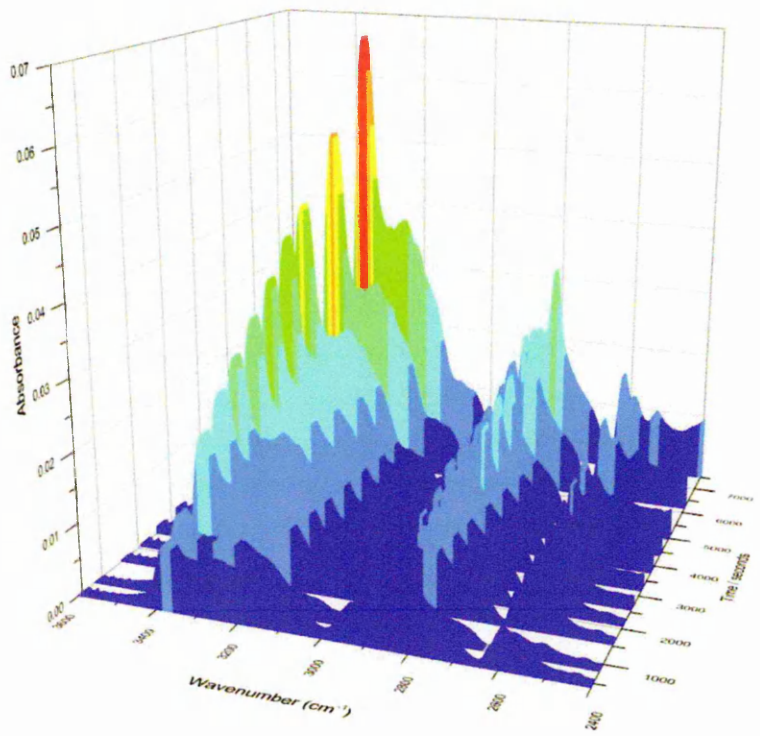

Figure 6.12 Evolution of products with irradiation time for the simultaneous electron irradiation and deposition of NH_3:CH_3OH (1:1) mixture at 10 K, 3600-2400 cm^{-1} region.

Glycol aldehyde (CH_3OHCO) and methyl formate ($HCOOCH_3$) are formed through similar reactions,

$$H_2CO + HCO + H \rightarrow CH_3OHCO \qquad 6.11$$

$$H_2CO + HCO + H \rightarrow HCOOCH_3 \qquad 6.12$$

Dimethyl ether (CH_3OCH_3) and methylamine (CH_3NH_2) were formed through secondary reactions [Bennett et al. 2008]. Further studies are needed to confirm the reaction pathways of these species as well as cyanopolyines. Dimethyl ether (CH_3OCH_3) and methylamine (CH_3NH_2) may well have been involved in the formation of nitrogen bearing complex organic molecules, cyanopolyines.

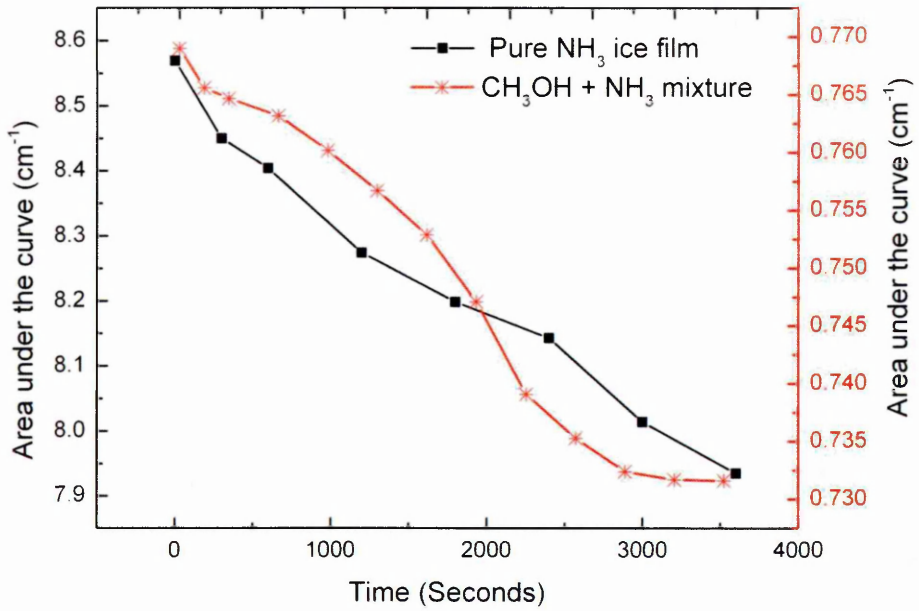

Figure 6.13 Evolution of absorption feature of NH_3 at 3213 cm^{-1} during electron (1 keV) irradiation of pure NH_3 and NH_3:CH_3OH (1:1) mixture ice films.

The column density of NH_3 after 60 minutes of electron irradiation of ice film of pure NH_3 ice film was compared with simultaneous deposition-irradiation of the NH_3:CH_3OH (1:1) mixture, the results shows interesting trend (**Figure 6.13**), even though both follow a decreasing trend, they are different. In case of irradiation of ice film of NH_3:CH_3OH (1:1) mixture, NH_3 steadily decreases with time but in the later case, the kinetics is multi channel,

$$NH_3 \rightarrow NH_2 + H$$

NH_2 is formed through electron dissociation of NH_3 reaction 6.7 and formation of NH_3^+ ion formation from NH_3 [Zheng 2008]. And in case of pure NH_3 film the reduction in column density due to sputtering of the sample is also accounting for this trend. In case of mixture, the sputtering rate is low when compared to the pure ice film of NH_3.

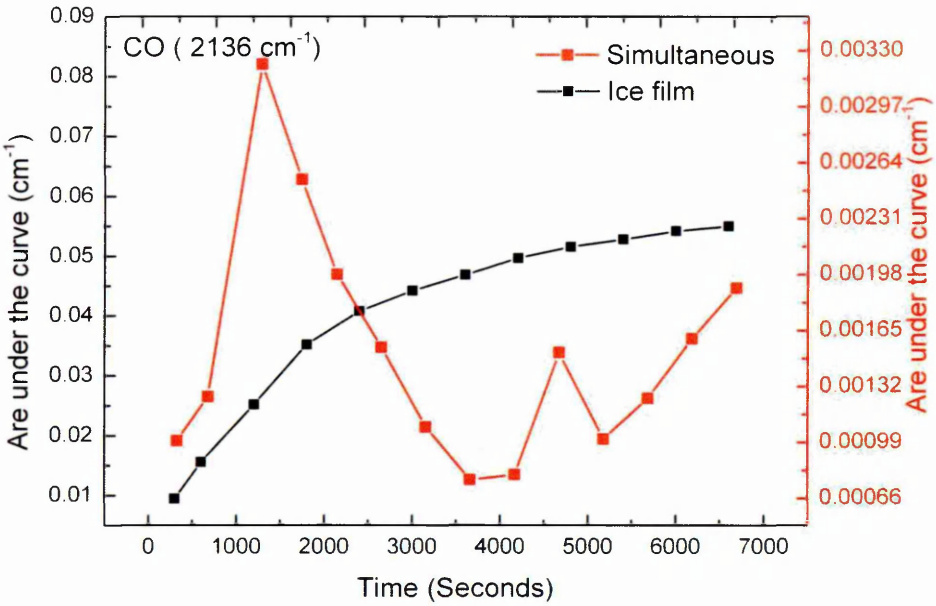

Figure 6.14 Evolution of absorption feature of CO at 2136 cm^{-1} during electron (1 keV) irradiation of NH_3:CH_3OH (1:1) mixture ice films and simultaneous irradiation-deposition of the NH_3:CH_3OH (1:1) mixture.

The column density of CO formed after 60 minutes of simultaneous electron irradiation-deposition of NH_3:CH_3OH (1:1) mixture is estimated to be 1.73×10^{14} molecules cm^{-2}; it is almost five times less than that of CO synthesized by direct irradiation of a deposited ice film of the same mixture. Even though the column density of products formed through simultaneous irradiation-deposition, all the products such as CO_2, H_2CO and CH_4 were strictly following the same evolution trend (with respect to irradiation fluence) as in the case of processing of NH_3:CH_3OH (1:1) mixture. However, CO exhibits a different trend in evolution during irradiation, evolution of absorption feature of CO at 2136 cm^{-1} during electron (1 keV) irradiation of NH_3:CH_3OH (1:1) mixture ice films and simultaneous irradiation-deposition of the same mixture is shown in **Figure 6.14**. CO yields in the simultaneous irradiation-deposition (I-D) are different from CO produced on a surface, this may due to the

contribution of CO towards the formation of HCO through a surface formation route [Tielens 2006],

$$CO + H \rightarrow HCO \qquad 6.13$$

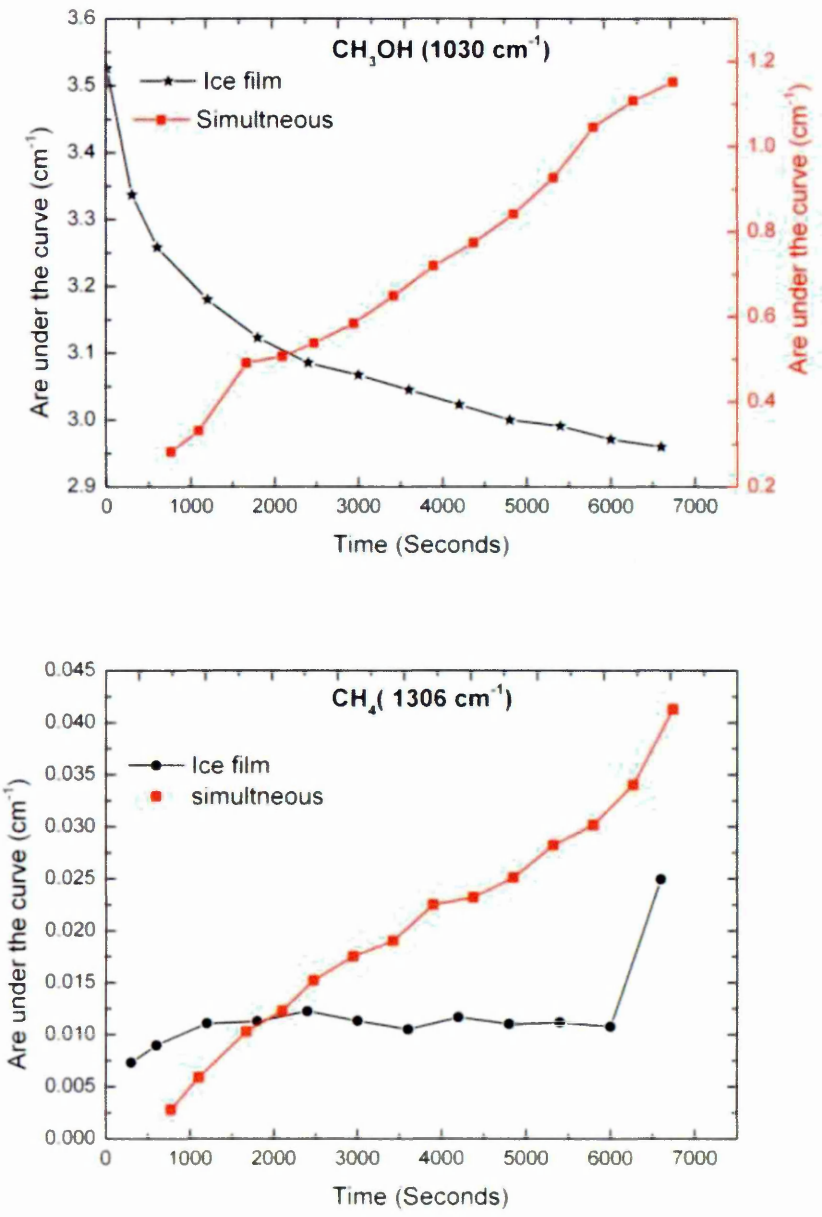

Figure 6.15 Evolution of absorption feature of CH_3OH at 1030 cm^{-1} and CH_4 at 1306 cm^{-1} during electron (1 keV) irradiation of NH_3:CH_3OH (1:1) mixture ice films and simultaneous irradiation-deposition of the same mixture.

From reaction route 6.13, it is evident that the evolution of CO (from simultaneous I-D) will not follow the same trend as in the case of ice film processing. Since, in the case of ice film, the synthesized CO will get trapped in the ice and thus the mobility is limited and this restrict further reactions to form products such as HCO and H_2CO [Bennett et al. 2008].

The column density of CH_4 (1304 cm^{-1}), CO_2 (2342 cm^{-1}) and H_2CO(1726 cm^{-1}) formed after 60 minutes of electron irradiation of ice film of NH_3:CH_3OH (1:1) mixture is estimated to be 1.57×10^{15} molecules cm^{-2}, 7.90×10^{14} molecules cm^{-2} and $9.56 \pm 0.23 \times 10^{14}$ molecules cm^{-2} respectively, 1.34×10^{15} molecules cm^{-2} of ethanol (C_2H_5OH) (1045 cm^{-1}) were also synthesized during the process. C_2H_5OH is formed through surface hydrogenation pathway of CO,

$$CO + H \rightarrow HCO \qquad 6.13$$

$$HCO + H \rightarrow H_2CO \qquad 6.14$$

$$H_2CO + H \rightarrow CH_3O \rightarrow CH_3OH \qquad 6.15$$

Further reaction of CO with CH_3OH and successive hydrogenation leads to C_2H_5OH. As discussed above formamide ($HCONH_2$) is formed through reaction 6.9 or 6.10. In case of simultaneous irradiation and deposition, formamide follows an unusual pattern (**Figure 6.16**), this is mainly due to the electron impact dissociation of $HCONH_2$ into OCN^-, $HCONH_2$, 15-20 % of synthesized $HCONH_2$ is dissociated and leads to further products.

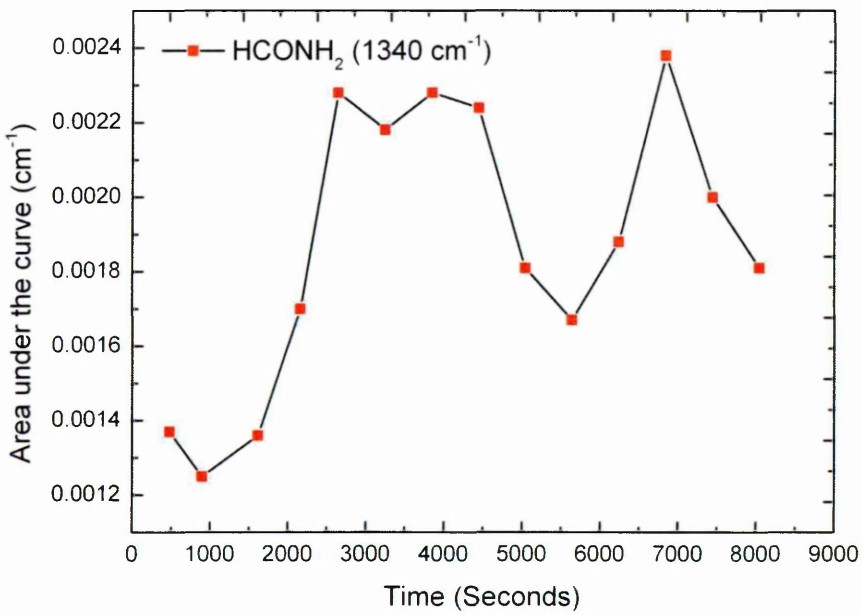

Figure 6.16 Evolution of absorption feature of $HCONH_2$ at 1340 cm^{-1} during (1 keV electron) simultaneous irradiation-deposition of CH_3OH+NH_3 (1:1) mixture.

The column density of glycol aldehyde after the simultaneous irradiation-deposition is estimated to be 5×10^{13} molecules cm^{-2}, and the column density of its structural isomer, methyl formate ($HCOOCH_3$) is 8.16×10^{15} molecules cm^{-2}.

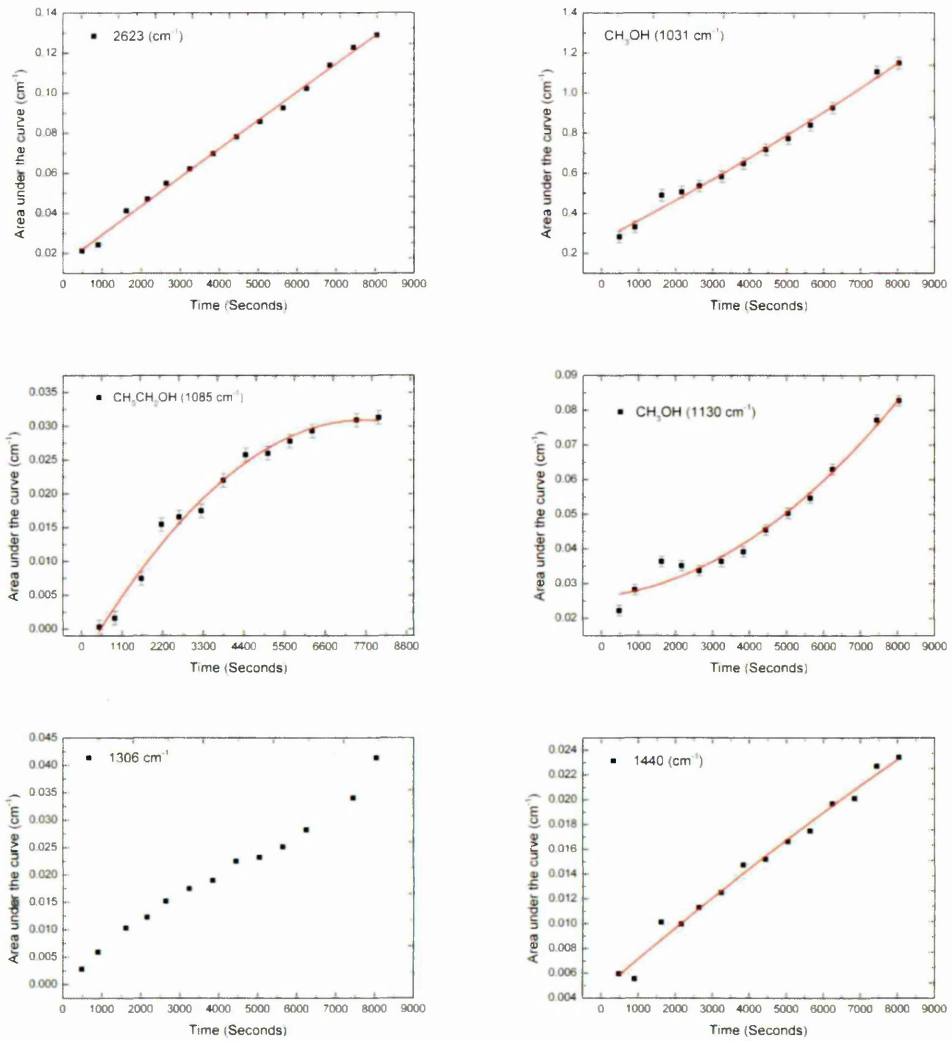

Figure 6.17 Evolution of absorption feature of CH_3OH at 1030 cm^{-1}, 1130 cm^{-1}, CH_3CH_2OH at 1085 cm^{-1}, CH_4 at 1306 cm^{-1} and $HCOOCH_3$ at 1440 cm^{-1} during (1 keV electron) simultaneous irradiation-deposition of (NH_3:CH_3OH (1:1) mixture.

Evolution of a column density of CH_3OH at 1030 cm^{-1}, 1130 cm^{-1}, CH_3CH_2OH at 1085 cm^{-1}, CH_4 at 1306 cm^{-1} and $HCOOCH_3$ at 1440 cm^{-1} during (1 keV electron) simultaneous irradiation-deposition of (NH_3:CH_3OH (1:1) mixture is shown in **Figure 6.17.** The column density of formic acid (HCOOH) is estimated to be 1.76×10^{14} molecules cm^{-2}, but HCOOH was absent in the irradiation of a pure ice film of the same mixture.

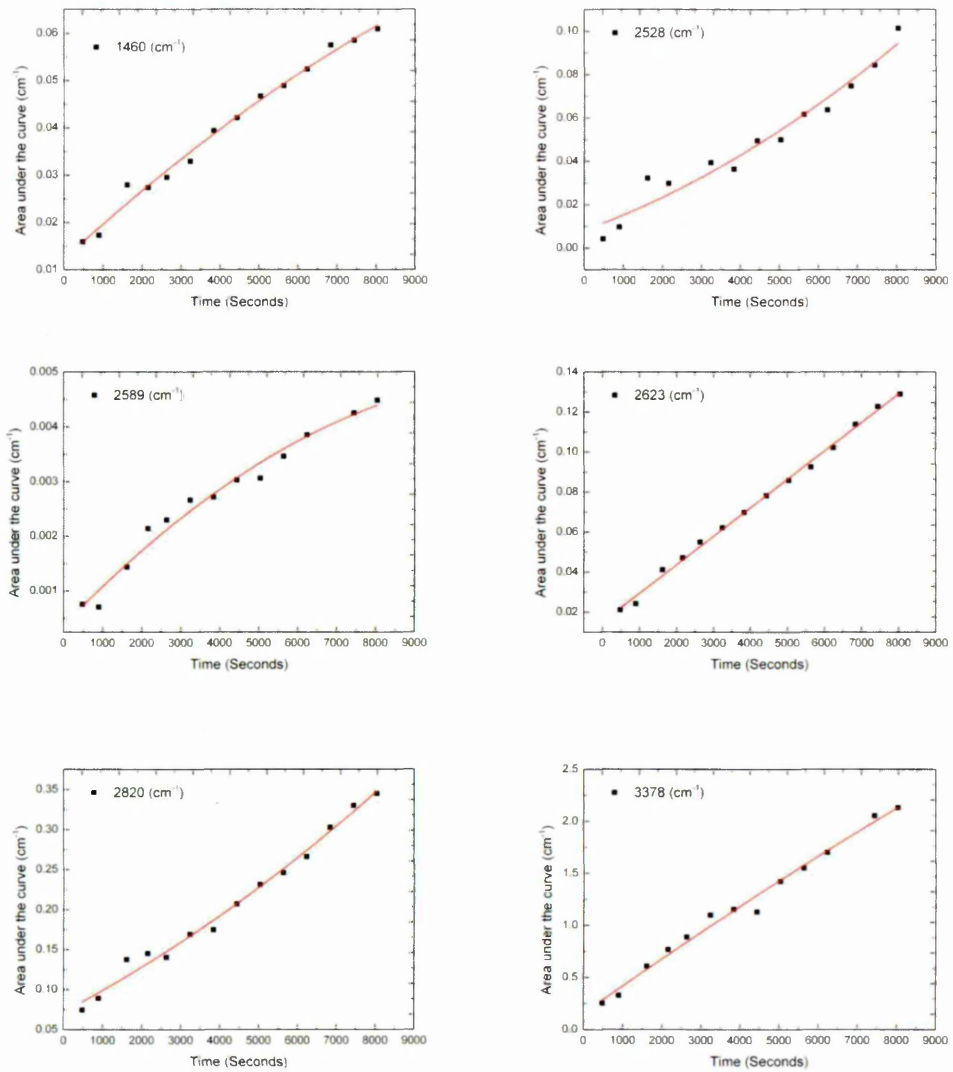

Figure 6.18 Evolution of absorption feature of $HCOOCH_3$ at 1460 cm^{-1}, CH_3OH at 2528 cm^{-1} CH_3OH at 2820 cm^{-1}, NH_3 at 2623 cm^{-1} and 3378 cm^{-1} during (1 keV electron) simultaneous irradiation-deposition of a NH_3:CH_3OH (1:1) mixture.

Ethylene glycol ($C_2H_6O_2$) at 1090 cm^{-1} and acetone ($(CH_3)_2CO$) at 1344 cm^{-1} were also synthesized in the simultaneous irradiation and deposition processes, the estimated column density of these species are 5.04×10^{14} molecules cm^{-2} for $C_2H_6O_2$ and 1.69×10^{14} molecules cm^{-2} for $(CH_3)_2CO$.

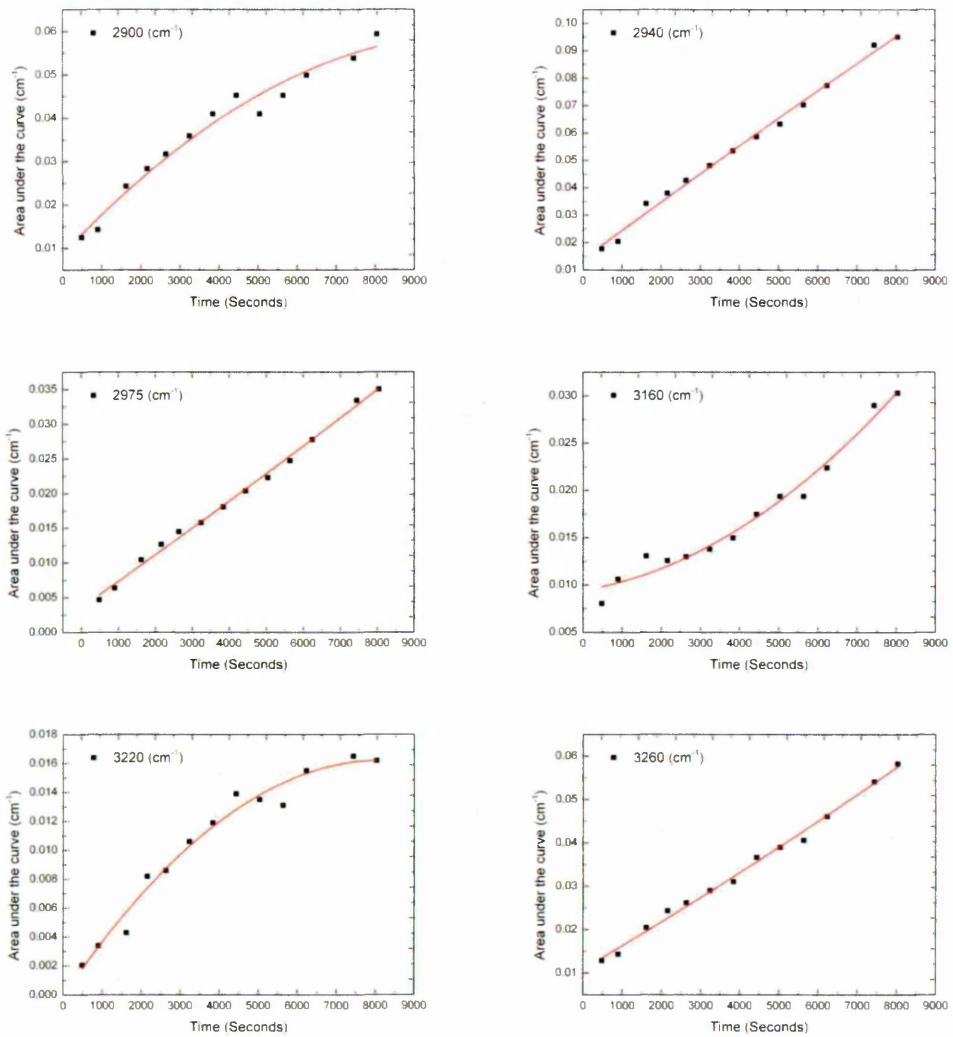

Figure 6.19 Evolution of absorption feature of C_2H_5N at 2900 cm^{-1}, C_3H_7N at 2940 cm^{-1}, NH_3 at 2975 cm^{-1}, CH_3OH at 3160, 3220 cm^{-1} and CH_3N at 3260 cm^{-1}, during (1 keV electron) simultaneousirradiation-deposition of a NH_3:CH_3OH (1:1) mixture.

Table 6.3 Column density of products formed after electron irradiation of ice film of CH3OH+ NH_3 (1:1) and simultaneous irradiation-deposition of the same mixture.

Products	Peak position (cm^{-1})	Integrated absorbance 'A' (cm molecules^{-1})	Column density (molecules cm^{-2})	
			Simultaneous Depo-irr	Ice film
$HCONH_2$	1386	0.68×10^{-17} [1]	$3.90 \pm 0.54 \times 10^{14}$	
CO	2134	1.1×10^{-17} [2]	1.73×10^{14}	9.42×10^{14}
CH_4	1304	7.0×10^{-18} [2]	5.90×10^{15}	1.57×10^{15}
CO_2	2342	7.6×10^{-17} [2]	2.05×10^{15}	7.90×10^{14}
Glycolaldehyde	1747	2.6×10^{-17} [2]	5.00×10^{13}	
CH_3OH	1031	1.94×10^{-17} [2]	5.94×10^{16}	Before irradiation 1.81×10^{17}
				After irradiation 1.5×10^{17}
CH_3CH_2OH	1045	1.9×10^{-17} [2]	1.65×10^{15}	1.34×10^{15}
HCOOH	1224	1.51×10^{-17} [2]	1.76×10^{14}	
$HCOOCH_3$	916	4.0×10^{-18} [2]	8.16×10^{15}	
Ethelyne glycol	1090	3.65×10^{-18} [2]	5.04×10^{14}	
H_2CO	1726	1.8×10^{-17} [2]	$8.50 \pm 0.23 \times 10^{14}$	$9.56 \pm 0.23 \times 10^{14}$
Acetone	1344	1.07×10^{-17} [2]	1.69×10^{14}	
OCN	2160	13×10^{-17} [3]	1.50×10^{15}	
HCO	1852	1.5×10^{-17} [2]	2.80×10^{14}	
NH_3	3213	1.2×10^{-17} [4]		Before irradiation 1.71×10^{17}
				After irradiation 1.43×10^{17}

1. Brucato et al. 2006 ; 2. Bennett and Kaiser 2011; Bennett et al. 2007 3. Hudson et al. 2001; 4. Zheng et al. 2008

The estimated column density of HCO at 1852 cm^{-1} was 2.80×10^{14} molecules cm^{-2}, but the column density estimation of the other stable intermediates were much more difficult to estimate due to the strong over lapping of fundamental absorption features of CH_3OH and NH_3. The evolution of absorption feature of $HCOOCH_3$ at 1460 cm^{-1}, CH_3OH at 2528 cm^{-1} CH_3OH at 2820 cm^{-1}, NH_3 at 2623 cm^{-1} and 3378

cm^{-1} during (1 keV electron) simultaneous irradiation-deposition of (NH_3:CH_3OH (1:1) mixture is shown in Figure 6.18. A polynomial fit of these evolution plots can elucidate the kinetics of the processes. The evolution of absorption feature of $HCOOCH_3$ at 1460 cm^{-1}, CH_3OH at 2528 cm^{-1} CH_3OH at 2820 cm^{-1}, NH_3 at 2623 cm^{-1} and 3378 cm^{-1} during (1 keV electron) simultaneous irradiation-deposition of (NH_3:CH_3OH (1:1) mixture are shown in **Figure 6.18**.

6.4.2 Thermal processing

Thermal processing of ice films of pure NH_3, pure CH_3OH, CH_3OH+ NH_3 (1:1) mixture and films formed after simultaneous irradiation-deposition of CH_3OH+ NH_3 (1:1) mixture was conducted at 5 K/ minute steps. During the thermal processing of un-irradiated CH_3OH ice film it is observed that basic fundamental band at 3261 cm^{-1} (OH stretch) (**Figure 6.20)** bifurcates and forms two sharp bands at 3182 $cm^{-1}$and 3297 cm^{-1} . The transformation starts around 100 K and at 120 K the ice film is completely transformed into polycrystalline ice, the phase transition occurring around 116 K.

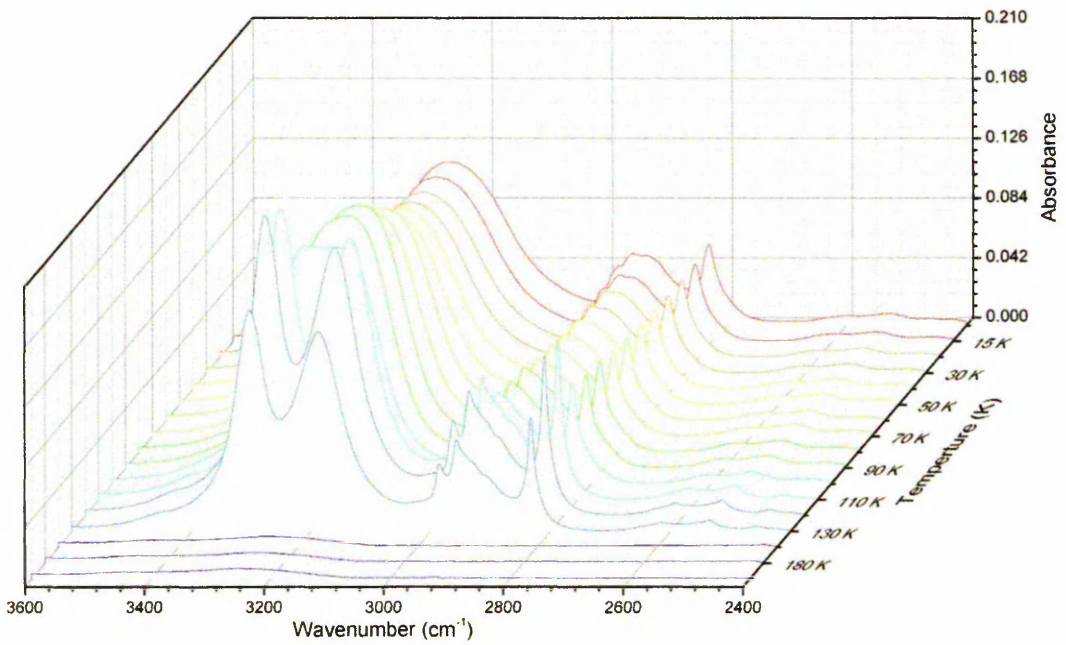

Figure 6.20 Thermal evolution of pure ice film of CH_3OH from 10 K to 200 K region (3600-2400 cm^{-1}).

other fundamental bands are also exhibiting similar behaviour of the feature at 2955 cm^{-1} (CH_3 stretch), bifurcates into two new bands at

3001 cm^{-1} and 2959 cm^{-1}, this transformation occurs at the same temperature ranges as mentioned above. The broad absorption feature at 2828 cm^{-1} (CH_3 stretch) and 2527 cm^{-1} (combination) transform into sharp bands around 120 K and all these features are stable until the sublimation. After warming up to 120 K, we cooled the ice back to 10 K and all the above mentioned features were highly stable and it is confirmed that phase change is irreversible in case of CH_3OH ice film deposited at 10 K.

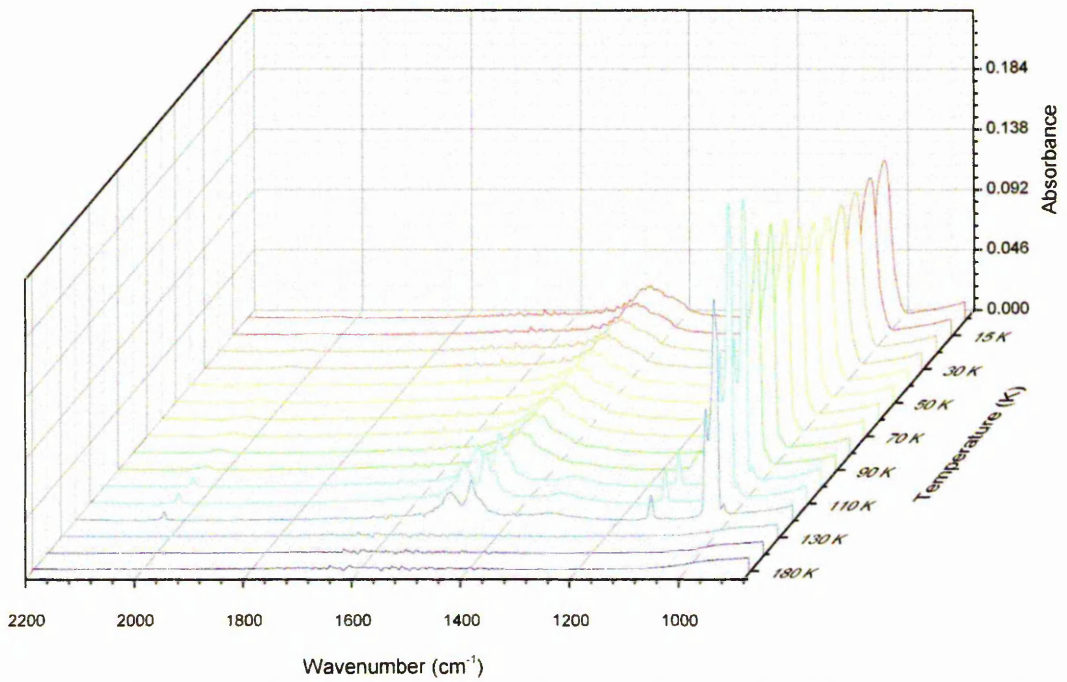

Figure 6.21 Thermal evolution of pure ice film of CH_3OH from 10 K to 200 K (region 2200-800 cm^{-1}).

Other fundamental features exhibiting the same behaviour are the features at 1029 cm-1 (CO stretch) which trifurcates into 1038 cm-1, 1072 cm-1 and 1010 cm-1, this features completely follows the same temperature ranges as mentioned above, and completely transforms at 120 K. The bands at 1130 cm-1 (CH3 deformation) and 1472 cm-1 (combination) depend on the temperature and transform from broad to

sharp bands at 120 K. With methanol sublimating around 130 K (chamber pressure ~ 10^{-9} mbar). The same procedure was followed for an ice film of pure CH_3OH.

The results of thermal processing of pure NH_3 ice film is shown in **Figure 6.22** and **6.23;** fundamental band at 1076 cm^{-1} resolved into four new peaks at 1050 cm^{-1} , 1090 cm^{-1}, 1108 cm^{-1} , 1117 cm^{-1}. The transformation started around 80 K and completed at 105 K, at 110 K the ice film is completely transferred into polycrystalline phase. Another broad band at 1626 cm^{-1} became sharp around 105 K and is shifted to 1637 cm^{-1}. The band at 3213 cm^{-1} and 3377 cm^{-1} change into a sharp peak at 80 K and in case of later peak there is a broad shoulder emerges at 65 K and sustains until sublimation.

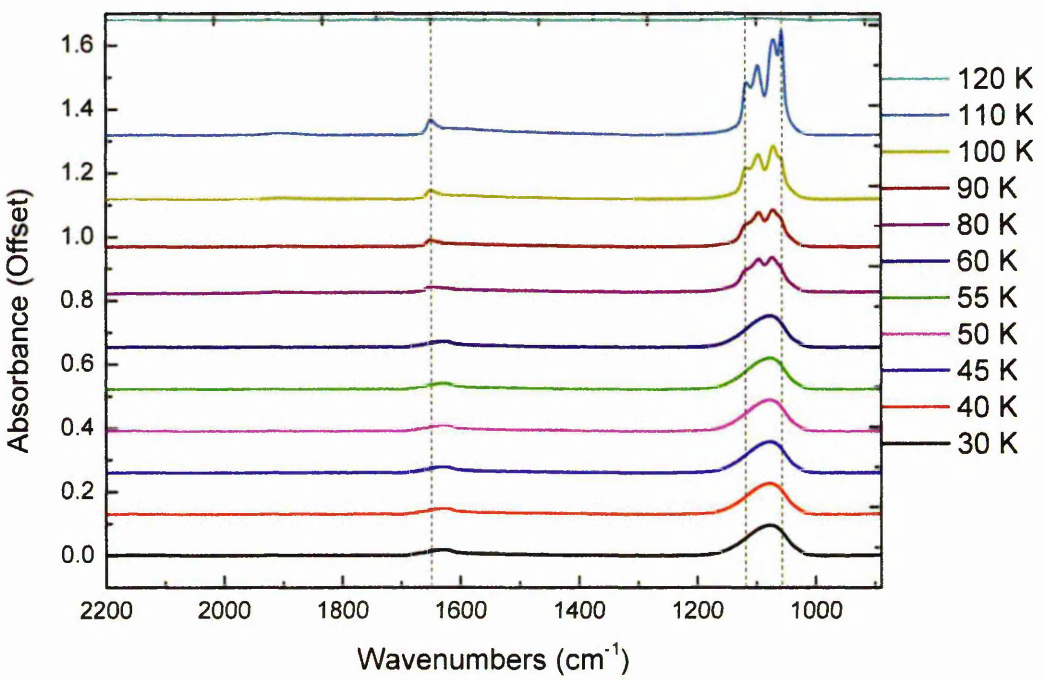

Figure 6.22 Thermal evolution of pure ice film of CH_3OH from 10 K to 200 K (region 2200-800 cm^{-1}).

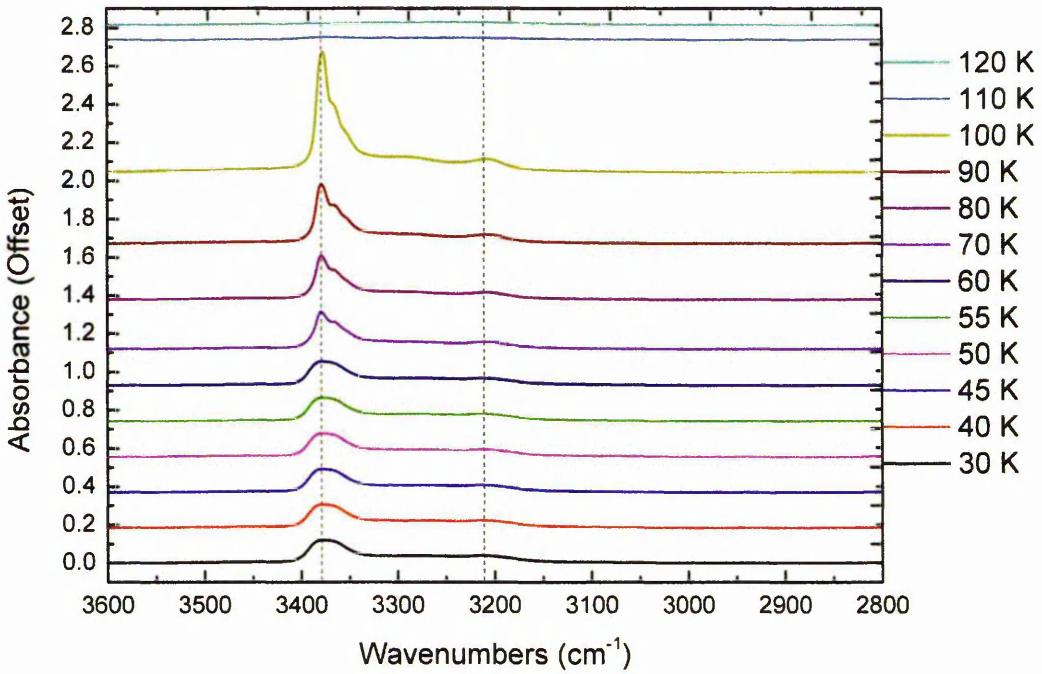

Figure 6.23 Thermal evolution of pure ice film of NH_3 from 10 K to 200 K (region 2200-800 cm^{-1}).

NH_3 sublimates at 120 K and no residue is left in the case of both the irradiated and unirradiated ice film of NH_3.

The ice film formed though the electron irradiation and simultaneous deposition of CH_3OH + NH_3 (1:1) mixture was thermally processed at 5 K/minute cycle. The fundamental absorption features of methanol and ammonia are exhibiting similar behaviour as in the pure ice and mixed ice films with only slight changes in peak positions. The fundamental band of CH_3OH at 3261 cm^{-1} (OH stretch) (**Figure 6.24),** 2955 cm^{-1} (CH_3 stretch), broad absorption feature at 2828 cm^{-1} (CH_3 stretch) and 2527 cm^{-1} (combination), are exhibiting same behaviour as in case of pure ice film. Other fundamental features at 1029 cm^{-1} (CO stretch), 1130 cm^{-1} (CH_3 deformation) and 1472 cm^{-1} (combination) evolve with temperature and transform from broad to sharp bands at 120 K. In addition the fundamental bands of NH_3 at 1076 cm^{-1} and 1626 cm^{-1} 3213 cm^{-1} and 3377 cm^{-1} exhibit the same behaviour as in

the case of pure ice film. In case of ice film formed after irradiation ice film of same mixture as well as in this case, all the features of both CH_3OH and NH_3 are maintained up to 110 K, see Figure 6.24and 6.25, then as the ice is cooled back to 10 K and all the above mentioned features remained showing that they were highly stable and it is confirmed that phase change is irreversible in this case.

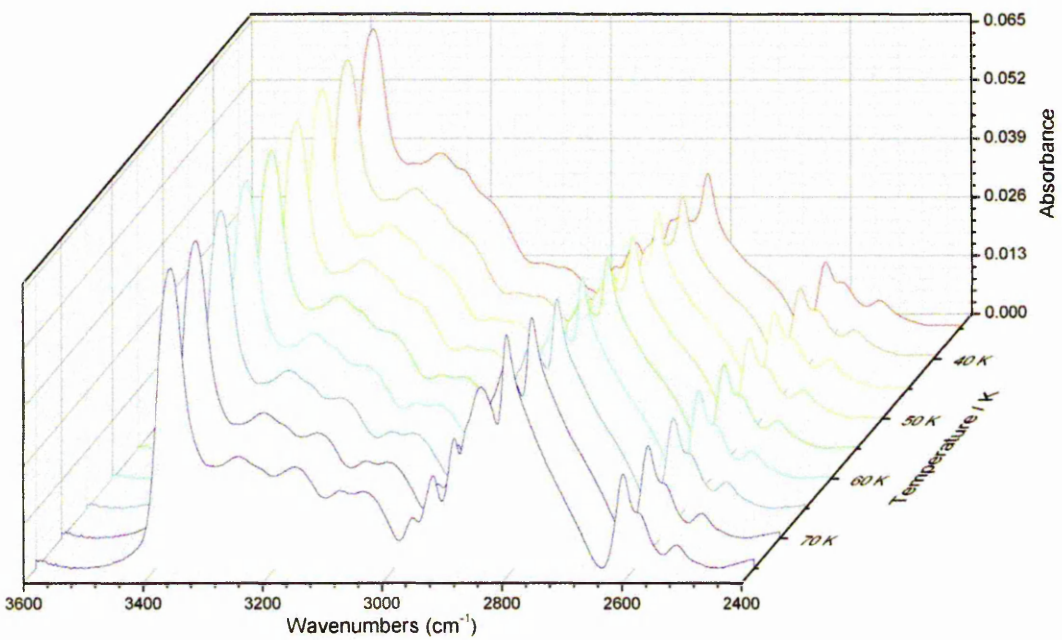

Figure 6.24 Evolution of products with thermal processing of the ice film, formed through simultaneous electron irradiation and deposition of NH_3:CH_3OH (1:1) mixture (3600-2400 cm^{-1} region).Ice film was annealed at a rate of 1 K/ min until sublimation, spectra from 30 K up to 70 K with 10 K interval is shown here.

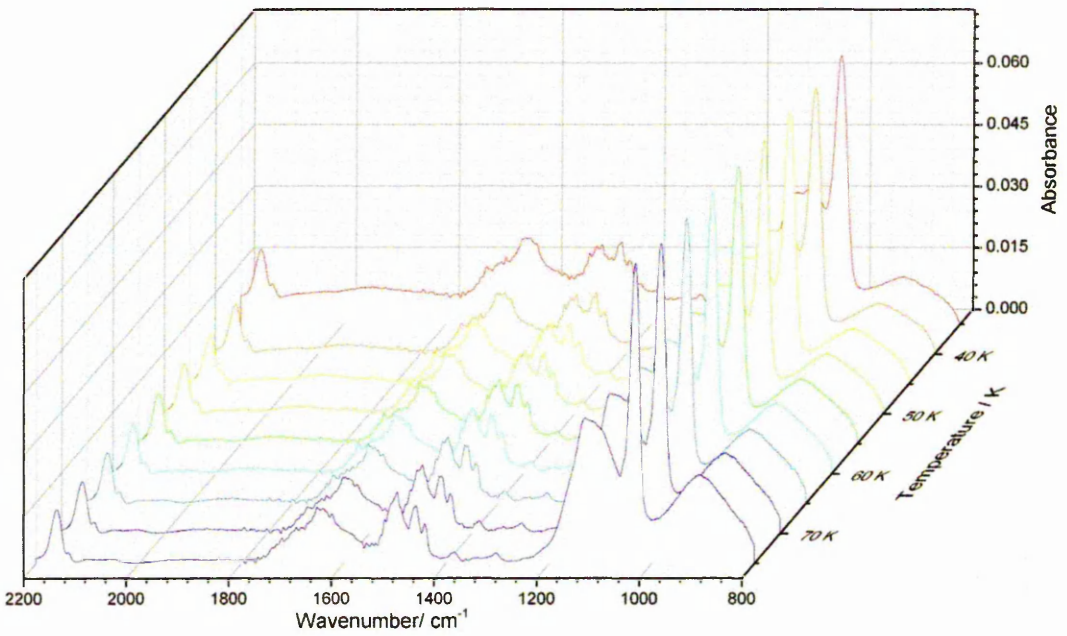

Figure 6.25 Evolution of products with thermal processing of the ice film formed through simultaneous electron irradiation and deposition of NH_3:CH_3OH (1:1) mixture (2200-800 cm^{-1} region).Ice film was annealed at a rate of 1 K/ min until sublimation, spectra from 30 K up to 70 K with 10 K interval is shown here.

Warming up the sample was found to release the condensed NH_3 when the ice temperature reaches around 90 K, with subsequent loss of OCN^- at about 105 K. Because of the complex composition of this ice resolving the thermal desorption of individual components of residues were difficult but a non-volatile residue of $(CN)_n$ compounds was retained at 300 K reveal the multiple steps in this kind of processes. A significant amount of volatile residue (5% of the total column density of products) was stable at room temperature. Residues were further processed thermally up to 350 K, the residue start to desorb above 390 K and completed the processes at 440 K. This highly stable residue mainly consist of $(CN)_n$ and C-C species, as evident from the broad absorption from 2400 to 2000 cm^{-1}.

6.5 Conclusion and astrophysical implications

The present study has demonstrated the effects of keV electrons on a methanol ammonia mixture ice film and simultaneous irradiation-deposition of the same mixture. Cosmic rays of energy ~ 5 GeV or greater, when interact with dark clouds generate secondary electrons with energies ranging from 1 to 5 keV, therefore, in both experiments the electronic energy is selectively restricted in the range of 1-5 keV. These electrons further process the ices through similar electronic transfer processes. It is therefore expected that the species found to form during the irradiation of our experiments can be expected to be produced in interstellar medium. Simultaneous electron irradiation and physisorption of amorphous 1:1 mixture of CH3OH, NH_3 ice at 10 K resulted in the formation of species such as OCN^-, CHN, HNO, HNO_3, H_2CO, $HCONH_2$, $HCOOCH_3$, C_2H_5OH, C_2H_5N, C_3H_7N, CH_3N, CH_2CHO, CH_2CHOH, HCOOH, C_2H_6O and several other intermediate compounds. Subsequent thermal processing of the irradiated samples results in the thermal evolution of products in a methanol ice matrix. Simultaneous irradiation and deposition have very high yield of production and has a greater efficiency to form large amount of radicals and stable products. To appreciate the cosmic ray interaction of interstellar ices, this experiment simulates the most probable reactions and therefore the result of the experiments can be incorporated into astrochemical models to investigate influence of such processes.

Whether OCN^- is formed via electron or proton irradiation, photolysis or even spontaneously, its significance is paramount since it may be involved in the formation of other, more complex compound.

In the ISM molecules can be pre-processed before adsorption onto the surface or post-processed by energetic interaction, both processes are crucial but analyzing such a process is complex. Therefore we investigate this phenomenon using step by

step approach, first we conducted electron irradiation of pure ice films of NH_3, CH_3OH and NH_3+CH_3OH (1:1) ice mixture and then simultaneous irradiation-deposition of NH_3+CH_3OH (1:1) mixture and then compared the kinetics of each process. It is found that simultaneous irradiation-deposition of NH_3+CH_3OH (1:1) mixture generate higher column densities of daughter species hence is more efficient than the processing of an ice film, moreover the number and variety of the complex species formed reveals the probabilities of several pathways of formation of such species. Simultaneous irradiation-deposition of mixtures of molecules are very important to understand and draw a comprehensible picture of energetic processing, particularly cosmic ray interactions in a cold dense molecular cloud like environment

CHAPTER 7

CONCLUSION AND FUTURE WORK

7.1 Summary of completed work

7.1.1 Temperature dependent VUV photo-absorption studies.

Temperature dependent VUV photo-absorption spectra of various molecular ices have been measured. The VUV photo-absorption cross-section of these molecules at 10 K has calculated and in addition, temperature dependent absorption of these molecular ices from 10 K to sublimation temperatures investigated in detail. The majority of the samples exhibit changes in absorption behaviour during the phase transformation, therefore spectra in VUV region are an excellent tool for investigating the morphology of molecular ice films.

It is difficult to distinguish the individual features of electronic transitions in condensed- amorphous ice spectra, but condensed phase electronic spectra can reveal the strength of hydrogen bonding as well as influence of intermolecular interactions. Hydrogen bonding is one of the major factors affecting the shift in an electronic transition from gas to solid phase; in the case of formamide it is observed that there is a considerable blue shift (~1.52 eV) in terms of valence transitions at 7.40 eV (298 K) to 8.92 eV (30 K), Rydberg transitions are suppressed in all the condensed phase spectra and quenching of Rydberg transitionsis observed in all the compounds (e.g. in case of formamide state between 7.40 eV 8.92 eV are quenched in the VUV spectra of

the condensed film), these effects are due to the molecular interactions in the condensed phase.

Temperature dependent variations in VUV spectra of methyl acetate and dimethyl ether are reported for the first time. Gas phase spectra of the molecules have been analysed but the changes in absorption with annealing of methyl acetate and dimethyl ether ice is not well understood. The works presented in this thesis provide an overall understanding of behaviour of molecular ice films of formamide, methyl formate, formic acid, methyl acetate, propionic acid, benzene and ozone in VUV region. In addition, temperature dependent VUV spectra of simple molecules such as benzene (C_6H_6), methyl formate ($HCOOCH_3$), formic acid (HCOOH), allyl alcohol and formamide ($HCONH_2$) are investigated and results are presented in this thesis.

The VUV spectrum of condensed ozone presented in this thesis is unique as it is the first VUV spectra of pure condensed ozone. An ice film of ozone was synthesized from pure oxygen and then annealed to form pure ozone ice matrix, the condensed phase spectra of ozone also reveals the nature of ozone clusters. Indeed our results confirm the existence of O_3-O complex formation and ozone dimer formation in ozone matrix discussed by Sivaraman et al. 2006. Photo-absorption cross-section data are incorporated to the Virtual Atomic and Molecular Data Centre (VAMDC) and is available at http://ipc.iisc.ernet.in/astroices/searchmolucule.php.

7.1.2 Electron irradiation of pure and mixed molecular ice films.

Electron processing of condensed ice films of pure and binary mixtures of simple molecules provides an insight into the electron driven chemistry in interstellar medium. In this thesis competition between different channels of electron driven

processes are investigated and verified. Electron driven chemical synthesis in formamide ice identifies an alternate channel of production for OCN^- from $HCONH_2$.

Electron irradiation and thermal processing of methyl formate and acetic acid were investigated to understand discrepancies in the observed abundance of these species in the ISM. It was observed that methyl formate is highly stable in interstellar conditions due to the morphology of the ice film as well as due to the molecular interactions between the molecules. Therefore survivability of condensed methyl formate is high compared to that of its structural isomers.

Electron irradiation of nitric oxide was investigated under different temperature conditions to understand the influence of formation and stability of radicals in such systems. Irradiation at 30 K and 11.5 K produced entirely different results and is attributed to the influence of radicals. Several set of oxides of nitrogen are formed as a result of electron processing. However the absence of O_3 was noted, in these studies compared to earlier work. Thermal evolution of newly formed products was also studied; thermal processing of an unirradiated nitric oxide sample revealing a phase transformation at 65 K.

Electron irradiation of an amorphous 1:1mixture of CH_3OH, NO ice at 28 K resulted in the formation of species such as CHN, HNO_2 and $C_2N_2O^+$ C_2N_2O, HNO_3, N_2O_3, NO_2, N_2O_5 N_2O_3, C_2O and O_3. Thermal processing of the irradiated sample, results in the thermal evolution of these products in a methanol ice matrix. Thermal evolution of such species from ice surface is crucial to understand the chemistry of PDRs and hot molecular cores in which icy grain mantle are subject to heating due to the presence of a parent star.

VUV spectroscopy of condensed films of pure simple molecules such as SO_2, OCS, CS_2, HNO_3 and NO are planned in the next beam run. Photo-absorption cross-

section of these molecules will be incorporated to the Virtual Atomic and Molecular Data Centre. VUV photo processing of water mixtures and polarization dependent studies are also planned.

7.1.3 Simultaneous electron irradiation and physisorption of binary mixtures of simple molecules.

Simultaneous electron irradiation and physisorption of amorphous 1:1 mixture of CH_3OH, NH_3 ice at 28 K resulted in the formation of species such as CHN, HNO_2, HNO_3, H_2CO. Further thermal processing of the irradiated sample results in the thermal evolution of these products in case of a methanol ice matrix. Simultaneous irradiation and deposition have very high yields of production and has a greater efficiency to form large amount of radicals and stable products than irradiation of a pure ice film. To appreciate the cosmic ray interaction of interstellar ices, this experiment simulates the most probable reactions and therefore the result of my experiments can be incorporated into astrochemical models to investigate influence of such processes. Further simultaneous irradiation-deposition experiments involving other compounds are planned for understanding such complex processes.

7.2 Modification of Temperature programmed desorption apparatus.

A Temperature Programmed Desorption apparatus was designed by modifying and adapting an already existing UHV chamber in the Molecular Physics laboratory at The Open University, UK. Figure 7.1 shows the schematic of top view of the chamber. A stainless steel UHV chamber used for electron irradiation studies has been modified with intelligent temperature controlling systems (Oxford instruments). An

ITC 502 controller along with a high precision silicon diode (Lakeshore 371), K-P type thermocouples and precision heating mechanism was employed to generate a temperature programmed desorption apparatus. Temperature measurements from three independent thermocouple junctions situated very close to a substrate are controlled by ITC 502.

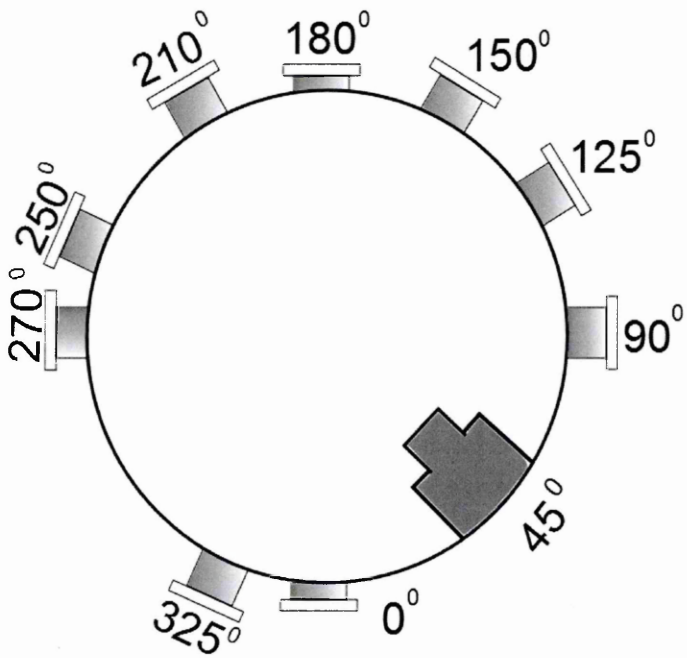

Figure 7.1 Top view of the TPD chamber

The substrate is covered by a radiation shield and the chamber was adapted for back ground deposition. A quadrupole mass spectrometer (Hiden Analytical) was used to record the desorbing species from the substrate; line-of-sight mass spectrometry was employed to improve the sensitivity of TPD. The substrate is directed towards the quadrupole and kept at an optimal distance of 50 mm from the substrate.

Temperature conditions are achieved by using a closed cycle helium cryostat (Leybold), which can readily attain <10 K. The cryostat is connected to a sample holder tip made of pure OFHC copper coated with gold. In transmission mode

experiments we used ZnSe s a substrate. UHV conditions are achieved by combining a MagLev turbo with a backing of rotary vane pump. Pressure conditions of 5 x 10^{-10} mbar are attained after baking. The chamber was baked at 200^0c and kept pumping for 2 weeks to attain moisture less clean conditions. Heating lamps are employed to keep the ambient air moisture free. A load lock mechanism is used to change the substrates without breaking the vacuum. A separate turbo pump backed with rotary is used to pump the dosing line. TPD chamber with load locking mechanism is shown in **Figure 7.2.**

Conditions inside the UHV chamber are calibrated using the residual gas measurements. Constituents of residual gas before and after baking are shown in Figure 7.4 and 7.5. The condition after baking is highly stable and suitable for a TPD experiment.

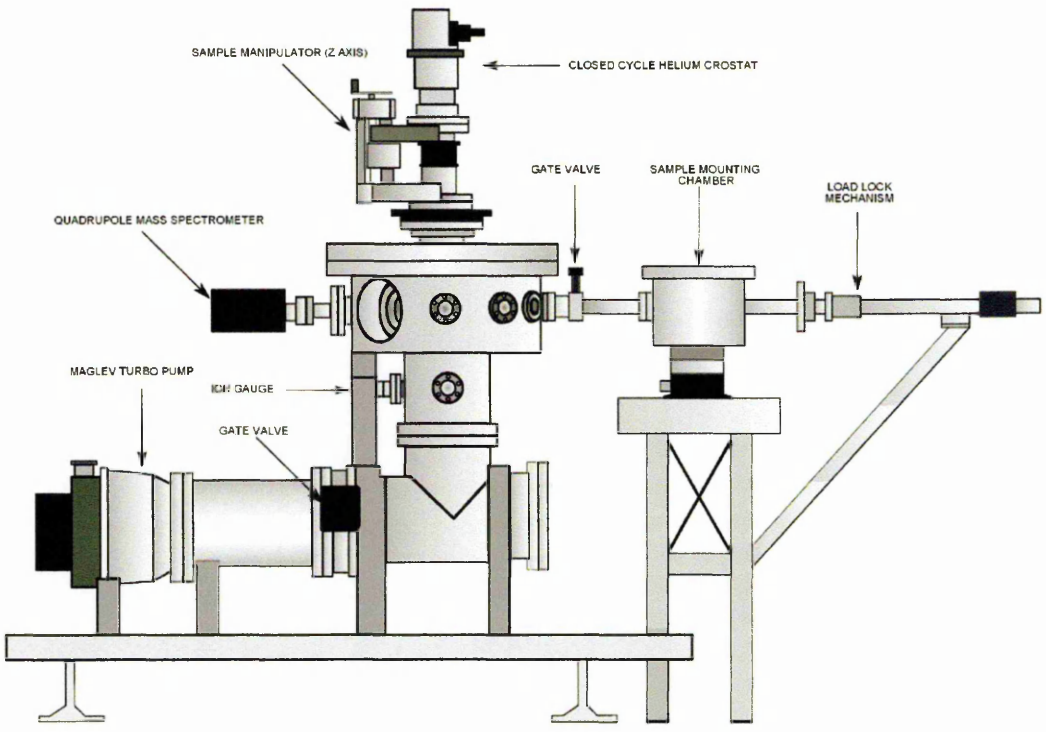

Figure 7.2 UHV chamber for conducting temperature, programmed desorption

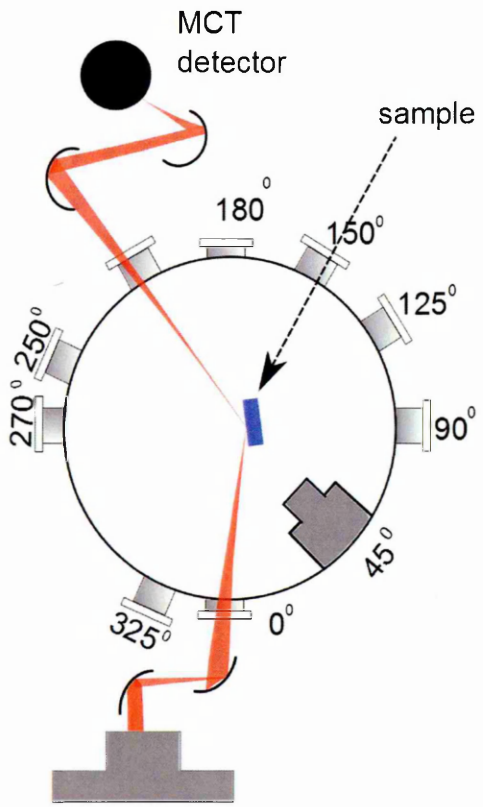

Figure 7.3 Reflection absorption infrared arrangements on TPD apparatus.

A set of preliminary TPD experiments were carried out with water and nitric oxide. Preliminary results obtained from the nitric oxide (NO) are discussed here. The experiments were carried out using the TPD apparatus at The Open University, UK. Using a closed cycle helium cryostat the sample substrate was cooled down to 10 K while the apparatus was maintained at 8.0 x 10^{-10} mbar pressure. A chemically inert and mid-infrared (2-25 μm) transparent Zinc Selenide (ZnSe) window was used as the substrate onto which NO (99.98 % Fisher Scientific) was deposited at 10 K. Using pressure-time deposition method, NO sample at 298 K is introduced at 1 x 10^{-6} mbar (1 Langmuir) pressure for 100 seconds.

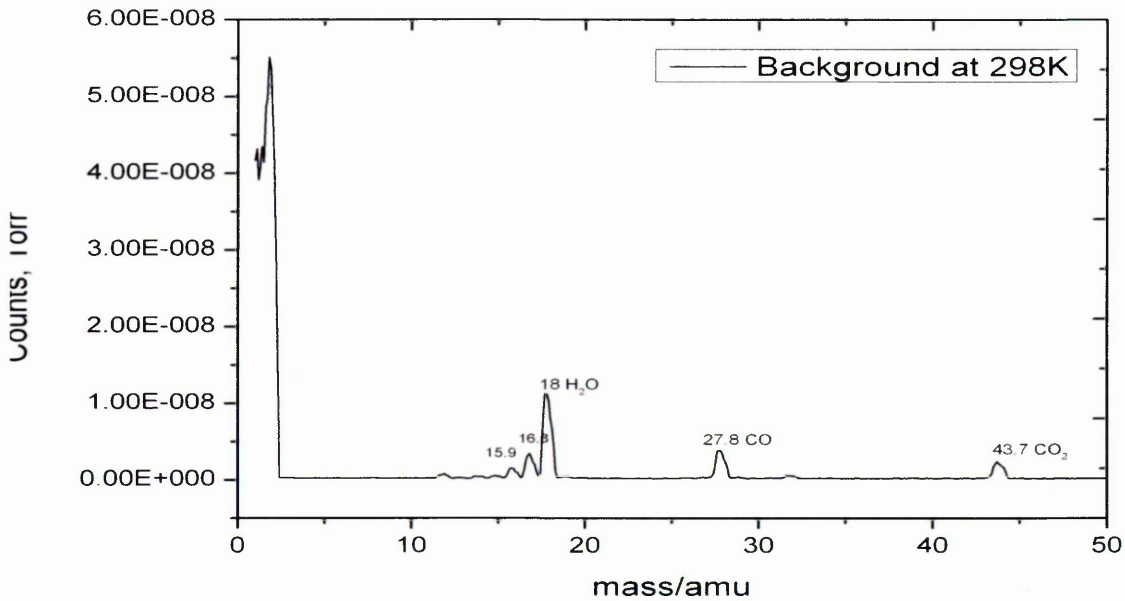

Figure 7.4 Mass spectrum of residual gas component of TPD apparatus before baking.

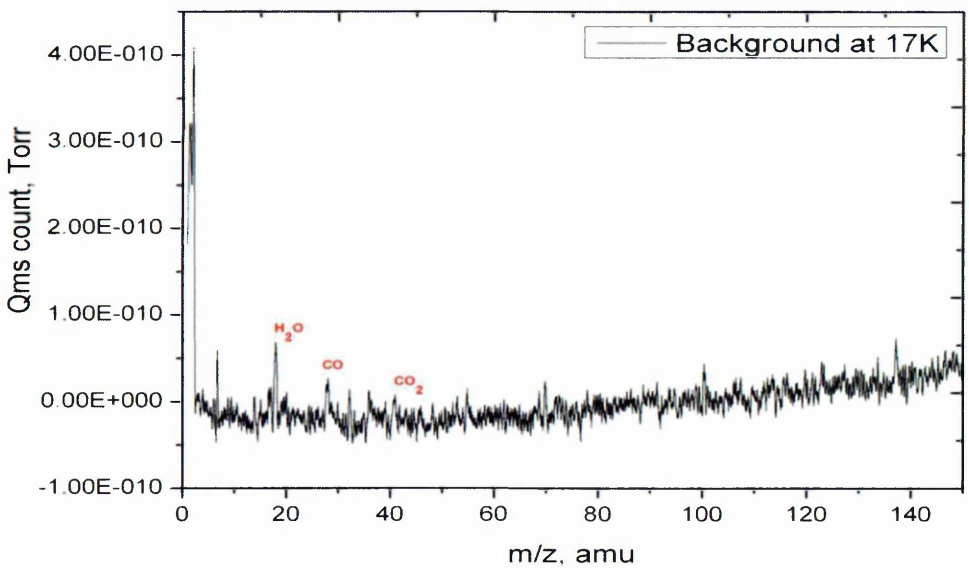

Figure 7.5 Mass spectrum of residual gas component of TPD apparatus after baking.

By theoretical estimates the film formed should be 90 monolayers on a 20 mm diameter substrate. The formed sample is processed thermally with a pre-programmed desorption mechanism. ITC 502 controller controls the heating through a precision

PID control. The sample is heated at a linear rate of 1 K per minute and the desorbed sample is measured by line-of-sight mass spectrometry.

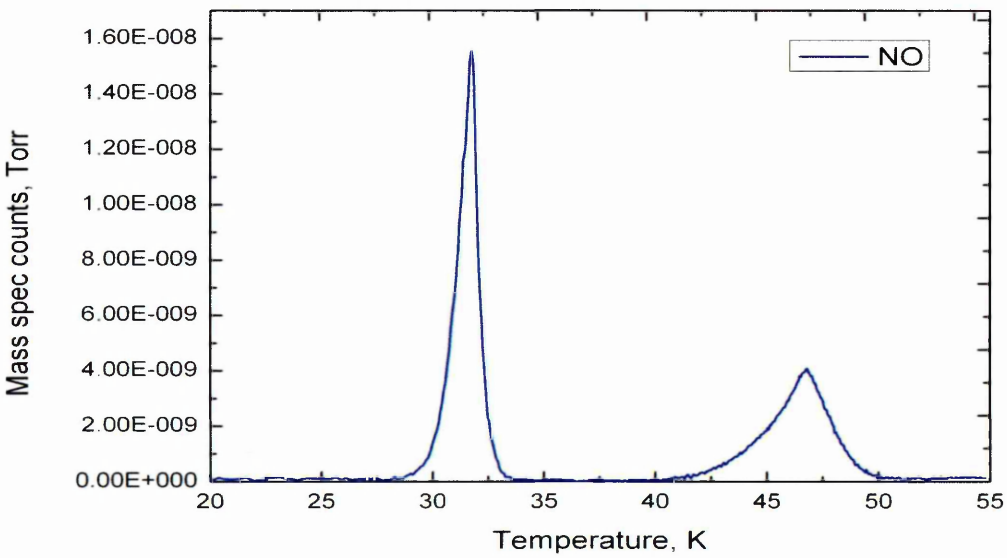

Figure 7.6 Temperature programmed desorption curve of pure NO from ZnSe substrate. Peaks at 32 K and 46 K correspond to two different adsorption sites.

The resultant TPD curve of NO on a ZnSe substrate is shown in Figure 7.6. Nitric oxide has two desorption peaks, a sharp peak centred around 32 K and a broad less intense peak centred around 46 K. This result is preliminary and further investigations are necessary to confirm the effect of surface coverage, rate of heating and influence of substrate etc.

Temperatures programmed desorption of NO + H_2O mixtures, co-deposited and layer deposited on single crystal substrate is a future priority. TPD experiments of methanol mixtures and simple molecules are also planned. A modified setup with RAIRS will be employed for better understanding of the processes, Figure 7.3 shows the schematic of RAIRS aligned with the TPD apparatus. More generally, you should note that coincident desorption of two species at temperatures well above their normal

desorption temperatures is characteristic of the decomposition of a more complex surface species.

7.3 Final conclusions

Understanding the complex organic synthesis prevalent in the interstellar medium remains one of the principal challenges of current astrochemistry. Laboratory astrochemistry experiments discussed in this thesis support various observational evidences. Spectroscopic investigation of ices at cryogenic conditions reveals the influence of low temperature chemistry in the formation of complex molecules from simple atoms and radicals. Results discussed in this thesis propose new surface mechanisms and also quantify the probability conditions of surface processes in a controlled environment. In addition the mid-IR spectra and VUV absorption cross-sections of astrochemically important molecules discussed in this thesis can be used as reference spectra for observations in these wavelength regions. Therefore, simulating the ambient interstellar conditions in the laboratory and monitoring the energetic processing of interstellar ice analogues and to record spectra of interstellar ice analogues provides an insight into Astrochemistry and hence the Astrobiology of the Universe.

REFERENCES

Allamandola, Louis J.; Bernstein, Max P.; Sandford, Scott A.; Walker, Robert L. 1999., Evolution of interstellar ices, *Space Science Reviews*, v. 90, Issue 1/2, p. 219-232 [Doi: 0.1023/A:1005210417396]

Allan, D. and Clark, S., 1999., Impeded Dimer Formation in the High-Pressure Crystal Structure of Formic Acid. *Physical Review Letters*, 82(17), pp.3464–3467.

Bahou, M., Schriver-Mazzuoli, L. & Schriver, a., 2001., Infrared spectroscopy and photochemistry at 266 nm of the ozone dimer trapped in an argon matrix. *The Journal of Chemical Physics*, 114(9), p.4045.

Banwell, C.N and Elaine M. Mc Cash, 1995., Fundamentals of molecular spectroscopy, Mc Graw-Hill, London.

Bass, A.M.; Ledford, A.E., Jr.; Laufer, A.H., 1976., J. Res. *Natl. Bur. Std.*, 80A, 143.

Beckers, H.; Zeng, X.; Willner, H., 2010., Intermediates Involved in the Oxidation of Nitrogen Monoxide: Photochemistry of the, *Chem. Eur. J.*, 16, 5, 1506.

Bennett, C. J., Hama, T., Kim, Y. S., Kawasaki, M., & Kaiser, R. I., 2011., Laboratory studies on the formation of formic acid (HCOOH) in interstellar and cometary ices., *The Astrophysical Journal*, *727*(1), 27. [Doi:10.1088/0004 637X/727/1/27]

Bennett, C.J. & Kaiser, R.I., 2005., Laboratory Studies on the Formation of Ozone (O 3) on Icy Satellites and on Interstellar and Cometary Ices. *The Astrophysical Journal*, 635(2), pp.1362–1369.

Bennett, C.J. & Kaiser, R.I., 2007., On the formation of glycolaldehyde (HCOCH2 OH) and methyl formate (HCOOCH3) in interstellar ice analogs. *The Astrophysical Journal*, 661, 899-909

Bennett, C.J. & Kaiser, R.I., 2007., The Formation of Acetic Acid (CH3COOH) in Interstellar Ice Analogs. *The Astrophysical Journal*, 660(2), pp.1289–1295. [Doi: 10.1086/513267]

Bennett, C.J. et al., 2011., Laboratory studies on the formation of formic acid (HCOOH) in interstellar and cometary ices. *The Astrophysical Journal*, 727(1), p.27. [Doi: 10.1088/0004-637X/727/1/27]

Bergin, E.A., 2000., Implications of Submillimeter Wave Astronomy Satellite Observations for Interstellar Chemistry and Star Formation. *The Astrophysical Journal*, 539(2), pp.L129–L132.

Bernstein, M. P., Sandford, S. A., & Allamandola, L. J., 1996., "Hydrogenated Polycyclic Aromatic Hydrocarbons (Hn-PAHs) and the 2940 and 2850 Wavenumber (3.40 and 3.51 Micron) Infrared Emission Features", *The Astrophysical Journ*al., 472, L127-L130

Bernstein, M. P., Sandford, S. A., Allamandola, L. J., Chang, S., & Scharberg, M. A., 1995., "Organic Compounds Produced by Photolysis of Realistic Interstellar and Cometary Ice Analogs Containing Methanol", *The Astrophysical Journal.*, 454, 327-344

Bernstein, Max P.; Sandford, Scott A.; Allamandola, Louis J.; Chang, Sherwood; Sch arberg, Maureen A., 1995., Organic Compounds Produced by Photolysis of Realistic Interstellar and Cometary Ice Analogs Containing Methanol, *The Astrophysical Journal* 454, 327. [Doi: 10.1086/176485]

Bibart, C.H.; Ewing, G.E., 1974., *Vibrational spectrum of gaseous N2O3, J. Chem. Phys.*, 61, 4, 1293

Bisschop, S. E., Fuchs, G. W., Boogert, C., van Dishoeck, E. F., & Linnartz, H. 2007., Infrared spectroscopy of HCOOH in interstellar ice analogues, Astronomy *and Astrophysics*, *470*(2), 749–759. [Doi: 10.1051/0004-6361:20077464]

Bisschop, S. E., Fuchs, G. W., van Dishoeck, E. F., & Linnartz, H., 2007., H-atom bombardment of CO_2, HCOOH, and CH_3CHO containing ices. *Astronomy and Astrophysics*, *474*(3), 1061–1071. [Doi: 10.1051/0004-6361:20078210]

Bossa, J A, P. Theulé, F. Duvernay, F. Borget, and T. Chiavassa, 2008., *Astronomy and Astrophysics*, 492, 719–724. [Doi: 10.1051/0004-6361:200810536]

Bottinelli, S., Ceccarelli, C., Lefloch, B., Williams, J. P., Castets, A., Caux, E., Tielens, A. G. G. M., 2004., Complex Molecules in the Hot Core of the Low Mass Protostar NGC 1333 IRAS 4A. *The Astrophysical Journal*, *615*(1), 354–358. [Doi: 10.1086/423952]

Brown, R. D., Crofts, J. G., Godfrey, P. D., Gardner, F. F., Robinson, B. J., & Whiteoak, J. B., 1975., Discovery of interstellar methyl formate, *The Astrophysical Journal*, *197*, L29. [Doi: 10.1086/181769]

Brucato J. R., G. A. Baratta and G. Strazzulla, An infrared study of pure and ion irradiated frozen formamide, *Astronomy and Astrophysics*, 455, 2, 2006., [http://dx. DOI.org/10.1051/0004-6361:20065095]

Bruston P, 1994., *Physical Chemistry Chemical Physics*, *12*(48), 15734–43. [Doi: 10.1039/c0cp00051e]

Callahan, M. P., Gerakines P. A., M. G. Martin, Z. Peeters, and R. L. Hudson. 2013., "Irradiated benzene ice provides clues to meteoritic organic chemistry." *Icarus* 226 (2): 1201-1209. [Doi: 10.1016/j.icarus.2013.07.033]

Cernicharo, J. et al., 2001., Infrared Space Observatory's Discovery of C4H2, C6H2, and Benzene in CRL 618. *The Astrophysical Journal*, 546(2), pp.L123–L126.

Cernicharo, J., Heras, A. M., Tielens, A. G. G. M., Pardo, J. R., Herpin, F., Guélin, M., & Waters, L. B. F. M., 2001., Infrared Space Observatory'sDiscovery of C4H2, C6H2, and Benzene in CRL 618, *The Astrophysical Journal*, *546*(2), L123–L126. [Doi: 10.1086/318871]

Chapman, D. 1956., The infrared spectra of liquid and solid formic acid. *Journal of the Chemical Society (Resumed)* 48, 225–229. [Doi: 10.1039/jr9560000225]

Chen, W., 1992., Photolysis of nitric acid in solid nitrogen. *The Journal of Chemical Physics*, 97(10), p.7167. [Doi: /jcp/97/10/10.1063/1.463541].

Chen, W.; Liu, J.; Ng, C.Y., 2003., Vacuum Ultraviolet Pulsed Field Ionization-Photoelectron Study for N2O+ in the energy range of 16.3-21.0 eV, *J. Phys. Chem. A*, 107, 40, 8086.

Churchwell, E., Nash, A., Rahe, J., Walmsley, C. M., Lochner, O., & Winnewisser, G. 1980., Abundances and excitation of interstellar methyl formate. *The Astrophysical Journal*, *241*, L169. [Doi: 10.1086/183384]

Chyba C. F., Hand K. P., 2005., Annual *Review of Astronomy and Astrophysics*, 43, 31

Cole, C. a., Wehres, N., Yang, Z., Thomsen, D. L., Snow, T. P., & Bierbaum, V. M. 2012., A gas-phase formation route to interstellar trans-methyl formate, *The Astrophysical Journal*, *754*(1), L5. [Doi:10.1088/2041-8205/754/1/L5]

Crovisier, J., Bockel e-Morvan, D., Colom, P., Biver, N., Despois, D., Lis, D. C., & 2004., The composition of ices in comet C/1995 O1 (Hale-Bopp) from radio spectroscopy., *Astronomy and Astrophysics*, *418*(3), 1141–1157. [Doi:10.1051/0004-6361:20035688]

Cyriac, J., & Pradeep, T. 2005., Structural transformation in formic acid on ultra cold ice surfaces, *Chemical Physics Letters*, *402*(1-3), 116–120. [Doi:10.1016/j.cplett.2004.12.003]

Black J. and Dalgarno A., 1977, *The Astrophysical Journal Suppl.,* 34, 405

Dawes, A., Mukerji, R. J., Davis, M. P., Holtom, P. D., Webb, S. M., Sivaraman, B., Mason, N. J. 2007., Morphological study into the temperature dependence of solid ammonia under astrochemical conditions using vacuum ultraviolet and Fourier-transform infrared spectroscopy. *The Journal of chemical physics*, *126*(24), 244711. [Doi:10.1063/1.2743426]

Demyk, K., Dartois, E., D'Hendecourt, L., 1998., Astronomy and Astrophysics, 339, 553, *Astronomy and Astrophysics,* 339 553.

Dows D.A., 1957., Torsional vibrations in CO2 and N2O crystals, *Journal of Chemical Physics*, 26, pp. 745 [Doi: 10.1016/0371-1951(59)80033-3]

Draine, B. T., & Salpeter, E. E. 1979., On the physics of dust grains in hot gas. *The Astrophysical Journal*, *231*, 77. [Doi: 10.1086/157165]

Ehrenfreund, P., & Charnley, S. B. 2000., Organic molecules in the interstellar medium, comets, and meteorites: A Voyage from Dark Clouds to the Early Earth. *Annual Review of Astronomy and Astrophysics*, *38*(1), 427–483. [Doi:10.1146/annurev.astro.38.1.427]

Ellder, J., Friberg, P., Hjalmarson, A., Hoglund, B., Johansson, L. E. B., Olofsson, H., Irvine, W. M. 1980., On methyl formate, methane, and deuterated ammonia in Orion A., *The Astrophysical Journal*, *242*, L93. [Doi: 10.1086/183410]

Fateley W.G., Bent H.A., B. Crawford, 1959., Infrared spectra of the frozen oxides of nitrogen, *Journal of Chemical Physics,* 31, pp. 204

Feng, R., Cooper, G. & Brion, C.., 2002., Dipole (e,e+ion) spectroscopic studies of benzene: absolute oscillator strengths for molecular and dissociative photoionization in the VUV and soft X-ray regions. *Journal of Electron Spectroscopy and Related Phenomena*, 123(2-3), pp.211–223.

Flakus, H. T., & Stachowska, B. 2006., A systematic study of polarized IR spectra of the hydrogen bond in formic acid crystals., *Chemical Physics*, *330* (1-2), 231–244. [Doi:10.1016/j.chemphys.2006.08.019]

Friedel, D. N., & Widicus Weaver, S. L. 2012., Complex Organic Molecules At High Spatial Resolution Toward Orion-KL. Ii. Kinematics., *The Astrophysical Journal Supplement Series*, *201*(2), 17. [Doi:10.1088/0067-0049/201/2/17]

Gadermann, M., Vollmar, D.& Signorell, R. 2007., Infrared spectroscopy of acetic acid and formic acid aerosols: pure and compound acid/ice particles., *Physical chemistry chemical physics 9*(32), 4535–44. [Doi: 10.1039/b704600f]

Garrod, R. T., & Herbst, E. 2006., Formation of methyl formate and other organic species in the warm-up phase of hot molecular cores. *Astronomy and Astrophysics*, *457*(3), 927–936. [Doi: 10.1051/0004-6361:20065560]

Gerakines P.A., Moore M.H., Hudson R.L., 2004., Ultraviolet photolysis and proton irradiation of astrophysical ice analogs containing hydrogen cyanide, *Icarus*, Volume 170,1, 202-213, [Doi: 10.1016/j.icarus.2004.02.005]

Gerakines, P. A., M. H. Moore, and R. L. Hudson. 2000., "Carbonic Acid Production in H2O:CO2 ices UV Photolysis vs Proton Bombardment." *Astronomy and Astrophysics* 357 793-800

Gerakines, P. A., M. H. Moore, and R. L. Hudson. 2001., "Energetic Processing of Laboratory Ice Analogs: UV Photolysis versus Ion Bombardment." *Journal of Geophysical Research* 106 (E12): 33381-33386

Gibb, E., Nummelin, A., Irvine, W. M., Whittet, D. C. B., & Bergman, P. 2000., Chemistry of the Organic rich Hot Core G327.3−0.6. *The Astrophysical Journal*, 545(1), 309–326. [Doi: 10.1086/31780]

Gibb, E.L. et al., 2000., An Inventory of Interstellar Ices toward the Embedded Protostar W33A. *The Astrophysical Journal*, 536(1), pp.347–356.

Gingell J. M., N. J. Mason, H. Zhao, I. C. Walker, M. R. F. Siggel, 1997., VUV optical-absorption and electron-energy-loss spectroscopy of formamide , *Chem. Phys.*, 220, 191-205,.

Gingell, J. et al., 1997., VUV optical-absorption and electron-energy-loss spectroscopy of formamide. *Chemical Physics*, 220(1-2), pp.191–205. [Doi: 10.1016/S0301-0104(97)00137-7]

Goncharov, A., Manaa, M., Zaug, J., Gee, R., Fried, L., & Montgomery, W. 2005., Polymerization of Formic Acid under High Pressure. *Physical Review Letters*, *94*(6), [Doi:10.1103/PhysRevLett.94.065505]

Green Sheldon, 1981., Interstellar chemistry: Exotic molecules in space, *Ann. Rev. Phys.*, 32:103-38, 10.1146/annurev.pc.32.100181.000535

Guillory and Bernstein, 1975., Infrared spectrum of matrix isolated nitric acid, *J. Chem. Phys.* 62, 1058, [http://dx.doi.org/10.1063/1.430519]

Gupta Devinder, Lang Wang, Leonrd M. Hanssen, Jack J. Hsia, Raju U. Datla, 1995., *NIST special publications* 260-122,], http://www.nist.gov/srm/upload/SP260-122.

Hunt H. D., W. T. Simpson, 1953., Spectra of Simple Amides in the Vacuum Ultraviolet, *J. Am. Chem. Soc.*, 75 (18), 4540-4543.

Hamada Y., Hashiguchi, K., Tsuboi, M. Koga, Y. Kondo, S., 1984., Pyrolysis of amines: Infrared spectrum of methyleneimine, *J. Mol. Spectrosc.*, 105, 1, 70. [Doi: 10.1016/0022-2852(84)90104-8]

Heller J.M., L.R. Painter, R.D. Birkhoff, 1979., Optical studies of liquid formamide in the vacuum ultraviolet, *J. Chem. Phys.*, 71 (11), 4641-4645,

Herbst, E., 1995., Chemistry in the Interstellar Medium. *Annual Review of Physical Chemistry*, *46*(1), 27–54. [Doi:10.1146/annurev.pc.46.100195.000331]

Herbst, E., 2005., Chemistry of star-forming regions, *The Journal of Physical Chemistry. A*, 109(18), 4017–29. [Doi: 10.1021/jp050461c]

Herbst, E., & van Dishoeck, E. F., 2009., Complex Organic Interstellar Molecules, *Annual Review of Astronomy and Astrophysics*, *47*(1), 427–480. [Doi: 10.1146/annurev-astro-082708-101654]

Hollenbach, D. J., & Tielens, a. G. G. M., 1997., Dense photodissociation regions (PDRs) 1. *Annual Review of Astronomy and Astrophysics*, *35*(1), 179–215. [Doi:10.1146/annurev.astro.35.1.179]

Hollis, J. M., Lovas, F. J., & Jewell, P. R., 2000., Interstellar Glycolaldehyde: The First Sugar., *The Astrophysical Journal*, *540*(2), L107–L110. [Doi: 10.1086/312881]

Hollis, J. M., Pedelty, J. A., Boboltz, D. A., Liu, S.-Y., Snyder, L. E., Palmer, P., Jewell, P. R., 2003., Kinematics of the Sagittarius B2 (N-LMH) Molecular Core. *The Astrophysical Journal*, *596*(2), L235–L238. [Doi:10.1086/379315]

Holtom, P.D. et al., 2005., A Combined Experimental and Theoretical Study on the Formation of the Amino Acid Glycine (NH 2 CH 2 COOH) and Its Isomer (CH 3 NHCOOH) in Extraterrestrial Ices. *The Astrophysical Journal*, 626(2), pp.940–952. [Doi: 10.1086/513267]

Holtzberg, F., Post, B., & Fankuchen, I. 1953., The crystal structure of formic acid. *Acta Crystallographica*, *6*(2), 127–130. [Doi:10.1107/S0365110X53000478]

Horn, A., Mollendal, H., Sekiguchi, O., Uggerud, E., Roberts, H., Herbst, E., Fridgen, T. D., 2004., The Gas Phase Formation of Methyl Formate in Hot Molecular Cores. *The Astrophysical Journal*, *611*(1), 605–614. [Doi:10.1086/422137]

Hovington Pierre, Dominique Drouin and Raynald Gauvin, 1997., volume 19, Issue 1, pages 1–14, Doi: 10.1002/sca.4950190101 http://dx.doi.org/10.1016/S0301-0104 (97)00137-7 (Webpage)

Huang, C.-Y. & Pohl, M., 2008., Production of neutrinos and secondary electrons in cosmic sources. *Astroparticle Physics*, 29(4), pp.282–289.

Hudson, R. L., M. H. Moore, and P. A. Gerakines. 2001., "The Formation of Cyanate Ion (OCN-) in Interstellar Ice Analogs." *The Astrophysical Journal* 550 1140-1150

Hudson, R.L., Moore, M.H. & Cook, A.M., 2005., IR characterization and radiation chemistry of glycolaldehyde and ethylene glycol ices. *Advances in Space Research*, 36(2), pp.184–189.

Huffman, R.E., 1969., Absorption cross-sections of atmospheric gases for use in aeronomy. *Canadian Journal of Chemistry*, 47(10), pp.1823–1834.

Hunt, H.D. & Simpson, W.T., 1953., Spectra of Simple Amides in the Vacuum Ultraviolet 1. *Journal of the American Chemical Society*, 75(18), pp.4540–4543.

Ikeda, M., Ohishi, M., Nummelin, A., Dickens, J. E., Bergman, P., Hjalmarson, A., & Irvine, W. M., 2001., Survey Observations of C_2H_4O and CH_3CHO toward Massive Star forming Regions. *The Astrophysical Journal*, *560*(2), 792–805. [Doi:10.1086/322957]

Ioppolo, S., Cuppen, H. M., van Dishoeck, E. F., & Linnartz, H., 2011., Surface formation of HCOOH at low temperature., *Monthly Notices of the Royal Astronomical Society*, *410*(2), 1089–1095. [Doi:10.1111/j.1365-2966.2010.17515.x]

Jacox, M.E.; Thompson, W.E., 1990., *The vibrational spectra of molecular ions isolated in solid neon. IV. NO+, NO-, ONNO+, and ONNO-*, *J. Chem. Phys.*, 93, 11, 7609.

Jamieson C.S., C.J. Bennett, A.M. Mebel, R.I. Kaiser, 2005., Investigating the mechanism for the formation of nitrous oxide [N 2O(X 1Σ+)] in extraterrestrial ices, *The Astrophysical Journal*, 624, pp. 436

Jefferts, K. B., Penzias, A. A., and Wilson, R. W., 1970., Observation of the CN Radical in the Orion Nebula and W51., *The Astrophysical Journal*, *161*, L87. [Doi: 10.1086/180576]

Jewitt D. and J. Luu 2004., Crystalline Water Ice in Kuiper Belt Object (50000) Quaoar. *Nature,* 432, 731-733

Jheeta, S., A. Domaracka et al., 2012., "The irradiation of pure CH3OH and 1:1 mixture of NH3:CH3OH ices at 30 K using low energy electrons." *Chemical Physics Letters* 460(1-3): 108-111. 556: 359–364

John H Black et al., 1987., Molecules at early epochs, *The Astrophysical Journal*, Part 1 (ISSN 0004-637X), vol. 317, 442-449.

Johnstone W M, Mason N J, Newell W R, Biggs P, Marston G and Wayne R P, 1992., *J. Phys. B: At. Mol. Opt.Phys.* **25** 1

Jones, B.M. et al., 2011., Formation of benzene in the interstellar medium. *Proceedings of the National Academy of Sciences of the United States of America*, 108(2), 452– 457.

Jones, B.M., Bennett, C.J. & Kaiser, R.I., 2011., Mechanistical Studies on the Production of Formamide (H2NCHO) Within Interstellar Ice Analogs. *The Astrophysical Journal*, 734(2), p.78. [Doi: 10.1088/0004-637X/734/2/78]

Jurgen. Hinze , Curl R. F., 1964., Infrared Spectrum of N-Methylenemethylamine, J. Am. Chem. Soc., 86 (23), pp.5068–5070. [Doi: 10.1021/ja01077a004]

K. ltoh and T. Shimanouchi, 1972., *J. Mol. Spectrosc.* 43 86.

Kalmus, E. & Hercules, D.M., 1972., A Mechanistic Study of the Photo-Fries Rearrangement of Phenyl Acetate'. , 3(1), pp.449–456.

Kang, T.Y., Shin, S.K. & Kim, H.L., 2003., Photodissociation Dynamics of Allyl Alcohol at 193 nm. *The Journal of Physical Chemistry A*, 107(50), pp.10888–10892.

Kato, H. et al., 2011., A study of electron scattering from benzene: excitation of the 1B1u, 3E2g, and 1E1u electronic states. *The Journal of chemical physics*, 134(13), p.134308.

Katon, J. E., & Ranieri, N. L. 1978., The Infrared Spectrum of Crystalline Methyl Formate. *Spectroscopy Letters*, *11*(6), 367–373. [Doi:10.1080/00387017808067757]

Katsumata, S.; Shiromaru, H.; Kimura, T., 1984., Photoelectron angular distribution and assignment of photoelectron spectrum of ozone, Bull. *Chem. Soc. Japan.*, 57, 1784. (O3+)

Khanna R. K., M. S. Lowenthal ,H. L. Ammon, M. H. Moore, 2002., *Astrophysical Journal Supp.* 140, 457.

Kuo, Y.-P. et al., 2007., Absorption spectra in the vacuum ultraviolet region of methanol in condensed phases., *Chemical Physics Letters*, 447(1-3), pp.168–174.

Laas, J. C., Garrod, R. T., Herbst, E., & Widicus Weaver, S. L. 2011., Contributions from grain surface and gas phase chemistry to the formation of methyl formate and its structural isomers., *The Astrophysical Journal*, *728*(1), 71. DOI:10.1088/0004-637X/728/1/71

Ladell J., Post B., 1954., *Acta. Cryst.*7 559.

Lafosse, a. et al., 2009., Surface functionalization by low-energy electron processing of molecular ices. *Surface Science*, 603(10-12), pp.1873–1877.

Lafosse, A., Bertin, M. and Azria, R., 2009., Electron driven processes in ices: Surface functionalization and synthesis reactions., *Progress in Surface Science*, 84(5-6), pp.177–198.

Langford, S. R., Batten, A. D., Kono, M., & Ashfold, M. N. R. 1997., Near-UV photodissociation dynamics of formic acid., *Journal of the Chemical Society, Faraday Transactions*, *93*(21), 3757–3764. [Doi: 10.1039/a704119e]

Lapinski, A., J. Spanget-Larsen, J. Waluk, J.G. Radziszewski, 2001., Vibrations of nitrous oxide: Matrix isolation Fourier transform infrared spectroscopy of twelve N2O isotopomers, *Journal of Chemical Physics*, 115, pp. 1757

Leach, S., Schwell, M., Dulieu, F., Chotin, J.-L., Jochims, H.-W., & Baumgrtel, H. 2002., Photophysical studies of formic acid in the VUV absorption spectrum in the 6.22 eV region, *Physical Chemistry Chemical Physics*, *4*(20), 5025–5039. [Doi: 10.1039/b205729h]

Leung, C. M., Herbst, E., & Huebner, W. F. 1984., Synthesis of complex molecules in dense interstellar clouds via gas-phase chemistry - A pseudo time-dependent calculation., The Astrophysical Journal Supplement Series, 56, 231. [Doi:10.1086/190982]

Liu, S., Girart, J. M., Remijan, A., & Snyder, L. E. 2002., Formic Acid in Orion KL from 1 Millimeter Observations with the Berkeley Illinois Maryland Association Array., *The Astrophysical Journal*, *576*(1), 255–263. [Doi: 10.1086/341620]

Liu, S., Mehringer, D. M., & Snyder, L. E. 2001., Observations of Formic Acid in Hot Molecular Cores., *The Astrophysical Journal*, *552*(2), 654–663. [Doi: 10.1086/320563]

Liu, X.-W. et al., 2001., Chemical abundances of planetary nebulae from optical recombination lines - III. The Galactic bulge PN M 1-42 and M 2-36. *Monthly Notices of the Royal Astronomical Society*, 327(1), pp.141–168.

M. Räsänen, 1983, *J. Mol. Struct.* 101 275-286.

Maçôas, E. M. S., Lundell, J., Pettersson, M., Khriachtchev, L., Fausto, R., and Räsänen, M. 2003., Vibrational spectroscopy of cis- and trans-formic acid in solid argon., *Journal of Molecular Spectroscopy*, *219*(1), 70–80. [Doi: 10.1016/S0022-2852(03)00018-3]

Mardyukov, E. Sánchez-Garcia, P. Rodziewicz, N. L. Doltsinis, W. Sander, 2007. *J. Phys. Chem. A.* 42 10552.

Maréchal, Y., 1987., IR spectra of carboxylic acids in the gas phase: A quantitative reinvestigation. *The Journal of Chemical Physics*, *87*(11), 6344–6353. [Doi:10.1063/1.453464]

Mason N.J., A. Dawes, P.D. Holtom, R.J. Mukerji, M.P. Davis, B. Sivaraman, R.I. Kaiser, S.V. Hoffmann, D.A. Shaw, 2006. *Faraday Discussions*, 133, 311.

Mason, N J, Gingell, J M, Davies, J A, Zhao, H, Walker, Isobel, Siggel, M R F., 1996., VUV optical absorption and electron energy-loss spectroscopy of ozone. *Journal of Physics B Atomic Molecular and Oprtical Physics*, *29*(14), pp. 3075–3089. [Doi:10.1088/0953-4075/29/14/019]

Mason, N.J. et al., 2014., Electron induced chemistry: a new frontier in astrochemistry., *Faraday Discussions*. [Doi: 10.1039.c4fd00004h]

Mason, N.J. et al., 2005., Atmospheric chemistry with synchrotron radiation. *Journal of Physics B: Atomic, Molecular and Optical Physics*, 38(9), pp.S893–S911.

Mathis, J. S. 1990., Interstellar Dust and Extinction., *Annual Review of Astronomy and Astrophysics*, *28*(1), 37–70. [Doi:10.1146/annurev.aa.28.090190.000345]

McGraw, G.E.; Bernitt, D.L.; Hisatsune, I.C.,1965., Vibrational Spectra of Isotopic Nitric Acids, J. Chem. Phys., 42, 1, 237. [Doi:10.1063/1.1695682]

Mehringer, R. Moreno, G. Paubert, T. G. Phillips, H. Rauer, 2000., *Astronomy and Astrophysics* 353 1101.

Melvin B robin, 1974., Higher excited state of polyatomic molecules, , volume 1, 2, Academic press, London

Millar, T. J., Walsh, C., Cordiner, M. A., Ní Chuimín, R., & Herbst, E., 2007., Hydrocarbon Anions in Interstellar Clouds and Circumstellar Envelopes, *The Astrophysical Journal*, *662*(2), L87–L90. [Doi: 10.1086/519376]

Modica, P., & Palumbo, M. E., 2010., Formation of methyl formate after cosmic ion irradiation of icy grain mantles, *Astronomy and Astrophysics*, *519*, A22. [Doi:10.1051/0004-6361/201014101]

Modica, P., Palumbo, M.E. & Strazzulla, G., 2012., Formation of methyl formate in comets by irradiation of methanol-bearing ices. *Planetary and Space Science*, 73(1), pp.425–429. [Doi: 10.1016/j.cplett.2012.10.005]

Moore, M. H., R. L. Hudson, and P. A. Gerakines. 2001., "Mid- and Far-Infrared Spectroscopic Studies of the Influence of Temperature, Ultraviolet Photolysis, and Ion Irradiation on Cosmic-Type Ices." *Spectrochimica Acta A* 57 pp.843-858

Morgan H.W, Staats P.A, Goldstein J.H, 1957., Infrared spectra of $N^{15}H_3$ and $N^{15}H_4^+$, *J. Chem. Phys.*, 27,1212-1213

Nguyen, J., 2011., *Phys. Chem. A 115*, 841–851.

Nunes, Y., Martins, G., Mason, N. J., Duflot, D., Hoffmann, S. V, Delwiche, J., Limão-Vieira, P., 2010., Electronic state spectroscopy of methyl formate probed by high resolution VUV photoabsorption, He(i) photoelectron spectroscopy and ab initio calculations, *Physical chemistry chemical physics*, *12*(48), 15734–43. [DOI: 10.1039/c0cp00051e]

Öberg, K.I. et al., 2010., A cold complex chemistry toward the low-mass protostar b1-b: evidence for complex molecule production in ices. *The Astrophysical Journal*, 716(1), pp.825–834.

Park, J., & Woon, D. E. 2006., Theoretical Modeling of Formic Acid (HCOOH), Formate ($HCOO^-$), and Ammonium ($NH4^+$). *The Astrophysical Journal*, *648*(2), 1285–1290. [Doi:10.1086/506175]

Parsons, B.F., Szpunar, D.E. & Butler, L.J., 2000., Emission Spectroscopy of Dissociative Allyl Iodide and Allyl Alcohol Excited at 199.7 nm. *The Journal of Physical Chemistry A*, 104(46), pp.10669–10674.

Pickett, L.W., Muntz, M. & McPherson, E.M., 1951., Vacuum Ultraviolet Absorption Spectra of Cyclic Compounds. I. Cyclohexane, Cyclohexene, Cyclopentane, Cyclopentene and Benzene 1. *Journal of the American Chemical Society*, 73(10), pp.4862–4865.

Pilling, S. et al., 2012., Formation of unsaturated hydrocarbons in interstellar ice analogues by cosmic rays. *Monthly Notices of the Royal Astronomical Society*, 423(3), pp.2209–2221.

Plekan, O., Cassidy, A., Balog, R., Jones, N. C., & Field, D., 2012., Spontaneous electric fields in films of cis-methyl formate. *Physical chemistry chemical physics*, *14*(28), 9972–9976. [Doi:10.1039/c2cp41229b]

Prasad S.S. and Huntress W.T., 1980., *The Astrophysical Journal Suppliments*. **43,** 1-35

Prasad, S.S. & Tarafdar, S.P., 1983., UV radiation field inside dense clouds - Its possible existence and chemical implications. *The Astrophysical Journal*, 267, p.603. [http://adsabs.harvard.edu/DOI/10.1086/160896]

Raunier. S, T. Chiavassa, F. Duvernay, F. Borget, J.P. Aycard, E. Dartois, L. dHendecourt, 2004., *Astronomy and Astrophysics*. 416 165.

Remijan, A. J., Wyrowski, F., Friedel, D. N., Meier, D. S., & Snyder, L. E., 2005., A Survey of Large Molecules toward the Proto–Planetary Nebula CRL 618. *The Astrophysical Journal*, *626*(1), 233–244. [Doi: 10.1086/429750]

Remijan, A., Shiao, Y. S., Friedel, D. N., Meier, D. S., & Snyder, L. E., 2004., A Survey of Large Molecules of Biological Interest toward Selected High Mass Star forming Regions. *The Astrophysical Journal*, *617*(1), 384–398. [Doi: 10.1086/425266]

Requena-Torres, M. A., Martín-Pintado, J., Rodríguez-Franco, A., Martín, S., Rodríguez-Fernández, N. J., & de Vicente, P. 2006., Organic molecules in the Galactic center., *Astronomy and Astrophysics*, *455*(3), 971–985. [Doi: 10.1051/0004-6361:20065190]

Robin Melvin B., 1974., Higher excited state of polyatomic molecules, Academic Press, 1, P-86, London.

Rodgers, S. D., & Charnley, S. B. 2001., Organic synthesis in the coma of Comet Hale-Bopp, *Monthly Notices of the Royal Astronomical Society*, *320*(4), L61–L64. [Doi:10.1046/j.1365-8711.2001.04208.x]

Rubin R.H., G.W. Swenson, Jr., R.C. Solomon, H.L. Flygare, 1971., *The Astrophysical Journal* 169 L39.

Sakai, N., Sakai, T., & Yamamoto, S., 2007., Methyl Formate in the NGC 2264 IRS 1 Region., *The Astrophysical Journal*, *660*(1), 363–369. [Doi: 10.1086/512774]

Salpeter, E. E., 1977., Formation and Destruction of Dust Grains., *Annual Review of Astronomy and Astrophysics*, *15*(1), pp. 267–293. [Doi:10.1146/annurev.aa.15.090177.001411]

Savage, B. D., & Mathis, J. S., 1979., Observed Properties of Interstellar Dust. *Annual Review of Astronomy and Astrophysics*, *17*(1), pp. 73–111. [Doi:10.1146/annurev.aa.17.090179.000445]

Schutte, W. A., Boogert, A. C. A., Tielens, A. G. G. M., Whittet, D. C. B., Gerakines, P. A., Chiar, J. E., & Ehrenfreund, P. 1999., Weak ice absorption features at 7. 24 and 7. 41 μm in the spectrum of the obscured young stellar object W 33A, *Astronomy and Astrophysics*, *343*, pp. 966–976.

Sheppard and Erkelens, 1984., Vibrational Spectra of Species Adsorbed on Surfaces: Forms of Vibrations and Selection Rules for Regular Arrays of Adsorbed Species. *Appl. Spec.* 38, pp. 471-485

Shimanouchi, T., 1972., Tables of Molecular Vibrational Frequencies Consolidated Volume I, National Bureau of Standards, 1-160.

Sims I. R., J. L. Queffelec, D. Travers, B. R.Rowe, L. B. Herbert, J. Karthäuser, and I. W. M. Smith, 1993., *Chem. Phys. Lett.* 211 (4-5), 461

Sivaraman B et al., 2012., VUV spectroscopy of formamide ices, *Chemical Physics Letters*, 554, pp. 57–59

Sivaraman, B. et al., 2014., Electron impact dissociation and VUV photoabsorption of frozen formamide. *Chemical Physics Letters*, 608, pp.404–407. [Doi: 10.1016/j.cplett.2014.05.080]

Sivaraman, B., Raja Sekhar, B. N., Nair, B. G., Hatode, V., & Mason, N. J. 2013., Infrared spectrum of formamide in the solid phase. *Spectrochimica acta. Part A, Molecular and biomolecular spectroscopy*, *105*, pp. 238–244. [Doi:10.1016/j.saa.2012.12.039]

Snow, T. P., and McCall, B. J. 2006., Diffuse Atomic and Molecular Clouds. *Annual Review of Astronomy and Astrophysics*, *44*(1), pp. 367–414. [Doi:10.1146/annurev.astro.43.072103.150624]

Strazzulla, G. & Baratta, G., 1991., Laboratory study of the IR spectrum of ion-irradiated frozen benzene. *Astronomy and Astrophysics*, 241, pp.310–316.

Su, H., He, Y., Kong, F., Fang, W., and Liu, R. 2000., Photodissociation of formic acid. *The Journal of Chemical Physics*, *113*(5), pp. 1891–1897. [Doi:10.1063/1.482076]

Susan L. Boyd and Russell J. Boyd, 2007., A density functionl theory of methanol clusters, *J. Chem. Theory Comput.*, 3 (1), pp. 54–61 [Doi: 10.1021/ct6002912]

Teolis, B.D., Famá, M. & Baragiola, R. a, 2007., Low density solid ozone. *The Journal of chemical physics*, 127(7), p.074507.

Tercero, B. et al., 2013., Discovery of Methyl Acetate and Gauche Ethyl Formate in Orion. *The Astrophysical Journal*, 770(1), p.L13.

Tielens AGGM, 2013, The molecular universe, *Rev. Mod. Phys.*, 85, 1021

Tielens AGGM 2006., Physics and chemistry of interstellar medium, Cambridge University press, [http://dx.DOI.org/10.1017/CBO9780511819056]

Turner, B. E., & Zuckerman, B. 1974., Microwave Detection of Interstellar CH. *The Astrophysical Journal, 187*, L59. [Doi:10.1086/181396]

van Broekhuizen, J.V. Keane, W.A. Schutte, 2004., *Astronomy and Astrophyics* 415 425.

Van Dishoeck, E. F. 2004., ISO spectroscopy of gas and dust: From Molecular Clouds to Protoplanetary Disks. *Annual Review of Astronomy and Astrophysics, 42*(1), pp. 119–167. [Doi:10.1146/annurev.astro.42.053102.134010]

Vicente, a. et al., 2009., Photoabsorption measurements and theoretical calculations of the electronic state spectroscopy of propionic, butyric, and valeric acids. *Physical Chemistry Chemical Physics*, 11(27), p.5729.

Wachtershauser G., Origin of life. Life as we don't know it, 2000., *Science*, 289, 1307

Ward, H.R. & Wishnok, J.S., 1968., Vacuum ultraviolet photolysis of benzene. *Journal of the American Chemical Society*, 90(20), pp.5353–5357.

Webber, W. R. 1998, *The Astrophysical Journal*, 506, 329

Woods, P.M., 2011., The Formation of Benzene in Dense Environments. *EAS Publications Series*, 46, pp.235–240.

Yu, G.; Duxbury, G., 1992., High-resolution diode laser spectroscopy of the Î½16 band of N-methylmethylenimine, *J. Mol. Spectrosc.*, 155, 1, 105. [Doi:10.1016/0022-2852(92)90551-X]

Zheng, W. & Kaiser, R.I., 2007., An infrared spectroscopy study of the phase transition in solid ammonia. *Chemical Physics Letters*, 440(4-6), pp.229–234. [Doi: 10.1016/j.cplett.2007.04.070]

Zheng, W. et al., 2008., Formation of Nitrogen and Hydrogen bearing Molecules in Solid Ammonia and Implications for Solar System and Interstellar Ices. *The Astrophysical Journal*, 674(2), pp.1242–1250. [Doi: 10.1086/523783]

Zuckerman, B., Ball, J. A., & Gottlieb, C. A. 1971., Microwave Detection of Interstellar Formic Acid, *The Astrophysical Journal, 163*, L41. [Doi: 10.1086/180663]

PUBLICATIONS

- Vacuum ultraviolet and infrared spectra of condensed methyl acetate on cold astrochemical dust analogs, Sivaraman, B., **Nair, B. G.,** Lo, J.-I., Kundu, S., Davis, D., Prabhudesai, V., Raja Sekhar, B. N., Mason, N. J. Cheng, B. M., Krishnakumar, E., *The Astrophysical Journal*, *778*(2), 2013. 10.1088/0004-637X/778/2/157
- Infrared spectrum of formamide in the solid phase, B. Sivaraman, B.N. Raja Sekhar, **B.G. Nair**, V. Hatode, N.J. Mason, *Spectrochimica Acta Part A: Molecular and Biomolecular Spectroscopy*,105, 2013. http://dx.doi.org/10.1016/j.saa.2012.12.039
- VUV photo-absorption spectroscopy of condensed formic acid and methyl formate, **B. G. Nair**, B. Sivaraman, E. Zymanska, S. V. Hoffman, N C Jones, N. J. Mason (Submitted to *Physical Chemistry Chemical Physics, July 2014*).
- Vacuum Ultraviolet Photoabsorption of Interstellar Solid Ozone and Presence of Ozone on Moon, B. Sivaraman, **B. G. Nair**, B. N. Raja Sekhar, J. I. Lo, R. Sridharan, B. M. Cheng, N. J. Mason, *Chemical Physics Letters*, 603, 2014. http://dx.doi.org/10.1016/j.cplett.2014.04.021
- Electron Impact Dissociation and VUV Photo-absorption of Frozen Formamide, B. Sivaraman, **B. G. Nair**, B. N. Raja Sekhar, N. C. Jones, S. V. Hoffman, N. J. Mason , *Chemical Physics letters,* 608, *2014.* DOI: 10.1016/j.cplett.2014.05.080 http://www.sciencedirect.com/science/article/pii/S000926141400462X
- Electron Induced Chemistry: A New Frontier in Astrochemistry, Nigel J Mason, **Binukumar G Nair**, Sohan Jeehta and Ewelina Szymanska, *Faraday Discussions, 2014, http://pubs.rsc.org/en/content/articlelanding/2014/fd/c4fd00004h#!divAbstract* 10.1039/C4FD00004H
- The temperature effect on glycine decomposition induced by 2 keV electron bombardments in space analog conditions, Pilling S., **Nair B.G**, Escobar A., Fraser H. Mason N.J, EPJ D, 68:58, 2014, http://dx.doi.org/10.1140/epjd/e2014-40739-9.

- Processing of simulated 'Enceladus' surface ice by energetic electrons, A. Bergantini, S. Pilling, **B. G. Nair**, N.J. Mason, H.J. Fraser, (Accepted for publication in *Astronomy and Astrophysics, August 2014*).
- Temperature dependent VUV photo-absorption spectroscopy of solid benzene, **B. G. Nair**, B. Sivaraman, E. Zymanska, S. V. Hoffman, N C Jones, N. J. Mason (To be submitted to *Chemical Physics Letters*).
- Electron impact dissociation and thermal processing of methanol, ammonia mixtures in interstellar medium conditions (In preparation).
- Electron processing of condensed ice films of nitric oxide (NO) and nitric oxide, water ($NO:H_2O(1:1)$) mixtures (In preparation).
- Electron irradiation and thermal processing of interstellar ice analogues of methyl formate ($HCOOCH_3$), acetic acid (CH_3COOH) and glycol aldehyde ($C_2H_4O_2$) (In preparation).

CONFERENCE CONTRIBUTIONS

ORAL PRESENTATIONS

1. Temperature dependent VUV and FTIR spectroscopy of condensed formic acid and methyl formate, LYDAN, January 2014, Leiden Observatory, Leiden University, The Netherlands
2. VUV photo-absorption studies of ozone (O_3) at 10 K
   ANUMOCP XXIII, July 2013, Nottingham University, Nottingham, UK
3. Spectroscopy and chemical synthesis of interstellar ice analogues
   CEPSAR, Science meeting, May 2013, The Open University, UK
4. Electron irradiation and temperature processing of isomers of acetic acid
   The molecular Universe, COST action meeting, April 2013, Windsor, UK
5. Electron irradiation of methyl formate
   Atomic and molecular interaction group-IOP, June 2012, UCL, London, UK
6. Electron irradiation of interstellar ice analogues
   CEPSAR, Science meeting, May 2012, The Open University, UK

POSTER PRESENTATIONS

1. Electron irradiation of interstellar ice analogues
   B.G. Nair and N J Mason
   The Molecular Universe, Posters from the proceedings of the 280th Symposium of the International Astronomical Union, 2011, Toledo, Spain
   2011IAUS..280P.272N
2. VUV spectroscopy of interstellar ice analogues
   B. G. Nair, B. Sivaraman, E. Zymanska, S. V. Hoffman, N C Jones , N. J. Mason, ASTROSURF meeting, June, 2011, Herriot Watt University, Edinburgh, UK
3. VUV photo-absorption studies of condensed formamide
   B. G. Nair, B. Sivaraman, E. Zymanska, S. V. Hoffman, N C Jones , N. J. Mason, COST action meeting, August, October 2011 Valetta, Malta
4. Temperature dependent VUV spectroscopy of frozen benzene
   B.G. Nair and N. J. Mason, CDAMOP 2011, University of Delhi, India
5. Electron irradiation of methyl formate and acetic acid in solid amorphous water
   B.G. Nair and N. J. Mason, YAM meeting, November 2012, UCL, London, UK
6. Electron irradiation of structural isomers of acetic acid
   B.G. Nair and N. J. Mason, LASSIE workshop, November 2012, Paris, France